Studies of Intermolecular Interactions in Atmospheric Aggregates: From Molecular Clusters to Aerosols

by

Elijah G. Schnitzler

A thesis submitted in partial fulfillment of the requirements for the degree of

Doctor of Philosophy

Department of Chemistry

University of Alberta

© Elijah G. Schnitzler, 2016

Abstract

Intermolecular interactions dictate the fate and impact of atmospheric oxygenated organic compounds that form from the photo-oxidation of hydrocarbons. Here, intermolecular interactions in aggregates involving photo-oxidation products of aromatic precursors are examined using an interdisciplinary approach. Molecular-scale aggregates – in particular, complexes of water and carboxylic acids – were investigated using rotational spectroscopy. The lowest-energy structures of the monohydrates of two aromatic carboxylic acids, benzoic acid and *o*-toluic acid, were determined experimentally; the water and acid moieties hydrogen bond to give six-membered intermolecular rings. The percentage of each acid hydrated in the gas phase is predicted to be low, but these interactions are important for aromatic acids at the air-water interface of aqueous particles. The two lowest-energy isomers of the oxalic acid–water complex, a probable nucleation precursor, were also observed. In the lowest-energy isomer, water bridges the two acid groups and lowers the barrier to decarboxylation. In the other isomer, water hydrogen bonds to only one group and increases the barrier. For larger dicarboxylic acids, the latter topology is predicted to be the most stable, so water-catalysed enhancement of overtone-induced decarboxylation is plausible for only oxalic acid. The spectra, structures, and internal dynamics of four methyl- and dimethylnaphthalenes, small polycyclic aromatic hydrocarbons present in the atmosphere, were also investigated. Nano-scale aerosols – in particular, internally-mixed particles of black carbon and secondary organic aerosol – were investigated using smog chamber experiments. The morphological evolution of black carbon due to coatings of secondary organic aerosol is the same for a series of four aromatic precursors. The evolution of black carbon is found to be dependent on the coating surface tension; higher

surface tensions lead to more compact black carbon particles, as intermolecular interactions between molecules in the coating become stronger. Based on the observed surface tension-dependence, the surface tension of secondary organic aerosol derived from *m*-xylene was determined, providing an essential constraint on global climate models. Cumulatively, these investigations provide insights into the fate and impact of oxidation products in the gas phase, at the air-water interface, and in the bulk aerosol phase.

Preface

The nature and extent of my contributions to the research included in this thesis are briefly summarized below.

Chapter 3 of this thesis has been published as "The benzoic acid-water complex: a potential atmospheric nucleation precursor studied using microwave spectroscopy and *ab initio* calculations" by E. G. Schnitzler and W. Jäger [*Phys. Chem. Chem. Phys.* **2014**, *16*, 2305-2314]. I was responsible for the calculations, measurements, data analysis, and preparation of the manuscript. W. Jäger was the supervisory author and was involved with concept formation and manuscript composition.

Chapter 4 has been published as "Rotational spectroscopy of the atmospheric photo-oxidation product *o*-toluic acid and its monohydrate" by E. G. Schnitzler, B. L. M. Zenchyzen, and W. Jäger [*Phys. Chem. Chem. Phys.* **2016**, *18*, 448-457]. I was responsible for the calculations, measurements, data analysis, and preparation of the manuscript. B. L. M. Zenchyzen assisted with calculations and measurements. W. Jäger was the supervisory author and was involved with concept formation and manuscript composition.

Chapter 5 has been published as "Contrasting effects of water on the barriers to decarboxylation of two oxalic acid monohydrates: a combined rotational spectroscopic and ab initio study" by E. G. Schnitzler, C. Badran, and W. Jäger [*J. Phys. Chem. Lett.* **2016**, *7*, 1143-1147]. I was responsible for the calculations, measurements, data analysis, and preparation of the manuscript. C. Badran assisted with calculations and measurements. W. Jäger was the supervisory author and was involved with concept formation and manuscript composition.

Chapter 6 has been published as "High-resolution Fourier-transform microwave spectroscopy of methyl- and dimethylnapthalenes" by E. G. Schnitzler, B. L. M. Zenchyzen, and W. Jäger [*Astrophys. J.* **2015**, *805*, 141 (7 pp.)]. I was responsible for the calculations, measurements, data analysis, and preparation of the manuscript. B. L. M. Zenchyzen assisted with the calculations and measurements. W. Jäger was the supervisory author and was involved with concept formation and manuscript composition.

Chapter 8 has been published as “Soot aggregate restructuring due to coatings of secondary organic aerosol derived from aromatic precursors” by E. G. Schnitzler, A. Dutt, A. M. Charbonneau, J. S. Olfert, and W. Jäger [*Environ. Sci. Technol.* **2014**, *48*, 14309-14316]. I was responsible for experiment design, measurements, data analysis, and preparation of the manuscript. A. Dutt assisted with measurements; A. M. Charbonneau assisted with the design of the counter-flow parallel-plate membrane denuder; J. S. Olfert and W. Jäger were the supervisory authors and were involved with concept formation and manuscript composition.

Chapter 9 has been submitted for publication as “Surface tension of secondary organic aerosol derived from soot aggregate aging” by E. G. Schnitzler, J. M. Gac, and W. Jäger. I was responsible for experiment design, measurements, data analysis, and preparation of the manuscript, excluding the description and results of a model constructed by J. M. Gac, which are not presented here. W. Jäger was the supervisory author and was involved with concept formation and manuscript composition.

For my mother

Acknowledgements

First, I would like to thank my supervisor, Prof. Wolfgang Jäger, for his guidance, encouragement, and patience during the course of this research. I am also grateful for the opportunity to work in two distinctive laboratories and to share my results at many conferences; for the many group outings and soccer matches; and for my proximity to the espresso machine.

I thank Prof. Yunjie Xu for many helpful discussions about *ab initio* calculations and spectroscopy, Dr. Matthew Parsons for introducing me to smog chamber experiments, and Prof. Karen McDonald for introducing me to the topic of secondary organic aerosols. I also thank the technical staff in the department, especially Allan Chilton, Jason Dibbs, Vincent Bizon, and Dirk Kelm, for their assistance during this research.

I am grateful to the members of my supervisory committee – Prof. Gabriel Hanna and Prof. Jason S. Olfert – for their advice and support. I thank Prof. Jason S. Olfert, too, for his instruction in aerosol science and technology and introducing me to the topic of soot aggregates. I am grateful to Prof. Sarah Styler for agreeing to be on my exam committee. I am also grateful to Prof. Allan K. Bertram for agreeing to be my external examiner.

I thank past and current members of the Jäger and Xu groups for their camaraderie. Amin, Angelo, Chrissy, Christian, Fahim, Javix, Jiao, Joseph, Nate, Prasanta, Reza, Supriya, Zahra – thanks to you all for being great colleagues and friends.

Funding from the Natural Sciences and Engineering Research Council, Environment Canada, Alberta Innovates, and the University of Alberta is gratefully acknowledged.

I am grateful to my family and friends – in particular, Jon Riener, Olivia Georget, Erin Wagner, and Melissa and Scott Rosen and their family – who helped make Edmonton my home. I am also grateful to Melinda Tanghe for many helpful discussions about writing through the years. Finally, I thank my mother, Meagan Schnitzler, for fostering my early love of learning, encouraging my later academic goals, taking an interest in my research, and providing emotional and tangible support during this work.

Table of Contents

List of Tables

List of Figures

List of Symbols

A, B, C	Rotational constants
B_p	Mechanical mobility
c	Speed of light
C^*	Effective saturation concentration
C_c	Cunningham slip correction factor
C_p	Pre-exponential factor for mass-mobility relationship
D_0	Dissociation energy
D_j	Nozzle diameter
d_m	Mobility diameter
D_m	Mass-mobility exponent
d_p	Particle diameter
d_p^*	Kelvin diameter
$d_a^{\perp}$	Particle aerodynamic diameter having 50% impaction efficiency
d_{ve}	Volume-equivalent diameter
e	Elementary charge
E	Energy
E_0	Electronic energy corrected for ZPE
E_0^{BSSE}	Electronic energy corrected for ZPE and BSSE
E_D	Dissociation energy estimated using pseudo-diatomic model
E_e	Electronic energy
E_{rot}	Rotational energy
E_{vib}	Vibrational energy
F_0	Methyl top rotation constant
F_{12}	Methyl top-methyl top interaction constant
F_D	Drag force
g	Gravitational constant
Gfd	Diameter growth factor

Gfm	Mass growth factor
$\hat{\mathrm{H}}$	Molecular Hamiltonian operator
h	Planck constant
HC	Hydrocarbon concentration
HC_0	Initial hydrocarbon concentration
$\hat{\mathrm{H}}_{\mathrm{rot}}$	Rigid rotor Hamiltonian
$\mathbf{I}$	Diagonal inertial tensor
I_a, I_b, I_c	Moments of inertia about principal axes
J	Rotational quantum number
$\hat{\mathrm{J}}_\mathrm{a}$, $\hat{\mathrm{J}}_\mathrm{b}$, $\hat{\mathrm{J}}_\mathrm{c}$	Angular momentum about principal axes
K	Projection of J onto the principal symmetry axis
k	Force constant
K_a	Quantum number at the oblate limit
k_B	Boltzmann constant
K_c	Quantum number at the prolate limit
k_dep	Particle deposition rate constant
k_dil	Dilution rate constant
k_E	Coulomb constant
k_HC	Reaction rate constant
K_p	Equilibrium constant of hydration
k_s	Force constant of intermolecular stretching vibration
k_w	Gas wall-loss rate constant
L	Length of DMA
M	Molar mass
m_i	Mass of atom i
M_o	Organic aerosol mass concentration
M_p	Aerosol mass concentration
m_p	Particle mass
N	Number concentration
$\overline{N}$	Mean number of counts
N_A	Avogadro constant

N_e	Electronic population
p	Partial pressure
$p^{\ominus}$	Ambient pressure
P_c	Planar moment of inertia
p_s	Saturation vapour pressure
$q^{\ominus}$	Total partition function
Q	Flow rate
$\mathbf{r}$	Electronic coordinates
R	Universal gas constant
r	Distance between an atom and a certain principal axis; Radial position of particle in DMA or CMPA
$\mathbf{R}$	Nuclear coordinates
R_{cm}	Distance between the centres of mass of moieties in a complex
S	Line strength
SOA	SOA concentration
S_r	Saturation ratio
Stk_{50}	Stokes number for 50% impaction
t	Reaction time
T	Temperature
U, V, W	Coherence and population difference terms in density matrix formalism
v	Vibrational quantum number
$V(r)$	Electronic potential energy density
V_3	Three-fold barrier to internal rotation
V_a	Atomic volume
V_{DMA}	Voltage applied in DMA
v_m	Molecular speed
V_{TS}	Terminal settling velocity
x	Mole ratio
Z_p	Electrical mobility
α	Size parameter
γ	Surface tension

δ	Angle between methyl top axis and the *a* principal inertial axis
Δ	Inertial defect
Δ_{corr}	Methyl-top-corrected Δ
ΔE_{int}	Interaction energy
Δ_J, Δ_{JK}, Δ_K, δ_J, δ_K	Quartic centrifugal distortion constants
$\Delta\nu$	Difference between excitation ν and transition ν
ε	Angle between the projection of the methyl top axis onto the *bc* plane and the *b* principal axis
κ	Asymmetry parameter
λ	Wavelength
μ	Reduced mass
μ_a, μ_b, μ_c	Dipole moments about the principal axes
μ_g	Gas viscosity
ν	Frequency
ρ_e	Electron density
ρ_{eff}	Effective density
ρ_p	Particle density
ρ_{SOA}	Material density of SOA from certain precursor
ρ_{soot}	Material density of soot
ς	Activity coefficient
σ	Symmetry number
σ_{fit}	Standard deviation of spectroscopic fit
ϕ	Equivalence ratio
χ	Percentage hydrated; Dynamic shape factor
χ_e	One-electron wavefunction
Ψ	Molecular wavefunction
Ψ_e	Electronic wavefunction
Ψ_N	Nuclear wavefunction
$\nabla\rho$	Electron density gradient
$\nabla^2\rho$	Laplacian of electron density

List of Abbreviations

APM	Aerosol particle mass; e.g. APM analyzer
BA	Benzoic acid
BC	Black carbon
BCP	Bond critical point
BSSE	Basis set superposition error
CAM	Combined axis method
CCN	Cloud condensation nuclei
CPC	Condensation particle counter
CPMA	Centrifugal particle mass analyzer
CPMD	Counter-flow parallel-plate membrane denuder
DCA	Dicarboxylic acid
DFT	Density functional theory
DHC	Dihydroxycarbene
DMA	Differential mobility analyzer
DMN	Dimethylnaphthalene
DOAS	Differential optical absorption spectroscopy
FTMW	Fourier-transform microwave; e.g. FTMW spectrometer
HF	Hartree-Fock method
IF	Intermediate frequency
ISM	Interstellar medium
IVR	Intramolecular vibration redistribution
MN	Methylnaphthalene
MP2	Second-order Møller-Plesset perturbation theory
MW	Microwave
OA	Oxalic acid
OTA	*o*-Toluic acid
PAH	Polycyclic aromatic hydrocarbon

PANH	Polycyclic aromatic nitrogen hetero-cycles
PES	Potential energy surface
PFA	Perfluoroalkoxy; e.g. PFA film
PM	Particulate matter
QTAIM	Quantum theory of atoms in molecules
RF	Radiative forcing
RH	Relative humidity
SAPT	Symmetry adapted perturbation theory
SAPT0	Zeroth-order SAPT
SMPS	Scanning mobility particle sizer
SOA	Secondary organic aerosol
STP	Standard temperature and pressure
TD	Thermo-denuder
UIE	Unidentified infrared emission; e.g. UIE bands
UV	Ultra-violet
VOC	Volatile organic compound
ZPE	Zero-point energy

1 Introduction

Aerosols, suspensions of liquid or solid particles in air, are abundant atmospheric constituents. The total emission rate of atmospheric aerosols on Earth is estimated to be about 2×10^{13} kg yr^{-1} in global models.[1] Over 95% of this mass is composed of sea salt from breaking waves and mineral dust from erosion,[1] but these particles, with diameters of about 10 μm, settle out of the atmosphere quickly and constitute the coarse particle mode in a typical size distribution of atmospheric aerosols.[2] Other natural (biogenic) sources of aerosols are volcanic eruptions[3] and biological detritus.[4] Anthropogenic sources of aerosols include agriculture,[5] industry,[6] and transportation;[7] classes of anthropogenic aerosols include sulfate and nitrate aerosols and soot particles composed primarily of black carbon (BC). Soot is an example of a primary aerosol, because it is emitted as an aerosol by its sources; nitrate and (certain) sulfate aerosols are examples of secondary aerosols, because they are formed in the atmosphere from gas emissions – for example, secondary sulfate aerosol is a product of the oxidation of sulfur dioxide.[8] (Sulfate aerosols can also be of primary origin,[9] emitted directly from coal or fossil fuel combustion, for example.[10]) Similarly, secondary organic aerosol (SOA), discussed below, is a product of the oxidation of hydrocarbons.[11]

One of the reasons atmospheric aerosols are of significant interest is their negative effects on human health. Severe aerosol exposure has been linked to a wide range of human cardiopulmonary diseases,[12,13] including respiratory distress, hypertension,[14] and lung cancer.[15] Nanoparticles are particularly hazardous, because a large fraction passes through the upper respiratory tract and deposits in the alveoli of the lungs.[16,17] For this reason, classification of fine particulate matter ($PM_{2.5}$), consisting of particles with aerodynamic diameters less than 2.5 μm,

is helpful in environmental monitoring and policy-making. In terms of a typical size distribution of atmospheric aerosols, $PM_{2.5}$ includes the nucleation and accumulation modes.[2] Particles retained in the lungs may be reactive or toxic. For example, known carcinogens, like nitro-substituted polycyclic aromatic hydrocarbons (PAHs),[18] occur in atmospheric aerosols.[19]

Atmospheric aerosols also have substantial effects on climate, which are the overarching motivation for the present research. Climate effects are often quantified in terms of "radiative forcing," which may be defined as the perturbation of the energy balance on Earth in terms of watts per square meter of Earth's surface since the year 1750.[20] Aerosols can affect climate directly, by scattering or absorbing solar radiation. For example, BC absorbs solar radiation at all visible wavelengths, so it has a warming effect on climate – denoted by its positive radiative forcing, which is more than half that of carbon dioxide, as shown in Figure 1.1.[20] In contrast, non-absorbing aerosols, which scatter solar radiation into space, have a cooling effect. In addition to these direct effects, several indirect effects complicate the role of aerosols in climate. Aerosols may act as cloud condensation nuclei (CCN), increasing the number concentration and total cross-sectional area of droplets in a cloud and, in turn, increasing scattering.[21] Since the

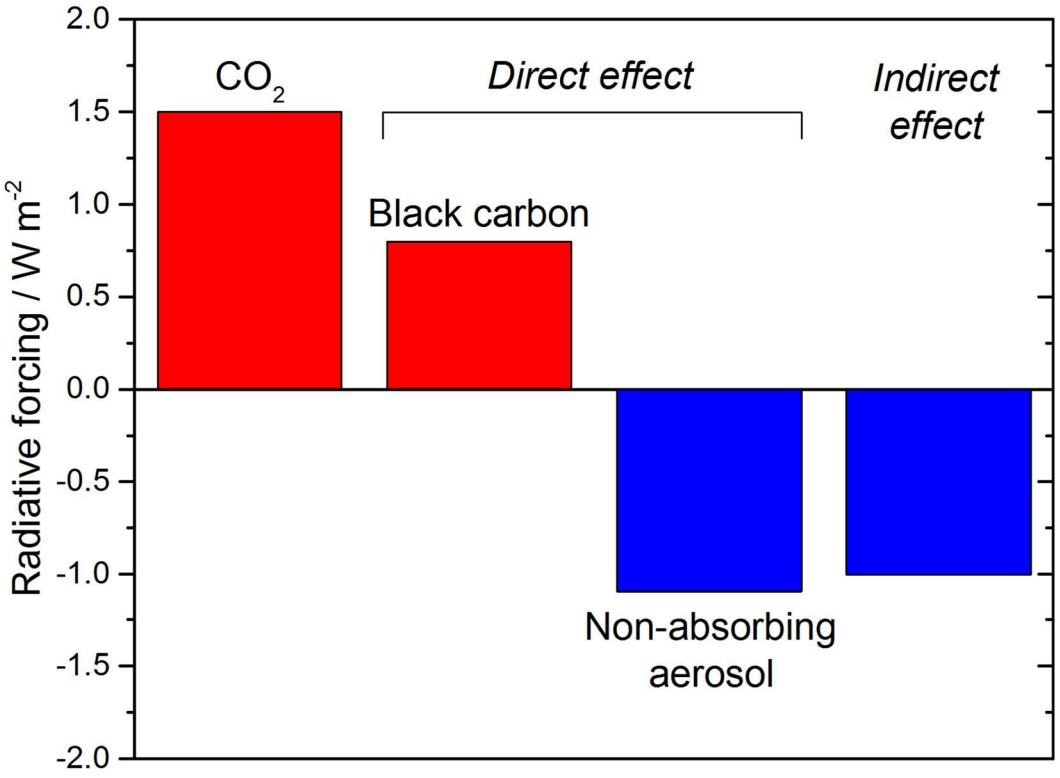

Figure 1.1. Radiative forcings due to the direct and indirect effects of aerosols. The radiative forcing of carbon dioxide is included for comparison. (Adapted from Reference 20.)

cloud droplets are smaller, they have longer lifetimes, further increasing scattering.[22] Another "semi-direct" effect is the evaporation of clouds that occurs when BC absorbs solar radiation and warms the surrounding air, causing further warming.[23] Because of these complex, interconnected effects, aerosols have the most uncertain radiative forcings of all atmospheric constituents, and further constraints in climate models are needed.[24]

One area of uncertainty is the fate and impact of oxygenated organic compounds that form from reactions of anthropogenic and biogenic volatile organic compounds (VOCs) with

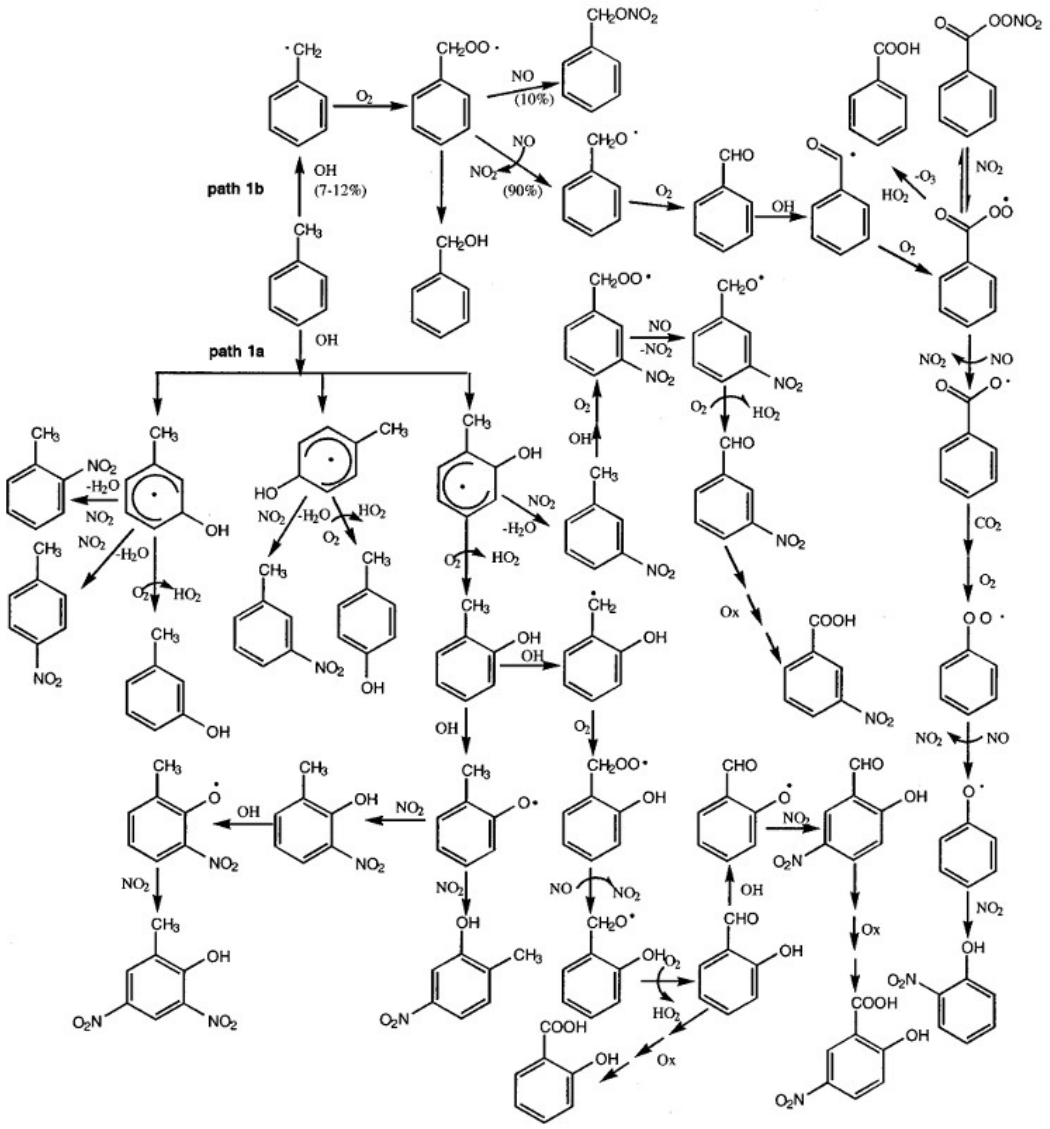

Figure 1.2. Photo-oxidation mechanism of toluene. Path "1a" is hydroxyl radical addition, and path "1b" is hydrogen abstraction. (Reprinted with permission from Reference 26. Copyright 2001 American Chemical Society.)

oxidants, including hydroxyl radical and ozone. Among all anthropogenic VOCs, aromatic hydrocarbons, ubiquitous industrial emissions,[6] are the most important precursors of oxygenated organic compounds.[25] To illustrate the wide array of oxidation products of aromatics in general, the mechanism of hydroxyl radical-initiated oxidation of toluene is shown in Figure 1.2.[26] The mechanism begins with hydroxyl radical addition to the aromatic ring, leading to the constitutional isomers of cresol, or, in a minor route, hydrogen abstraction from the methyl group. Within a few generations, a diverse ensemble of products – including species with hydroxyl, carbonyl, carboxyl, peroxy, nitrate, and nitro functional groups – results from the many possible reactions with oxidants and other atmospheric constituents, like NO_x (NO and NO_2). Among these products, carboxylic acids are particularly abundant.[27]

The fate and impact of products of VOC oxidation in the atmosphere can vary. If the products have sites for hydrogen-bonding, they may participate in complexes with water, sulfuric acid, and ammonia in the gas phase, leading to new particle formation in the absence of pre-existing particles.[28] For example, the addition of aromatic carboxylic acids to mixtures of sulphuric acid and water in the gas phase enhances new particle formation.[29] If the products have hydrophobic and hydrophilic regions, they may become surfactants at the air-water interface of aqueous aerosols, potentially inhibiting further gas uptake and enhancing cloud formation.[30] For example, exposing aqueous ammonium sulfate particles to acetaldehyde enhances the CCN activity of the particles.[31] If the oxidation products are in the presence of pre-existing (seed) particles, they may undergo gas-to-particle partitioning to form SOA, because most of the oxidation products have much lower vapour pressures than their precursors.[11] In the case of toluene, the minor route of hydrogen abstraction by hydroxyl radical leads to the formation of benzaldehyde, and hydrogen abstraction from benzaldehyde leads to the formation of benzoic acid.[26] At 298 K, toluene, benzaldehyde, and benzoic acid have vapour pressures of 3770, 165.1, and 0.1064 Pa, respectively; the increase in the number of oxygenated functional groups leads to more hydrogen bonding in the condensed phase, so the vapour pressure decreases. If the seed particles happen to be BC, the SOA may form a coating that affects the morphological and optical properties of BC.[32] In each of the above scenarios, intermolecular interactions dictate the fate and impact of the oxidation products.

In this thesis, I describe my studies of intermolecular interactions in atmospheric aggregates involving products of aromatic VOC photo-oxidation. An interdisciplinary approach

was taken to study aggregates ranging in size from molecular complexes to nanoparticles. To investigate intermolecular interactions in molecular complexes – in particular, those of water and carboxylic acids – I used quantum chemical calculations and rotational spectroscopy to determine the structures and internal dynamics of these species. To investigate intermolecular interactions in nanoparticles – in particular, internally-mixed particles of BC and SOA – I used smog chamber experiments and aerosol instrumentation to examine the morphological evolution of BC upon coatings.

The organization of the thesis reflects this two-pronged approach. In Chapter 2, I describe how Fourier-transform microwave (FTMW) spectroscopy can be used to study the structures and internal dynamics of atmospherically-relevant species in the gas phase; in fact, rotational spectroscopy is one of the most precise methods for determining the structures of gas-phase species. In Chapters 3 and 4, I describe my FTMW spectroscopic investigations of interactions between water and two aromatic carboxylic acids, benzoic acid and *o*-toluic acid; these interactions are involved in the formation of hydrates,[33] nucleation precursors,[28] and surfactant films.[34] In Chapter 5, I describe my FTMW spectroscopic and computational study of hydrogen-bonding between water and oxalic acid, the most abundant dicarboxylic acid in the atmosphere; these interactions are important in new particle formation[35] and gas-phase decarboxylation.[36] In Chapter 6, I describe my FTMW spectroscopic study of monomers of methyl- and dimethylnaphthalenes, PAHs that are SOA precursors[37] and soot constituents;[38] this work bridges the preceding chapters on rotational spectroscopy and the following chapters on smog chamber experiments. In Chapter 7, I describe how aerosol instrumentation and smog chamber experiments can be used to study the effects of coatings on BC. In Chapter 8, I describe my smog chamber investigation of the evolution of BC morphology due to coatings of SOA from four aromatic VOCs: benzene, toluene, ethylbenzene, and *p*-xylene. In Chapter 9, I describe a further smog chamber investigation of the evolution of BC morphology due to neat liquid coatings and a determination of the surface tension of SOA from *m*-xylene. The findings in Chapters 8 and 9 provide important constraints on the direct and indirect effects of aerosols on climate.[32,39] In Chapter 10, I summarize the most significant results of my research and provide an overview of their implications.

References

1 Textor, C.; *et al.* Analysis and quantification of the diversities of aerosol life cycles with AeroCom. *Atmos. Chem. Phys.* **2006**, *6*, 1777-1813. See bibliography for complete list of authors.

2 Seinfeld, J. H.; Pandis, S. N. Atmospheric composition, global cycles, and lifetimes. *Atmospheric Chemistry and Physics: From Air Pollution to Climate Change*; Wiley: New York, 1998; pp. 49-124.

3 Langmann, B.; Folch, A.; Hensch, M.; Matthias, V. Volcanic ash over Europe during the eruption of Eyjafjallajökull on Iceland, April-May 2010. *Atmos. Environ.* **2012**, *48*, 1-8.

4 Jaenicke, R. Abundance of cellular material and proteins in the atmosphere. *Science* **2005**, *308*, 73.

5 Telloli, C.; Malaguti, A.; Mircea, M.; Tassinari, R.; Vaccaro, C.; Berico, M. Properties of agricultural aerosol released during wheat harvest threshing, plowing and sowing. *J. Environ. Sci. (China)* **2014**, *26*, 1903-1912.

6 Simpson, I. J.; *et al.* Characterization of trace gases measured over Alberta oil sands mining operations: 76 speciated C_2-C_{10} volatile organic compounds (VOCs), CO_2, CH_4, CO, NO, NO_2, NO_y, O_3 and SO_2. *Atmos. Chem. Phys.* **2010**, *10*, 11931-11954. See bibliography for complete list of authors.

7 Tritscher, T.; *et al.* Changes of hygroscopicity and morphology during ageing of diesel soot. *Environ. Res. Lett.* **2011**, *6*, 034026 (10 pp.). See bibliography for complete list of authors.

8 Holloway, A. M.; Wayne, R. P. Sources and sinks of atmospheric species. *Atmospheric Chemistry*; RSC: Cambridge, 2010; pp 25-40.

9 Holt, B. D.; Kumar, R.; Cunningham, P. T. Primary sulfates in atmospheric sulfates: Estimation by oxygen isotope ratio measurements. *Science* **1982**, *217*, 51-53.

10 Guo, Z.; Li, Z.; Farquhar, J.; Kaufman, A. J.; Wu, N.; Li, C.; Dickerson, R. R.; Wang, P. Identification of sources and formation processes of atmospheric sulfate by sulfur isotope and scanning electron microscope measurements. *J. Geophys. Res.* **2010**, *115*, D00K07.

11 Donahue, N. M.; Robinson, A. L.; Stanier, C. O.; Pandis, S. N. Coupled partitioning, dilution, and chemical aging of semivolatile organics. *Environ. Sci. Technol.* **2006**, *40*, 2635-2643.

12 Pope, C. A., III; Dockery, D. W. Health effects of fine particulate air pollution: Lines that connect. *J. Air Waste Manage. Assoc.* **2006**, *56*, 709-742.

13 Valavanidis, A.; Fiotakis, K.; Vlachogianni, T. Airborne particulate matter and human health: Toxicological assessment and importance of size and composition of particles for oxidative damage and carcinogenic mechanisms. *J. Environ. Sci. Health C* **2008**, *26*, 339-362.

14 Brook, R. D.; Kousha, T. Air pollution and emergency department visits for hypertension in Edmonton and Calgary, Canada: A case-crossover study. *Am. J. Hypertens.* **2015**, *28*, 1121-1126.

15 Tie, X.; Wu, D.; Brasseur, G. Lung cancer mortality and exposure to atmospheric aerosol particles in Guangzhou, China. *Atmos. Environ.* **2009**, *43*, 2375-2377.

16 Heyder, J.; Gebhart, J.; Rudolf, G.; Schiller, C. F.; Stahlhofen, W. Deposition of particles in the human respiratory tract in the size range 0.005-15 μm. *J. Aerosol Sci.* **1986**, *17*, 811-825.

17 Lippmann, M.; Yeates, D. B.; Albert, R. E. Deposition, retention, and clearance of inhaled particles. *Brit. J. Ind. Med.* **1980**, *37*, 337-362.

18 Fu, P. P.; Herreno-Saenz, D.; Von Tungeln, L. S.; Lay, J. O.; Wu, Y.-S.; Lai, J.-S.; Evans, F. E. DNA adducts and carcinogenicity of nitro-polycyclic aromatic hydrocarbons. *Environ. Health Perspect.* **1994**, *102*, 177-184.

19 Ravindra, K.; Bencs, L.; Wauters, E.; de Hoog, J.; Deutsch, F.; Roekens, E.; Bleux, N.; Berghmans, P.; Van Grieken, R. Seasonal and site-specific variation in vapour and aerosol phase PAHs over Flanders (Belgium) and their relation with anthropogenic activities. *Atmos. Environ.* **2006**, *40*, 771-785.

20 Hansen, J.; *et al.* Efficacy of climate forcings. *J. Geophys. Res.* **2005**, *110*, D18104 (45 pp.). See bibliography for complete list of authors.

21 Twomey, S. Pollution and the planetary albedo. *Atmos. Environ.* **1974**, *8*, 1251-1256.

22 Albrecht, B. A. Aerosols, cloud microphysics, and fractional cloudiness. *Science* **1989**, *245*, 1227-1230.

23 Ackerman, A. S.; Toon, O. B.; Stevens, D. E.; Heymsfield, A. J.; Ramanathan, V.; E. J. Welton. Reduction of tropical cloudiness by soot. *Science* **2000**, *288*, 1042-1047.

24 Boucher, O.; *et al.* Clouds and aerosols. In *Climate Change 2013: The Physical Science Basis. Contribution of Working Group I to the Fifth Assessment Report of the Intergovernmental Panel on Climate Change*; Stocker, T. F., Qin, G.-K., Plattner, M., Tignor, M., Allen, S. K., Boschung, J., Nauels, A., Xia, Y., Bex, V., Midgley, P. M., Eds.; Cambridge University Press: Cambridge, 2013; pp. 571-657. See bibliography for complete list of authors.

25 Henze, D. K.; Seinfeld, J. H.; Ng, N. L.; Fu, T.-M.; Jacob, D. J.; Heald, C. L. Global modelling of secondary organic aerosol formation from aromatic hydrocarbons: High- vs. low-yield pathways. *Atmos. Chem. Phys.* **2008**, *8*, 2405-2420.

26 Jang, M.; Kamens, R. M. Characterization of secondary organic aerosol from the photooxidation of toluene in the presence of NO_x and 1-propene. *Environ. Sci. Technol.* **2001**, *35*, 3626-3639.

27 Liu, S.; Day, D. A.; Shields, J. E.; Russell, L. M. Ozone-driven daytime formation of secondary organic aerosol containing carboxylic acid groups and alkane groups. *Atmos. Chem. Phys.* **2011**, *11*, 8321-8341.

28 Zhao, J.; Khalizov, A.; Zhang, R.; McGraw, R. Hydrogen-bonding interaction in molecular complexes and clusters of aerosol nucleation precursors. *J. Phys. Chem. A* **2009**, *113*, 680-689.

29 Zhang, R.; Suh, I.; Zhao, J.; Zhang, D.; Fortner, E. C.; Tie, X.; Molina, L. T.; Molina, M. J. Atmospheric new particle formation enhanced by organic acids. *Science* **2004**, *304*, 1487-1490.

30 McNeill, V. F.; Sareen, N.; Schwier, A. N. Surface-active organics in atmospheric aerosols. *Top. Curr. Chem.* **2014**, *339*, 201-260.

31 Sareen, N.; Schwier, A. N.; Lathem, T. L.; Nenes, A.; McNeill, V. F. Surfactants from the gas phase may promote cloud droplet formation. *Proc. Natl. Acad. Sci. U. S. A.* **2012**, *110*, 2723-2728.

32 Peng, J.; *et al.* Markedly enhanced absorption and direct radiative forcing of black carbon under polluted urban environments. *Proc. Natl. Acad. Sci. U. S. A.* **2016**, doi: 10.1073/pnas.1602310113. See bibliography for complete list of authors.

33 Vaida, V.; Headrick, J. E. Physicochemical properties of hydrated complexes in the Earth's atmosphere. *J. Phys. Chem. A* **2000**, *104*, 5401-5412.

34 Ottosson, N.; Romanova, A. O.; Söderström, J.; Björneholm, O.; Öhrwall, G.; Fedorov, M. V. Molecular sinkers: X-ray photoemission and atomistic simulations of benzoic acid and benzoate at the aqueous solution/vapor interface. *J. Phys. Chem. B* **2012**, *116*, 13017-13023.

35 Xu, Y.; Nadykto, A. B.; Yu, F.; Jiang, L.; Wang, W. Formation and properties of hydrogen-bonded complexes of common organic oxalic acid with atmospheric nucleation precursors. *THEOCHEM* **2010**, *951*, 28-33.

36 Staikova, M.; Oh, M.; Donaldson, D. J. Overtone-induced decarboxylation: A potential sink for atmospheric diacids. *J. Phys. Chem. A* **2005**, *109*, 597-602.

37 Chan, A. W. H.; Kautzman, K. E.; Chhabra, P. S.; Surratt, J. D.; Chan, M. N.; Crounse, J. D.; Kürten, A.; Wennberg, P. O.; Flagan, R. C.; Seinfeld, J. H. Secondary organic aerosol formation from photooxidation of naphthalene and alkylnaphthalenes: Implications for oxidation of intermediate volatility organic compounds (IVOCs). *Atmos. Phys. Chem.* **2009**, *9*, 3049-3060.

38 Slowik, J. G.; *et al.* An inter-comparison of instruments measuring black carbon content of soot particles. *Aerosol Sci. Technol.* **2007**, *41*, 295-314. See bibliography for complete list of authors.

39 Riipinen, I.; Yli-Juuti, T.; Pierce, J. R.; Petäjä, T.; Worsnop, D. R.; Kulmala, M.; Donahue, N. M. The contribution of organics to atmospheric nanoparticle growth. *Nature Geosci.* **2012**, *5*, 453-458.

2 Theoretical and experimental approaches to investigate the structures and internal dynamics of atmospherically-relevant species in the gas phase

2.1. Introduction

In this chapter, I describe how rotational spectroscopy can be used to study the structures, energetics, and internal dynamics of atmospherically-relevant species in the gas phase, including carboxylic acid-water complexes, which may be precursors to nucleation in the atmosphere, as discussed in Chapter 1. Specifically, some theoretical and experimental aspects of cavity-based Fourier-transform microwave spectroscopy are presented. In Section 2.1, the concept of the potential energy surface (PES) is introduced, and in Section 2.2, the capability of rotational spectroscopy to discriminate between minimum-energy geometries on the PES is explained. In Section 2.3, the preparation of a cold sample using a supersonic expansion is discussed. Finally, in Section 2.4, the excitation of the cold sample using a pulse of microwave radiation and the subsequent detection of emitted molecular signal is described.

2.2. Potential energy surface

In Chapters 3 to 6, the use of rotational spectroscopy to identify minimum energy structures on a given PES is discussed. In this section, the concept of the PES is briefly discussed in terms of quantum theory. The time-independent Schrödinger equation can be applied to molecules in the absence of external electromagnetic fields; it states that the eigenvalue that results when the molecular Hamiltonian operator, $\hat{H}$, acts on the wavefunction, Ψ, is the energy, E, of the stationary state of the molecule.[1] For the simplest molecule, H_2^+, this is shown in Equation (2.1).

$$\hat{H}(\mathbf{r},\mathbf{R_1},\mathbf{R_2})\Psi(\mathbf{r},\mathbf{R_1},\mathbf{R_2}) = E\Psi(\mathbf{r},\mathbf{R_1},\mathbf{R_2}) \quad (2.1)$$

Here, **r** is the vector giving the coordinates of the lone electron, and $\mathbf{R_1}$ and $\mathbf{R_2}$ are vectors giving the coordinates of nuclei 1 and 2. Since both the electronic and nuclear coordinates are variables in Equation (2.1), the time-independent Schrödinger equation cannot be solved easily using the total Hamiltonian.[1,2] However, since the electron often moves much faster than the nuclei, the nuclei may be considered as stationary on the timescale of the electronic motion. In such cases, one may make the Born-Oppenheimer approximation,[1,2] which allows the wavefunction to be separated into an electronic wavefunction, $\Psi_e(\mathbf{r};\mathbf{R_1},\mathbf{R_2})$, and a nuclear wavefunction, $\Psi_N(\mathbf{R_1},\mathbf{R_2})$, as shown in Equation (2.2).

$$\Psi(\mathbf{r},\mathbf{R_1},\mathbf{R_2}) = \Psi_N(\mathbf{R_1},\mathbf{R_2})\Psi_e(\mathbf{r};\mathbf{R_1},\mathbf{R_2}) \quad (2.2)$$

The nuclear wavefunction will be discussed further in Section 2.2. The electronic wavefunction can be used in the electronic Schrödinger equation, in which the nuclear coordinates are parameters – not variables – as shown in Equation (2.3).

$$\hat{H}_e(\mathbf{r},\mathbf{R_1},\mathbf{R_2})\Psi_e(\mathbf{r};\mathbf{R_1},\mathbf{R_2}) = E_e(\mathbf{R_1},\mathbf{R_2})\Psi_e(\mathbf{r};\mathbf{R_1},\mathbf{R_2}) \quad (2.3)$$

The eigenvalue, $E_e(\mathbf{R_1},\mathbf{R_2})$, is now the electronic energy, instead of the total energy, and it is a function of the nuclear coordinates.

The PES of a molecule composed of n nuclei is $E_e(\mathbf{R_1},\mathbf{R_2},\ldots,\mathbf{R_n})$. The number of dimensions of the PES is equal to the number of vibrational degrees of freedom, which is $3n$ - 5 for linear molecules and $3n$ - 6 for non-linear molecules.[3] Consequently, it is impossible to visualize the full PES of even a triatomic molecule in only three dimensions. However, a full PES is often not necessary to identify all possible stationary points, geometries at which the partial derivatives of electronic energy with respect to all vibrational degrees of freedom are zero.[3]

For example, consider the potential energy of *o*-toluic acid along a single degree of freedom, the internal rotation defined by the C(CH_3)-C-C=O dihedral angle, θ, as shown by in Figure 2.1. Two minima, for which the second partial derivative of electronic energy with respect to the dihedral angle is positive, occur at about $\theta = 0°$ and $\theta = 180°$; the corresponding structures will be labelled conformers **I** and **II**, as in Chapter 4. Conformer **I** is the global minimum, lying 377 cm^{-1} below **II**. The minima are separated by an energy barrier; the maximum energy along this barrier occurs at the transition state, for which the second partial derivative of electronic energy with respect to the dihedral angle is negative. Since there are only two rotatable bonds (defined as sigma bonds between non-terminal heavy atoms, so the

O-H bond is discounted), the remaining minima can be located by varying the O=C-O-H dihedral angle in **I** and **II**, so a PES of only two dimensions, rather than 48, is adequate to identify all of the stationary points of *o*-toluic acid.

At small displacements from a particular minimum, the potential energy can be approximated by that of a harmonic oscillator,[4] as shown in Figure 2.1. (This approximation is poor, as it is for **II**, in cases of anharmonicity.) According to Equation (2.4), the vibrational frequency, ν, of a harmonic oscillator is proportional to the square-root of the force constant, k, which is positive since the minimum is bound.

$$\nu = \frac{1}{2\pi c}\sqrt{\frac{k}{\mu}} \tag{2.4}$$

Here, c is the speed of light, and μ is the reduced mass. In contrast, at small displacements from the transition state, the potential energy can be approximately represented by that of an *inverted*

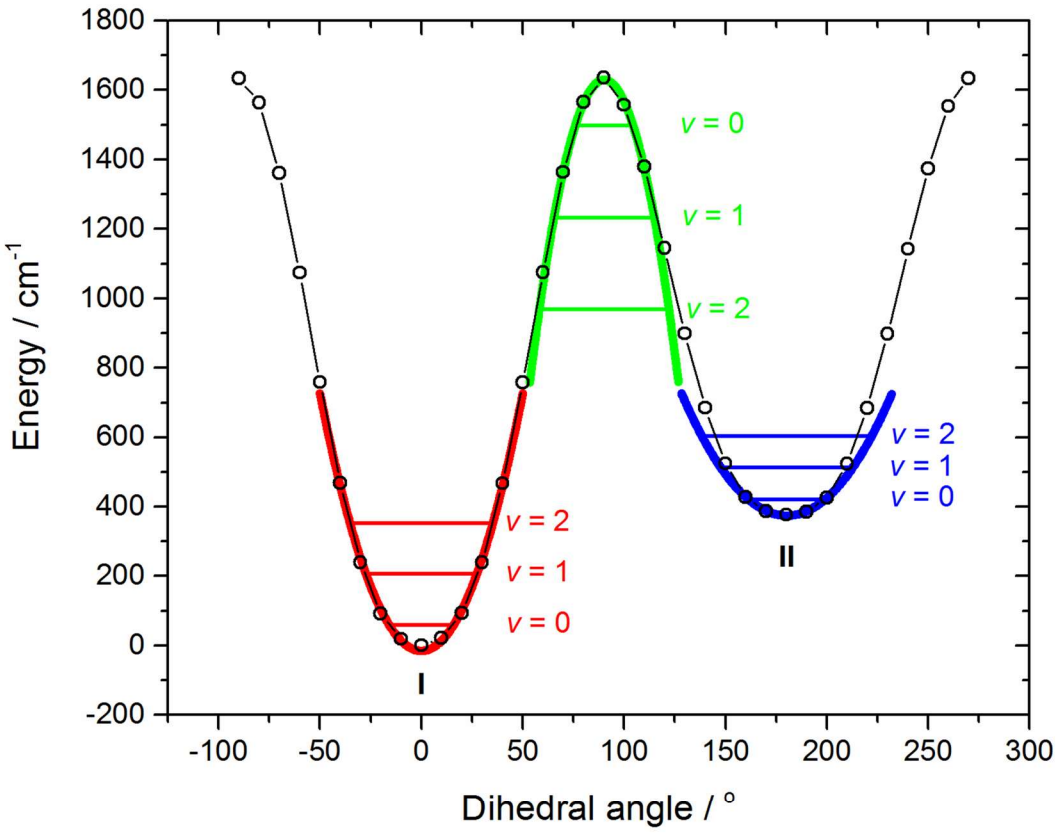

Figure 2.1. Potential energy curve for o-toluic acid along the internal coordinate defined by the C(CH_3)-C-C=O dihedral angle, a measure of the relative orientation of the aromatic ring and the carboxylic acid group, calculated at the B3LYP/6-311++G(d,p) level of theory. The dihedral angle was stepped, and the remaining internal coordinates were optimized. Harmonic oscillator fits to the minima and transition state are also shown, along with their first three vibrational energy levels, scaled by a factor three for clarity.

harmonic oscillator. Since the force constant is negative, the vibrational frequency is imaginary. One imaginary frequency is the universal criteria for a transition state.[3] Higher order saddle-points in the PES have more imaginary frequencies; for example, hilltops are maxima in two dimensions, so they have two imaginary frequencies, like the one discussed in Section 4.3.2.

The relative populations of any two conformers – for example *i* and *j* – can be calculated by assuming a Boltzmann distribution,[5] as shown in Equation (2.5).

$$\frac{N_i}{N_j} = e^{-(E_i - E_j)/k_B T} \tag{2.5}$$

Here, N is number density, E is energy, k_B is the Boltzmann constant, and T is temperature. As discussed above, conformer **I** of *o*-toluic acid lies 377 cm^{-1} (or 4.5 kJ mol^{-1}) above **II**, so at room temperature (298 K), the ratio of number concentration of **I** and **II** is about 6:1. If the energy difference between two conformers is greater than 11.4 kJ mol^{-1}, the ratio of their number concentrations will be greater than 100:1 at room temperature, so the higher-energy conformer can be neglected. (The Boltzmann distribution is also the basis of the Maxwell-Boltzmann distribution that dictates the velocities of gases, as described in Section 2.3.)

The potential energy curve shown in Figure 2.1 was calculated using computational chemistry software,[6] which evaluates Equation (2.1) for molecules using several assumptions. For example, after applying the Born-Oppenheimer approximation to separate nuclear and electronic wavefunctions, the electronic Schrödinger equation still cannot be solved exactly for a species with two or more electrons, since there is more than one variable.[7] The Hartree-Fock method resolves this problem by separating the electronic wavefunction, Ψ_e, into one-electron wavefunctions, χ_e, also called orbitals – leading this method to also be called the orbital approximation.[7-9] This approximation is shown for the helium atom in Equation (2.6), which is an example of a Slater determinant.[8]

$$\Psi_e(\mathbf{r_1},\mathbf{r_2},\mathbf{R}) = \chi_{e,1}(\mathbf{r_1},\mathbf{R})\chi_{e,2}(\mathbf{r_2},\mathbf{R}) \tag{2.6}$$

Here, $\mathbf{r_1}$ and $\mathbf{r_2}$ give the coordinates of electrons 1 and 2, and $\mathbf{R}$ gives the coordinates of the nucleus. The orbitals must be antisymmetric to account for spin, and they are constructed from basis set functions.[8] The accuracy of the calculations depends on the size and attributes of the basis set, and it can be evaluated using the variational principle, which states that for the ground state the energy calculated by an approximate method is higher than or equal to the actual energy.[10]

The Hartree-Fock method accounts for only one aspect of electron correlation – spin.[9] It does not represent the instantaneous Coulombic repulsion between electrons explicitly; instead, the Hamiltonian includes a kinetic energy term that accounts only for repulsion between a given electron and the average charge distribution of the others. This approximation is particularly problematic for calculations of weakly-bound complexes, which are held together by dispersive interactions. An extension of the Hartree-Fock method, Møller-Plesset perturbation theory treats electron correlation as a perturbation, and calculates the correlation energy by incorporating virtual orbitals, instead of using only a single Slater determinant.[2,11] In Chapters 3 to 6, second-order Møller-Plesset perturbation theory (MP2) is used, which incorporates doubly-excited virtual orbitals.[2,11] In contrast to the Hartree-Fock method, MP2 is not a variational method, so the approximate energy may be lower than the exact energy.[12]

Density functional theory (DFT) is an alternative approach to calculate the energy – based on the electron density, rather than the wave-function.[2] Specifically, DFT states that the energy of a molecule is a functional of the electron density. However, the form of the functional is not known. DFT is a variational method, though, so the accuracy of a proposed functional can be evaluated in the same way as that of a guess HF wave-function. The functionals used in Chapters 3 to 6 are the B3LYP[13] and M06-2X[14] functionals. DFT also differs from the HF and MP2 methods in that it is not strictly an *ab initio* method – functionals are parameterized against experimental data, so they are semi-empirical. For example, the M06-2X functional often performs better than B3LYP when modeling dispersion interactions,[15] because complexes are contained in the training set of species. The electron density is also the basis of the quantum theory of atoms in molecules (QTAIM),[16,17] which is applied to *o*-toluic acid-water and oxalic acid-water in Chapters 4 and 5, respectively.

2.3. Rotational spectroscopy

In Equation (2.2), the molecular wavefunction was given in terms of nuclear and electronic wavefunctions. Above, the electronic wavefunction was shown to be the basis of the PES. Here, the nuclear wavefunction and the origin of the rotational Hamiltonian is discussed. The total energy is the sum of electronic and nuclear energies. This has already been implied in the discussion of *o*-toluic acid; its total energy in the ground state is the sum of the electronic energy, E_e, at the equilibrium position on the PES (Figure 2.1), and the vibrational zero-point energy –

a contribution of the nuclei to the total energy. For the present discussion, the nuclear energy is assumed to be composed of only vibrational and rotational energies, E_{vib} and E_{rot}, respectively, so the total energy of a given minimum structure on the PES is given by Equation (2.7).[18-20]

$$E = E_{\text{e}} + E_{\text{vib}} + E_{\text{rot}} \tag{2.7}$$

The electronic Schrödinger equation is given above, as Equation (2.3). The vibrational Schrödinger equation can be expressed using the harmonic oscillator as a first approximation.[21] In its simplest form, the rotational Schrödinger equation can be expressed using the rigid rotor approximation, for which the Hamiltonian is given by Equation (2.8).[18,22]

$$\hat{\text{H}}_{\text{rot}} = \frac{\hat{\text{J}}_a^{\,2}}{2I_a} + \frac{\hat{\text{J}}_b^{\,2}}{2I_b} + \frac{\hat{\text{J}}_c^{\,2}}{2I_c} \tag{2.8}$$

Here, $\hat{\text{J}}_{\text{a}}$ and I_{a}, for example, are the angular momentum and moment of inertia, respectively, about the *a* principal inertial axis. The principal inertial axes are chosen such that the moments of inertia are the non-zero elements of the diagonal inertial tensor, as shown in Equation (2.9).[22]

$$\mathbf{I} = \begin{bmatrix} I_a & 0 & 0 \\ 0 & I_b & 0 \\ 0 & 0 & I_c \end{bmatrix} \tag{2.9}$$

The principal moment of inertia about the *a* principal axis, for example, is calculated according to Equation (2.10).[22]

$$I_a = \sum_i m_i r_i^2 \tag{2.10}$$

Here, m_i is the mass of atom *i*, and r_i is the distance between atom *i* and the *a* principal axis. Rotational constants can be defined in terms of the principal moments of inertia; for example, the rotational constant *A* is calculated according to Equation (2.11).[22]

$$A = \frac{h}{8\pi^2 I_a} \tag{2.11}$$

Here, *h* is the Planck constant. The principal moments of inertia are sensitive to very small structural changes, allowing isotopologues, isomers, and conformers to be unambiguously distinguished by their rotational constants.

It is useful to classify molecules in terms of their principal moments of inertia or rotational constants. Most molecules have three different rotational constants, and they are classified as asymmetric tops.[23-24] The principal axes described above are labelled such that $A > B > C$; in other words, the *a* principal moment of inertia is the smallest. If a molecule has

three identical rotational constants, it is classified as a spherical top.[23] If a molecule has two identical rotational constants, it is classified as a symmetric top.[23] Two sub-classes of symmetric tops occur. A molecule with rotational constants $A > B = C$ is an oblate symmetric top, and a molecule with rotational constants of $A = B > C$ is a prolate symmetric top. For example, in sports, a hockey puck is an oblate top, and an American football is a prolate top. The rigid rotor model is exactly solvable for a linear or symmetric top molecule, so it is to rotational motion what the particle-in-a-box model is to translational motion and the harmonic oscillator model is to vibrational motion.[4]

For symmetric tops, a quantum number K gives the projection of the rotational quantum number, J, onto the principal symmetry axis.[22] However, for asymmetric tops, there is no quantum number that can describe this projection – K is not a good quantum number.[25] In a

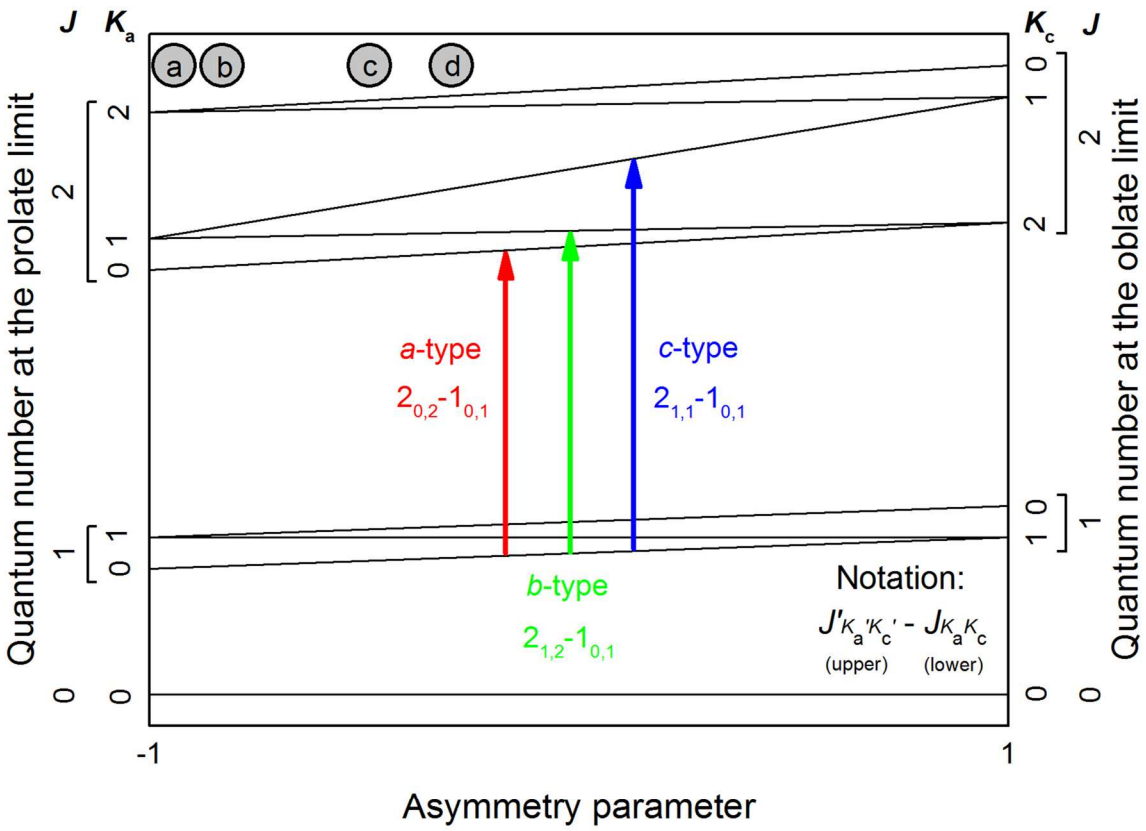

Figure 2.2. Correlation diagram showing the relationship between the asymmetric-top energy levels and those at the prolate and oblate limits. Representative *a*-, *b*-, and *c*-type transitions are depicted. Circles give asymmetry parameters of several species observed during this thesis research: (a) benzoic acid-water; (b) *o*-toluic acid-water; (c) oxalic acid-water (lowest energy isomer); and (d) 1-methylnaphthalene. (Adapted from Reference 23.)

macroscopic analogy, an asymmetric object will not spin about a single axis like a children's toy top or dreidel, examples of symmetric tops. Quantum mechanically, there is, in general, no exact solution to the Schrödinger equation for an asymmetric top, and the Hamiltonian must be represented in a matrix, with elements that are solutions of symmetric tops.[25] The basis set is composed of oblate and prolate top wavefunctions, and the respective energy levels are labelled with J and the so-called pseudo quantum numbers K_a and K_c. Figure 2.2 shows how the energy levels of asymmetric tops correlate to those of the limiting symmetric top cases.[23] The independent variable in the correlation diagram is the asymmetry parameter, κ, which is calculated from the rotational constants, according to Equation (2.12).[26]

$$\kappa = \frac{2B - A - C}{A - C} \tag{2.12}$$

For near-oblate tops, κ is close to +1; for near-prolate tops, κ is close to -1. Most molecules have more prolate character than oblate. Asymmetry parameters of four representative species from Chapters 3 to 6 are shown in Figure 2.2; for each, κ is negative. In practice, the exact energies of rotational levels are calculated using computer programs like PGOPHER.[27]

Example transitions are also shown in Figure 2.2. In order for microwave radiation to induce rotational excitation in a molecule, the molecule must have a permanent dipole moment. More specifically, if ΔK_a is even and ΔK_c is odd, as for the $2_{0,2}$-$1_{0,1}$ transition, the transition requires a non-zero dipole moment about the a principal axis ($\mu_a \neq 0$), and it is called a-type. If ΔK_a is odd and ΔK_c is odd, as for the $2_{1,2}$-$1_{0,1}$, $\mu_b \neq 0$, and the transition is b-type. If ΔK_a is odd and ΔK_c is even, as for the $2_{1,1}$-$1_{0,1}$, $\mu_c \neq 0$, and the transition is c-type.[25]

The energy levels are slightly perturbed by the apparent force acting on the nuclei as the molecule rotates in the principal axes system, since it is not an inertial frame.[25] For flexible molecules and, especially, van der Waals and hydrogen-bonded complexes, this perturbation cannot be neglected. In Watson's A-reduction Hamiltonian, it is accounted for using the following quartic centrifugal distortion constants: Δ_J, Δ_{JK}, Δ_K, δ_J, and δ_K.[28]

In flexible molecules or complexes, the rotational energy levels may also be perturbed by hindered motions,[29-31] such as water tunnelling[32] and methyl internal rotation,[33] which are discussed further in Chapters 3 to 6. Here, methyl internal rotation is presented as a general example and depicted in Figure 2.3. Conceptually, it is clear that internal rotation, a vibrational motion, must be coupled with molecular rotation; the separation of vibrational and rotational motion shown in Equation (2.7) is no longer valid,[29] so the effect of the internal rotor must be

included in the Hamiltonian.[29] Since a methyl group has three equivalent hydrogen atoms, one revolution brings the system through three minima, as shown in Figure 2.3. In classical mechanics, if the energy of molecule were below the energy of the barrier, no internal rotation would occur. In quantum mechanics, even in the lowest energy state, far below the barrier, tunnelling allows internal rotation, and the total wavefunction is a linear combination of the wavefunctions in the three wells.[35] Since three wavefunctions go into the combinations, three must result when the hindered rotation Schrödinger equation is solved. Two of the three states are degenerate; these are the *E* states, and the remaining one is the *A* state. In the torsional ground state, for which $v = 0$, the effective barrier is highest, so the tunnelling probability is lowest, and the energy difference between the *A* and *E* states is small. In the first excited state, for which $v = 1$, the effective barrier decreases, and splitting increases. In the limit of an infinitely high barrier, the splitting is infinitesimal. Chapter 4 presents examples of species, *o*-toluic acid and

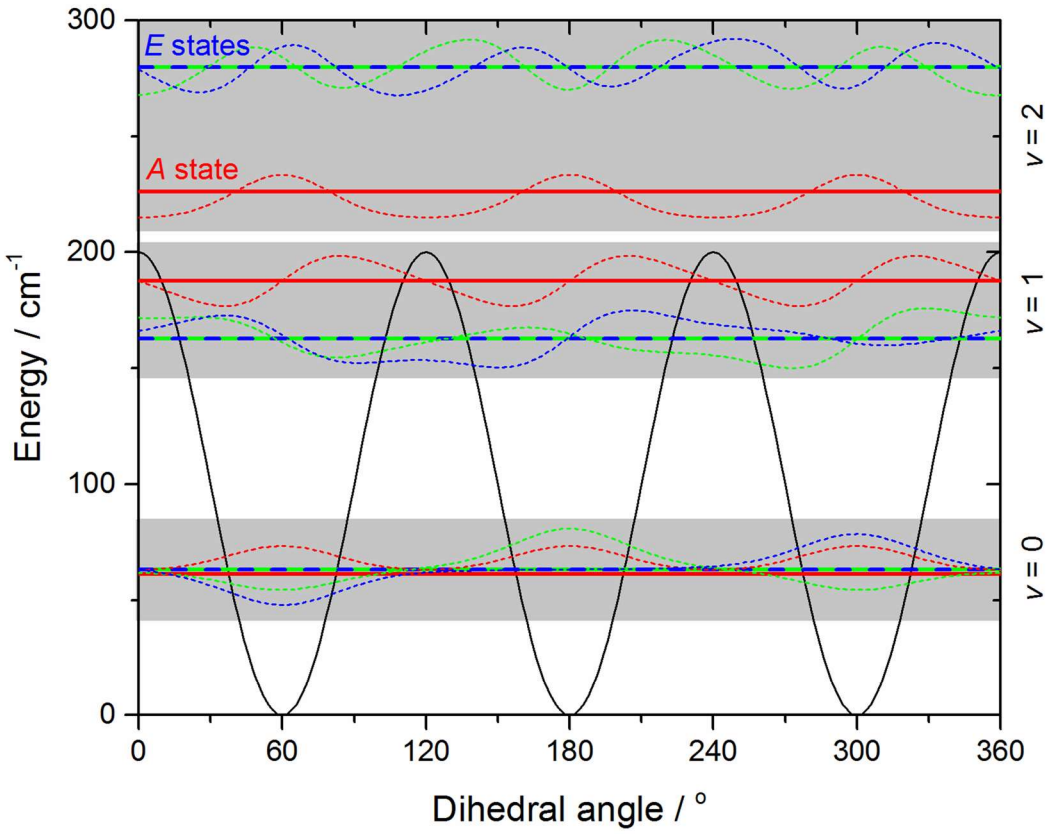

Figure 2.3. Potential energy curve along the methyl internal rotation coordinate in a low barrier example. The eigenvalues (energy levels) and eigenvectors (wave-functions) of the *A* states are shown in red; those of the *E* states are shown in green and blue. For each vibrational quantum number, *v*, the two *E* states are degenerate. (Eigenvalues and eigenvectors calculated using Reference 34.)

o-toluic acid-water, with barriers that are too high to resolve the splitting experimentally. Chapter 6 presents examples of species, methyl-substituted polycyclic aromatic hydrocarbons, with intermediate barrier heights, leading to resolvable splittings. These splittings can be used to derive the barrier height using programs like XIAM.[33] The intensity ratio of A and E states depends on symmetry and nuclear statistics; for a non-deuterated methyl internal rotor, the ratio is 1:1.[36]

Line intensities are directly proportional to line strength, S, and number concentration, N. In turn, the line strength depends on the quantum number J, the rotational temperature, and the transition dipole moment for the transition under consideration; for asymmetric tops, line strengths can be calculated using many spectroscopic programs, such as PGOPHER.[27] In Chapters 3 to 6, dipole moment components are taken from computational chemistry calculations, but they can also be determined experimentally by applying an external electric field and measuring the splitting resulting from the Stark effect.[37] Relative line intensities allow estimates of relative abundances, as in Chapter 5 for two isomers of oxalic acid-water.

2.4. Supersonic expansion

In Chapters 3 to 6, rotational spectra were measured using a Fourier-transform microwave (FTMW) spectrometer, which has been described in detail in the past.[38,39] The sample "container" is a cavity composed of two aluminum mirrors housed in a vacuum chamber, which is evacuated using a diffusion pump backed by a rotary pump. The electronics used to produce the excitation pulse of microwave radiation and detect the molecular emission are discussed in the next section. In this section, the generation of sample complexes using a supersonic expansion is described.

A brief description of a static gas, which does not move or flow as a whole, serves to highlight the advantages of a supersonic expansion in high-resolution spectroscopic studies, especially those of complexes. For an ideal static gas, the distribution of atomic or molecular speeds, $f(v_m)$, is represented by the Maxwell-Boltzmann distribution, shown in Equation (2.13), which is analogous to the Boltzmann distribution of populations described in Section 2.1.[5]

$$f(v_m) = 4\pi \left(\frac{M}{2\pi RT}\right)^{3/2} v_m^2 e^{-Mv_m^2/2RT} \tag{2.13}$$

Here, M is the molar mass, R is the universal gas constant, and T is the temperature. The effect of temperature is exhibited by the difference between speed distributions of neon at 298 K and 5 K; at the higher temperature, the mean speed increases and the distribution widens, as shown in Figure 2.4. If sample molecules have a broad distribution of speeds, their emission following excitation will be Doppler broadened; for example, radiation emitted from two molecules that happen to be travelling away from a detector at two slightly different speeds will be red-shifted to different degrees. The broad distribution of speeds also results in many collisions. If a molecule that is in an excited state is involved in one of these collisions, its lifetime is cut short, leading to further broadening by the time-energy uncertainty principle. Furthermore, because the mean speed is high, each collision imparts significant kinetic energy, which can dissociate complexes of interest, especially since they already populate excited vibrational energy levels at room temperature. As a result, the equilibrium constant of complexation is small, and the concentration of complexes is low. These short-comings with respect to resolution and sensitivity are overcome by using a cold sample, generated in a supersonic expansion.

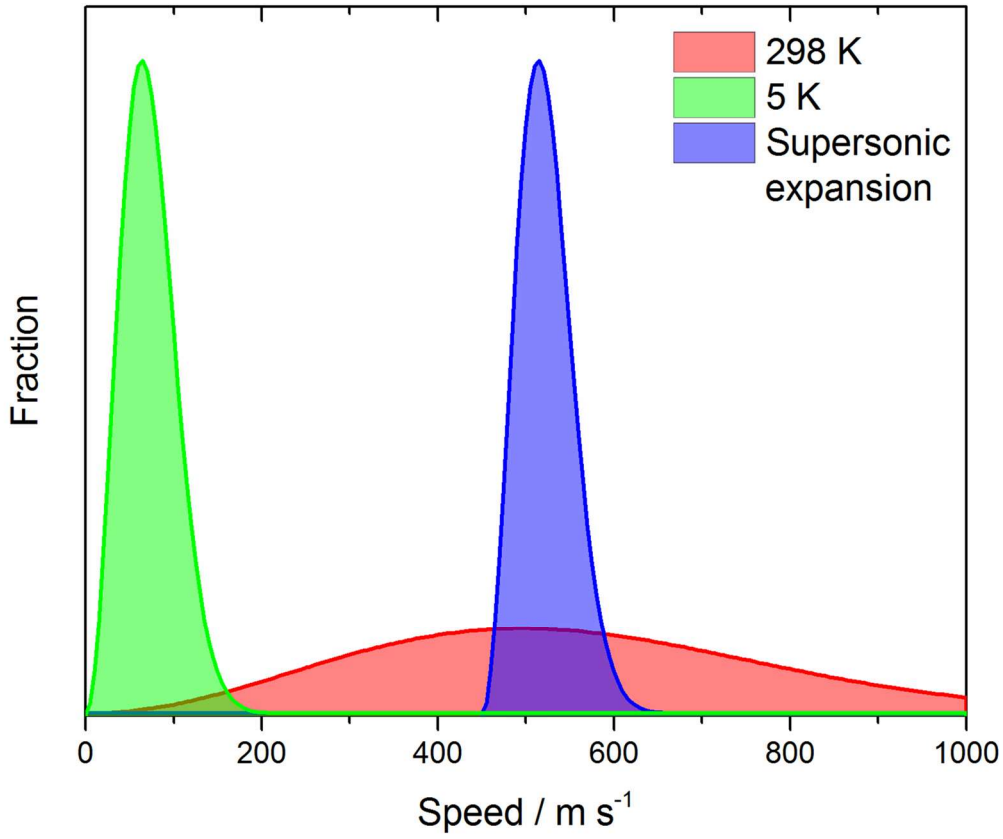

Figure 2.4. Molecular speed distributions for a static sample of neon at 298 and 5K and a supersonic expansion of neon.

A supersonic expansion occurs when a gas at a high stagnation pressure is passed through an orifice into a chamber at low pressure.[40-43] In Chapters 3 to 6, neon was used as a backing gas. If the orifice diameter is much larger than the mean free path of neon at the high pressure, many collisions occur as it passes through the orifice. The expansion is approximately adiabatic, meaning that any loss of gas enthalpy must equal the kinetic energy of the resulting jet. The maximum kinetic energy (and, consequently, flow velocity) occurs when all gas enthalpy is converted through collisions into directed mass flow. As a result, the distribution is narrow, like a static gas at very low temperatures, but the mean speed is high, as illustrated in Figure 2.5. The use of the descriptor "supersonic" stems from the Mach number in the expansion, which is the ratio of the flow velocity to the speed of sound in the expansion. The local speed of sound is proportional to the square-root of temperature, so it is lowered by the cooling in the expansion. In contrast, the flow velocity increases. As a result, the molecules are travelling much faster than the local sound of speed, signified by Mach numbers far greater than unity. If neon is seeded with a second species at sufficiently high stagnation pressures, the seeded species will be carried along with neon, so that both species have the same flow velocity and temperature at a given distance from the nozzle. After many collisions, the temperature becomes so low that further collisions are rare – the species enters the free molecular regime – so temperature can no longer decrease. Before this point is reached, translational and rotational degrees of freedom are cooled more quickly than vibrational degrees of freedom; as a result, the rotational temperature is lower than the vibrational temperature. The conformational degrees of freedom, linked to large amplitude vibrational modes, may be cooled very poorly if significant barriers separate conformers.

2.5. Excitation and detection

Above, it was shown that the time-independent Schrödinger equation describes molecules in the absence of external electromagnetic fields. In the presence of radiation, however, the molecules are no longer in a stationary state. In a non-stationary state, the time-dependent Schrödinger equation must be used, instead.[44-47] A rotational transition can be modelled with a two-level system. It can be shown that using the density matrix formalism leads to a unit vector, where the x, y, and z axes correspond to U and V, two terms related to the coherence, and W, a term related to the population difference.[46] A molecular ensemble populating its ground state has

maximum population difference and no coherence. Applying radiation with a frequency resonant to the transition for long enough to move all the molecules into the excited state corresponds to population inversion (a π pulse). Applying radiation for half that time (a π/2 pulse) results in half the molecules being in each state, equating to zero population difference, and maximum polarization. In this condition, the ensemble will spontaneously emit coherent radiation.

For rotational transitions, the frequency of the excitation pulse and subsequent emission often lies in the gigahertz range. To overcome the hurdle of digitizing such high frequencies, the instrument incorporates superheterodyne detection to down-convert these frequencies, as depicted in Figure 2.5. Generation of the excitation pulse begins with a 1-20 GHz microwave (MW) synthesizer, which generates a signal of frequency ν, taken as 10 GHz in Figure 2.5. This signal is then passed through a power divider, which directs half of the radiation to the excitation branch of electronics and the other half to the detection branch. In the excitation branch, the signal is then passed through an isolator, which transmits radiation in only one direction, on its way to a switch, which is controlled by a pulse generator, referenced to a 10 MHz frequency standard in the MW synthesizer. If the switch is open, radiation then passes to a double-balanced mixer. The mixer is supplied with a 20 MHz signal derived from the frequency standard, so it produces radiation with frequencies of 10 GHz ± 20 MHz from the incident radiation. The radiation is then passed through a circulator, which directs the radiation to the cavity. The cavity consists of two aluminum mirrors, one of which can be translated with a motor. If the cavity is tuned into resonance with the 10 GHz - 20 MHz signal, a standing wave results. For a hypothetical species with a rotational transition close to this frequency, excitation will occur. For a properly timed (π/2) pulse, macroscopic polarization will occur. Since the transition does not need to be at exactly the same frequency as the excitation radiation, the radiation exiting the cavity will not be exactly 10 GHz - 20 MHz, but offset by $\Delta\nu$. The bandwidth of the pulse is narrower for longer pulses, based on the time-frequency uncertainty principle. Since molecules are travelling away from the antenna, but emit in all directions, all transitions are split into two components, because of the Doppler effect. For species with small molecular dipole moment components, an amplifier is placed between the double-balanced mixer and the switch, leading to macroscopic polarization in a shorter time period than would be required for less intense MW radiation. This was the case for 2-methylnaphthalene and 1,3-dimethylnaphalene in Chapter 6.

The circulator directs the resulting molecular emission signal from the cavity to the detection branch of the electronics. A switch is situated after the circulator, and this is controlled by the pulse generator. During the excitation pulse, the switch is closed to protect the detection branch of the electronics. If the switch is open, the MW radiation is then passed through a MW amplifier and an image rejection mixer, also supplied with the original MW signal from the synthesizer. The image rejection mixer generates an intermediate frequency (IF) of 20 MHz, offset by $\Delta\nu$. The IF signal is passed through an IF amplifier followed by a mixer supplied with

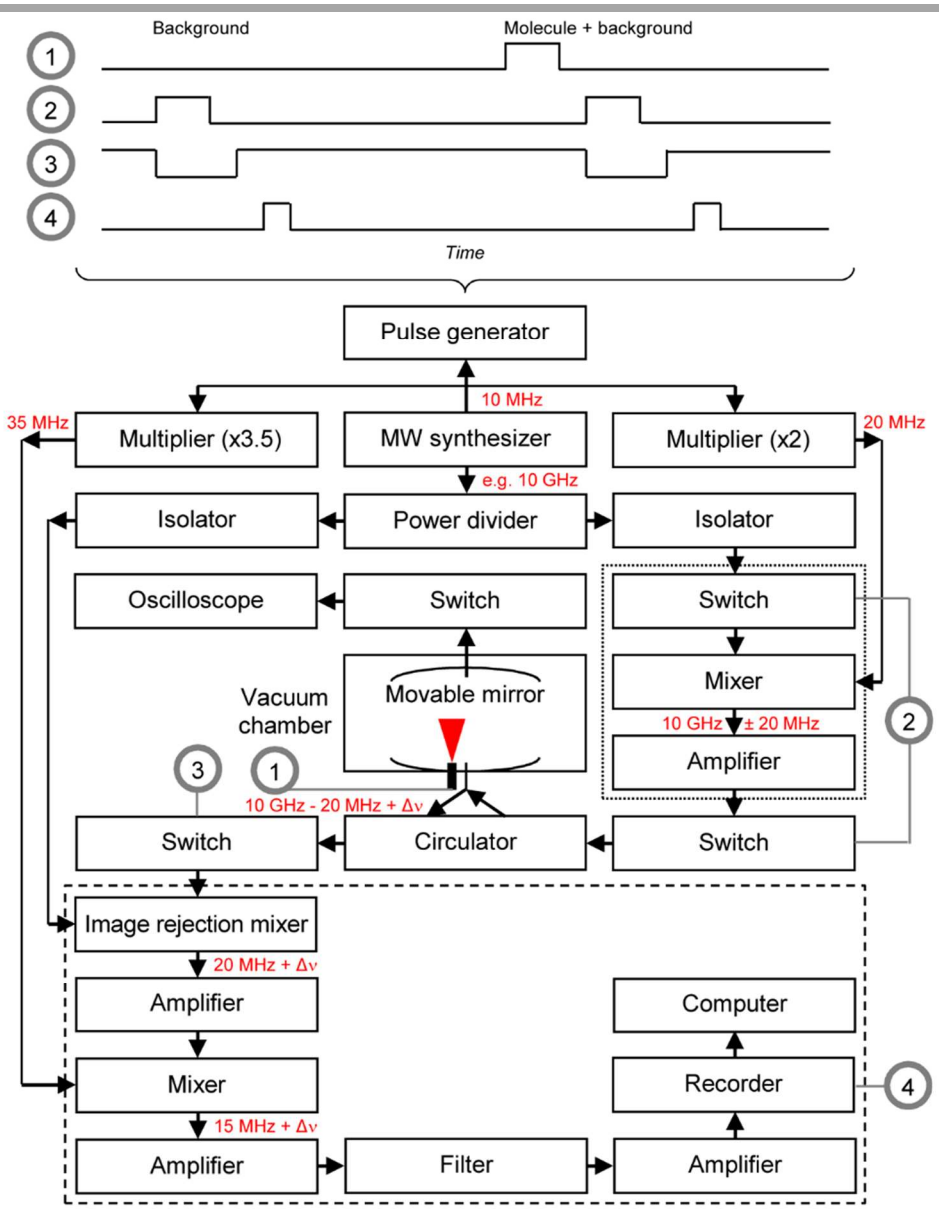

Figure 2.5. Schematic of spectrometer and pulse sequence. The excitation branch is denoted with the dotted rectangle; the detection branch is denoted with the dashed rectangle. (Adapted from Reference 38.)

an in-phase 35 MHz signal, which produces an IF signal with a frequency of about 15 MHz, also off-set by Δv. This signal is low enough in frequency to be easily digitized. The digitized time domain signal of subsequent experiments can be averaged for signal-to-noise improvement and is then Fourier-transformed to give a frequency spectrum. In each experiment, a background spectrum – measured without the introduction of sample, as shown in the pulse sequence in Figure 2.5 – is subtracted from the sample spectrum.

References

1 Bunker, P. R.; Jensen, P. The Born-Oppenheimer approximation and the electronic wavefunction. *Molecular Symmetry and Spectroscopy*, 2nd ed.; NRC Research Press: Ottawa, 2006; pp 173-201.

2 Jensen, J. H. Calculating the energy. *Molecular Modeling Basics*; CRC Press: Boca Raton, 2010; pp. 25-76.

3 Jensen, J. H. The potential energy surface. *Molecular Modeling Basics*; CRC Press: Boca Raton, 2010; pp. 1-24.

4 Woodbury, G. Three exactly solvable models. *Physical Chemistry*; Brooks/Cole: Pacific Grove, 1997; pp. 413-454.

5 McClelland, B. J. Maxwell-Boltzmann statistics. *Statistical Thermodynamics*; Studies in Chemical Physics Series; Chapman and Hall: London, 1973; pp. 13-28.

6 Frisch, M. J.; *et al. Gaussian 09*, Rev. D.01; Gaussian, Inc.: Wallingford, CT, **2013**. See bibliography for complete list of authors.

7 Pauling, L.; Wilson, E. B., Jr. Many-electron atoms. *Introduction to Quantum Mechanics with Applications to Chemistry*; Dover: New York, 1985; pp 230-258.

8 Szabo, A.; Ostlund, N. S. Many electron wave functions and operators. *Modern Quantum Chemistry: Introduction to Advanced Electronic Structure Theory*; Dover: New York, 1996; pp. 39-107.

9 Szabo, A.; Ostlund, N. S. The Hartree-Fock approximation. *Modern Quantum Chemistry: Introduction to Advanced Electronic Structure Theory*; Dover: New York, 1996; pp. 108-230.

10 Pauling, L.; Wilson, E. B., Jr. The variation method and other approximate methods. *Introduction to Quantum Mechanics with Applications to Chemistry*; Dover: New York, 1985; pp 180-206.

11 Møller, C.; Plesset, M. S. Note on an approximation treatment for many-electron systems. *Phys. Rev.* **1934**, *46*, 618-622.

12 McCarthy, S. P.; Thakkar, A. J. When does the non-variational nature of second-order Møller-Plesset energies manifest itself? All-electron correlation energies for open-shell atoms from K to Br. *J. Chem. Phys.* **2012**, *136*, 054107 (8 pp.).

13 Becke, A. D. Density-functional thermochemistry. III. The role of exact exchange. *J. Chem. Phys.* **1993**, *98*, 5648-5652.

14 Zhao, Y.; Truhlar, D. G. The M06 suite of density functionals for main group thermochemistry, thermochemical kinetics, noncovalent interactions, excited states, and transition elements: Two new functionals and systematic testing of four M06-class functionals and 12 other functionals. *Theor. Chem. Acc.* **2008**, *120*, 215-241.

15 Elm, J.; Bilde, M.; Mikkelsen, K. V. Assessment of density functional theory in predicting structures and free energies of reaction of atmospheric prenucleation clusters. *J. Chem. Theory Comput.* **2012**, *8*, 2071-2077.

16 Bader, R. F. W. A quantum theory of molecular structure and its applications. *Chem. Rev.* **1991**, *91*, 893-928.

17 Bader, R. F. W. A bond path: A universal indicator of bonded interactions. *J. Phys. Chem. A* **1998**, *102*, 7314-7323.

18 Bunker, P. R.; Jensen, P. The rotation and vibration wavefunctions. *Molecular Symmetry and Spectroscopy*, 2nd ed.; NRC Research Press: Ottawa, 2006; pp 238-264.

19 Wilson, E. B., Jr.; Decius, J. C.; Cross, P. C. The separation of rotation and vibration. *Molecular Vibrations: The Theory of Infrared and Raman Vibrational Spectra*; Dover: New York, 1980; pp 273-284.

20 Pauling, L.; Wilson, E. B., Jr. The rotation and vibration of molecules. *Introduction to Quantum Mechanics with Applications to Chemistry*; Dover: New York, 1985; pp 259-293.

21 Wilson, E. B., Jr.; Decius, J. C.; Cross, P. C. The vibration of molecules. *Molecular Vibrations: The Theory of Infrared and Raman Vibrational Spectra*; Dover: New York, 1980; pp 11-33.

22 Levine, I. N. Rotation of polyatomic molecules. *Molecular Spectroscopy*; Wiley: New York, 1975; pp 195-234.

23 Townes, C. H.; Schawlow, A. L. Asymmetric-top molecules. *Microwave Spectroscopy*; Dover: New York, 1975; pp 83-114.

24 Gordy, W.; Smith, W. V.; Trambarulo, R. F. Microwave spectroscopy of gases. *Microwave Spectroscopy*; Wiley: New York, 1953; pp 84-153.

25 Kroto, H. W. Angular momentum and the energy levels of a rigid rotor. *Molecular Rotation Spectra*; Dover: New York, 1992; pp. 22-60.

26 Ray, B. S. Über die Eigenwerte des asymmetrischen Kreisels. *Z. Phys.* **1932**, *78*, 74-91.

27 Western, C. M. *PGOPHER, A Program for Simulating Rotational Structure*, University of Bristol: Bristol, UK. http://pgopher.chm.bris.ac.uk.

28 Watson, J. K. G. Determination of centrifugal distortion coefficients of asymmetric-top molecules. *J. Chem. Phys.* **1967**, *46*, 1935-1949.

29 Kroto, H. W. Flexible molecules. *Molecular Rotation Spectra*; Dover: New York, 1992; pp. 196-223.

30 Bunker, P. R.; Jensen, P. Nonrigid molecules. *Molecular Symmetry and Spectroscopy*, 2nd ed.; NRC Research Press: Ottawa, 2006; pp 476-549.

31 Townes, C. H.; Schawlow, A. L. The ammonia spectrum and hindered motions. *Microwave Spectroscopy*; Dover: New York, 1975; pp 300-335.

32 Evangelisti, L.; Caminati, W. Internal dynamics in complexes of water with organic molecules. Details of the internal motions in *tert*-butylalcohol-water. *Phys. Chem. Chem. Phys.* **2010**, *12*, 14433-14441.

33 Hartwig, H.; Dreizler, H. The microwave spectrum of trans-2,3-dimethyloxirane in torsional excited states. *Z. Naturforsch.* **1996**, *51A*, 923-932.

34 Johnson, R. D., III. *FGH1D*, National Institute of Standards and Technology: Gaithersburg. http://nist.gov/mml/csd/informatics_research/fourier_grid_hamiltonian_ interface.cfm#11.

35 Ercolani, G. Numerical evaluation of energy levels and wave functions for hindered internal rotation. *J. Chem. Ed.* **2000**, *77*, 1495.

36 Wollrab, J. E. Internal rotation. *Rotational spectra and molecular structure*; Physical Chemistry Series; Academic Press: New York, 1967; pp. 145-202.

37 Brauer, C.; Sedo, G.; Leopold, K. R. Dipole moment of the H_2SO_4-H_2O complex. *Geophys. Res. Lett.* **2006**, *33*, L23805 (5 pp.).

38 Xu, Y.; Van Wijngaarden, J.; Jäger, W. Microwave spectroscopy of ternary and quaternary van der Waals clusters. *Int. Rev. Phys. Chem.* **2005**, *24*, 301-338.

39 Xu, Y.; Jäger, W. Evidence for heavy atom large amplitude motions in RG-cyclopropane van der Waals complexes (RG=Ne, Ar, Kr) from rotation-tunneling spectroscopy. *J. Chem. Phys.* **1997**, *106*, 7968-7980.

40 Johnston, M. V. Supersonic jet expansions in analytical spectroscopy. *Trends Anal. Chem.* **1984**, *3*, 58-61.

41 Morse, M. D. Supersonic beam sources. In *Atomic, Molecular, and Optical Physics: Atoms and Molecules*; Dunning, F. B., Hulet, R. G., Eds.; Experimental Methods in the Physical Sciences; Academic Press: San Diego, 1996; Vol. 29B, pp. 21-47.

42 Van de Meerakker, S. Y. T.; Bethlem, H. L.; Meijer, G. Taming molecular beams. *Nature Phys.* **2008**, *4*, 595-602.

43 Steinfeld, J. I. From molecular beams to masers to lasers. *Molecules and Radiation: An Introduction to Modern Molecular Spectroscopy*; Dover: New York, 2005; pp. 293-326.

44 Levine, I. N. Time-dependent states and spectroscopy. *Molecular Spectroscopy*; Wiley: New York, 1975; pp 110-141.

45 Kroto, H. W. Interaction of radiation with a rotating molecule. *Molecular Rotation Spectra*; Dover: New York, 1992; pp. 61-94.

46 Allen, L.; Eberly, J. H. Two-level atoms in steady fields. *Optical Resonance and Two-Level Atoms*; Dover: New York, 1987; pp. 52-77.

47 Steinfeld, J. I. Optical resonance spectroscopy. *Molecules and Radiation: An Introduction to Modern Molecular Spectroscopy*; Dover: New York, 2005; pp. 327-355.

3 The benzoic acid–water complex: A potential atmospheric nucleation precursor studied using microwave spectroscopy and *ab initio* calculations

3.1. Introduction

Water clusters play an important and complex role in the atmosphere.[1,2] For example, clusters of water and atmospheric oxidants, like ozone and hydroxyl radical, may influence Earth's radiative balance by shifting and broadening the absorption of solar and terrestrial emission by water.[3] Water clusters can also affect other atmospheric reactions, such as the decarboxylation of malonic acid, in which the water moiety acts as a catalyst.[4]

Recent theoretical studies of water clusters with carboxylic acids[5,6] indicate a growing interest in how water clusters can also act as nucleation precursors, potentially bridging the gap between gas-phase species and nano-particles in the atmosphere.[7,8] This interest can be traced to the experimental work of Zhang *et al.*,[9] who demonstrated, with smog chamber experiments, that benzoic acid (BA) increases the rate of particle formation in the presence of water and (or solely) sulphuric acid.[10] This effect is attributed to the stability of the BA-sulphuric acid dimer, which could compensate for the large entropic expense of going from individual gas molecules to a more ordered phase.[11] The addition of a few more sulphuric acid or water moieties to the dimer may result in the critical nucleus, a nano-particle to which gas molecules spontaneously condense.[12] Since water is ubiquitous in the atmosphere, determining the structure and binding energy of the BA-H_2O dimer may be a further step towards characterizing the critical nucleus.

BA occurs in the atmosphere as a primary pollutant from engine exhaust[13] and a secondary pollutant from the photo-oxidation of aromatic hydrocarbons, such as toluene, which leads to secondary organic aerosol.[14,15] BA is often detected in particulate matter in field studies.[16,17] Near the Pearl Delta River, China, for example, BA was found to account for up to

10% of the organic carbon mass in particulate matter. Absolute concentrations as high as 200 ng m^{-3} were measured.[17]

BA is interesting also for its importance in other areas of chemistry. In organic synthesis, a substituent is characterized by its effects on substituted BA derivatives, according to the Hammett rule.[18] Moreover, BA is a building block in a variety of emerging drugs[19,20] and nano-materials.[21,22]

The BA monomer has been studied in the gas phase, using microwave spectroscopy[23,24] and electron diffraction.[25] Onda *et al.* reported the first microwave spectroscopic study; using two instruments, a Stark-modulated spectrometer and a Fourier-transform microwave (FTMW) spectrometer, they derived two sets of rotational constants.[23] No splitting in either *a*- or *b*-type transitions was observed, so the authors concluded that the barrier to rotation of the carboxylic acid group was considerable.[23] Very recently, Godfrey and McNaughton reported a second microwave spectroscopic study; using a millimetre-wave Stark-modulated free-jet absorption spectrometer, they discriminated between the two sets of rotational constants reported by Onda *et al.* and observed the spectrum of the *syn*-conformer (in which the O=C−O−H dihedral angle is 0°).[24] Using electron diffraction, Aarset *et al.* have also observed only the *syn*-conformer.[25]

Before this work, the only structural study of the BA-H_2O dimer has been theoretical. Using the MP2/6-311++G(d,p)//MP2/6-31G(d) level of theory, Nagy *et al.*[26] found that the monohydrate of the *syn*-conformer of BA is about 37 kJ mol^{-1} lower in energy than the monohydrate of the *anti*-conformer. Estimated energies of hydration for the *syn*- and *anti*-conformers were cited as −40 kJ mol^{-1} and −34 kJ mol^{-1}, respectively, so single hydration of both conformers causes significant stabilization. The *syn*-conformer has two hydrogen bonds, so it is representative of many biological systems (in which water acts as both proton donor and acceptor), as well as the first step in bulk solvation of BA.

More recently, microwave spectroscopic studies of monohydrates of other carboxylic acids (including formic,[27] acetic,[28] and propanoic[29] acids) have been reported. The experimental results agree with the earlier theoretical predictions; *syn*-conformers with two hydrogen bonds as part of six-membered rings were observed.

Motivated by the above considerations, I recorded rotational spectra of BA-H_2O and its doubly-deuterated isotopologue, BA-D_2O, using a FTMW spectrometer. The measured transition frequencies were used in a fitting procedure to obtain rotational constants. In addition,

centrifugal distortion constants were derived for BA-H_2O. By comparing experimental constants to calculated values from three computational methods (B3LYP, M06-2X, and MP2), I find that the equilibrium structure from the B3LYP calculations gives the best prediction. Narrow splittings were observed in two very weak *b*-type transitions of BA-H_2O, and I discuss possible tunnelling motions in terms of calculated barrier heights. Structural parameters for the hydrates were extracted from their rotational constants and are compared to results from the calculations. The interaction energy (of hydration) and spectroscopic dissociation energy were calculated. I conclude with the calculation of the equilibrium constant for hydration and a discussion of potential atmospheric implications.

3.2. Methods

3.2.1. Experimental

I used reagent grade BA (Aldrich, ≥99.5%) without further purification. The melting point of BA is 395 K, so the sample was heated in a stainless steel cell. Before the cell, I placed a coil of copper tubing, warmed by a resistive heating tape. I also wrapped a heating tape around the tubing from the cell to the spectrometer (including the outside surface area of the nozzle). This heating tape was adjusted to an outside temperature of roughly 453 K. The BA sample inside the cell did not melt, but its solid vapour pressure was high enough to allow sublimation.[30] Using this heating apparatus, BA monomer transitions were very strong; averaging only 10 cycles often resulted in a signal-to-noise ratio greater than 5000. Ne (Praxair) was used as backing gas, at a pressure of 1-2 atm. For BA-H_2O, I prepared a mixture of water, roughly 0.04%, in Ne. For BA-D_2O, I used heavy water (Aldrich, 99.9%).

Rotational spectra were measured in the range of 4-14 GHz using a FTMW spectrometer, which has been described in detail earlier.[31,32] Briefly, the sample mixture is introduced into an evacuated microwave resonator through a pulsed nozzle. In the resulting supersonic expansion, the sample is cooled to a temperature of about 1-2 K and travels coaxially to the axis of the resonator. Rotational transitions are then excited with a microwave pulse. Subsequently, the molecular ensemble emits radiation with the rotational transition frequencies, which is digitized, averaged, and Fourier transformed to give the frequency spectrum. Since the emitted radiation travels both parallel and anti-parallel to the resonator axis, all observed transitions are Doppler-doubled. I take the arithmetic mean of each Doppler pair as the rest

frequency. The pulse repetition rate was set to 2.5 Hz. Targeted automated scans were collected in 0.2 MHz steps.

3.2.2. Computational

To aid in the assignment of the spectrum of BA-H_2O, I performed density functional theory (DFT) and wavefunction (MP2) calculations for the dimer. Using the calculated rotational constants, I was able to specify promising frequency ranges for automated search scans. A comparison of the calculated and experimental rotational constants is useful, too, in evaluating the general performance of the respective methods. For hydrogen bonded systems, the MP2 level of theory has been proven to provide structural parameters that result in rotational constants of sufficient accuracy for initial spectroscopic searches.[33,34] For DFT calculations, I used the B3LYP[35] and M06-2X[36] functionals. B3LYP calculations have also been used to provide structural parameters for microwave spectroscopic studies, even if only preliminary to MP2 calculations.[24,37] The recently parameterized M06-2X functional performed well in a structural evaluation using a test set of water clusters with sulphur-containing compounds.[38] On the other hand, for a larger cluster, rotational constants calculated using M06-2X deviated further from experimental values than those calculated using B3LYP did.[39] The calculations that form the basis of our discussions of equilibrium geometry, interaction and dissociation energies, and equilibrium constant were done using Gaussian 09,[40] with the 6-311++G(2df,2pd) basis set. I note that the present level of theory is higher than that used by Nagy *et al.* in their computational investigation of BA-H_2O.[26] Every equilibrium geometry optimization was followed by a frequency calculation to ensure that the stationary point is a minimum. In order to allow us to calculate the spectroscopic dissociation energies using the different methods, I also performed calculations for the monomers. I accounted for the basis set superposition error (BSSE) in the dimer energy calculations using counterpoise corrections.[41] The internal dynamics calculations, not previously performed by Nagy *et al.*,[26] were done at the B3LYP/6-311++G(d,p) level of theory.

Transition frequencies were predicted from the calculated rotational constants using PGOPHER.[42] In turn, the frequencies of the observed and assigned transitions were fitted using the PGOPHER program, employing Watson's A-reduction Hamiltonian.[43] The PMIFST program, a part of the suite PROSPE,[44] was used to predict rotational constants for BA-D_2O.

3.3. Results and discussion

3.3.1. Rotational spectra

In order to identify potential transitions of the complex, I accounted for known transitions of $(H_2O)_2$[45] and the BA monomer.[23,24] I noted at the outset that the BA monomer rotational constants derived by Onda *et al.* from their wave guide spectrum did not agree with the line list from their FTMW spectrum.[23] Godfrey and McNaughton discuss this discrepancy in detail and report rotational constants (derived from their millimetre-wave spectrum) that agree with the previously reported line list.[24] Though BA was not the focus of this study, I observed 66 transitions of the monomer during the course of this work. All transition frequencies are listed in Table A.1 (Appendix). I fitted rotational parameters, including rotational and centrifugal distortion constants, to this expanded data set. The resulting constants are listed in Table 3.1. Consistent with the earliest study,[23] I did not observe splittings in either *a*- or *b*-type transitions, indicative of a relatively high barrier to rotation of the carboxylic acid group. When searching for the BA-D_2O transitions, I noticed that the acidic hydrogen atom exchanges with deuterium to some extent during sample injection. I used rotational constants reported by Godfrey and McNaughton for the R-OOD isotopologue of BA to identify its transitions, which were less than one tenth as intense as those of the parent isotopologue.[24]

Table 3.1. Experimental rotational constants, quartic centrifugal distortion constants, and planar moment of inertia, determined by fitting to observed transition frequencies.

	BA	BA-H_2O	BA-D_2O
A / MHz	3872.2778(3)[a]	3838.173(1)	3811.5(2)
B / MHz	1227.31481(3)	652.48725(9)	623.425(7)
C / MHz	932.56599(2)	558.44067(8)	536.944(7)
Δ_K / kHz	0.39(6)	0	0
Δ_{JK} / kHz	0[b]	0.049(4)	0
Δ_J / kHz	0.0337(2)	0.0236(2)	0
δ_K / kHz	0.095(3)	0.14(2)	0
δ_J / kHz	0.0089(1)	0.0036(2)	0
P_c / uÅ^2	0.183	0.616	1.015
N[c]	66	42	12
σ[d] / kHz	0.6	0.8	9.7

[a] One standard deviation of fitted parameters, in units of the least significant digit, is shown in parentheses. [b] Parameter was fixed at zero during fitting. [c] Number of lines included in fit. [d] Root-mean-square of residuals.

I began my search for transitions of BA-H_2O using the rotational constants and dipole moment components from B3LYP, M06-2X, and MP2 calculations, shown in Table 3.2. With all three levels of theory, one global minimum energy conformer was found, in which water acts as both a hydrogen bond donor and acceptor in a six-membered ring, as pictured in Figure 3.1. Since the predicted *a*-dipole moment is much larger than the *b*-dipole moment, regardless of level of theory, I first searched for the $7_{1,7}\leftarrow6_{1,6}$, $7_{0,7}\leftarrow6_{0,6}$, and $7_{1,6}\leftarrow6_{1,5}$ transitions by performing automated scans in frequency ranges defined by ±2% deviations in the calculated rotational constants. The transitions were found less than 50 MHz lower in frequency than the B3LYP-predicted frequencies. Using these three transition frequencies in a preliminary determination of *A*, *B*, and *C* rotational constants, I was able to locate further *a*-type transitions, giving 40 in all, whose frequencies were then used in a spectroscopic fit. At this stage, the Δ_J and δ_J centrifugal distortion parameters were fixed at zero. The highest rotational transition I observed is the $11_{1,10}\leftarrow10_{1,9}$ transition. I did not observe any splitting in the *a*-type transitions. A representative *a*-type transition is shown in Figure 3.2a.

Next, I searched for *b*-type transitions, and located the $4_{1,4}$-$3_{0,3}$ and $7_{1,7}$-$6_{0,6}$ transitions, each less than 25 kHz lower in frequency than given by the fit of *a*-type transitions. Both transitions were very weak, consistent with the small predicted *b*-dipole moment component.

Table 3.2. Predicted rotational constants, planar moment of inertia, relative deviation from experimental rotational constants, and dipole moment components of BA-H_2O, calculated using DFT and MP2 methods with the 6-311++G(2df,2pd) basis set.

	B3LYP	M06-2X	MP2
A / MHz	3864.41	3880.34	3849.97
B / MHz	655.83	660.36	662.27
C / MHz	561.31	564.92	565.69
P_c / uÅ^2	0.508	0.471	0.492
$(\Delta A/A)^a$ / %	0.68	1.10	0.31
$(\Delta B/B)$ / %	0.51	1.21	1.50
$(\Delta C/C)$ / %	0.51	1.16	1.30
Ave^b / %	0.57	1.16	1.03
$\lvert\mu_a\rvert$ / D	1.1	1.1	1.3
$\lvert\mu_b\rvert$ / D	0.3	0.2	0.3
$\lvert\mu_c\rvert$ / D	1.3	1.3	1.3

[a] Relative deviation; for example, $[(A_{calc}-A_{exp})/A_{exp}]\times100\%$. [b] Average deviation of *A*, *B*, and *C* rotational constants.

Repeated averages of 5 000 to 30 000 cycles revealed a complicated splitting pattern consisting of four components (Doppler pairs). A representative *b*-type transition is shown in Figure 3.2b. The observed splitting will be discussed in more detail in the Tunnelling section. The centre frequencies were included in a final fit to give the rotational and centrifugal distortion constants listed in Table 3.1. A complete line list is given in Table A.2. I also searched for, but did not observe, *c*-type transitions, although the predicted *c*-dipole moment component is similar in magnitude to the predicted *a*-dipole moment. I conclude that large amplitude motion of the unbound hydrogen of the water moiety across the *ab* plane averages out to give an effectively planar structure. This observation is consistent with previous studies of other carboxylic acid-water clusters.[28,29]

By comparing the experimental *A*, *B*, and *C* rotational constants with the predicted values, I can draw some conclusions about the performance of the respective *ab initio* methods. As shown in Table 3.2, at all three levels of theory, the equilibrium structures correspond to rotational constants that exceed the experimental rotational constants. The rotational constants determined from the B3LYP structure are in the best agreement with experimental values, with an average discrepancy of 0.57%. Equilibrium structures calculated using the M06-2X and MP2

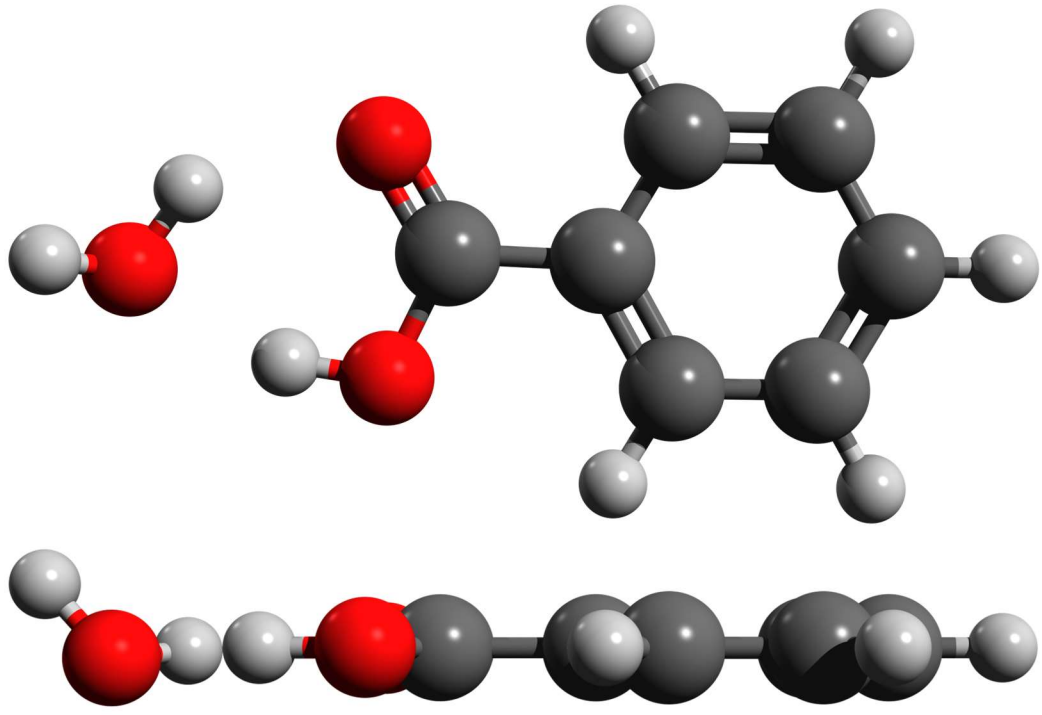

Figure 3.1. Minimum energy structure of BA-H_2O calculated at the MP2/6-311++G(2df,2pd) level of theory and viewed in the *ab* (upper) and *ac* (lower) planes.

methods correspond to rotational constants that more grossly exceed the experimental rotational constants; average discrepancies are 1.16 and 1.03%, respectively. The frequencies of the *a*-type transitions of BA-H_2O are most sensitive to the *B* and *C* rotational constants, which B3LYP predicts more accurately than the other methods. For example, the discrepancies in the values of *B* predicted by B3LYP and MP2 are 0.51 and 1.50%, respectively. Based on this comparison, B3LYP is the most suitable method for this complex, both more accurate and computationally affordable than MP2.

I also measured transitions of the BA-D_2O dimer, in the hopes of observing splitting of its *b*-type transitions, which could then be compared to that of the *b*-type transitions of BA-H_2O. I began my search by looking for *a*-type transitions, predicted using the PMIFST program, by taking the B3LYP equilibrium geometry of BA-H_2O and substituting the hydrogen atoms of the water moiety with deuterium atoms. Following overnight conditioning of the sample cylinder and all tubing, I was able to observe weak transitions. In all, 12 *a*-type transitions were measured and these are listed in Table A.3. Although my primary motivation in studying the BA-D_2O dimer was to see if the greater mass of deuterium atoms would affect splitting of the *b*-type

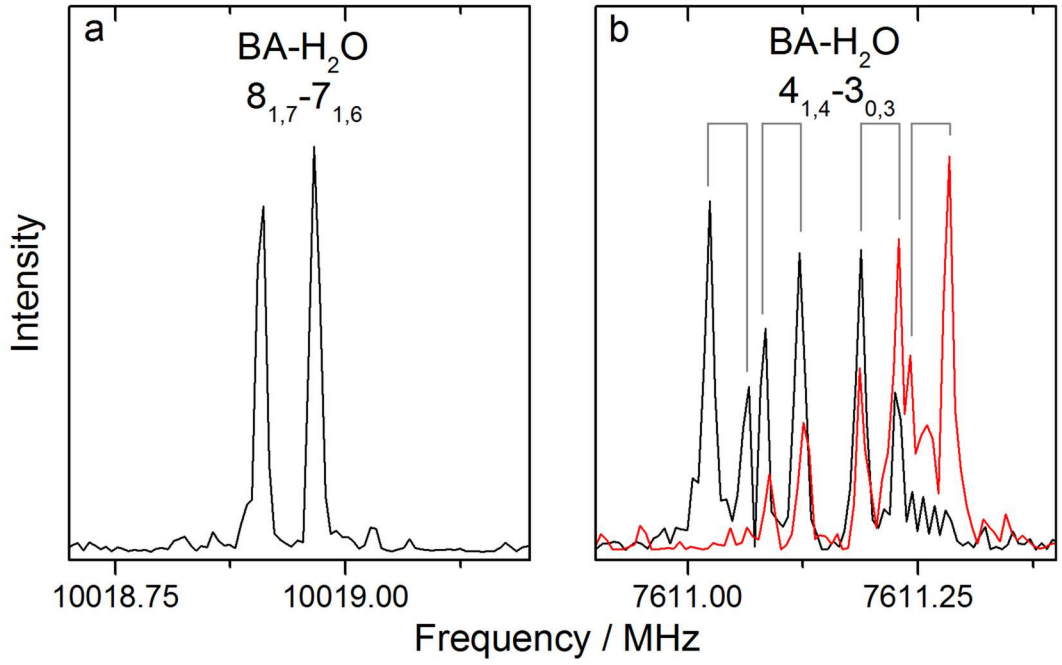

Figure 3.2. Representative transitions of BA-H_2O, measured using 0.5 mW excitation pulses. Panel (a) illustrates an average of 250 cycles, measured with an excitation pulse length of 2 μs; panel (b) illustrates an average of 10 000 cycles, measured with an excitation pulse length of 3 μs. Doppler pairs are denoted with grey brackets.

transitions, the low intensity of even the expectedly intense *a*-type transitions precluded measurement of the *b*-type transitions. Nonetheless, fitted *A*, *B*, and *C* rotational constants are listed in Table 3.1. I note that *A* is not well determined because no *b*-type transitions were observed.

3.3.2. Structure

In keeping with the relatively close agreement in rotational constants between the three levels of theory, the respective equilibrium geometries are fairly consistent, as demonstrated by the bond lengths and angles listed in Table 3.3. Given that the equilibrium geometry calculated using B3LYP gives the best spectral agreement, I expect that it is the closest to reality. In this structure, the distance between the oxygen and hydrogen atoms participating in the C=O···H−O hydrogen bond is 1.95 Å; the corresponding distance in the O−H···O hydrogen bond is 1.80 Å. For the trifluoroacetic acid-H_2O dimer,[46] these distances are 2.235 Å and 1.746 Å, respectively. The C=O···H−O hydrogen bond in BA-H_2O is significantly shorter, indicating it is a stronger bond. This difference is consistent with the inductive effect: the highly electronegative fluorine atoms in trifluoroacetic acid decrease the electron density on the oxygen atoms of the carboxylic acid functional group and weaken the hydrogen bonds in trifluoroacetic acid-H_2O. However, the inductive effect also weakens (lengthens) the O−H bond, so the total O−H···O bond length is about the same for both complexes.

Table 3.3. Bond lengths, bond angles, interaction energies, and dissociation energies of BA-H_2O from DFT and MP2 calculations, using the 6-311++G(2df,2pd) basis set.

	B3LYP	M06-2X	MP2
R(C=O) / Å	1.22	1.21	1.22
R(C−O) / Å	1.34	1.33	1.33
R(O-H) / Å	0.99	0.98	0.99
R(C=O···H-O) / Å	1.95	1.98	1.93
R(O-H···O) / Å	1.80	1.78	1.76
α(O-H···O)[a] / °	139.5	136.1	139.4
α(O···H-O)[b] / °	157.4	157.4	158.2
Δ*E*[c] / kJ mol^{-1}	-41.4	-48.2	-41.9
D_0[d] / kJ mol^{-1}	30.5	38.0	31.7

[a] Angle of long hydrogen bond. [b] Angle of short hydrogen bond. [c] Counterpoise corrected interaction energy. [d] ZPE-corrected dissociation energy.

Although an exact structural determination from experiment requires many single isotopic substitutions (so that even my BA-D_2O spectrum is unhelpful in this respect), I make some general observations below, based on the planar moment of inertia, P_c, calculated according to Equation (3.1).

$$P_c = \sum m_i c_i^2 = \frac{1}{2}(I_A + I_B - I_C) = \frac{h}{16\pi^2}\left(\frac{1}{A} + \frac{1}{B} - \frac{1}{C}\right) \quad (3.1)$$

Here, m_i is the mass of atom i; c_i is its coordinate along the c principal axis; I_A, I_B, and I_C are moments of inertia of the dimer about its principal inertial axes; h is the Planck constant; and A, B, and C are the rotational constants. As mass distribution outside the ab plane increases, so does P_c. Values of P_c from DFT and MP2 calculations are included in Table 3.2, and the experimentally determined values for BA-H_2O and BA-D_2O are included in Table 3.1. For both structures, the small non-zero values of P_c indicate that they are essentially planar. The DFT-calculated value is closest to experiment, since P_c depends on all three rotational constants.

Since BA-H_2O is nearly planar, the ab planes of BA and BA-H_2O roughly overlap. Following the method derived by Ouyang and Howard,[29] I determined the angle θ between the a principal axis of BA and the intermolecular axis of BA-H_2O, according to Equation (3.2).

$$\sin^2\theta = \frac{I_A\left(\mu R_{cm}^2 + I_a + I_b - I_A\right) - I_a(\mu R_{cm}^2 + I_b)}{\mu R_{cm}^2 (I_b - I_a)} \quad (3.2)$$

Here, I_a, I_b, and I_c are the moments of inertia of the BA monomer about its principal inertial axes; μ is the reduced mass of the dimer, defined as the product of the monomer masses divided

Table 3.4. Orientation of the BA and H_2O moieties in BA-H_2O and BA-D_2O and force constant and binding energy of BA-H_2O, calculated using a pseudo-diatomic model (ref. 50).

	BA-H_2O				BA-D_2O
	Experiment	B3LYP	M06-2X	MP2	Experiment
θ^a / °	4.9	0.1	0.3	0.3	6.4
$R_{cm}{}^b$ / Å	4.81	4.78	4.77	4.75	4.82
$D_J{}^c$ / kHz	0.0309	–	–	–	–
$k_s{}^d$ / N m^{-1}	13.2	–	–	–	–
$E_D{}^e$ / kJ mol^{-1}	25.4	–	–	–	–

[a] Angle between the a principal inertial axis of the BA moiety and the intermolecular axis. [b] Distance between the centres of mass of monomers. [c] Centrifugal distortion constant in Watson's S-reduction. [d] Force constant for the intermolecular stretching vibration of the dimer. [e] Dissociation energy of the dimer; though it is the same property as D_0 (listed in Table 3.3 for the *ab initio* calculations), it is historically denoted differently.

by their sum; and R_{cm} is the distance between the centres of mass of the monomers, which was calculated using Equation (3.3).

$$\mu R_{cm}^2 = I_C - I_c \quad (3.3)$$

I did not use my DFT or MP2 calculations to introduce *ad hoc* corrections to this simple model of the cluster; the results are compared to the same parameters for the predicted equilibrium geometries in Table 3.4. Both methods result in a value of θ less than 5°, so the intermolecular bonding axis is nearly parallel to the *a* principal inertial axis of BA. My R_{cm} value of 4.81 Å is considerably larger than that observed for propanoic acid-H_2O, 3.619 Å,[29] simply since BA is a larger carboxylic acid, so that its centre of mass lies further away along the intermolecular axis.

3.3.3. Tunnelling

The complicated splitting pattern in the observed *b*-type transitions (see Figure 3.2b) is an indication of quantum mechanical tunnelling. Since the *b*-dipole moment is so small, calculated to be 0.1 D, only two *b*-type transitions could be measured. There is insufficient information to determine any tunnelling barrier heights from the spectroscopic data. Instead, I investigated the potential tunnelling motions using DFT calculations. Initially, I looked at four different motions. First, I considered motions analogous to the three described by Ouyang *et al.*,[46] for trifluoroacetic acid-H_2O, and by Canagaratna *et al.*,[47] for nitric acid-H_2O: (1) wagging of the unbound hydrogen atom of water, through the mirror plane of the BA moiety; (2) rotation of water about the lone pair hydrogen-bonded to BA; and (3) rotation of water about its C_2 axis. Additionally, I considered (4) exchange of the two hydrogen-bonded protons, a motion similar to that described for the BA-formic acid dimer.[37]

Often, calculations of tunnelling barriers are done by scanning one internal coordinate, which is supposed to be associated with the tunnelling motion, while all others are fixed. Using an alternate method, I searched for transition states connecting the minima on either side of the tunnelling barriers using the synchronous transit-guided quasi-Newton method.[48] The transition states were then confirmed by running transition state optimization (option opt=ts in Gaussian) and frequency calculations. Finally, counterpoise correction calculations were run. For each transition state, one imaginary frequency was observed. Displacement vectors based on normal mode analyses showed that the vibrations associated with the imaginary frequencies lie along the tunnelling paths.

Tunnelling motion (1) is the wagging of the unbound hydrogen atom of water, through the mirror plane of BA. The transition state has C_s symmetry, with all atoms in the plane, as illustrated in Figure 3.3a. Considering only the electronic energy of the minimum and transition state, tunnelling motion (1) involves a small barrier of 2.3 kJ mol^{-1}. However, effects of the zero-point energy (ZPE) and basis set superposition error (BSSE) to both the minimum and transition state must be taken into account. The ZPE and BSSE are 2.1 kJ mol^{-1} and 1.0 kJ mol^{-1}, respectively, greater for the equilibrium structure than for the transition state, such that the barrier disappears and the transition state turns into a shallow minimum I note that the small negative difference, –0.8 kJ mol^{-1}, between the fully-corrected energies of the initial transition state and minimum could be due to counterpoise corrections being applied after the geometry optimizations; since BSSE actually alters the potential energy surface, the minimum and transition state geometries might not be absolutely correct.[49] In any case, the absence of a barrier to tunnelling motion (1) is consistent with large amplitude motion of the unbound hydrogen, which I invoked above to explain the absence of *c*-type transitions.

Tunnelling motion (2) is the rotation of the water moiety about an axis that includes the oxygen atom and the lone pair of electrons hydrogen-bonded to BA. The transition state has C_s symmetry, with the hydrogen atoms of water unbound and pointing out of the mirror plane, as illustrated in Figure 3.3b. After correcting for ZPE and BSSE, the barrier height is calculated to be 7.0 kJ mol^{-1} or 590 cm^{-1}. The barrier to the analogous motion in trifluoroacetic acid-H_2O has previously been calculated to be of similar magnitude, about 1000 cm^{-1}. It is possible that, had the highest energy trifluoroacetic acid-H_2O structure along the tunnelling path been subjected to a transition state optimization, the barrier height may have been lowered.

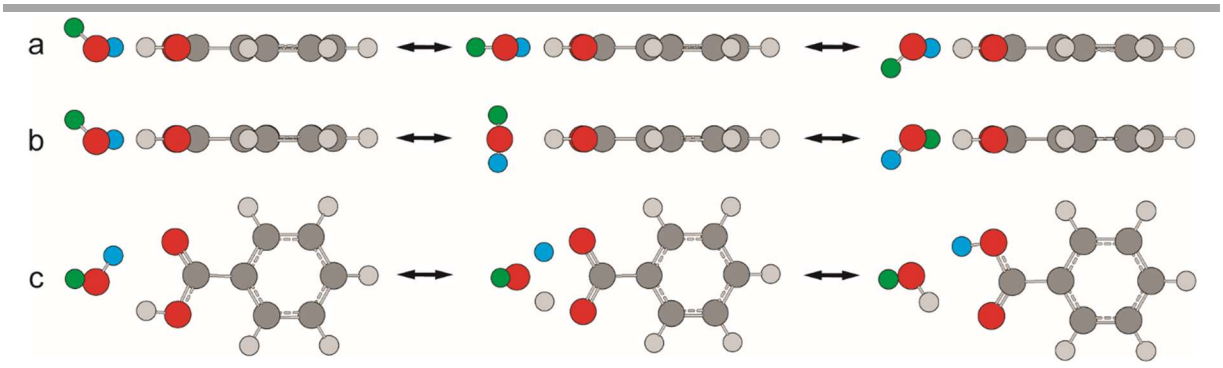

Figure 3.3. Internal motions 1 (a), 2 (b), and 4 (c) involving the water moiety.

Tunnelling motion (3) is the rotation of water about its C_2 axis. For the analogous motion in trifluoroacetic acid-H_2O, Ouyang *et al.* calculated a large barrier of 4500 cm^{-1}, which is consistent with the breaking of both hydrogen bonds.[46] Repeated computational searches for a transition state associated with this motion in BA-H_2O, beginning with slightly different proposed structures with roughly 90° rotation of the water moiety, always ended with the transition state for tunnelling motion (2). For the purpose of comparison, I tried to locate the transition state for tunnelling motion (3) in trifluoroacetic acid-H_2O. Similarly, this search resulted in the transition state associated with tunnelling motion (2), rotation of water about the lone pair hydrogen-bonded to the acid. I conclude that the proposed transition state in fact lies on the "bank" of a saddle-point, to which it relaxes in the course of the calculation: in other words, it is not a minimum in any coordinate.

Tunnelling motion (4) is the exchange of the two hydrogen-bonded protons. The transition state has C_s symmetry, with the mirror plane of the complex perpendicular to the mirror plane of BA, as illustrated in Figure 3.3c. After correcting for ZPE and BSSE, the barrier height was calculated to be 47 kJ mol^{-1} or 4000 cm^{-1}, certainly too great to contribute significantly to the observed small tunnelling splittings. I note that this barrier is greater than those determined for proton exchange in carboxylic acid dimers. For example, the barrier to proton exchange in BA-formic acid has been experimentally determined to be about 2400 cm^{-1}.[37]

In summary, tunnelling motion (2) is likely the only candidate for the observed splitting. However, how this tunnelling motion can cause a relatively complicated splitting pattern with four components remains unclear.

3.3.4. Interaction and dissociation energies

Using my results from DFT and MP2 calculations, I have predicted the interaction and spectroscopic dissociation energies of BA-H_2O at different levels of theory. Following Boys and Bernardi,[41] I calculated the counterpoise-corrected interaction energy, ΔE_{int}, using Equation (3.4).

$$\Delta E_{int} = E_{AB}^{\alpha\beta}(AB) - E_{AB}^{\alpha\beta}(A) - E_{AB}^{\alpha\beta}(B) \quad (3.4)$$

Here, superscript $\alpha\beta$ denotes the basis set of dimer AB, subscript AB denotes the geometry of the dimer, and E is the energy of the species in parentheses, so that the last term, for example,

is the energy of monomer B "frozen" in the geometry it adopted in the optimized dimer, evaluated using the basis set of the dimer. Values for the interaction energy at the three levels of theory are listed in Table 3.3. The MP2-predicted interaction energy, −41.9 kJ mol^{-1}, is in excellent agreement with the value calculated by Nagy *et al.*, roughly −40 kJ mol^{-1}, using a slightly lower level *ab initio* calculation.[26] The DFT-predicted interaction energy is slightly less negative, indicating that hydration of the *syn*-conformer is less stabilizing at this level of theory. The M06-2X-predicted interaction energy is much more negative, in fact, anomalously so. This excess stabilization could be an indication that dispersive interactions are being over-estimated.

The dissociation energy, D_0, can be calculated using Equation (3.5).

$$D_0 = - \Delta E_{\text{int}} - (\text{ZPE}_{\text{BA-H}_2\text{O}} - \text{ZPE}_{\text{BA}} - \text{ZPE}_{\text{H}_2\text{O}}) \tag{3.5}$$

The values for the ZPE of the dimer calculated using the B3LYP, M06-2X, and MP2 methods are 369, 373, and 371 kJ mol^{-1}, respectively. The combined ZPE corrections ($- \Delta E_{\text{int}} - D_0$) calculated using the B3LYP, M06-2X, and MP2 methods are 10.9, 10.2, and 10.2 kJ mol^{-1}, respectively. Resulting values for the spectroscopic dissociation energy are listed in Table 3.3. The MP2-predicted value, 31.7 kJ mol^{-1}, is similar to that of the glycine-H_2O dimer, another doubly hydrogen-bonded cluster incorporating a six-membered ring.[39] Again, the B3LYP-predicted value is similar, but the M06-2X-predicted value is over 6 kJ mol^{-1} greater, as a result of the much more negative interaction energy. Écija *et al.* observed a similar discrepancy for a variety of biologically-relevant monohydrates.[39]

Using a simple pseudo-diatomic model, I also determined a rough estimate of the dissociation energy from experimental rotational and centrifugal distortion constants. The force constant of the intermolecular stretching vibration, k_s, can be calculated using Equation (3.6).[50]

$$k_s = 16 \frac{\pi^4 \mu^2 {R_{\text{cm}}}^2}{h D_J} \left[4B^4 + 4C^4 - (B - C)^2 (B + C)^2 \right] \tag{3.6}$$

Here, μ is the reduced mass of the monomers, R_{cm} is the distance from the centres of mass of the monomers, h is the Planck constant, D_J is a distortion constant in Watson's S-reduction Hamiltonian,[43] and B and C are the experimental rotational constants. The distortion constant D_J was calculated using Equation (3.7).[51]

$$D_J = \Delta_J - \frac{2\delta_K (B - C)}{2A - B - C} \tag{3.7}$$

Here, A, B, and C are the measured rotational constants; and Δ_J and δ_K are centrifugal distortion constants in Watson's A-reduction Hamiltonian.[43] As shown by Novick *et al.*,[52] for a Lennard-Jones potential, the dissociation energy can be calculated using Equation (3.8).

$$E_{\mathrm{D}} = \frac{1}{72} k_s R_{\mathrm{cm}}{}^2 \tag{3.8}$$

The results of these calculations for BA-H_2O are summarized in Table 3.4. The force constant was found to be 13.2 N m^{-1}, almost three times the value reported for the fluorobenzene-H_2O dimer, 5.3 N m^{-1}, another hydrogen-bonded cluster.[51] A dissociation energy of 25.4 kJ mol^{-1} was estimated. Certainly, this simplified model is not as accurate as my MP2 calculations, which yielded a dissociation energy of 31.7 kJ mol^{-1}, but it does provide an appealing and intuitive picture of intermolecular bonding. Écija *et al.* reported E_{D} values typically one half of *ab initio* results,[39] so the far better agreement observed in the present work is surprising and attests to the utility of this simple model for some systems.

3.3.5. Equilibrium constant and atmospheric implications

Equilibrium constants can be calculated from statistical thermodynamics using two methods.[53] Using the first method, one calculates the equilibrium constant from the Gibbs free energy change in going from reactants to products, without investigating the partition functions on which it is based, as illustrated, for example, by Vaida and Headrick.[54] Using the second method, the equilibrium constant is calculated directly from the partition functions of reactants and products, as illustrated, for example, by Ouyang and Howard.[29] The latter method is advantageous, because experimental parameters can be easily introduced; for example, the rotational partition function can be calculated from the reported experimental values, better constraining the total partition function. Furthermore, differences between equilibrium constants can be thoroughly rationalized if the translational, rotational, and vibrational partition functions are investigated individually.

The partition functions of BA, H_2O, and BA-H_2O are calculated according to basic statistical mechanics.[55] The translational partition function of each species depends simply on its mass. The rotational partition function of each species depends on its symmetry number, σ, and rotational constants. For H_2O, $\sigma = 2$, and rotational constants are reported by Messer *et al.*[56] For BA and BA-H_2O, $\sigma = 2$ and $\sigma = 1$, respectively, and rotational constants are reported above. The vibrational partition function of each species is calculated on the basis of vibrational

frequencies calculated for the equilibrium geometry at the MP2/6-311++G(2df,2pd) level of theory. The electronic partition function of each species is 1, and the total partition function is the product of the four contributions. The equilibrium constant for hydration is calculated using Equation (3.9).

$$K_{p,\mathrm{BA\text{-}H_2O}} = (2q^{\ominus}_{\mathrm{BA\text{-}H_2O}} e^{\frac{D_0}{kT}} N_A)/(q^{\ominus}_{\mathrm{BA}} q^{\ominus}_{\mathrm{H_2O}}) \quad (3.9)$$

Here, $q_i^{\ominus}$ is the overall partition function of species i, D_0 is dissociation energy, k_B is the Boltzmann constant, T is temperature in Kelvin, and N_A is Avogadro's constant. I follow Ouyang and Howard, multiplying the typical expression by 2, to account for large amplitude motion of the unbound hydrogen, which gives two enantiomers.[29] D_0 is taken as the value from my MP2 calculations, discussed above.

Temperature is known to affect nucleation[57] and condensational growth[58] of aerosols in the atmosphere, for instance, by changing the saturation vapour pressures of trace gases.[59] For different regions, I estimated the effect of changing altitude, with its attendant changes in

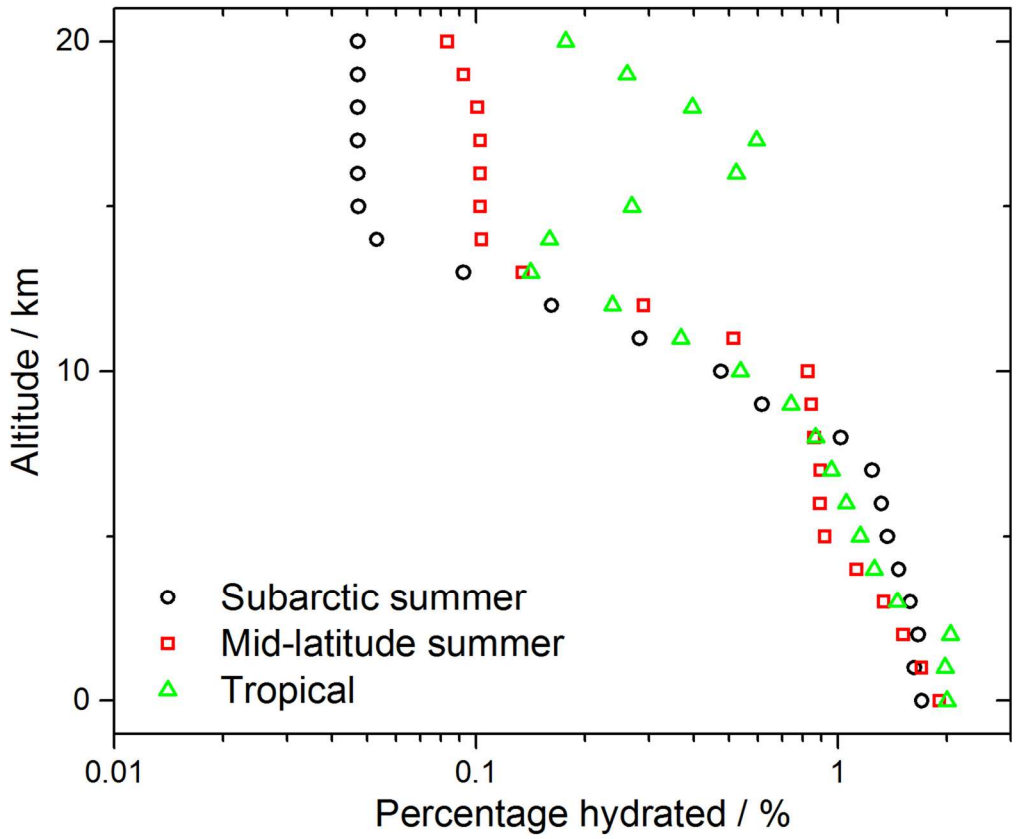

Figure 3.4. Variations in percentage of BA hydrated as a function of altitude in different regions.

temperature and water saturation vapour pressure, on K_p and the percent of BA hydrated, χ, calculated using Equation (3.10).[46]

$$\chi = K_{p,\mathrm{BA\text{-}H_2O}} \frac{p_{\mathrm{H_2O}}}{p^{\ominus}} 100\% \qquad (3.10)$$

Here, $p_{\mathrm{H_2O}}$ is the partial pressure of water, and $p^{\ominus}$ is the ambient pressure. I refer to Ellingson *et al.*[60] for subarctic summer, mid-latitude summer, and tropical atmospheric conditions. The resulting profiles of χ are shown in Figure 3.4. At ground level, χ is about the same in all three regions. Some variations occur at higher altitudes, most notably at 14 km and above. The oscillation of χ in the tropical region is due simply to an oscillation of temperature.

I also estimated the effect of seasonal variations on χ at a monitoring site in Alberta, Canada, for which temperature and relative humidity measurements are available during the period of January 2010 to January 2013. Measurements were extracted from the Clean Air Strategic Alliance database[61] for the "Calgary Northwest" monitoring station. Calgary Northwest is located in Calgary, Alberta, a major city with a population of over 1 million.

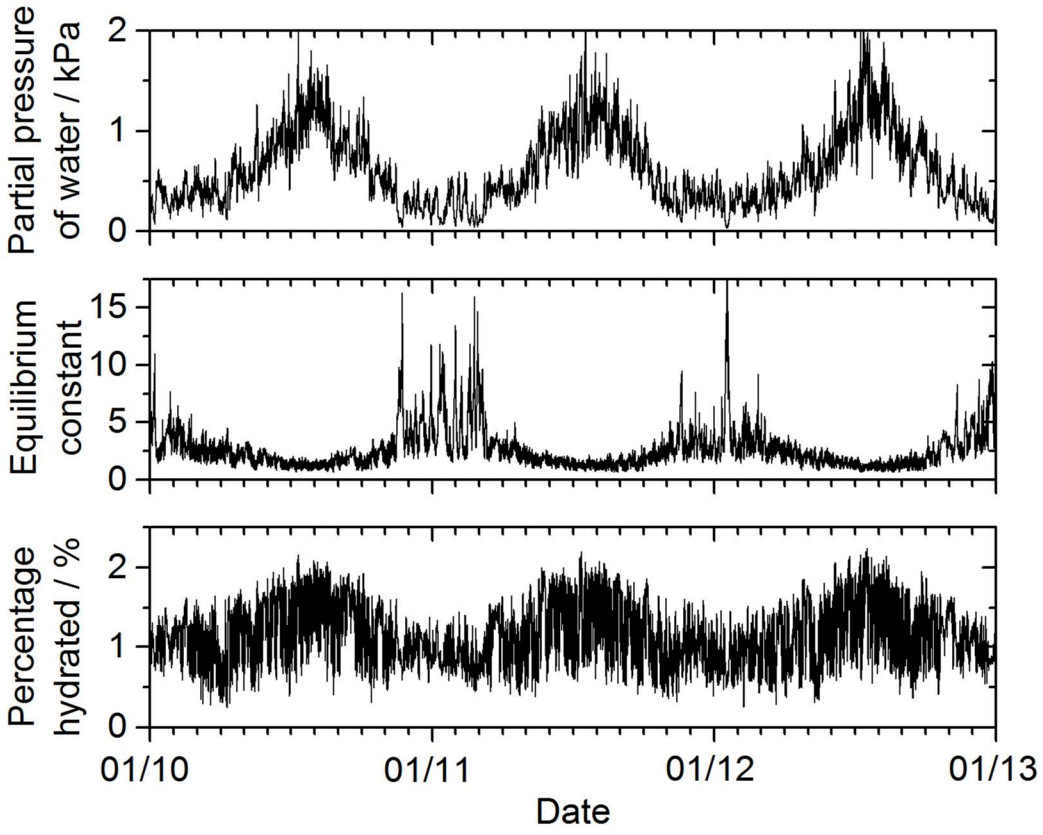

Figure 3.5. Seasonal variations in partial pressure of water, equilibrium constant, and percentage of hydrate, based in part on vibrational frequencies and dissociation energy at the MP2/6-311++G(2df,2pd) level of theory.

Seasonal variations in temperature and water vapour concentration at the site are extreme. To calculate the saturation vapour pressure of water as a function of temperature, I use the parameterization of Hyland and Wexler,[62] which has been validated both above and below 273.15 K (in the latter case, for super-cooled water).[63] Results are illustrated in Figure 3.5. Extremely low winter temperatures, occasionally as severe as 233 K, result in higher values of K_p and lower values of p_{H_2O}, though relative humidity may be high (because the saturated vapour pressure of water is very low at these winter temperatures). Summer temperatures result in lower values of K_p and higher values of p_{H_2O}. I find that the percent of BA hydrated varies only slightly with season; the maxima correspond to maxima in p_{H_2O}, so the trend in p_{H_2O} dominates the trend in K_p. The yearly average is about 1%, similar to the value of 1.4% calculated by Ouyang and Howard for propanoic acid-H_2O.[29] However, when substituting the dissociation energy calculated using MP2 with that calculated using M06-2X, the yearly average increases to about 18%. Thus, deviations in dissociation energy, one of the few estimated parameters, cause relatively large changes in K_p, and χ is consequently approximate.

Whether or not BA-H_2O is prevalent in the gas phase, it represents the first step in the hydration of BA in aqueous aerosols, both in the bulk and at the air-water interface. Since BA is amphiphilic, it is surface active, decreasing the surface tension of water[64] and potentially enhancing cloud formation.[65] In the observed isomer of BA monohydrate, the acid group participates in a six-membered hydrogen-bonded ring; furthermore, in the predicted minimum energy isomer of BA dihydrate, the acid participates in a cooperative eight-membered hydrogen-bonded ring. Consequently, at the interface, the acid group is expected to participate in a hydrogen bond network with water molecules, while the hydrophobic aromatic ring buoys the molecule. This general representation is consistent with recent observations of BA at the air-water interface in liquid jet experiments.[66]

3.4. Conclusions

This is the first experimental investigation of the structure of BA-H_2O. The good agreement between the experimental rotational constants and those from the *ab initio* equilibrium geometry is definitive evidence that a six-membered, hydrogen-bonded ring forms between BA and H_2O, as has been observed for other carboxylic acid-H_2O complexes. In addition, the stability of the complex was investigated using *ab initio* calculations; in particular, the interaction energy,

dissociation energy, equilibrium constant, and percentage of hydrate were calculated. Although the predicted percentage of hydrate is only approximate, the complex is certainly stable enough to occur in the atmosphere.

References

1 Leopold, K. R. Hydrated acid clusters. *Annu. Rev. Phys. Chem.* **2011**, *62*, 327-349.

2 Klemperer, W.; Vaida, V. Molecular complexes in close and far away. *Proc. Natl. Acad. Sci. U. S. A.* **2006**, *103*, 10584-10588.

3 Sennikov, P. G.; Ignatov, S. K.; Schrems, O. Complexes and clusters of water relevant to atmospheric chemistry: H_2O complexes with oxidants. *ChemPhysChem* **2005**, *6*, 392-412.

4 Staikova, M.; Oh, M.; Donaldson, D. J. Overtone-induced decarboxylation: A potential sink for atmospheric diacids. *J. Phys. Chem. A* **2005**, *109*, 597-602.

5 Weber, K. H.; Morales, F. J.; Tao, F.-M. Theoretical study on the structure and stabilities of molecular clusters of oxalic acid with water. *J. Phys. Chem. A* **2012**, *116*, 11601-11617.

6 Xu, W.; Zhang, R. Theoretical investigation of interaction of dicarboxylic acids with common aerosol nucleation precursors. *J. Phys. Chem. A* **2012**, *116*, 4539-4550.

7 Xu, Y.; Nadykto, A. B.; Yu, F.; Jiang, L.; Wang, W. Formation and properties of hydrogen-bonded complexes of common organic oxalic acid with atmospheric nucleation precursors. *THEOCHEM* **2010**, *951*, 28-33.

8 Zhao, J.; Khalizov, A.; Zhang, R.; McGraw, R. Hydrogen-bonding interaction in molecular complexes and clusters of aerosol nucleation precursors. *J. Phys. Chem. A* **2009**, *113*, 680-689.

9 Zhang, R.; Suh, I.; Zhao, J.; Zhang, D.; Fortner, E. C.; Tie, X.; Molina, L. T.; Molina, M. J. Atmospheric new particle formation enhanced by organic acids. *Science* **2004**, *304*, 1487-1490.

10 Schrader, W. Atmosphere, a chemical reactor – formation pathways of secondary organic aerosols. *Angew. Chem. Int. Ed.* **2005**, *44*, 1444-1446.

11 Zhang, R.; Khalizov, A.; Wang, L.; Hu, M.; Xu, W. Nucleation and growth of nanoparticles in the atmosphere. *Chem. Rev.* **2012**, *112*, 1957-2011.

12 Zhang, R. Getting to the critical nucleus of aerosol formation. *Science* **2010**, *328*, 1366-1367.

13 Kawamura, K.; Ng, L.-L.; Kaplan, I. R. Determination of organic acids (C_1-C_{10}) in the atmosphere, motor exhausts, and engine oils. *Environ. Sci. Technol*. **1985**, *19*, 1082-1086.

14 Hamilton, J. F.; Webb, P. J.; Lewis, A. C.; Reviejo, M. M. Quantifying small molecules in secondary organic aerosol formed during the photo-oxidation of toluene with hydroxyl radicals. *Atmos. Environ.* **2005**, *39*, 7263-7275.

15 Jang, M.; Kamens, R. M. Characterization of secondary organic aerosol from the photooxidation of toluene in the presence of NO_x and 1-propene. *Environ. Sci. Technol.* **2001**, *35*, 3626-3639.

16 Fu, P. Q.; *et al.* Diurnal variations of organic molecular tracers and stable carbon isotopic composition in atmospheric aerosols over Mt. Tai in the North China Plain: An influence of biomass burning. *Atmos. Chem. Phys.* **2012**, *12*, 8359-8375. See bibliography for complete list of authors.

17 Ho, K. F.; Ho, S. S. H.; Lee, S. C.; Kawamura, K.; Zou, S. C.; Cao, J. J.; Xu, H. M. Summer and winter variations of dicarboxylic acids, fatty acids and benzoic acid in $PM_{2.5}$ in Pearl Delta River Region, China. *Atmos. Chem. Phys.* **2011**, *11*, 2197-2208.

18 Hammett, L. P. The effect of structure upon the reactions of organic compounds. Benzene derivatives. *J. Am. Chem. Soc.* **1937**, *59*, 96-103.

19 Flores, N.; Jiménez, I. A.; Giménez, A.; Ruiz, G.; Gutiérrez, D.; Bourdy, G.; Bazzocchi, I. L. Antiparasitic activity of prenylated benzoic acid derivatives from Piper species. *Phytochemistry* **2009**, *70*, 621-627.

20 Müller, J.; Limban, C.; Stadelmann, B.; Missir, A. V.; Chirita, I. C.; Chifiriuc, M. C.; Nitulescu, G. M.; Hemphill, A. Thioureides of 2-(phenoxymethyl)-benzoic acid 4-R substituted: A novel class of anti-parasitic compounds. *Parasitol. Int.* **2009**, *58*, 128-135.

21 Kim, Y. H.; Hwang, J.; Son, J. I.; Shim, Y. B. Synthesis, electrochemical, and spectroelectrochemical properties of conductive poly-[2,5-di-(2-thienyl)-1*H*-pyrrole-1-(*p*-benzoic acid)]. *Synthetic Met.* **2010**, *160*, 413-418.

22 Chuang, W.-T.; Sheu, H.-S.; Jeng, U.-S.; Wu, H. H.; Hong, P. D.; Lee, J.-J. Tetragonally perforated layer structure via columnar ordering of 4'-(3,4,5-trioctyloxybenzoyloxy)-benzoic acid in a supramolecular complex with polystyrene-*block*-poly(4-vinylpyridine). *Chem. Mater.* **2009**, *21*, 975-978.

23 Onda, M.; Asai, M.; Takise, K.; Kuwae, K.; Hayami, K.; Kuroe, A.; Mori, M.; Miyazaki, H.; Suzuki, N.; Yamaguchi, I. Microwave spectrum of benzoic acid. *J. Mol. Struct.* **1999**, *482-483*, 301-303.

24 Godfrey, P. D.; McNaughton, D. Structural studies of aromatic carboxylic acids via computational chemistry and microwave spectroscopy. *J. Chem. Phys.* **2013**, *138*, 024303 (8 pp.).

25 Aarset, K.; Page, E. M.; Rice, D. A. Molecular structures of benzoic acid and 2-hydroxybenzoic acid, obtained by gas-phase electron diffraction and theoretical calculations. *J. Phys. Chem. A* **2006**, *110*, 9014-9019.

26 Nagy, P. I.; Smith, D. A.; Alagona, G.; Ghio, C. *Ab initio* studies of free and monohydrated carboxylic acids in the gas phase. *J. Phys. Chem.* **1994**, *98*, 486-493.

27 Priem, D.; Ha, T.-K.; Bauder, A. Rotational spectra and structures of three hydrogen-bonded complexes between formic acid and water. *J. Chem. Phys.* **2000**, *113*, 169-175.

28 Ouyang, B.; Howard, B. J. The monohydrate and dihydrate of acetic acid: A high-resolution microwave spectroscopic study. *Phys. Chem. Chem. Phys.* **2009**, *11*, 366-373.

29 Ouyang, B.; Howard, B. J. High-resolution microwave spectroscopic and *ab initio* studies of propanoic acid and its hydrates. *J. Phys. Chem. A* **2008**, *112*, 8208-8214.

30 De Kruif, C. G.; Blok, J. G. The vapour pressure of benzoic acid. *J. Chem. Thermodynamics* **1982**, *14*, 201-206.

31 Xu, Y.; Van Wijngaarden, J.; Jäger, W. Microwave spectroscopy of ternary and quaternary van der Waals clusters. *Int. Rev. Phys. Chem.* **2005**, *24*, 301-338.

32 Xu, Y.; Jäger, W. Evidence for heavy atom large amplitude motions in RG-cyclopropane van der Waals complexes (RG=Ne, Ar, Kr) from rotation-tunneling spectroscopy. *J. Chem. Phys.* **1997**, *106*, 7968-7980.

33 Feng, G.; Gou, Q.; Evangelisti, L.; Xia, Z.; Caminati, W. Conformational equilibria in carboxylic acid bimolecules: A rotational study of acrylic acid-formic acid. *Phys. Chem. Chem. Phys.* **2013**, *15*, 2917-2922.

34 Tanjaroon, C.; Jäger, W. High-resolution microwave spectrum of the weakly bound helium-pyridine complex. *J. Chem. Phys.* **2007**, *127*, 034302 (6 pp.).

35 Becke, A. D. Density-functional thermochemistry. III. The role of exact exchange. *J. Chem. Phys.* **1993**, *98*, 5648-5652.

36 Zhao, Y.; Truhlar, D. G. The M06 suite of density functionals for main group thermochemistry, thermochemical kinetics, noncovalent interactions, excited states, and transition elements: Two new functionals and systematic testing of four M06-class functionals and 12 other functionals. *Theor. Chem. Acc.* **2008**, *120*, 215-241.

37 Evangelisti, L.; Écija, P.; Cocinero, E. J.; Castano, F.; Lesarri, A.; Caminati, W.; Meyer, R. Proton tunneling in heterodimers of carboxylic acids: A rotational study of the benzoic acid-formic acid bimolecule. *J. Phys. Chem. Lett.* **2012**, *3*, 3770-3775.

38 Elm, J.; Bilde, M.; Mikkelsen, K. V. Assessment of density functional theory in predicting structures and free energies of reaction of atmospheric prenucleation clusters. *J. Chem. Theory Comput.* **2012**, *8*, 2071-2077.

39 Écija, P.; Basterretxea, F. J.; Lesarri, A.; Millán, J.; Castano, F.; Cocinero, E. J. Single hydration of the peptide bond: The case of the Vince lactam. *J. Phys. Chem. A* **2012**, *116*, 10099-10106.

40 Frisch, M. J.; *et al. Gaussian 09*, Rev. D.01; Gaussian, Inc.: Wallingford, CT, **2013**. See bibliography for complete list of authors.

41 Boys, S. F.; Bernardi, F. The calculation of small molecular interactions by the difference of separate total energies. Some procedures with reduced errors. *Mol. Phys.* **1970**, *19*, 553-566.

42 Western, C. M. *PGOPHER, A Program for Simulating Rotational Structure*, University of Bristol: Bristol, UK. http://pgopher.chm.bris.ac.uk.

43 Watson, J. K. G. Determination of centrifugal distortion coefficients of asymmetric-top molecules. *J. Chem. Phys.* **1967**, *46*, 1935-1949.

44 Kisiel, Z. Assignment and Analysis of Complex Rotational Spectra. In *Spectroscopy from Space*; Demaison, J., Sarka, K., Cohen, E. A., Eds.; Kluwer: Dordrecht, 2001; pp. 91-106.

45 Coudert, L. H.; Lovas, F. J.; Suenram, R. D.; Hougen, J. T. New measurements of microwave transitions in the water dimer. *J. Chem. Phys.* **1987**, *87*, 6290-6299.

46 Ouyang, B.; Starkey, T. G.; Howard, B. J. High-resolution microwave studies of ring-structured complexes between trifluoroacetic acid and water. *J. Phys. Chem. A* **2007**, *111*, 6165-6175.

47 Canagaratna, M.; Phillips, J. A.; Ott, M. E.; Leopold, K. R. The nitric acid-water complex: Microwave spectrum, structure, and tunneling. *J. Phys. Chem. A* **1998**, *102*, 1489-1497.

48 Peng, C.; Ayala, P. Y.; Schlegel, H. B.; Frisch, M. J. Using redundant internal coordinates to optimize equilibrium geometries and transition states. *J. Comp. Chem.* **1996**, *17*, 49-56.

49 Salvador, P.; Szczęśniak, M. M. Counterpoise-corrected geometries and harmonic frequencies of *N*-body clusters: Application to $(HF)_n$ (n=3,4). *J. Chem. Phys.* **2003**, *118*, 537-549.

50 Millen, D. J. Determination of stretching force constants of weakly bound dimers from centrifugal distortion constants. *Can. J. Chem.* **1985**, *63*, 1477-1479.

51 Brendel, K.; Mäder, H.; Xu, Y.; Jäger, W. The rotational spectra of the fluorobenzene···water and *p*-difluorobenzene···water dimers: Structure and internal dynamics. *J. Mol. Spectrosc.* **2011**, *268*, 47-52.

52 Novick, S. E.; Harris, S. J.; Janda, K. C.; Klemperer, W. Structure and bonding of KrClF: Intermolecular force fields in van der Waals molecules. *Can. J. Phys.* **1975**, *53*, 2007-2015.

53 McClelland, B. J. Equilibrium constants. *Statistical Thermodynamics*; Studies in Chemical Physics Series; Chapman and Hall: London, 1973; pp. 168-182.

54 Vaida, V.; Headrick, J. E. Physicochemical properties of hydrated complexes in the Earth's atmosphere. *J. Phys. Chem. A* **2000**, *104*, 5401-5412.

55 Atkins, P. Statistical thermodynamics: The machinery. *Physical Chemistry*, 6th ed.; Freeman: New York, 1998; pp. 593-617.

56 Messer, J. K.; De Lucia, F. C.; Helminger, P. The pure rotational spectrum of water vapor – a millimeter, submillimeter, and far infrared analysis. *Int. J. Infrared Milli.* **1983**, *4*, 505-539.

57 Hale, B. N. Temperature dependence of homogeneous nucleation rates for water: Near equivalence of the empirical fit of Wölk and Strey, and the scaled nucleation model. *J. Chem. Phys.* **2005**, *122*, 204509 (3 pp.).

58 Okuyama, K.; Kousaka, Y.; Motouchi, T. Condensational growth of ultrafine aerosol particles in a new particle size magnifier. *Aerosol Sci. Technol.* **1984**, *3*, 353-366.

59 Schnitzler, E. G.; McDonald, K. M. Characterization of low-temperature vapour pressure estimates for secondary organic aerosol applications. *Atmos. Environ.* **2012**, *56*, 9-15.

60 Ellingson, R. G.; Ellis, J.; Fels, S. The intercomparison of radiation codes used in climate models: Long wave results. *J. Geophys. Res.* **1991**, *96*, 8929-8953.

61 Clean Air Strategic Alliance Data Warehouse. http://www.casadata.org (accessed April 2013).

62 Hyland, R. W.; Wexler, A. Formulations for the thermodynamic properties of the saturated phases of H_2O from 173.15 K to 473.15 K. *ASHRAE Trans.* **1983**, *89*, 500-519.

63 Murphy, D. M.; Koop, T. Review of the vapour pressures of ice and supercooled water for atmospheric applications. *Q. J. R. Meteorol. Soc.* **2005**, *131*, 1539-1565.

64 Paluch, M.; Dynarowicz, P. Electrical properties of adsorbed films of some aromatic compounds at the water/air interface. *J. Colloid Interface Sci.* **1987**, *115*, 307-311.

65 McNeill, V. F.; Sareen, N.; Schwier, A. N. Surface-active organics in atmospheric aerosols. *Top. Curr. Chem.* **2014**, *339*, 201-260.

66 Ottosson, N.; Romanova, A. O.; Söderström, J.; Björneholm, O.; Öhrwall, G.; Fedorov, M. V. Molecular sinkers: X-ray photoemission and atomistic simulations of benzoic acid and benzoate at the aqueous solution/vapor interface. *J. Phys. Chem. B* **2012**, *116*, 13017-13023.

4 Rotational spectroscopy of the atmospheric photo-oxidation product *o*-toluic acid and its monohydrate

4.1. Introduction

In the atmosphere, photo-oxidation of volatile organic compounds (VOCs) is a significant source of carboxylic acids.[1] These and other low-volatility oxygenated products form secondary organic aerosol (SOA),[2] by condensing onto pre-existing particles[3] or first participating in nucleation.[4] For example, the addition of aromatic carboxylic acids to gas-phase mixtures of sulphuric acid and water increases the rate of nucleation;[5] at the molecular scale, a ternary critical nucleus (from which further particle growth is spontaneous)[6] may result from the inclusion of a single carboxylic acid molecule in an otherwise binary cluster.[7] One step towards characterizing critical nuclei is the characterization of carboxylic acid-water clusters.

Aromatic VOCs are the most important anthropogenic SOA precursors, accounting for up to 12% of global SOA.[8] The structural isomers of xylene are emitted by transportation and industry, such as oil refining.[9] For instance, the concentration of *o*-xylene measured over the Athabasca oil sands in Alberta is 85 times greater than the background concentration.[10] SOA mass yields of about 10-25% have been measured for the oxidation of *o*-xylene by hydroxyl radical,[11] and the reaction mechanism has been investigated thoroughly, both experimentally (in smog chambers)[12,13] and theoretically (using *ab initio* calculations).[14] Hydrogen abstraction from *o*-xylene by hydroxyl radical leads to the formation of *o*-tolualdehyde;[15] further oxidation leads to the formation of *o*-toluic acid (OTA).[16] OTA and its structural isomers, *m*- and *p*-toluic acid, have been detected in atmospheric aerosols sampled in the North China Plain, and the diurnal trend in their concentrations is similar to that of benzoic acid (BA),[17] possibly indicating a mutual source in addition to photo-oxidation, such as primary engine exhaust emissions.[18]

OTA has been investigated in earlier spectroscopic studies. Ito *et al.* used ultraviolet absorption spectroscopy to demonstrate increasing formation of the hydrogen-bonded OTA-OTA complex in solution with decreasing temperature.[19] More recently, Babu *et al.* investigated OTA in the solid phase using Fourier-transform infrared and Raman spectroscopies.[20] Using X-ray diffraction, Polito *et al.* determined that the crystal structure of OTA is composed of hydrogen-bonded ribbons; in each monomer unit, the carbonyl oxygen atom, rather than that bonded to the acidic hydrogen atom, is neighbouring the methyl group.[21] In the gas phase, the ionization energy of OTA has been measured by photo-ionization mass spectrometry;[22] however, the structure of OTA in the gas phase has not been investigated. Furthermore, the OTA-H_2O complex has not been investigated previously, either experimentally or theoretically.

Using high-resolution microwave spectroscopy, the structures (and, in some cases, dynamics) of hydrates of several atmospherically-relevant carboxylic acids have been characterized in the past, including BA,[23] formic acid,[24] and perfluorobutyric acid,[26] a persistent organic pollutant. In the minimum energy conformers of these complexes, water is bound to the acid by two hydrogen bonds, participating in the formation of a six-membered intermolecular ring by acting as both proton donor and acceptor.[23]

Here, I investigate the structure and dynamics of OTA and OTA-H_2O in the gas phase using high resolution microwave spectroscopy and *ab initio* calculations. Rotational transitions of one conformer of each species were observed, and the spectra were fitted using a conventional semi-rigid rotor Hamiltonian. Internal dynamics, including large amplitude motions of the methyl group and the water moiety, are discussed in terms of calculated barrier heights. Hydrogen bond energies and dissociation energies are discussed in the context of the quantum theory of atoms in molecules (QTAIM) and symmetry adapted perturbation theory (SAPT). Finally, the percentage of OTA hydrated in the atmosphere is estimated on the basis of dissociation energies and partition functions, using statistical thermodynamics.

4.2. Methods

4.2.1. Experimental

A cavity-based Fourier-transform (FTMW) spectrometer was used to measure the rotational spectra of OTA and OTA-H_2O in the range of 5-14 GHz. The spectrometer has been described in detail previously.[26,27] Briefly, the sample is injected through the nozzle, which is set near the

centre of one of two aluminium mirrors that compose the microwave resonator. The difference in pressure across the nozzle results in a supersonic expansion, in the earlier stages of which the sample molecules are cooled to a (rotational) temperature of about 1 K by collisions with backing gas molecules. A near-resonant $\pi/2$ microwave excitation pulse causes polarization of the sample, after which molecules spontaneously emit radiation at the transition frequency. The emission signal is digitized in the time domain, averaged, and Fourier-transformed into the frequency spectrum. Because the resonator axis and supersonic expansion are oriented coaxially, lines are split into Doppler pairs. The average is used as the rest frequency. Automated scans for targeted transitions were collected in 0.2 MHz increments.

Reagent grade OTA (Aldrich, 99%) was used without further purification. Because the melting point of OTA is 378 K, it was placed in a stainless steel container heated to about 383 K, downstream of a heated coil of copper tubing. Backing gas, Ne (3-5 atm), was passed over the melted sample before reaching a pulsed solenoid nozzle, which was heated to about 523 K in order to prevent deposition in the nozzle. To prepare OTA-H_2O, I passed a mixture of about 0.1% water in Ne over the OTA sample.

4.2.2. Computational

Optimized structures of OTA and OTA-H_2O were used to predict the rotational spectra of these species and to define frequency ranges to search for targeted transitions. Both density functional theory (DFT) and wavefunction-based electronic structure calculations were used in Gaussian09.[28] For DFT calculations, the B3LYP functional was used.[29] For wavefunction-based calculations, second order Møller-Plesset (MP2) perturbation theory was applied.[30] Both methods were implemented with the Pople basis set 6-311++G(2df,2pd).[31] Minimum energy structures were found using geometry optimizations, followed by frequency analyses to verify that no imaginary frequencies occurred. Zero-point energy (ZPE) corrections were also determined from frequency analyses. Transition states along coordinates associated with large amplitude motions were initially located using relaxed scans of the potential energy surface. Transition states were subsequently verified by geometry optimizations ("opt=ts") and frequency analyses, which gave one imaginary frequency. For the complex, the Boys and Bernardi counterpoise correction was used to correct for basis set superposition error (BSSE).[32] QTAIM,[33] as implemented in Multiwfn,[34] was used to analyse the calculated electron density

distributions of OTA and OTA-H_2O and to characterize inter- and intramolecular non-covalent bonding. In order to export the MP2-calculated wavefunctions to input files for Multiwfn, the keywords "density=current" and "output=wfx" were used. Atomic energies were corrected for errors resulting from numerical integration.[35] SAPT,[36] as implemented in PSI4,[37] was used as an alternate method to characterize the non-covalent bonding. As a compromise between accuracy and computing time, I used zeroth-order SAPT (SAPT0) with the jun-cc-pVDZ basis set.[38]

Rotational spectra were predicted from the calculated rotational constants using the PGOPHER program.[39] In turn, the measured transition frequencies were input in PGOPHER to fit rotational and quartic centrifugal distortion constants, using Watson's A-reduction Hamiltonian.[40]

4.3. Results and discussion

4.3.1. Spectrum, structure, and internal dynamics of the *o*-toluic acid monomer

Four conformers of the OTA monomer were located at the MP2/6-311++G(2df,2pd) level of theory, as illustrated in Figure 4.1. In the two most stable conformers, **I** and **II**, the carboxylic acid group is rotated slightly (about 7°) out of the plane of the aromatic ring, and the acidic hydrogen atom is oriented in a *syn*-conformation with respect to the carbonyl oxygen atom. In **I**, the carbonyl oxygen atom, rather than that of the hydroxyl moiety, is adjacent to the methyl group. Rotating about the bond between the aromatic ring and the carboxylic acid group by roughly 180° results in **II**. In the two least stable conformers, **III** and **IV**, the acidic hydrogen atom is oriented in an *anti*-conformation. In **III**, the carbonyl group is rotated approximately 35° out of the plane of the aromatic ring, and in **IV**, it is rotated about 180° from that of **III**. Relative energies (including ZPE corrections), relative free energies, abundances, rotational constants, and dipole moments for the optimized structures are shown in Table 4.1.

I began my spectral search by scanning for transitions of **I** and **II**, because **III** and **IV** are expected to be present at abundances of less than 0.5%, even at the elevated nozzle temperature. The predicted rotational constants of the two most stable conformers are very similar, so targeted transitions were predicted to vary in frequency only slightly. For example, I first targeted the $5_{1,5}$–$4_{1,4}$ transition using an automated scan in the range of 8500-8750 MHz; for **I** and **II**, the predicted frequencies of this transition are about 8666 and 8670 MHz,

respectively. In the experimental scan, however, only one candidate for this particular transition was observed. Among others, the $4_{1,3}$–$3_{1,2}$ and $5_{0,5}$–$4_{0,4}$ transitions were also in this range, and together these three lines were used in a preliminary spectroscopic fitting procedure. In all, 27 *a*-type transitions and 13 *b*-type transitions were observed (see Table A.4 in Appendix), whose frequencies were used to determine the rotational and quartic centrifugal distortion constants shown in Table 4.2. A representative transition is shown in Figure 4.2. The percent mean absolute discrepancies between predicted and experimental rotational constants are only 0.6 and 0.7% for **I** and **II**, respectively, so the rotational constants alone do not strictly allow assignment of the spectrum to either conformer. However, achieving optimal intensity for *b*-type transitions required a longer microwave pulse width than that required for *a*-type transitions, indicating that the *b*-dipole moment component is smaller than the *a*-dipole moment component. This observation is consistent with **I**, which has a predicted abundance of 77.6%, but not **II**. Conformer **I** has also been observed in the crystal structure of the acid.[21] Conformer **II** has a predicted abundance of 21.8% at the elevated nozzle temperature, and it is separated from **I** by a significant barrier, 17.2 kJ mol^{-1} at the B3LYP/6-311++G(d,p) level of theory, which likely

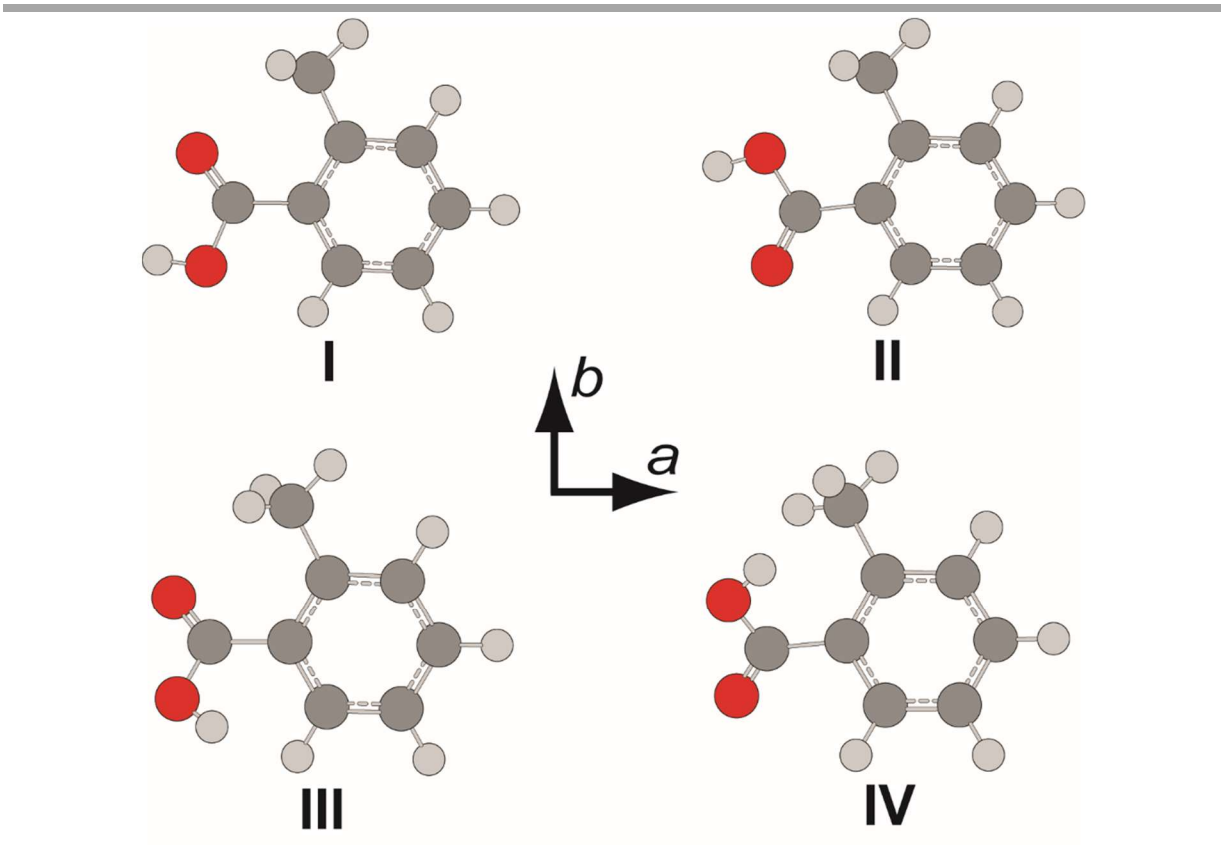

Figure 4.1. Conformers of OTA monomer, optimized at the MP2/6-311++G(2df,2pd) level of theory.

prevents conformational cooling in the molecular expansion. However, I failed to achieve adequate sensitivity to detect **II**, because (i) the gas-phase sample was difficult to generate, and (ii) the OTA spectrum is very dense – even at a rotational temperature of 1 K, many energy levels are populated.

Table 4.1. Calculated relative energies, abundances, rotational constants, and dipole moment components of four conformers of the OTA monomer at the MP2/6-311++G(2df,2pd) level of theory.

	I	II	III	IV
ΔE^a / kJ mol^{-1}	0	5.0	20.2	25.1
ΔG^b / kJ mol^{-1}	0	5.5	22.0	26.1
P^c / %	77.6	21.8	0.5	0.2
A / MHz	2230.28	2241.51	2236.61	2244.39
B / MHz	1218.58	1208.33	1188.66	1175.23
C / MHz	793.10	794.79	815.97	822.29
κ^d	-0.41	-0.43	-0.48	-0.50
$\lvert\mu_a\rvert$ / D	1.62	1.35	4.44	4.18
$\lvert\mu_b\rvert$ / D	1.03	1.99	1.31	2.85
$\lvert\mu_c\rvert$ / D	0.13	0.33	1.52	1.53

[a] Total energy (sum of electronic and ZPE) relative to the minimum energy conformer. [b] Relative free energy. [c] Percent abundance (based on relative free energy) at 523 K, the nozzle temperature. [d] Asymmetry parameter, $\kappa = (2B - A - C)/(A - C)$.

Table 4.2. Experimental rotational constants and quartic centrifugal distortion constants of the OTA monomer and monohydrate.

	I	I-H_2O
A / MHz	2216.3345(4)[a]	2190.358(1)
B / MHz	1210.6114(1)	641.7891(1)
C / MHz	787.99923(5)	498.88178(8)
Δ_J / kHz	0.0320(7)	0.0208(4)
Δ_{JK} / kHz	0.013(4)	0.077(5)
Δ_K / kHz	0.12(1)	0.2(2)
δ_J / kHz	0.0111(4)	0.0046(2)
δ_K / kHz	0.054(5)	0.11(2)
κ^b	-0.41	-0.83
N_t^c	40	36

[a] One standard deviation in the last decimal place before the parentheses. [b] Asymmetry parameter, $\kappa = (2B - A - C)/(A - C)$. [c] Number of transitions included in fit. [d] Root-mean-square deviation of fit.

No methyl internal rotation splittings were observed. At the MP2/6-311++G(2df,2pd) level of theory, the height of the three-fold barrier to methyl rotation, V_3, is 7.87 kJ mol^{-1}. This barrier is relatively high; for example, the experimentally-determined barriers of *o*-chlorotoluene[41] and *o*-fluorotoluene[42] are about 5.58 kJ mol^{-1} and 2.72 kJ mol^{-1}, respectively. In general, the more unsymmetrical the ring geometry on either side of the methyl substituent, the higher the barrier to methyl rotation, because of anisotropic steric repulsion.[43] Thus, as the size of the substituent at the *ortho* position of toluene increases, the barrier height increases, as well. Based on the experimental rotational and centrifugal distortion constants and the calculated structural parameters and V_3, the expected splittings can be predicted using the program XIAM.[44] The values of the structural properties δ (the angle between methyl top axis and the *a* principal inertial axis), ε (the angle between the projection of the methyl top axis onto the *bc* plane and *b* principal inertial axis), and F_0 (the methyl top rotation constant) are about 2.018 rad, 0.019 rad, and 161.8 GHz, respectively. The resulting splitting predicted for the $6_{4,2}$-$5_{4,1}$ transition is 28 kHz. Since no splitting is observed (see Figure 4.2a), the actual V_3 is likely higher than calculated. If I increase V_3 by 10%, to give 8.65 kJ mol^{-1}, the predicted splitting (12 kHz)

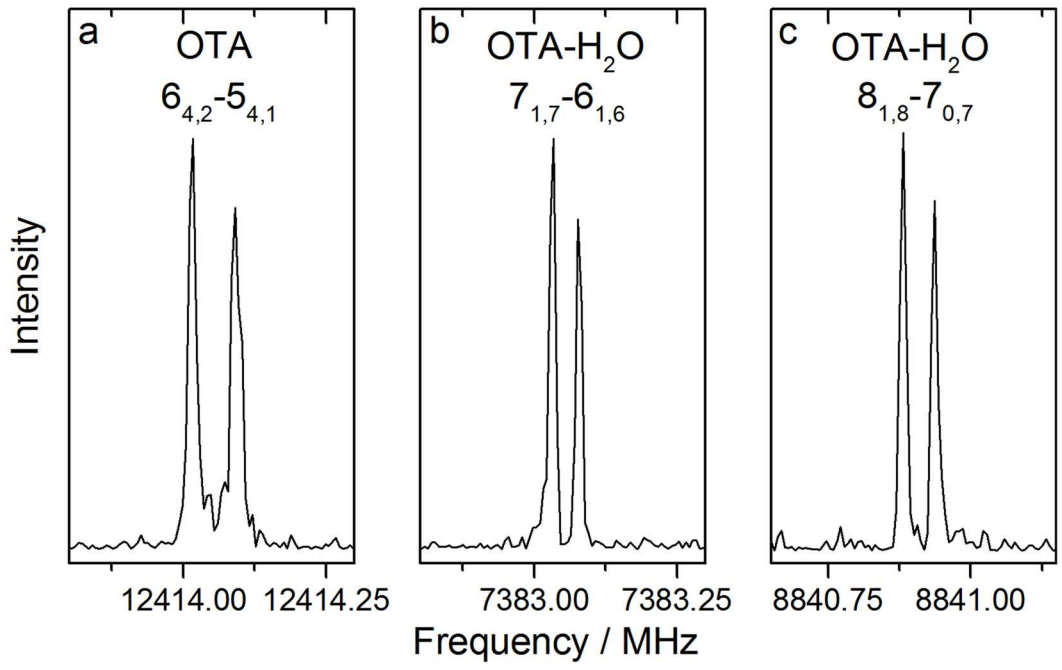

Figure 4.2. Transitions of OTA and OTA-H_2O, measured using 0.5 mW excitation pulses. Panel (a) shows an average of 100 cycles, measured with an excitation pulse length of 0.6 μs; panel (b) shows an average of 500 cycles, measured with an excitation pulse length of 0.8 μs; panel (c) illustrates an average of 3000 cycles, measured with an excitation pulse length of 1.5 μs.

is roughly twice the experimental resolution, so I would be able to measure one point between the two peaks. Consequently, 8.65 kJ mol^{-1} is likely a lower limit of the barrier height.

In the equilibrium structure of **I** calculated at the MP2/6-311++G(2df,2pd) level of theory, the carboxylic acid group is not in the plane of the aromatic ring, so the *c*-dipole moment component is small but non-zero. However, despite many averages, no *c*-type transitions were observed. The lowest energy normal mode vibration (22 cm^{-1}) is the large amplitude "rocking" motion of the carboxylic acid group. A transition state (whose one imaginary frequency normal mode corresponds to rocking of the carboxylic acid group) was found to connect the mirror-image minima. The symmetrical double-well potential along this coordinate is shown in Figure 4.3. The small barrier lies below the ZPE of the minima, so the average geometry is that of the transition state. The transition state has C_s symmetry, resulting in a *c*-dipole moment component of zero, which is consistent with the absence of *c*-type transitions. I note that the B3LYP/6-311++G(2df,2pd) level of theory fails to predict a double-well potential (see Figure 4.3). A similar observation has been made for isomers of dimethylbenzaldehydes.[45]

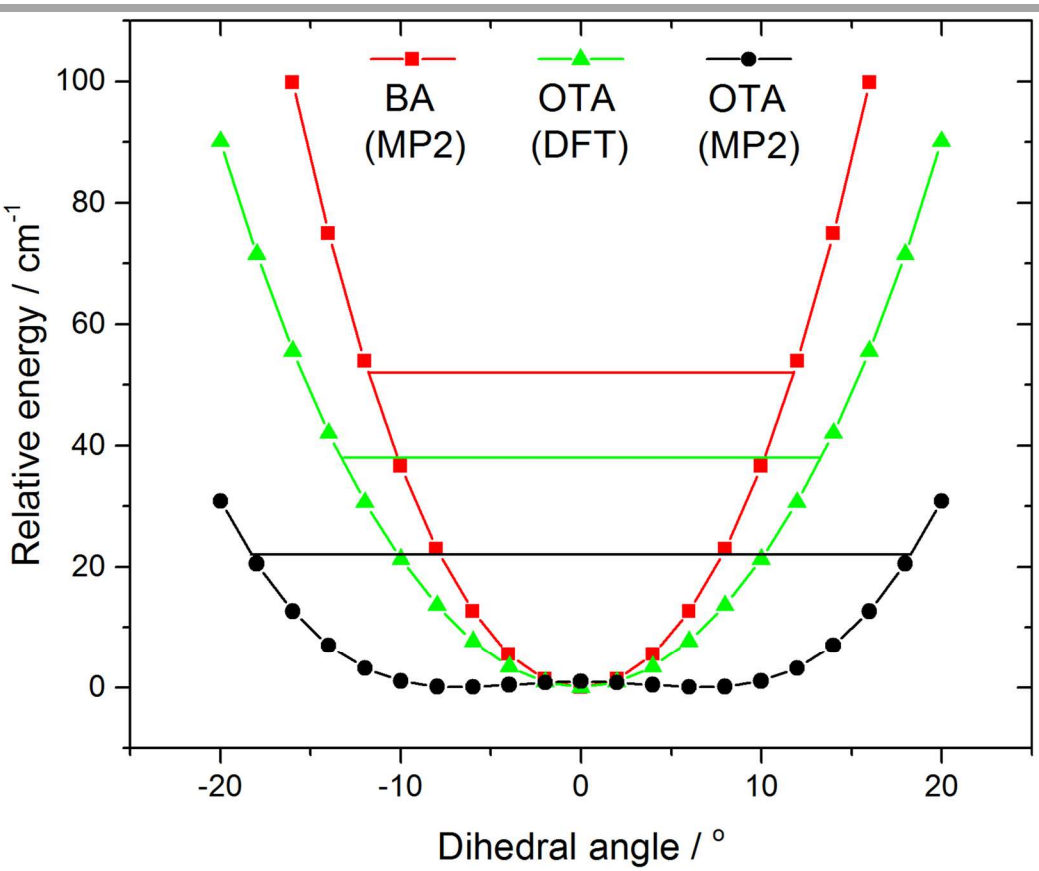

Figure 4.3. Potential energy curves of BA and OTA monomers along the "rocking" coordinate of the carboxylic acid group.

In the average structure of **I**, all the atoms lie in the plane of symmetry, except the two staggered hydrogen atoms of the methyl group. Even molecules that have planar equilibrium geometries may still have non-zero mass distributions outside of the plane, because of low-lying zero-point vibrations. The inertial defect is calculated according to Equation (4.1).[46]

$$\Delta = I_c - I_b - I_a \tag{4.1}$$

Here, I_a, I_b, and I_c are moments of inertia of the OTA monomer about its principal inertial axes. The inertial defect is a measure of this mass distribution outside of the plane.[46] For example, BA is calculated to have a planar equilibrium geometry at both the DFT and MP2 levels of theory, but it has a small negative inertial defect (-0.37 amu Å^2).[23,47] For non-planar molecules with a plane of symmetry, the inertial defect can be corrected for the masses of the out-of-plane atoms, so that it still reflects low-lying out-of-plane motions. For example, in molecules with methyl groups, the inertia of the out-of-plane hydrogen atoms must be added to the inertial defect to give a methyl-top-corrected inertial defect, Δ_{corr}, calculated using Equation (4.2).[48]

$$\Delta_{corr} = \Delta + 2\sum m_H c_H^2 \tag{4.2}$$

Here, m_H and c_H are the mass and c-coordinate, respectively, of a given out-of-plane hydrogen atom. For the present purposes, I take the c-coordinates from the MP2-calculated geometry of the transition state along the rocking coordinate of the carboxylic acid group. The resulting value of Δ_{corr} is -1.09 amu Å^2, significantly greater in magnitude than the inertial defect of BA. This difference is consistent with the greater number of low-lying out-of-plane vibrational modes (<400 cm^{-1}) predicted for OTA than BA, as shown in Table 4.3. Additionally, for the lowest-lying mode, rocking of the carboxylic acid group, the ZPE level intersects the potential energy

Table 4.3. Low-lying out-of-plane vibrations, calculated at the MP2/6-311++G(2df,2pd) level of theory, and inertial defects of BA and OTA.

	BA	OTA
ν_1 / cm^{-1}	52[a]	22[a]
ν_2 / cm^{-1}	159	130
ν_3 / cm^{-1}	–	205
ν_4 / cm^{-1}	–	228
Δ^b / amu Å^2	-0.37	-4.14
$\Delta_{corr}{}^c$ / amu Å^2	–	-1.09

[a] Rocking of the carboxylic acid group. [b] Inertial defect, $\Delta = I_c - I_b - I_a$. [c] Methyl-top-corrected inertial defect described in text.

curve at about ±18° in OTA and at about ±12° in BA, so this large amplitude motion involves greater out-of-plane displacement in OTA than in BA (see Figure 4.3).

4.3.2. Spectrum, structure, and internal dynamics of *o*-toluic acid monohydrate

Four minimum energy conformers were located at the MP2/6-311++G(2df,2pd) level of theory for the OTA monohydrate (see Figure 4.4). The two most stable conformers are complexes of **I** and **II**. In **I**-H_2O, the acid moiety is in the geometry of **I**, and it is bound to the water moiety by two hydrogen bonds, forming a six-membered intermolecular ring. The oxygen atom and the unbound hydrogen atom of the water moiety are out of the plane of the carboxylic acid group, which is itself rotated slightly out of the plane of the aromatic ring, resulting in a predicted *c*-dipole moment component of 1.24 D. The two higher energy conformers of OTA-H_2O are complexes of **III** and **IV**. These conformers are predicted to have abundances of about 0.1% even at the elevated nozzle temperature, so they are not my focus here. Relative energies (including ZPE corrections), relative free energies, abundances, rotational constants, and dipole moments for the optimized structures are shown in Table 4.4.

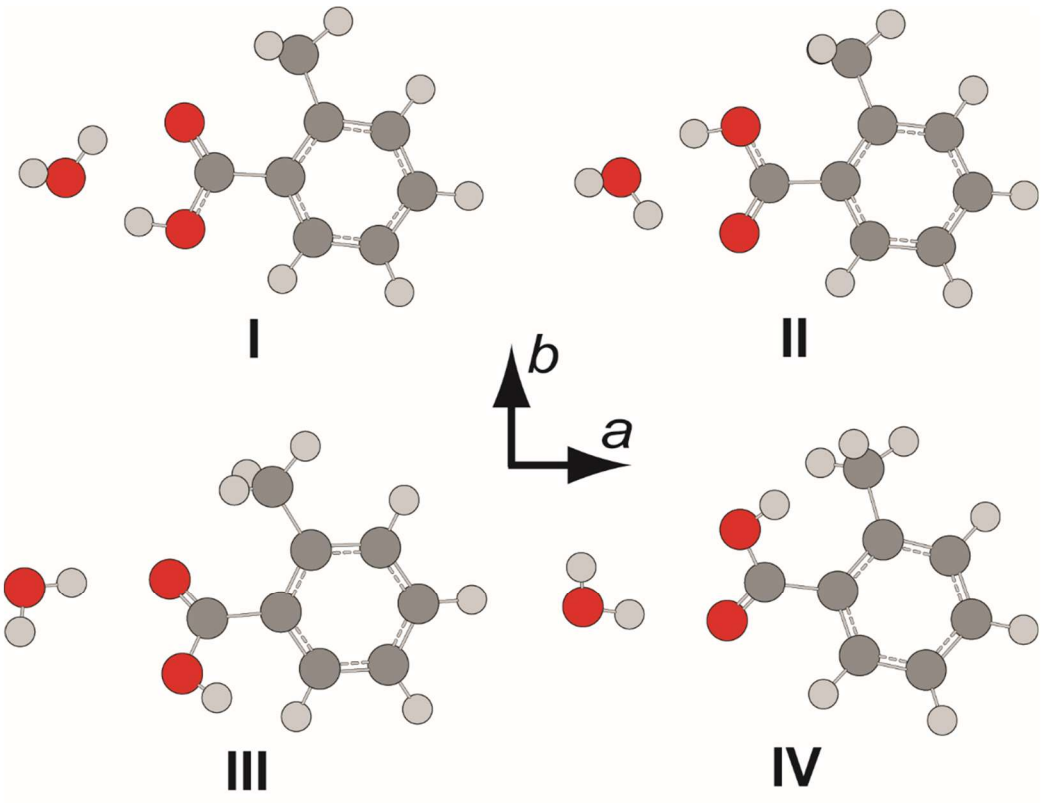

Figure 4.4. Conformers of OTA monomer, optimized at the MP2/6-311++G(2df,2pd) level of theory.

I first targeted the $7_{1,6}$-$6_{1,5}$, $7_{2,5}$-$6_{2,4}$, and $8_{1,8}$-$7_{1,7}$ transitions of **I**-H_2O and **II**-H_2O in an automated scan in the range of 8300-8500 MHz. Using 125 cycles per step, I observed three very weak candidate lines, which were used in my preliminary fit. In all, 32 *a*-type transitions and 4 *b*-type transitions were observed (see Table A.5). Two representative transitions are shown in Figure 4.2. On average, the rotational constants (see Table 4.2) are most consistent with the **I**-H_2O conformer. At first glance, the presence of *b*-type transitions would not be expected for the minimum energy structure, which has only a very small *ab initio b*-dipole moment component (< 0.01 D). However, as was the case for the monomer, rocking of the carboxylic acid group (see Figure 4.5a) is barrier-less in the monohydrate. The average structure is more similar to the geometry of the transition state along this coordinate, in which the acid group is in the plane of the aromatic ring, than the minimum. This transition state has a larger *b*-dipole moment component (0.20 D) than the minimum energy structure. Based on the intensity of lines from this conformer under optimal conditions, I expect that observing the second conformer would require several hundred cycles per step, so I did not continue my conformational search.

I searched ±10 MHz about the frequencies at which *c*-type transitions were predicted to occur by the final fit, but no *c*-type transitions were observed. Their absence is inconsistent with the large calculated *c*-dipole moment component (1.24 D). I located a transition state in which

Table 4.4. Calculated relative energies, abundances, rotational constants, and dipole moment components of four isomers of the OTA monohydrate at the MP2/6-311++G(2df,2pd) level of theory.

	I-H_2O	II-H_2O	III-H_2O	IV-H_2O
ΔE^a / kJ mol^{-1}	0.0	3.6	33.3	39.4
ΔG^b / kJ mol^{-1}	0.0	3.7	28.1	30.0
P^c / %	69.9	29.9	0.1	0.1
A / MHz	2203.87	2214.81	1814.48	2146.43
B / MHz	652.02	650.89	728.76	588.75
C / MHz	506.52	507.95	559.30	477.95
κ^d	-0.83	-0.83	-0.73	-0.87
$\lvert\mu_a\rvert$ / D	0.66	0.56	3.68	6.78
$\lvert\mu_b\rvert$ / D	<0.01	0.18	1.46	2.86
$\lvert\mu_c\rvert$ / D	1.24	1.23	1.44	1.69

[a] Total energy (sum of electronic and ZPE) relative to the minimum energy conformer. [b] Relative free energy. [c] Percent abundance (based on relative free energy) at 523 K, the nozzle temperature. [d] Asymmetry parameter, $\kappa = (2B - A - C)/(A - C)$.

the unbound hydrogen atom of water is in the plane of the carboxylic acid group. Though the electronic energy of the transition state is higher than that of the minimum, the ZPE of the minimum lies 10 cm^{-1} above the barrier. In the minimum energy structure, this large amplitude motion corresponds to a normal mode involving "wagging" of the unbound hydrogen atom of the water moiety (282 cm^{-1}). Since both rocking of the acid group and wagging of the free hydrogen atom are barrier-less, the average structure has a plane of symmetry, and a *c*-dipole moment component of zero, explaining the absence of *c*-type transitions. Similarly, *c*-type transitions were not observed for propanoic acid-H_2O[49] and BA-H_2O.[23]

The absence of tunnelling splittings is striking, in particular in light of the, sometimes complex, observed splittings in other carboxylic acid hydrates,[23,52] and warrants further consideration. Regarding only methyl internal rotation, their absence can be easily rationalized. Based on the calculated V_3 of 7.59 kJ mol^{-1}, as well as the values of δ, ε, and F_0 derived from the calculated structure (1.939 rad, 0.027 rad, and 161.7 GHz, respectively), none of the measured transitions are predicted to have splittings greater than 10 kHz. The value of V_3 is lower than the V_3 lower limit proposed above for OTA monomer (8.65 kJ mol^{-1}). For comparison, the experimentally-determined barrier of the acetic acid monohydrate is also lower than that of the acetic acid monomer.[50] Considering the water moiety,[51] however, the absence of tunnelling splittings is more difficult to rationalize. For example, water tunnelling splittings were observed for trifluoroacetic acid-H_2O[52] and BA-H_2O.[23] Since the current system is similar to these precedents, I discuss tunnelling in more detail below, which may also shed light, for example, on the nature of the, as of yet unexplained, complex splittings observed in BA monohydrate.

For OTA-H_2O, there are nominally two potential water motions, in addition to the wagging of the free hydrogen atom, which is barrier-less, as discussed above. The first motion is exchange of the hydrogen atoms involved in the intermolecular six-membered ring. However, this motion actually converts **I**-H_2O into **II**-H_2O. The second motion is rotation of water about the axis defined by the oxygen atom and its lone pair of electrons hydrogen-bonded to the acidic hydrogen atom. Along this coordinate (see Figure 4.5b), the dihedral angle between the carboxylic acid and aromatic groups is fixed at about 11° – even though the average angle is zero. Since the angle does not change with water rotation, the minima are not degenerate. In the global minimum (see Figure 4.5b, structure i), the free hydrogen atom is slightly further from

the methyl group than in the local minimum (see Figure 4.5b, structure iii). Since the ZPE levels of the two minima differ by 5 cm^{-1}, localized eigenstates exist for each well,[53] and no motion between the two will result in tunnelling splittings. Hence, the water rotation coordinate does not lead to tunnelling, though the barrier (6.16 kJ mol^{-1}) is similar to that of BA-H_2O (7.0 kJ mol^{-1} at the B3LYP/6-311++G(d,p) level of theory).

Despite the energy mismatch between the minima, rotation of water simultaneously accompanied by rocking of the carboxylic acid group could facilitate tunnelling (see Figure 4.5c), because it converts the global minimum to a structural degeneracy. A similar pathway has been proposed to explain splittings observed in the microwave spectrum of the glycolaldehyde-H_2O complex.[54] However, for the present complex, the structure connecting the degeneracies is not a true transition state, because it has two imaginary frequencies, each corresponding to one of the uncoupled motions; the hilltop is a virtual, rather than proper, saddle point of index = 2 – simply a geometrical superposition of two transition states.[55] I conclude that the motions are not concerted.

Since I rationalize the absence of water tunnelling splittings in terms of the asymmetric double-well potentials along the carboxylic acid rocking and water rotation coordinates of

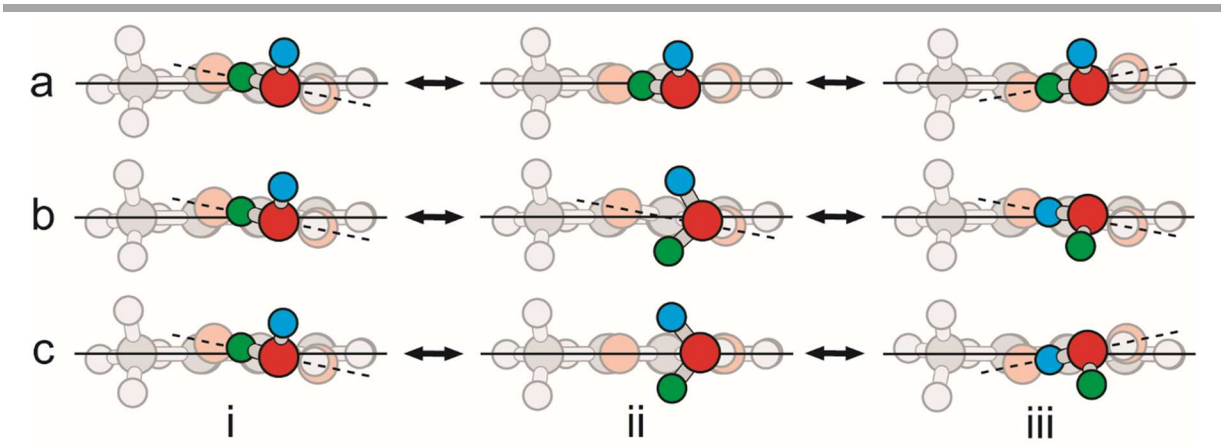

Figure 4.5. Three internal motions of OTA monohydrate: (a) rocking of the carboxylic acid group; (b) rotation of the water moiety; and (c) concerted rocking and rotation. The OTA moiety is faded to distinguish it from the water moiety. The point of view is in the plane of the aromatic ring, represented by the solid line. The plane defined by the four atoms of the carboxylic acid group is represented by the dashed line. The two inequivalent minima, as well as the transition states to the motions shown in (a) and (b), were optimized at the MP2/6-311++G(2df,2pd) level of theory. The structure bridging the equivalent minima illustrated in (c) was generated based on the above transition states, not optimized, and characterized using a single point calculation; it has two imaginary frequencies.

I-H_2O, a rotational spectroscopic study of the *m*-toluic acid-H_2O complex, which I have calculated to have single-well potentials along the same coordinates, like BA-H_2O, would provide further insight in this regard.

4.3.3. Inter- and intramolecular non-covalent bonding

QTAIM[33] is often used to investigate bonding.[56,57] In QTAIM, molecules are partitioned into atomic basins whose boundaries are defined by interatomic surfaces of zero flux of the electron density gradient, $\nabla\rho$. A given property of an individual atom can be determined by integrating over the volume of the atomic basin. Furthermore, the properties of critical points in the electron density distribution, where $\nabla\rho = 0$, provide insight into the interactions in a molecule or complex. For instance, the electron density distribution at bond critical points (BCPs), which are maxima in two dimensions (the third is tangential to the bond path), corresponds directly to the strength of the bond.

Table 4.5. Local bond critical point (BCP) properties and integrated atomic properties related to intermolecular hydrogen bonding in OTA and BA monohydrates.

	I-H_2O		BA-H_2O	
Bonding	OH···O=C	OH···OH	OH···O=C	OH···OH
r(H···O) / Å	1.930	1.772	1.933	1.765
ρ^a / au	0.0262	0.0355	0.0260	0.0362
$\nabla^2\rho$ / au	0.0976	0.1072	0.0970	0.1082
$V(r)$ / au	-0.0228	-0.0347	-0.0226	-0.0356
ΔN(H)^b / au	-0.0722	-0.0434	-0.0641	-0.0535
Δv(H) / au	-6.69	-7.06	-6.44	-7.62
ΔE(H) / au	0.0532	0.0308	0.0463	0.0395
$E_{HB}[V(r)]^c$ / kJ mol^{-1}	30.0	45.6	29.7	46.7
$E_{HB}(\rho_{BCP})^d$ / kJ mol^{-1}	23.1	32.4	22.9	33.2
ΔE^e / kJ mol^{-1}	-47.8		-49.2	
$\Delta E_{BSSE}{}^f$ / kJ mol^{-1}	-40.6		-41.9	
$\Delta E_{SAPT0}{}^g$ / kJ mol^{-1}	-47.8		-48.0	
$D_0{}^h$ / kJ mol^{-1}	30.3		31.7	

[a] Properties at BCPs: electron density, ρ; Laplacian of electron density, $\nabla^2\rho$; and electronic potential energy density, $V(r)$. [b] Changes in integrated atomic properties of hydrogen atom that occur upon formation of hydrogen bonds: electronic population, N(H); atomic volume, v(H); and atomic energy, E(H). [c] Hydrogen bond energy, based on electronic potential energy density, $V(r)$, at the BCP. [d] Hydrogen bond energy, based on electron density, ρ, at the BCP. [e] Interaction energy. [f] Counterpoise-corrected interaction energy. [g] Interaction energy based on SAPT0. [h] Dissociation energy, which is corrected for BSSE and ZPE.

As shown in Table 4.5, the electron density distribution and its Laplacian (curvature) at the (intermolecular) bond critical points of **I**-H_2O (see Figure 4.6) and BA-H_2O are similar. The values for both properties fall within the typical ranges for hydrogen bonds: 0.002-0.034 a.u. for electron density, and 0.024-0.139 a.u. for the Laplacian.[58] The OH···O=C BCP of **I**-H_2O has more electron density that that of BA-H2O, and the r(H···O) distance is slightly shorter; in contrast, the OH···OH BCP of **I**-H_2O has less electron density than that of BA-H_2O, and the r(H···O) distance is longer. Integrated atomic properties of the involved hydrogen atoms (see Table 4.5) are also consistent with the criteria for hydrogen bonding; for example, the hydrogen atoms experience a decrease in electron population and atomic volume upon complexation.

The hydrogen bond energy, E_{HB}, can be estimated from QTAIM properties.[59-61] I will consider two methods. In the first, E_{HB} is estimated based on the electronic potential energy density at the BCP, $V(r)$, according to Equation (4.3).[60]

$$E_{HB}[V(r)] = - 0.5a_0^3 V(r) \tag{4.3}$$

Here, a_0^3 is the Bohr radius. In the second method, E_{HB} is estimated based on the electron density at the BCP, ρ_{BCP}, according to Equation (4.4).[61]

$$E_{HB}(\rho_{BCP}) = - 3.09 + 239\rho_{BCP} \tag{4.4}$$

As shown in Table 4.5, $E_{HB}[V(r)]$ is greater for the OH···OH bond (45.6 kJ mol^{-1}) than the OH···O=C bond (30.0 kJ mol^{-1}). The same ranking occurs for $E_{HB}(\rho_{BCP})$, though the absolute energies are much smaller. These energies, as well as the r(H···O) distances (see Table 4.5), are characteristic of moderately strong hydrogen bonds.[62] The sums of hydrogen bond energies

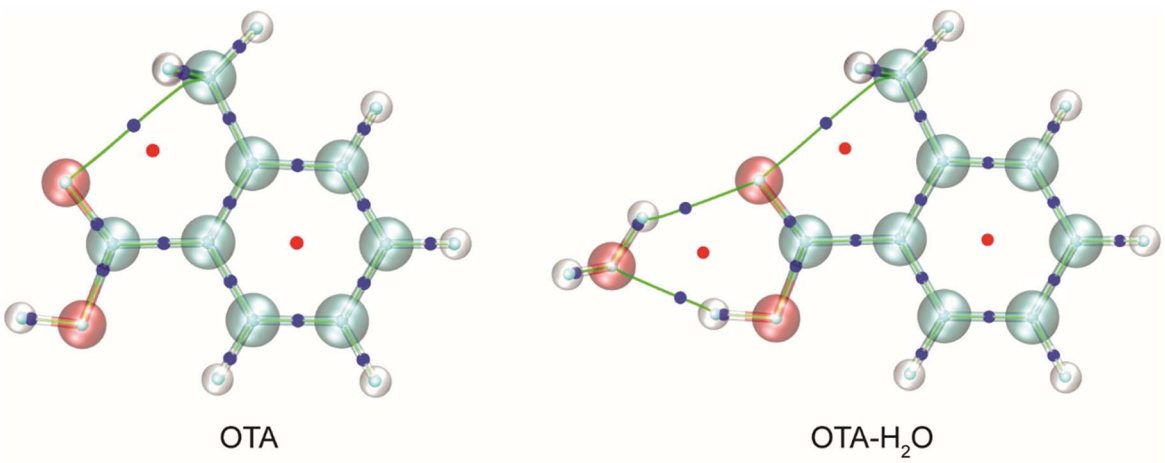

Figure 4.6. Molecular graphs of OTA monomer and monohydrate, calculated at the MP2/6-311++G(2df,2pd) level of theory. Bond critical points are shown in blue, and ring critical points are shown in red.

based on $V(r)$ and ρ_{BCP} are 75.6 and 55.5 kJ mol^{-1}, respectively. For **I**-H_2O, the raw interaction energy is -47.8 kJ mol^{-1}. Though some discrepancy between the sum of hydrogen bond energies and interaction energy is expected, since atoms not directly involved in hydrogen bonding may still be stabilized or destabilized by complexation, the relatively good agreement between ΔE and the sum of the hydrogen bond energies based on ρ_{BCP} suggests that this method is more accurate than the method based on V(r). The ZPE- and BSSE-corrected dissociation energy of **I**-H_2O (30.3 kJ mol^{-1}) is very similar to that of BA-H_2O (31.7 kJ mol^{-1}),[23] consistent with the similar hydrogen bond energies. For each acid, ΔE_{SAPT0} (which is BSSE-free[63]) is in better agreement with ΔE than ΔE_{BSSE}, so the BSSE may be over-predicted at this level of theory. Still, both QTAIM and SAPT predict slightly stronger intermolecular interactions for BA-H_2O than **I**-H_2O.

In passing, I note that BCPs are also present between the sp^3 carbon atom of the methyl group and the carbonyl oxygen atom of both the OTA monomer and monohydrate (see Figure 4.6). Mani and Arunan coined the term "carbon bonding" to describe interactions between highly electronegative atoms and carbon atoms covalently bonded to electron withdrawing groups;[64] the resulting non-covalent bonding is analogous to hydrogen bonding, and it meets the conventional criteria developed by Koch and Popelier.[58] As shown in Table 4.6, the local BCP properties are typical of hydrogen bonds; for example, though the electron density of the C(sp^3)···O=C BCP of monomer **I** (0.014 a.u.) is lower than that of the OH···O=C BCPs discussed above (for example, 0.026 a.u. for **I**-H_2O), it is still well within the typical range (0.002-0.034 a.u.).[58] To estimate the effect of this bonding on integrated atomic properties, I take the methyl carbon atom of **I** to represent the final (bonding) scenario and that of *p*-toluic acid to represent the initial (non-bonding) scenario, so the presence of the aromatic ring and its carboxylic acid substituent is taken into account. The resulting differences in electron population, atomic volume, and atomic energy (see Table 4.6) are further evidence of carbon bonding, since they are consistent with the Koch and Popelier criteria.[58] For example, the methyl carbon atom of OTA is slightly higher in energy than that of *p*-toluic acid; it is slightly destabilized by bonding with the nearby carbonyl oxygen atom in OTA. Consequently, I tentatively attribute the BCP to carbon bonding. Previously, intramolecular carbon bonding has also been identified in conformers of D-ribose.[65]

However, this potential instance of carbon bonding has several distinctive characteristics. Previously studied species contain many electron withdrawing groups covalently bonded to the sp^3 carbon (hydroxyl, amino, and cyano groups among them),[64,66] but not the phenyl group. In organic synthesis, the methyl group is a common electron-donating group;[67] its loss of electron density to the phenyl group in OTA makes it slightly more electropositive, facilitating carbon bonding with the electronegative carbonyl oxygen atom. Furthermore, previously studied C(sp^3)···O bonds have been linear, but the C-C(sp^3)···O angle in **I** is about 80°. Finally, the C(sp^3)···O=C BCP is present in the minimum energy structure along the coordinate defined by rotation of the methyl group, but not in the transition state – which contains a more conventional CH···C=O BCP, instead.

4.3.4. Atmospheric abundance of *o*-toluic acid monohydrate

The equilibrium constant of complexation of isomer i, $K_{p,i}$, can be calculated directly from the partition functions that underlie the free energy change, according to Equation (4.5).[68]

$$K_{p,i} = (2q^{\ominus}_{\mathrm{A\cdots B}} e^{\frac{D_0}{kT}} N_A)/(q^{\ominus}_{\mathrm{A}} q^{\ominus}_{\mathrm{B}}) \qquad (4.5)$$

Here, $q^{\ominus}$ is the total partition function of the species in the subscript, k is the Boltzmann constant, T is temperature in Kelvin, and N_A is the Avogadro constant. The coefficient of two is

Table 4.6. Local bond critical point properties and integrated atomic properties related to intramolecular carbon bonding in OTA.

	OTA
Bonding	C(sp^3)···O=C
r(C···O) / Å	2.773
ρ^a / au	0.0136
$\nabla^2\rho$ / au	0.0652
$V(r)$ / au	-0.0113
ΔN(C)^b / au	-0.0136
Δv(C) / au	-2.5
ΔE(C) / au	0.0010
$E_{\mathrm{HB}}[V(r)]^c$ / kJ mol^{-1}	14.8

[a] Properties at BCPs: electron density, ρ; Laplacian of electron density, $\nabla^2\rho$; and electronic potential energy density, $V(r)$. [b] Changes in integrated atomic properties of the carbon atom that occur upon formation of the carbon bond: electronic population, N(C); atomic volume, v(C); and atomic energy, E(C). [c] Carbon bond energy, based on electronic potential energy density, $V(r)$, at the BCP.

included, because (at the average position of the carboxylic acid group) the wagging motion of the free hydrogen atom of the water moiety results in mirror images.[49,69] Since the mole fractions of conformers **III** and **IV** are less than 1% at 298 K, I consider only conformers **I** and **II**.

In addition to the dissociation energies, the partition functions must be calculated. The total partition function of each species is the product of translational, rotational, vibrational, and electronic partition functions.[70] The translational partition function of a species can be calculated simply from its mass and the temperature. The rotational partition functions depend on temperature, rotational constants, and symmetry number. The rotational constants of water are known.[71] The rotational constants of **I** and **I**-H_2O are those reported above, and the rotational constants of **II** and **II**-H_2O are those of the calculated minimum energy structures. The symmetry numbers for H_2O, OTA, and OTA-H_2O are 2, 1, and 1.[69] The vibrational partition function, which is also dependent on temperature, is the product of the individual partition functions of each normal mode, which are most significant for modes below 400 cm^{-1}. The normal mode frequencies for all three species were taken from the MP2-calculated frequency analyses. Since no excited electronic states are accessible at ambient temperature, the electronic partition function is one.

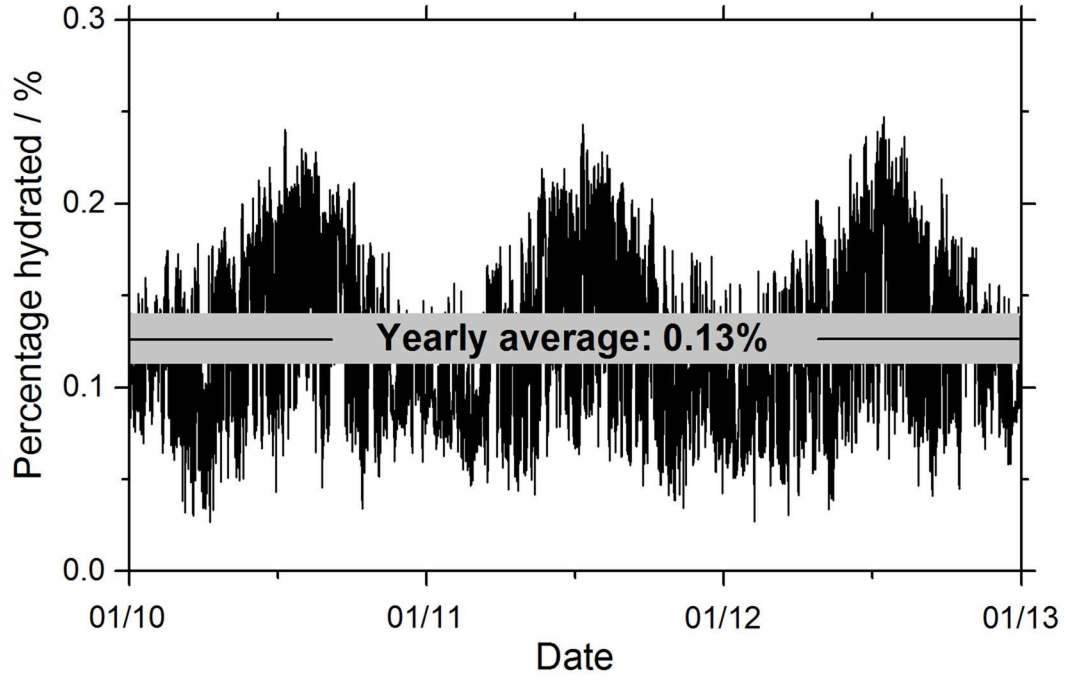

Figure 4.7. Seasonal fluctuation of the percentage of OTA hydrated in the atmosphere, under conditions reported in Calgary, Alberta.

The percentage of conformer i hydrated in the atmosphere, χ_i, depends on the concentration of water vapour, and it can be calculated according to Equation (4.6).[52]

$$\chi_i = K_{p,i} \frac{p_{H_2O}}{p^{\ominus}} 100\% \tag{4.6}$$

Here, p_{H_2O} is the partial pressure of water, and $p^{\ominus}$ is the ambient pressure. To investigate how the percentage of OTA hydrated changes with temperature and water concentration, I calculated χ_i for a monitoring site in Calgary, Alberta, using ambient temperature and relative humidity data from 2010 to 2013.[72] To determine the partial pressure of water, I used the vapour pressure parameterization of Hyland and Wexler.[73] The total percentage of OTA hydrated, χ, is calculated according to Equation (4.7).

$$\chi = x_I \chi_I + x_{II} \chi_{II} \tag{4.7}$$

Here, x_i is the mole fraction of conformer i at ambient temperature. The seasonal variation in χ is small (see Figure 4.7). The percentage of OTA hydrated is highest during the summer, when the partial pressure of water is highest, despite the fact that the equilibrium constants are lowest during the same period. The yearly averages of χ_I and χ_{II} are 0.12% and 0.16%, and the yearly average of χ is 0.13%.

At the same level of theory, the yearly average of percentage of BA hydrated is about 1%.[23] The decrease is due more to differences in the partition functions than the small difference between dissociation energies. Because the methyl group adds mass to OTA and OTA-H_2O, they have slightly greater translational partition functions than BA and its monohydrate. The rotational partition functions also increase, because the rotational constants increase and – in the case of the monomer – the symmetry number decreases from 2 for BA to 1 for OTA. In all, the rotational partition function increases by about a factor of 3 for OTA. The increase in the number of atoms in OTA and OTA-H_2O, compared to BA and BA-H_2O, results in a greater number of vibrational modes, and greater vibrational partition functions. In each of the cases above, the relative increase is greater for the OTA monomer than the monohydrate, so $K_{p,i}$ decreases. Though these calculations provide only a preliminary estimate, it is likely that less OTA is hydrated in the atmosphere than BA.

Nonetheless, the interactions between OTA and water characterized by the above structural and energetic results further our understanding of gas-phase clusters containing organic acids and water in the atmosphere, including precursors to nucleation. Furthermore,

since OTA has both hydrophilic and hydrophobic regions, the interactions probed here are likely involved in the behaviour of OTA at the air-water interface of aqueous aerosols, where it could contribute to the enhancement of cloud formation,[74] similar to BA. For example, the structural isomer *p*-toluic acid has been shown to decrease the surface tension of water.

4.4. Conclusions

I have measured the rotational spectra of the monomer and monohydrate of OTA, an important product of photo-oxidation in the atmosphere. The lowest-energy conformers of both species in the gas phase have been determined; the lowest-energy conformer of the monomer is the same as that previously observed in the crystal structure.[21] No methyl internal rotation splittings were observed in the spectra of either species, because the barriers are too high. The displacement of the carboxylic acid group during its rocking motion is greater in OTA than in BA, causing the inertial defect of OTA to be greater in magnitude than that of BA. For the monohydrate, minima on either side of the barrier to the same rocking motion are not degenerate, precluding water tunnelling splittings. The hydrogen bond energies (based on a QTAIM analysis) and, consequently, dissociation energies of OTA and BA monohydrates are similar, but less OTA is predicted to be hydrated in the atmosphere, because the presence of the methyl group increases the partition functions of the monomer to a greater extent than those of the monohydrate.

References

1 Liu, S.; Day, D. A.; Shields, J. E.; Russell, L. M. Ozone-driven daytime formation of secondary organic aerosol containing carboxylic acid groups and alkane groups. *Atmos. Chem. Phys.* **2011**, *11*, 8321-8341.

2 Ehn, M.; *et al.* A large source of low-volatility secondary organic aerosol. *Nature*, 2014, **506**, 476-479. See bibliography for complete list of authors.

3 Schnitzler, E. G.; Dutt, A.; Charbonneau, A. M.; Olfert, J. S.; Jäger, W. Soot aggregate restructuring due to coatings of secondary organic aerosol derived from aromatic precursors. *Environ. Sci. Technol.* **2014**, *48*, 14309-14316.

4 Riccobono, F.; *et al.* Oxidation products of biogenic emissions contribute to nucleation of atmospheric particles. *Science*, 2014, **344**, 717-721. See bibliography for complete list of authors.

5 Zhang, R.; Suh, I.; Zhao, J.; Zhang, D.; Fortner, E. C.; Tie, X.; Molina, L. T.; Molina, M. J. Atmospheric new particle formation enhanced by organic acids. *Science* **2004**, *304*, 1487-1490.

6 Zhang, R.; Khalizov, A.; Wang, L.; Hu, M.; Xu, W. Nucleation and growth of nanoparticles in the atmosphere. *Chem. Rev.* **2012**, *112*, 1957-2011.

7 McGraw, R.; Zhang, R. Multivariate analysis of homogeneous nucleation rate measurements. Nucleation in the *p*-toluic acid/sulfuric acid/water system. *J. Chem. Phys.* **2008**, *128*, 064508 (9 pp.).

8 Henze, D. K.; Seinfeld, J. H.; Ng, N. L.; Fu, T.-M.; Jacob, D. J.; Heald, C. L. Global modelling of secondary organic aerosol formation from aromatic hydrocarbons: High- vs. low-yield pathways. *Atmos. Chem. Phys.* **2008**, *8*, 2405-2420.

9 Bell, R. J.; Davey, N. G.; Martinsen, M.; Collin-Hansen, C.; Krogh, E. T.; Gill, C. G. A field-portable membrane introduction mass spectrometer for real-time quantification and spatial mapping of atmospheric and aqueous contaminants. *J. Am. Soc. Mass. Spectrom.* **2015**, *26*, 212-223.

10 Simpson, I. J.; *et al.* Characterization of trace gases measured over Alberta oil sands mining operations: 76 speciated C_2-C_{10} volatile organic compounds (VOCs), CO_2, CH_4, CO, NO, NO_2, NO_y, O_3 and SO_2. *Atmos. Chem. Phys.* **2010**, *10*, 11931-11954. See bibliography for complete list of authors.

11 Song, C.; Na, K.; Warren, B.; Malloy, Q.; Cocker, D. R, III. Secondary organic aerosol formation from the photooxidation of *p*- and *o*-xylene. *Environ. Sci. Technol.* **2007**, *41*, 7403-7408.

12 Zhou, Y.; Zhang, H.; Parikh, H. M.; Chen, E. H.; Rattanavaraha, W.; Rosen, E. P.; Wang, W.; Kamens, R. M. Secondary organic aerosol formation from xylenes and mixtures of toluene and xylenes in an atmospheric urban hydrocarbon mixture: Water and particle seed effects (II). *Atmos. Environ.* **2011**, *45*, 3882-3890.

13 Vivanco, M. G.; Santiago, M.; Martínez-Tarifa, A.; Borrás, E.; Ródenas, M.; Garciá-Diego, C.; Sánchez, M. SOA formation in a photoreactor from a mixture of organic gases and HONO for different experimental conditions. *Atmos. Environ.* **2011**, *45*, 708-715.

14 Huang, M.; Zhang, W.; Wang, Z.; Hao, L.; Zhao, W.; Liu, X.; Long, B.; Fang, L. Theoretical investigation on the detailed mechanism of the OH-initiated atmospheric photooxidation of *o*-xylene. *Int. J. Quantum Chem.* **2008**, *108*, 954-966.

15 Yu, J.; Jeffries, H. E.; Sexton, K. G. Atmospheric photooxidation of alkylbenzenes – I. Carbonyl product analyses. *Atmos. Environ.* **1997**, *31*, 2261-2280.

16 Clifford, G. M.; Hadj-Aïssa, A.; Healy, R. M.; Mellouki, A.; Muñoz, A.; Wirtz, K.; Martín-Reviejo, M.; Borrás, E.; Wenger, J. C. The atmospheric photolysis of *o*-tolualdehyde. *Environ. Sci. Technol.* **2011**, *45*, 9649-9657.

17 Fu, P. Q.; *et al.* Diurnal variations of organic molecular tracers and stable carbon isotopic composition in atmospheric aerosols over Mt. Tai in the North China Plain: An influence of biomass burning. *Atmos. Chem. Phys.* **2012**, *12*, 8359-8375. See bibliography for complete list of authors.

18 Kawamura, K.; Ng, L.-L.; Kaplan, I. R. Determination of organic acids (C_1-C_{10}) in the atmosphere, motor exhausts, and engine oils. *Environ. Sci. Technol*. **1985**, *19*, 1082-1086.

19 Ito, M.; Tsukioka, H.; Imanishi, S. Effect of temperature on ultraviolet absorption spectra of benzoic acids and its relation to hydrogen bonding. *J. Am. Chem. Soc.* **1960**, *82*, 1559-1564.

20 Babu, P. D. S.; Periandy, S.; Ramalingam, S. Vibrational spectroscopic (FTIR and FTRaman) investigation using *ab initio* (HF) and DFT (LSDA and B3LYP) analysis on the structure on toluic acid. *Spectrochim. Acta, Part A* **2011**, *78*, 1321-1328.

21 Polito, M.; D'Oria, E.; Maina, L.; Karamertzanis, P. G.; Grepioni, F.; Braga, D.; Price, S. L. The crystal structures of chloro and methyl *ortho*-benzoic acids and their co-crystal: Rationalizing similarities and differences. *Cryst. Eng. Comm.* **2008**, *10*, 1848-1854.

22 Gaie-Levrel, F.; Gutlé, C.; Jochims, H.-W.; Rühl, E.; Schwell, M. Photoionization of atmospheric aerosol constituents and precursors in the 7-15 eV energy region: Experimental and theoretical study. *J. Phys. Chem. A* **2008**, *112*, 5138-5151.

23 Schnitzler, E. G.; Jäger, W. The benzoic acid-water complex: A potential atmospheric nucleation precursor studied using microwave spectroscopy and *ab initio* calculations. *Phys. Chem. Chem. Phys.* **2014**, *16*, 2305-2314.

24 Priem, D.; Ha, T.-K.; Bauder, A. Rotational spectra and structures of three hydrogen-bonded complexes between formic acid and water. *J. Chem. Phys.* **2000**, *113*, 169-175.

25 Thomas, J.; Serrato, A., III; Lin, W.; Jäger, W.; Xu, Y. Perfluorobutyric acid and its monohydrate: A chirped pulse and cavity based Fourier transform microwave spectroscopic study. *Chem. Eur. J.* **2014**, *20*, 6148-6153.

26 Xu, Y.; Van Wijngaarden, J.; Jäger, W. Microwave spectroscopy of ternary and quaternary van der Waals clusters. *Int. Rev. Phys. Chem.* **2005**, *24*, 301-338.

27 Xu, Y.; Jäger, W. Evidence for heavy atom large amplitude motions in RG-cyclopropane van der Waals complexes (RG=Ne, Ar, Kr) from rotation-tunneling spectroscopy. *J. Chem. Phys.* **1997**, *106*, 7968-7980.

28 Frisch, M. J.; *et al. Gaussian 09*, Rev. D.01; Gaussian, Inc.: Wallingford, CT, **2013**. See bibliography for complete list of authors.

29 Becke, A. D. Density-functional thermochemistry. III. The role of exact exchange. *J. Chem. Phys.* **1993**, *98*, 5648-5652.

30 Møller, C.; Plesset, M. S. Note on an approximation treatment for many-electron systems. *Phys. Rev.* **1934**, *46*, 618-622.

31 Ditchfield, R.; Hehrf, W. J.; Pople, J. A. Self-consistent molecular-orbital methods. IX. An extended Gaussian-type basis for molecular-orbital studies of organic molecules. *J. Chem. Phys.* **1971**, *54*, 724-728.

32 Boys, S. F.; Bernardi, F. The calculation of small molecular interactions by the difference of separate total energies. Some procedures with reduced errors. *Mol. Phys.* **1970**, *19*, 553-566.

33 Bader, R. F. W. A quantum theory of molecular structure and its applications. *Chem. Rev.* **1991**, *91*, 893-928.

34 Lu, T.; Chen, F. Multiwfn: A multifunctional wavefunction analyzer. *J. Comput. Chem.* **2012**, *33*, 580-592.

35 Matta, C. F.; Boyd, R. J. An Introduction to the Quantum Theory of Atoms in Molecules. In *The Quantum Theory of Atoms in Molecules: From Solid State to DNA and Drug Design*; Matta, C. F., Boyd, R. J., Eds.; Wiley: New York, 2007; pp. 1-34.

36 Jeziorski, B.; Moszynski, R.; Szalewicz, K. Perturbation theory approach to intermolecular potential energy surfaces of van der Waals complexes. *Chem. Rev.* **1994**, *94*, 1887-1930.

37 Turney, J. M.; *et al.* PSI4: An open-source *ab initio* electronic structure program. *WIREs Comput. Mol. Sci.*, 2012, **2**, 556-565. See bibliography for complete list of authors.

38 Parker, T. M.; Burns, L. A.; Parrish, R. M.; Ryno, A. G.; Sherill, C. D. Levels of symmetry adapted perturbation theory (SAPT). I. Efficiency and performance for interaction energies. *J. Chem. Phys.* **2014**, *140*, 094106 (16 pp.).

39 Western, C. M. *PGOPHER, A Program for Simulating Rotational Structure*, University of Bristol: Bristol, UK. http://pgopher.chm.bris.ac.uk.

40 Watson, J. K. G. Determination of centrifugal distortion coefficients of asymmetric-top molecules. *J. Chem. Phys.* **1967**, *46*, 1935-1949.

41 Gerhard, D.; Hellweg, A.; Merke, I.; Stahl, W.; Baudelet, M.; Petitprez, D.; Wlodarczak, G. Internal rotation and chlorine nuclear quadrupole coupling of *o*-chlorotoluene studied by microwave spectroscopy and *ab initio* calculations. *J. Mol. Spectrosc.* **2003**, *220*, 234-241.

42 Jacobsen, S.; Anderson, U.; Mäder, H. Microwave spectra of *o*-fluorotoluene and its ^{13}C isotopic species: Methyl internal rotation and molecular structure. *Struct. Chem.* **2003**, *14*, 217-225.

43 Lu, K.-T.; Weinhold, F.; Weisshaar, J. C. Understanding barriers to internal rotation in substituted toluenes and their cations. *J. Chem. Phys.* **1995**, *102*, 6787-6805.

44 Hartwig, H.; Dreizler, H. The microwave spectrum of trans-2,3-dimethyloxirane in torsional excited states. *Z. Naturforsch.* **1996**, *51A*, 923-932.

45 Tudorie, M.; Kleiner, I.; Jahn, M.; Grabow, J.-U.; Goubet, M.; Pirali, O. Coupled large amplitude motions: A case study of the dimethylbenzaldehyde isomers. *J. Phys. Chem. A* **2013**, *117*, 13636-13647.

46 Oka, T. On negative inertial defect. *J. Mol. Struct.* **1995**, *352/353*, 225-233.

47 Godfrey, P. D.; McNaughton, D. Structural studies of aromatic carboxylic acids via computational chemistry and microwave spectroscopy. *J. Chem. Phys.* **2013**, *138*, 024303 (8 pp.).

48 Schnitzler, E. G.; Zenchyzen, B. L. M.; Jäger, W. High-resolution Fourier-transform microwave spectroscopy of methyl- and dimethylnapthalenes. *Astrophys. J.* **2015**, *805*, 141 (7 pp.).

49 Ouyang, B.; Howard, B. J. High-resolution microwave spectroscopic and *ab initio* studies of propanoic acid and its hydrates. *J. Phys. Chem. A* **2008**, *112*, 8208-8214.

50 Ouyang, B.; Howard, B. J. The monohydrate and dihydrate of acetic acid: A high-resolution microwave spectroscopic study. *Phys. Chem. Chem. Phys.* **2009**, *11*, 366-373.

51 Evangelisti, L.; Caminati, W. Internal dynamics in complexes of water with organic molecules. Details of the internal motions in *tert*-butylalcohol-water. *Phys. Chem. Chem. Phys.* **2010**, *12*, 14433-14441.

52 Ouyang, B.; Starkey, T. G.; Howard, B. J. High-resolution microwave studies of ring-structured complexes between trifluoroacetic acid and water. *J. Phys. Chem. A* **2007**, *111*, 6165-6175.

53 Albert, S.; Lerch, P.; Prentner, R.; Quack, M. Tunneling and tunneling switching dynamics in phenol and its isotopomers from high-resolution FTIR spectroscopy with synchrotron radiation. *Angew. Chem. Int. Ed.* **2013**, *52*, 346-367.

54 Aviles-Moreno, J.-R.; Demaison, J.; Huet, T. R. Conformational flexibility in hydrated sugars: The glycolaldehyde-water complex. *J. Am. Chem. Soc.* **2006**, *128*, 10467-10473.

55 Heidrich, D.; Quapp, W. Saddle points of index 2 on potential energy surfaces and their role in theoretical reactivity investigations. *Theor. Chim. Acta* **1986**, *70*, 89-98.

56 Petković, M.; Etinski, M. Intramolecular OHO bonding in dibenzoylmethane: Symmetry and spectral manifestations. *RSC Adv.* **2014**, *4*, 38517-38526.

57 Brovarets, O. O.; Zhurakivsky, R. O.; Hovorun, D. M. Is the DPT tautomerization of the long A·G Watson-Crick DNA base mispair a source of the adenine and guanine mutagenic tautomers? A QM and QTAIM response to the biologically important question. *J. Comput. Chem.* **2014**, *35*, 451-466.

58 Koch, U.; Popelier, P. L. A. Characterization of C-H-O hydrogen bonds on the basis of the charge density. *J. Phys. Chem.* **1995**, *99*, 9747-9754.

59 Schnitzler, E. G.; Poopari, M. R.; Xu, Y.; Jäger, W. Rotational spectroscopy of methyl benzoylformate and methyl mandelate: Structure and internal dynamics of a model reactant and product of enantioselective reduction. *Phys. Chem. Chem. Phys.* **2015**, *17*, 21942-21949.

60 Espinosa, E.; Molins, E.; Lecomte, C. Hydrogen bond strengths revealed by topological analyses of experimentally observed electron densities. *Chem. Phys. Lett.* **1998**, *285*, 170-173.

61 Nikolaienko, T. Y.; Bulavin, L. A.; Hovorun, D. M. Bridging QTAIM with vibrational spectroscopy: The energy of intramolecular hydrogen bonds in DNA-related biomolecules. *Phys. Chem. Chem. Phys.* **2012**, *14*, 7441-7447.

62 Jeffrey, G. A. Nature and properties. *An Introduction to Hydrogen Bonding*; Oxford: New York, 1997; pp. 11-32.

63 Van Duijneveldt, F. B.; van Duijneveldt-van de Rijdt, J. G. C. M.; van Lenthe, J. H. State of the art in counterpoise theory. *Chem. Rev.* **1994**, *94*, 1873-1885.

64 Mani, D.; Arunan, E. The X-C···Y (X=O/F, Y=O/S/F/Cl/Br/N/P) 'carbon bond' and hydrophobic interactions. *Phys. Chem. Chem. Phys.* **2013**, *15*, 14377-14383.

65 Azofra, L. M.; Quesada-Moreno, M. M.; Alkorta, I.; Avilés-Moreno, J. R.; López-González, J. J.; Elguero, J. Carbohydrates in the gas phase: Conformational preference of D-ribose and 2-deoxy-D-ribose. *New J. Chem.* **2014**, *38*, 529-538.

66 Varadwaj, P. R.; Varadwaj, A.; Jin, B.-Y. Significant evidence of C···O and C···C long-range contacts in several heterodimeric complexes of CO with CH_3-X, should one refer to them as carbon and dicarbon bonds! *Phys. Chem. Chem. Phys.* **2014**, *16*, 17238-17252.

67 Anson, C. W.; Thamattoor, D. M. Influence of substituents on the through-space shielding of aromatic rings. *J. Org. Chem.* **2012**, *77*, 1693-1700.

68 McClelland, B. J. Equilibrium constants. *Statistical Thermodynamics*; Studies in Chemical Physics Series; Chapman and Hall: London, 1973; pp. 168-182.

69 Fernández-Ramos, A.; Ellingson, B. A.; Meana-Pañeda, R.; Marques, J. M. C.; Truhlar, D. G. Symmetry numbers and chemical reaction rates. *Theor. Chem. Acc.* **2007**, *118*, 813-826.

70 Atkins, P. Statistical thermodynamics: The machinery. *Physical Chemistry*, 6th ed.; Freeman: New York, 1998; pp. 593-617.

71 Messer, J. K.; De Lucia, F. C.; Helminger, P. The pure rotational spectrum of water vapor – a millimeter, submillimeter, and far infrared analysis. *Int. J. Infrared Milli.* **1983**, *4*, 505-539.

72 Clean Air Strategic Alliance Data Warehouse. http://www.casadata.org (accessed April 2013).

73 Hyland, R. W.; Wexler, A. Formulations for the thermodynamic properties of the saturated phases of H_2O from 173.15 K to 473.15 K. *ASHRAE Trans.* **1983**, *89*, 500-519.

74 McNeill, V. F.; Sareen, N.; Schwier, A. N. Surface-active organics in atmospheric aerosols. *Top. Curr. Chem.* **2014**, *339*, 201-260.

75 Paluch, M.; Dynarowicz, P. Electrical properties of adsorbed films of some aromatic compounds at the water/air interface. *J. Colloid Interface Sci.* **1987**, *115*, 307-311.

5 The contrasting effects of water on the barriers to decarboxylation of two oxalic acid monohydrates: A combined rotational spectroscopic and *ab initio* study

5.1. Introduction

Dicarboxylic acids (DCAs) are among the most abundant classes of compounds in atmospheric particulate matter, including secondary organic aerosol (SOA); they have been detected around the world, from megacities[1] to the Tibetan Plateau,[2] from the tropics[3] to the Arctic.[4] Oxalic acid (OA), the most abundant DCA in the atmosphere,[1-4] has the greatest O:C ratio of the DCAs, so it is very hygroscopic. Particles of anhydrous OA take up water at low relative humidity (RH=20%), and they do not release this water even when returned to dry conditions.[5] The phase behavior of OA-water aggregates, following water uptake, has been modeled using molecular dynamics simulations.[6] OA is also a product of aqueous-phase hydroxyl radical-initiated oxidation of volatile organic compounds, such as glyoxal[7] and glycolaldehyde[8], and larger DCAs. OA accumulates in the aqueous phase, because it is less reactive than its larger homologues.[9] In the gas phase, clusters containing OA hydrogen-bonded to water and/or sulfuric acid, among other species, have been studied extensively using quantum chemistry calculations.[10-13] The large predicted interaction energies suggest that OA enhances nucleation in the atmosphere.[11]

A possible sink for atmospheric DCAs is decarboxylation induced by excitation of vibrational overtones.[14] Gas-phase decarboxylation of OA by thermal decomposition or photolysis has been studied in the past.[15-17] Most recently, overtone-induced decarboxylation of OA in a solid Ar matrix was observed upon irradiation at 532 nm.[18] Overtone-induced decarboxylation of other organic acids, including pyruvic and glyoxylic acids,[19,20] has been observed in the gas phase. Based on *ab initio* calculations, Staikova et al. proposed that water may act as a catalyst in the (OH stretching) overtone-induced decarboxylation of malonic acid,

since the barrier is lower for the monohydrate than the monomer.[21] On the other hand, they acknowledged that this isomer of malonic acid monohydrate is not predicted to be the most abundant in the atmosphere.[21] Furthermore, the lowering of the barrier is not unequivocal evidence of water catalysis, because intramolecular vibration redistribution (IVR) may allow energy initially absorbed during the overtone excitation to cause dissociation of the complex instead of decarboxylation.[22,23] Though the lowering is required for catalysis to be plausible, dynamical modeling, which accounts for the competition between decarboxylation and dissociation, is required to state with certainly that catalysis occurs.[22,23] In general, whether decarboxylation is important for DCA monohydrates in the atmosphere depends on the relative stabilities and absorption cross sections of the isomers and the roles of water in each scenario. OA, as the smallest and the most abundant DCA, is an excellent candidate for spectroscopic and *ab initio* investigation.

Rotational spectroscopy is suited to structural studies of gas-phase species, because conformers or isomers differing only very slightly can be easily distinguished by their rotational constants. Many atmospherically-relevant clusters with water and oxygenated organic compounds – including benzoic acid,[24] *o*-toluic acid,[25] and methyl salicylate[26] – have been characterized using rotational spectroscopy in the past. Here, I report the detection of the two most stable isomers of OA-H_2O clusters, based on rotational spectra measured using a Fourier-transform microwave (FTMW) spectrometer, and a theoretical investigation of decarboxylation.

5.2. Methods

5.2.1. Experimental

Spectra were measured using a Balle-Flygare-type FTMW spectrometer,[27] which has been described thoroughly in the past.[28,29] Reagent grade OA dihydrate (Caledon, >99.5%) was heated in a test tube at about 453 K to drive off the associated water. The resulting anhydrous OA was placed in a stainless steel sample container and heated to about 373 K, while a pulsed solenoid nozzle downstream was heated to about 453 K, in order to prevent deposition. This setup has been used to generate gaseous samples of other low-volatility species in the past.[30,31] A small amount of water (0.5%) was added to about 1-2 bar Ne backing gas.

5.2.2. Computational

All geometry optimizations and frequency analyses were obtained using the MP2 method[32] with the 6-311++G(d,p) basis set,[33] as implemented in Gaussian 09.[34] No imaginary frequencies were observed for any minima, and one imaginary frequency was observed for each transition state. The zero-point energy (ZPE) of each stationary point was determined from its frequency analyses. Forward and reverse intrinsic reaction coordinate calculations were used to verify that the located transition states connect the intended minima.[35] The Boys-Bernardi method of counterpoise correction was used; basis set superposition error (BSSE) was calculated for the monohydrates, as well as all the complexes along the decarboxylation reaction coordinate.[36] Bond critical points in the monohydrates, requisite for hydrogen bonding according to QTAIM,[37,38] were located using Multiwfn.[39] PGOPHER[40] was used to predict transition frequencies from calculated rotational constants and, in turn, to fit observed frequencies, using Watson's A-reduction Hamiltonian.[41]

5.3. Results and discussion

5.3.1. Spectrum, structure, and internal dynamics of two oxalic acid monohydrates

The conformational landscape of the OA monomer has been studied extensively in the past, both experimentally[42-44] and theoretically.[12] The conformers are illustrated in Figure 5.1. I follow the naming convention used by Weber et al., in which each conformer is distinguished by a three letter abbreviation.[12] The lowercase letters denote the orientation of the individual carboxylic acid groups: if the C-C-O-H dihedral angle is 0° (or 180°), the group is labelled "c" for *cis* (or "t" for *trans*). The uppercase letter denotes the orientation of the carboxylic acid groups, one to the other: if the O=C-C=O dihedral angle is 0° (or 180°), the label used is "C" (or "T"). Predicted relative energies, abundances, rotational constants, and dipole moments are listed in Table 5.1. Consistent with previous calculations[12,17] and measurements[44] cTc is the lowest energy conformer. This conformer has inversion symmetry, so it has a dipole moment of zero and cannot be observed using microwave spectroscopy. Only the next lowest energy conformer, cTt, has been previously observed by microwave spectroscopy,[43] and it exhibited intense transitions in my experiments. The next conformer, tTt, also has inversion symmetry. All three lower-energy conformers were observed by Maçôas et al. in argon matrix using infrared spectroscopy.[44] I attempted to observe the next most stable conformer, tCt. Though it

is predicted to have a significant dipole moment, it was not observed, because the energy difference is very large (about 10 kJ mol^{-1}).

The structural landscape of OA-H_2O is complicated, since each OA monomer has multiple sites to which water can bind. The five most stable isomers are illustrated in Figure 5.2, and the geometries are similar to those optimized earlier at a lower level of theory.[12] Predicted relative energies, abundances, rotational constants, and dipole moment components are listed in

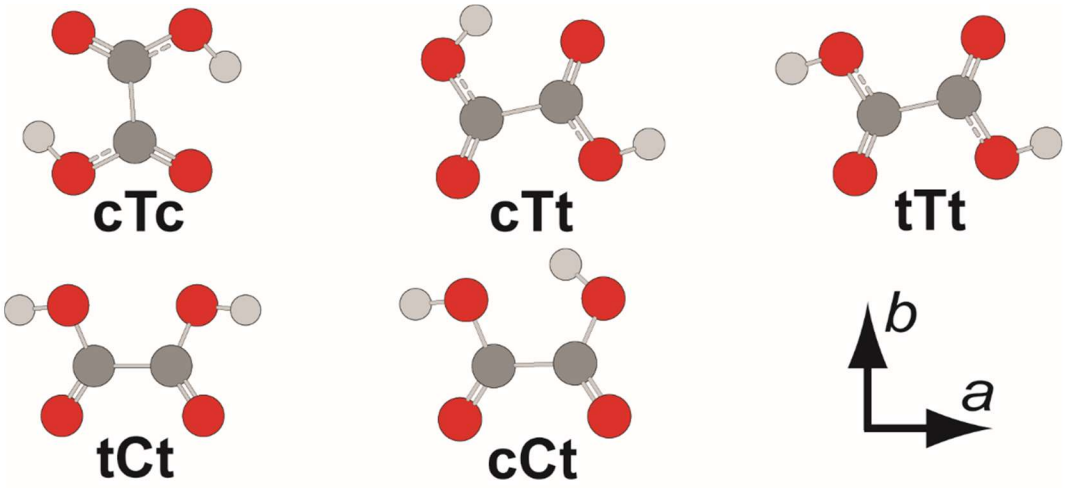

Figure 5.1. Geometries of the five conformers of oxalic acid monomer, optimized at the MP2/6-311++G(d,p) level of theory. The lowercase letters denote the orientation of the individual carboxylic acid groups: if the C-C-O-H dihedral angle is 0° (or 180°), the group is labelled "c" for *cis* (or "t" for *trans*). The uppercase letter denotes the orientation of the carboxylic acid groups, one to the other: if the O=C-C=O dihedral angle is 0° (or 180°), the label used is "C" (or "T").

Table 5.1. Calculated relative energies, abundances, rotational constants, and dipole moments of five conformers of OA monomer at the MP2/6 311++G(d,p) level of theory.

	cTc	cTt	tTt	tCt	cCt
ΔE_e[a] / kJ mol^{-1}	0	7.9	10.1	10.9	18.6
ΔE_0[b] / kJ mol^{-1}	0	7.2	8.6	9.9	16.5
A / MHz	5771.8	5902.7	6005.2	5973.9	5872.0
B / MHz	3813.2	3682.0	3596.8	3480.2	3636.1
C / MHz	2296.2	2267.5	2249.5	2315.8	2253.1
$\lvert\mu_a\rvert$ / D	0.0	3.2	0.0	0.0	3.3
$\lvert\mu_b\rvert$ / D	0.0	1.5	0.0	3.1	4.1
$\lvert\mu_c\rvert$ / D	0.0	0.0	0.0	0.0	0.2

[a] Electronic energy relative to the minimum energy conformer. [b] Relative electronic energy, following ZPE correction.

Table 5.2. The hydrogen bonds pictured were verified by locating bond critical points in the electron density, as shown in Figure 5.3, based on the quantum theory of atoms in molecules.[37,38] In the complex, water can bind to both carboxylic acid groups simultaneously, as in **I**, or it can bind to only one, as in **II**. I denote these general topologies as "bridging" and "terminal", respectively.

I began my spectral search by scanning for **I**, and I assigned 23 *a*-type and 14 *b*-type rotational transitions, as listed in Tables A.6 and A.7. Ten transitions, all *b*-type, exhibited resolved splittings with an intensity ratio of about 3:1, characteristic of a large amplitude water tunneling motion.[45] A representative *b*-type transition is shown in Figure 5.4. Two sets of spectral constants were fitted, as shown in Table 5.3. The more intense transitions are assigned to the 0^- state, based on nuclear spin statistics. The standard deviation of the 0^+ state is greater than that of the 0^- state, because those *b*-type transitions for which splittings were not resolved have centre frequencies closer to the more intense 0^- line than the 0^+ line. I then scanned for **II**, and assigned 20 *a*-type and 6 *b*-type transitions (Tables A.8 and A.9). All *b*-type transitions exhibited resolved splittings. When all spectroscopic parameters were allowed to float during fitting, the resulting Δ_K value for the *ortho* component was 0.2±0.3 kHz. Since the standard deviation was greater than the value itself, I fixed this parameter at the value predicted by a simple harmonic *ab initio* calculation, 0.096 kHz. The results of the two fits are shown in Table 5.2. For both **I** and **II**, I searched for *c*-type transitions using the final fits, but none were observed.

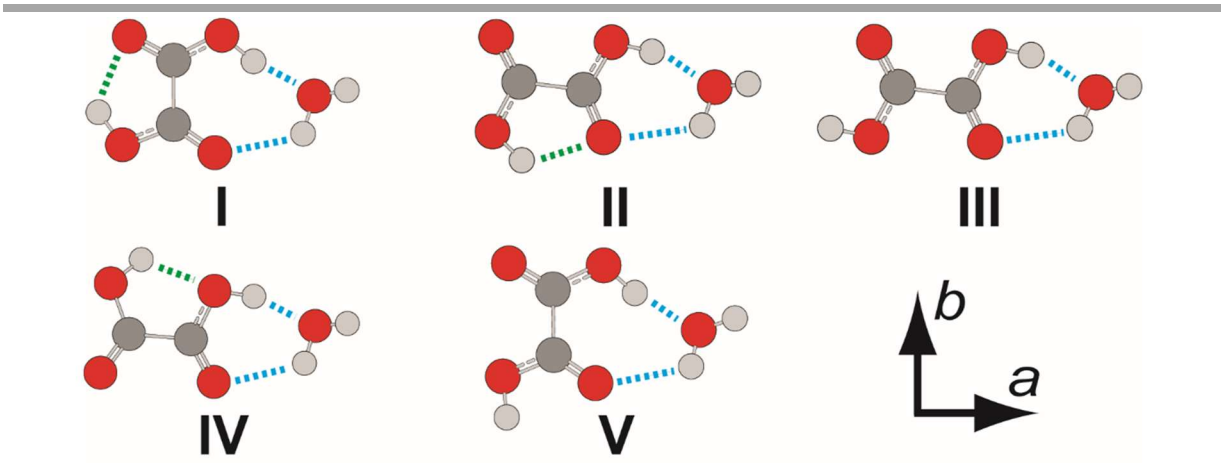

Figure 5.2. Geometries of the five most stable isomers of OA-H_2O, optimized at the MP2/6-311++G(d,p) level of theory. Intra- and intermolecular hydrogen bonds are denoted with green and blue dotted lines, respectively.

I note that, in general, the intensities of transitions of **I** were similar to those of the only observed monomer (cTt), while those of **II** were several times lower. Since **II** is predicted to have larger *a*- and *b*-dipole moment components than **I**, I conclude that **I** is much more abundant than **II** in the supersonic expansion. I assume that the relative intensities of **I** and **II** are an indication of the relative abundances of cTc and cTt, respectively, at the source (nozzle) temperature of 463 K. In this sense, water acts as a tag to observe the otherwise non-polar cTc and provides an experimental estimate of its relative stability. Based on a rotational temperature previously determined in a similar seeded expansion of neon (3.6 K)[46] and on the intensities of representative *a*-type transitions, cTt is 8 kJ mol^{-1} higher in energy than cTc, in good agreement with my calculated ZPE-corrected electronic energy, 7.2 kJ mol^{-1}.

Table 5.2. Relative energies, rotational constants, and dipole moment components of the five lowest energy isomers of OA-H_2O calculated at the MP2/6-311++G(d,p) level of theory.

	I	II	III	IV	V
ΔE_e[a] / kJ mol^{-1}	0	4.4	8.2	12	15.3
ΔE_0 / kJ mol^{-1}	0	4.3	8.1	11.2	14.2
ΔE_0^{BSSE} / kJ mol^{-1}	0	3.0	6.6	9.9	13.6
A / MHz	3718.0	5827.5	5919.2	5762.9	3535.9
B / MHz	1887.6	1378.4	1354.1	1384.5	1881.3
C / MHz	1254.6	1116.2	1127.2	1120.4	1247.8
$\lvert\mu_a\rvert$ / D	2.4	5.1	1.5	5.5	3.3
$\lvert\mu_b\rvert$ / D	1.1	2.5	1.1	2.5	4.2
$\lvert\mu_c\rvert$ / D	1.1	1.1	0.8	0.9	0.7

[a] ΔE_e, ΔE_0, and ΔE_0^{BSSE} are raw, ZPE-corrected, ZPE- and BSSE-corrected electronic energies, respectively, relative to the most stable isomer.

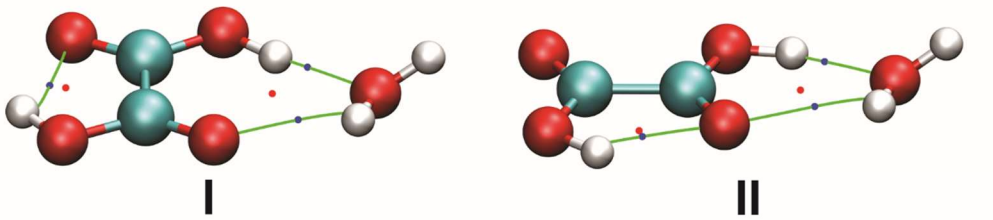

Figure 5.3. Molecular graphs of the two most stable isomers of oxalic acid monohydrate, calculated at the MP2/6-311++G(d,p) level of theory. Bond critical points are shown in blue, and ring critical points are shown in red.

I attribute the splittings in *b*-type transitions of **I** and **II** to water tunneling. At the outset,

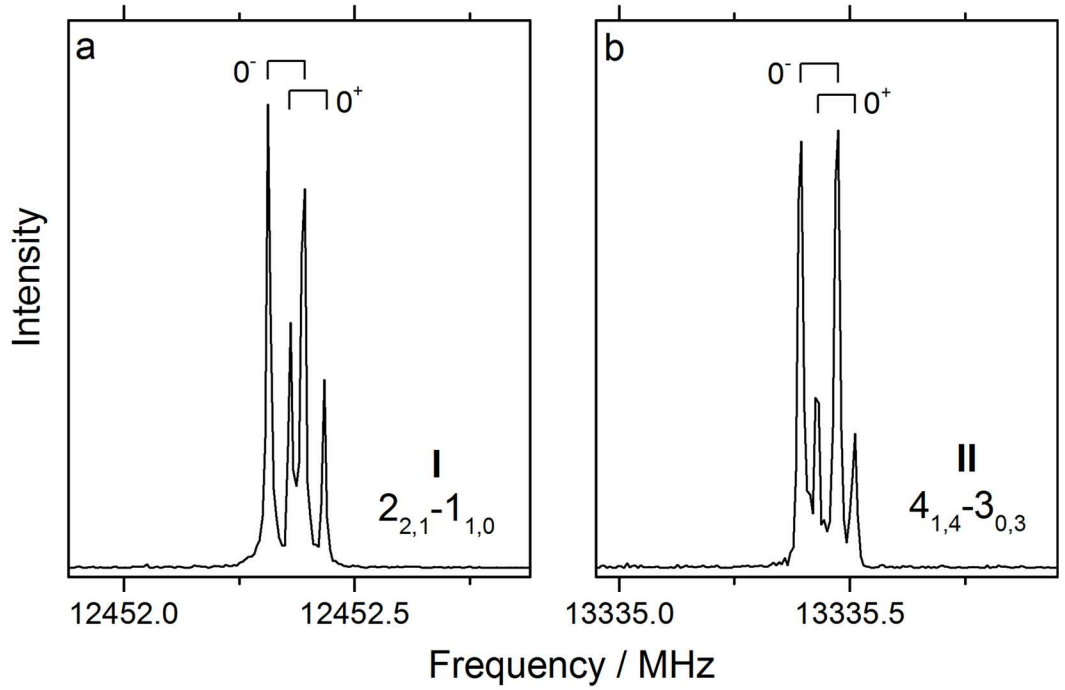

Figure 5.4. Representative transitions of oxalic acid monohydrate, measured using 0.5 mW excitation pulses. Panel (a) illustrates the average of 100 cycles, measured with an excitation pulse length of 0.6 μs, giving a signal–noise ratio of about 1000; panel (b) illustrates the average of 500 cycles, measured with an excitation pulse length of 0.7 μs, giving a signal–noise ratio of nearly 500.

Table 5.3. Experimental rotational constants and quartic centrifugal distortion constants of water tunneling states of two observed isomers of OA-H_2O.

	I (0^- state)	I (0^+ state)	II (0^- state)	II (0^+ state)
A / MHz	3731.8064(3)	3731.823(2)	5879.308(2)	5879.361(4)
B / MHz	1890.4531(2)	1890.457(1)	1376.9774(5)	1376.978(1)
C / MHz	1256.9487(1)	1256.9476(9)	1117.0365(4)	1117.0353(9)
Δ_J / kHz	0.520(3)	0.52(2)	0.300(3)	0.303(8)
Δ_{JK} / kHz	-0.32(1)	-0.17(9)	0.81(2)	0.75(4)
Δ_K / kHz	1.06(3)	1.1(2)	0.096[c]	0.096[c]
δ_J / kHz	0.179(1)	0.191(9)	0.058(2)	0.069(4)
δ_K / kHz	0.80(3)	0.6(2)	1.4(2)	1.5(4)
Δ / amu Å^2	-0.69	-0.69	-0.55	-0.55
N[a]	37	37	27	27
σ[b] / kHz	0.9	6.0	1.2	2.8

[a] Number of transitions in the fit. [b] Root-mean-square deviation of fit. For the spectroscopic parameters, one standard deviation is given in parentheses in the units of the least significant digit. [c] Fixed at the value predicted by a simple harmonic *ab initio* calculation.

two motions were considered, as shown in Figure 5.5 and Figure 5.6: (i) wagging of the free hydrogen atom of the water moiety, through the plane of the OA unit; and (ii) rotation of the entire water moiety. Wagging of the free hydrogen atom does not interchange the hydrogen atoms of water, so it cannot lead to the observed different spin statistical weights. However, it does explain the absence of *c*-type transitions. Though the transition state to wagging in **I** lies above the minimum in electronic energy (by about 2.7 kJ mol^{-1}), it lies below the ZPE level (by about 3.4 kJ mol^{-1}). For **II**, the transition state lies about 3.5 kJ mol^{-1} below the ZPE level. There is thus no barrier to wagging, and it is simply a vibrational mode. Since the average structures are planar, the average *c*-dipole moment components are zero. Hence, no *c*-type transitions were observed. Similar observations have been made for other complexes, such as benzoic acid-H_2O[24] and methyl salicylate-H_2O.[26] The second motion, rotation of the entire water moiety about

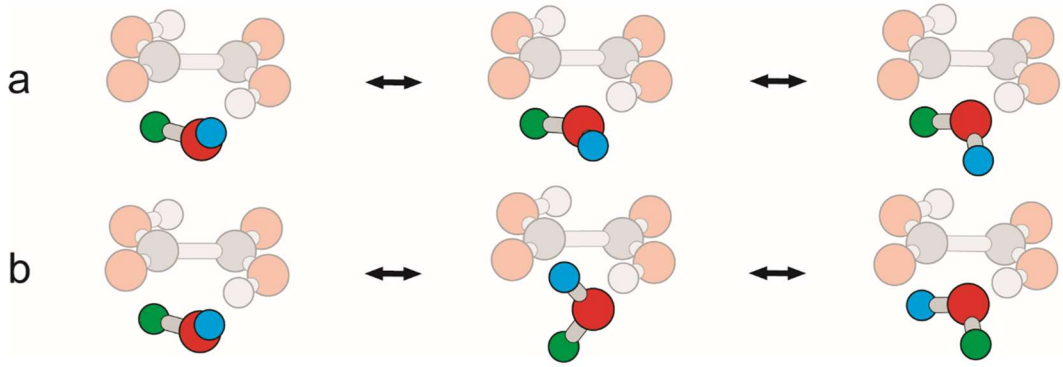

Figure 5.6. Internal motions of oxalic acid monohydrate **I**, calculated at the MP2/6-311++G(d,p) level of theory. Panel (a) illustrates wagging of the free hydrogen atom; panel (b) illustrates rotation of the water unit about an axis through the centre-of-mass of water and the oxygen lone pair involved in the H-bond.

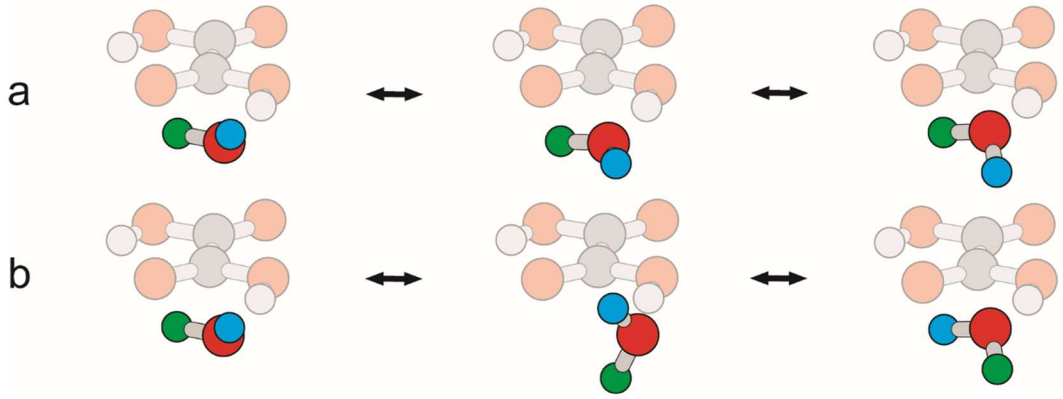

Figure 5.5. Internal motions of oxalic acid monohydrate **II**, calculated at the MP2/6-311++G(d,p) level of theory. Panel (a) illustrates wagging of the free hydrogen atom; panel (b) illustrates rotation of the water unit about an axis through the centre-of-mass of water and the oxygen lone pair involved in the H-bond.

an axis through its centre-of-mass and the oxygen lone pair involved in the H-bond, does interchange the two hydrogen atoms, so it is likely the cause of the water tunneling splittings. The corresponding barriers for **I** and **II** are 5.0 and 3.0 kJ mol^{-1}, respectively. As shown in Table 5.3, the inertial defects of **I** and **II** are -0.69 and -0.55 amu Å^2, respectively, values that are consistent with effectively planar structures with large-amplitude out-of-plane motions, like the proposed internal rotation of water.

5.3.2. Contrasting effects of water on barriers to decarboxylation

To probe possible atmospheric implications of the observed bridging and terminal topologies, I calculated the effects of water on the barriers along the decarboxylation pathway of OA theoretically. I first revisited the pathway previously proposed for the OA monomer,[17] calculating equilibrium geometries at a higher level of theory. The resulting structures and relative energies are shown in Figure 5.7 and Figure 5.8, respectively. The first step to decarboxylation is cleavage of the C-C bond, leading first to TS1 and then to dihydroxycarbene

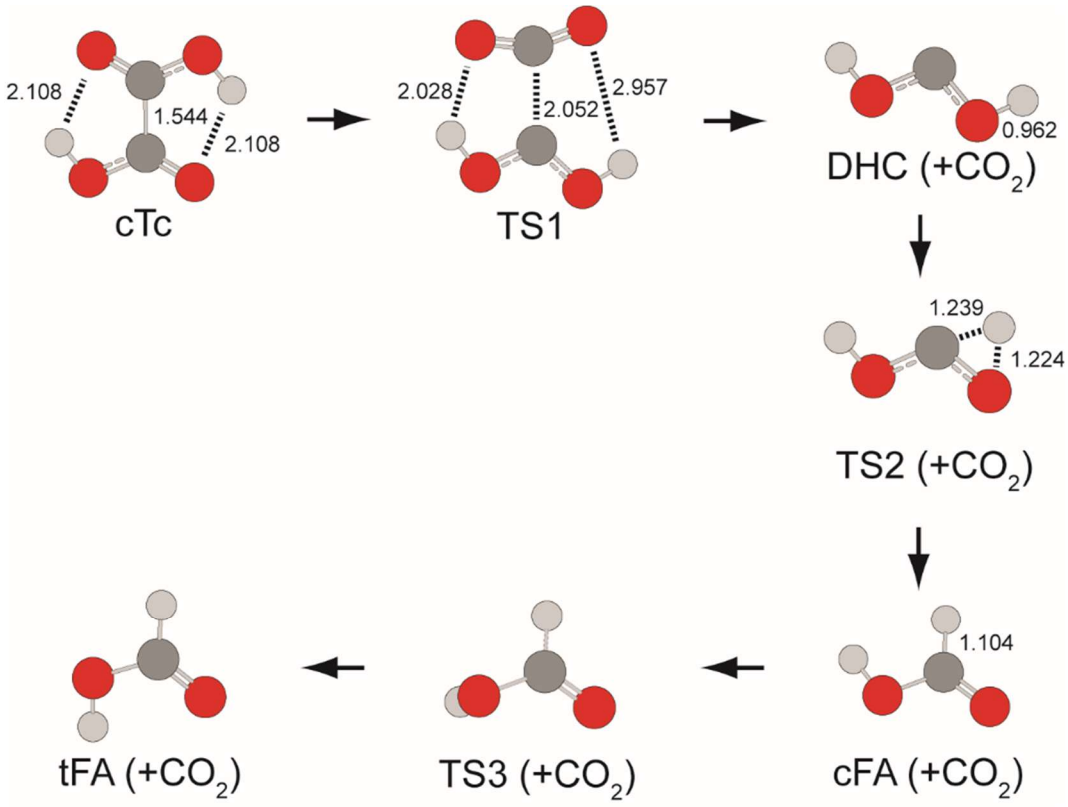

Figure 5.7. Decarboxylation pathway for the most stable conformer of oxalic acid monomer, calculated at the MP2/6-311++G(d,p) level of theory. Denoted bond and inter-nuclear distances are given in Å.

(DHC), as shown in Figure 5.8. In passing, I note that in the first spectroscopic identification of DHC, thermal decarboxylation of OA was used as the source.[47] Experimentally, two product channels for decarboxylation of OA were observed at 388 K: (i) CO_2 + formic acid (FA) and (ii) CO_2 + CO + H_2O.[42] The yield of the first channel was nearly three times that of the second, so I focus on this channel. From DHC, hydrogen excursion leads to TS2 and *cis*-FA (cFA). Finally, internal rotation about the C-O bond leads to TS3 and *trans*-FA (tFA).

Water has a significant effect on both barriers separating OA from FA; however, because the effect on the barrier between DHC and FA has been noted in the past,[17] I focus my attention on the first barrier, between OA and DHC. The structures and relative energies of species along the decarboxylation pathway involving water are shown in Figure 5.9 and Figure 5.8. The decarboxylation pathway of OA-H_2O begins with **I**, which lies about 24 kJ mol^{-1} below the constituent monomer. Similarly, TS1-H_2O lies below TS1, but the energy difference is greater (about 46 kJ mol^{-1}). Consequently, the barrier to decarboxylation of OA-H_2O (127 kJ mol^{-1}) is lower than that of OA (149 kJ mol^{-1}). Though the lowering is required for catalysis to be plausible, dynamical modeling, which accounts for the competition between decarboxylation

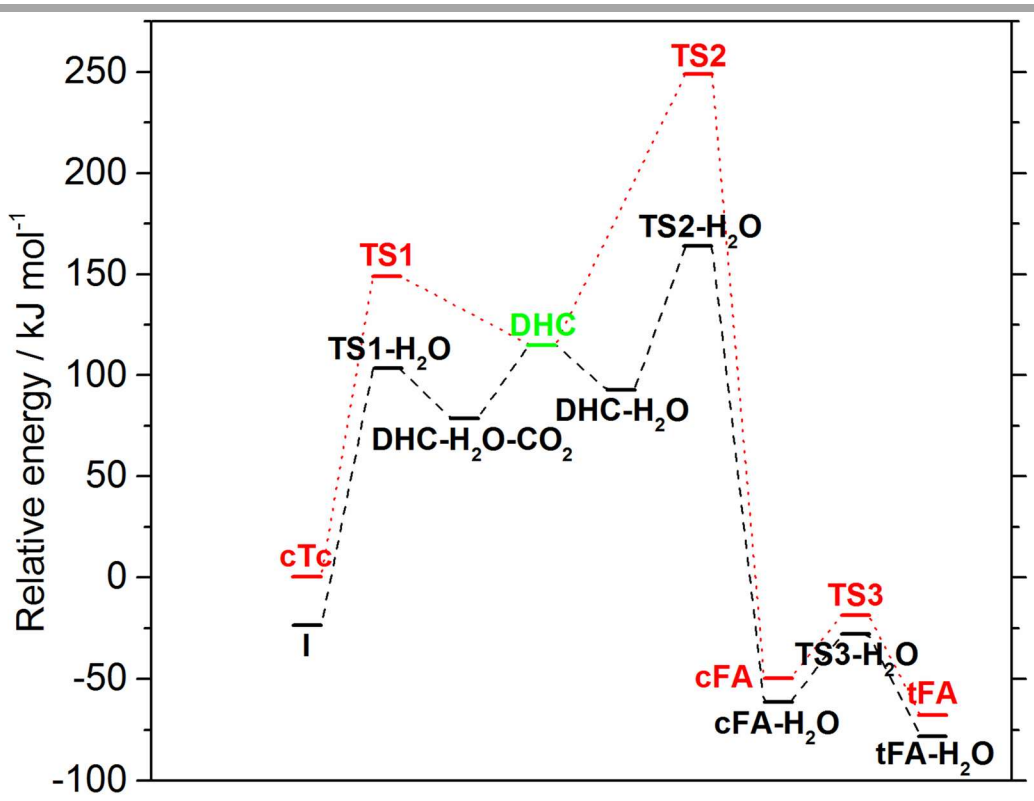

Figure 5.8. Decarboxylation reaction coordinates for the lowest energy conformer of the OA monomer (red) and isomer **I** of OA monohydrate (black). DHC (green) is involved in both pathways.

and dissociation (that is, dehydration) of the complex, would be required to state with certainty if catalysis occurs.[22]

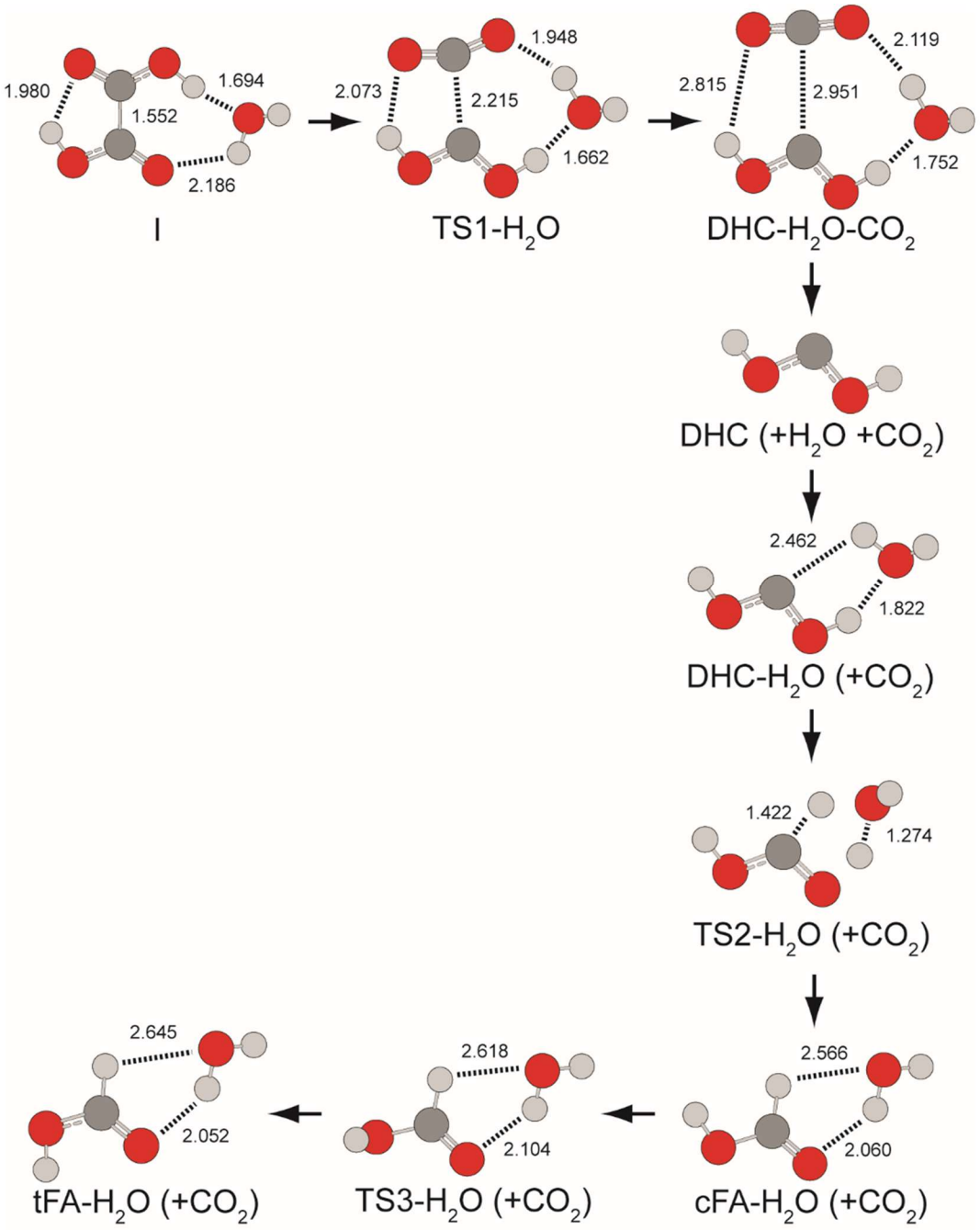

Figure 5.9. Decarboxylation pathway for the most stable isomer of oxalic acid monohydrate, calculated at the MP2/6-311++G(d,p) level of theory. Denoted bond and inter-nuclear distances are given in Å. I assume that the ternary complex, DHC-H_2O-CO_2, dissociates completely before DHC-H_2O forms. The presence of water has little effect on the barrier to conversion of cFA to tFA, since it involves only internal rotation of the hydroxyl group.

Furthermore, the lowering of the barrier is unique to this isomer of OA-H_2O. For the higher-energy conformer of the monomer, the transition state analogous to TS1 lies 157 kJ mol^{-1} above the minimum. However, the monohydrated transition state analogous to TS1-H_2O lies 194 kJ mol^{-1} above **II**, compared to 127 kJ mol^{-1} for **I.** Thus, water increases the barrier to decarboxylation in **II**, unequivocal evidence of *inhibition*, in stark contrast to potential catalysis in **I**. The difference in barrier height of nearly 70 kJ mol^{-1} indicates the significant effect of structure on decarboxylation of OA-H_2O. With the addition of more water molecules, this effect may change; furthermore, other routes – like dissociation of a proton – may be favourable.

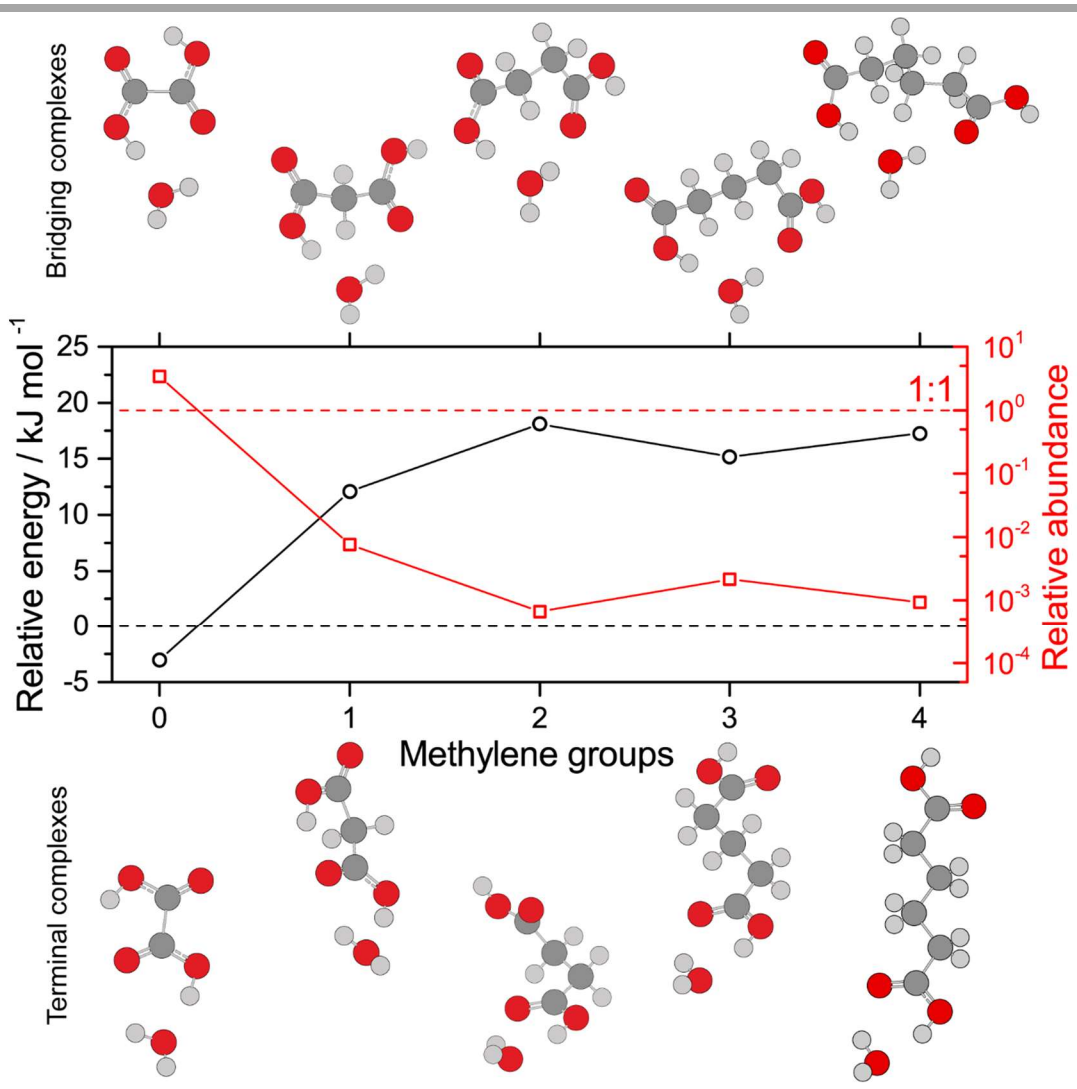

Figure 5.10. Energies and abundances (at 298 K) of the most stable bridging complexes relative to the most stable terminal complexes for monohydrates of the five smallest dicarboxylic acids, calculated at the MP2/6-311++G(d,p) level of theory. Energies are ZPE- and BSSE-corrected.

Based on calculations of the most stable bridging and terminal isomers of monohydrates of malonic, succinic, glutaric, and adipic acids, proceeding from a previous study of the monomers,[48] I conclude that OA is unique among these DCAs. As shown in Figure 5.10, for all of the DCAs except OA, the bridging isomer is less stable than the terminal isomer. For example, the bridging isomer of malonic acid-H_2O, discussed by Staikova et al.,[21] is about 12 kJ mol^{-1} higher in energy than the most stable terminal isomer, so its relative abundance at 298 K is expected to be less than one hundredth that of the lowest-energy isomer. The relative abundance of the bridging isomers of larger DCA monohydrates is even lower. Only for OA is the bridging isomer calculated to be most stable; at 298 K, the ratio of the bridging to terminal isomers is predicted to be greater than 3:1. I conclude that single-water catalysis of overtone-induced decarboxylation in the atmosphere is plausible for OA (provisionally, until dynamical modelling of OA-H_2O is reported) but not for larger DCAs.

5.4. Conclusions

I have observed the rotational spectra of the two most stable isomers of OA-H_2O. Splittings were observed for both and are attributed to rotation of the water moiety. In isomer **I**, water bridges the two carboxylic acid groups, facilitating hydrogen transfer. As a result, water lowers the barrier to decarboxylation in **I**. In contrast, water binds to only one carboxylic acid group in **II**, and it increases the barrier to decarboxylation; water is an inhibitor of decarboxylation in this topology. OA is the only DCA for which the bridging topology of the monohydrate is the most stable; for the others calculated, the atmospheric abundance of this topology is negligible. I conclude that OA is the only DCA for which single water-catalysed enhancement of overtone-induced decarboxylation in the atmosphere is plausible. Future investigations of oxalic acid monohydrate, including dynamical modelling, and higher hydrates can help to unravel to what extent dissociation through IVR competes with decarboxylation.

References

1 Ho, K. F.; Huang, R.-J.; Kawamura, K.; Tachibana, E.; Lee, S. C.; Ho, S. S. H.; Zhu, T.; Tian, L. Dicarboxylic acids, ketocarboxylic acids, α-dicarbonyls, fatty acids and benzoic acid in $PM_{2.5}$ aerosol collected during CAREBeijing-2007: An effect of traffic restriction on air quality. *Atmos. Chem. Phys.* **2015**, *15*, 3111-3123.

2 Meng, J.; Wang, G.; Li, J.; Cheng, C.; Cao, J. Atmospheric oxalic acid and related secondary organic aerosols in Qinghai Lake, a continental background site in Tibet Plateau. *Atmos. Environ.* **2013**, *79*, 582-589.

3 Kawamura, K.; Sakaguchi, F. Molecular distributions of water soluble dicarboxylic acids in marine aerosols over the Pacific Ocean including tropics. *J. Geophys. Res.* **1999**, *104*, 3501-3509.

4 Narukawa, M.; Kawamura, K.; Li, S.-M.; Bottenheim, J. W. Dicarboxylic acids in the Arctic aerosols and snowpacks collected during ALERT 2000. *Atmos. Environ.* **2002**, *36*, 2491-2499.

5 Ma, Q.; He, H.; Liu, C. Hygroscopic properties of oxalic acid and atmospherically relevant oxalates. *Atmos. Environ.* **2013**, *69*, 281-288.

6 Darvas, M.; Picaud, S.; Jedlovszky, P. Water adsorption around oxalic acid aggregates: A molecular dynamics simulation of water nucleation on organic aerosols. *Phys. Chem. Chem. Phys.* **2011**, *13*, 19830-19839.

7 Lee, A. K. Y.; Zhao, R.; Gao, S. S.; Abbatt, J. P. D. Aqueous-phase OH oxidation of glyoxal: Application of a novel analytical approach employing aerosol mass spectrometry and complementary off-line techniques. *J. Phys. Chem. A* **2011**, *115*, 10517-10526.

8 Perri, M. J.; Seitzinger, S.; Turpin, B. J. Secondary organic aerosol production from aqueous photooxidation of glycolaldehyde: Laboratory experiments. *Atmos. Environ.* **2009**, *43*, 1487-1497.

9 Enami, S.; Hoffmann, M. R.; Colussi, A. J. Stepwise oxidation of aqueous dicarboxylic acids by gas-phase OH radicals. *J. Phys. Chem. Lett.* **2015**, *6*, 527-534.

10 Xu, Y.; Nadykto, A. B.; Yu, F.; Jiang, L.; Wang, W. Formation and properties of hydrogen-bonded complexes of common organic oxalic acid with atmospheric nucleation precursors. *THEOCHEM* **2010**, *951*, 28-33.

11 Xu, W.; Zhang, R. Theoretical investigation of interaction of dicarboxylic acids with common aerosol nucleation precursors. *J. Phys. Chem. A* **2012**, *116*, 4539-4550.

12 Weber, K. H.; Morales, F. J.; Tao, F.-M. Theoretical study on the structure and stabilities of molecular clusters of oxalic acid with water. *J. Phys. Chem. A* **2012**, *116*, 11601-11617.

13 Weber, K. H.; Liu, Q.; Tao, F.-M. Theoretical study on stable small clusters of oxalic acid with ammonia and water. *J. Phys. Chem. A* **2014**, *118*, 1451-1468.

14 Vaida, V.; Donaldson, D. J. Red-light initiated atmospheric reactions of vibrationally excited molecules. *Phys. Chem. Chem. Phys.* **2014**, *16*, 827-836.

15 Yamamoto, S.; Back, R. The gas-phase photochemistry of oxalic acid. *J. Phys. Chem.* **1985**, *89*, 622-625.

16 Bock, C. W.; Redington, R. L. Isomerization and unimolecular dissociation channels of the oxalic acid monomer. *J. Chem. Phys.* **1986**, *85*, 5391-5400.

17 Higgins, J.; Zhou, X.; Liu, R.; Huang, T. T.-S. Theoretical study of thermal decomposition mechanism of oxalic acid. *J. Phys. Chem. A* **1997**, *101*, 2702-2708.

18 Olbert-Majkut, A.; Ahokas, J.; Pettersson, M.; Lundell, J. Visible light-driven chemistry of oxalic acid in solid argon, probed by Raman spectroscopy. *J. Phys. Chem. A* **2013**, *117*, 1492-1502.

19 Takahashi, K.; Plath, K. L.; Skodje, R. T.; Vaida, V. Dynamics of vibrational overtone excited pyruvic acid in the gas phase: Line broadening through hydrogen-atom chattering. *J. Phys. Chem. A* **2008**, *112*, 7321-7331.

20 Takahashi, K.; Plath, K. L.; Axson, J. L.; Nelson, G. C.; Skodje, R. T.; Vaida, V. Dynamics and spectroscopy of vibrational overtone excited glyoxylic acid and 2,2-dihydroxyacetic acid in the gas-phase. *J. Chem. Phys.* **2010**, *132*, 094305 (10 pp.).

21 Staikova, M.; Oh, M.; Donaldson, D. J. Overtone-induced decarboxylation: A potential sink for atmospheric diacids. *J. Phys Chem. A* **2005**, *109*, 597-602.

22 Kramer, Z. C.; Takahashi, K.; Skodje, R. T. Water catalysis and anticatalysis in photochemical reactions: Observation of a delayed threshold effect in the reaction quantum yield. *J. Am. Chem. Soc.* **2010**, *132*, 15154-15157.

23 Kramer, Z. C.; Takahashi, K.; Vaida, V.; Skodje, R. T. Will water act as a photocatalyst for cluster phase chemical reactions? Vibrational overtone-induced dehydration reaction of methanediol. *J. Chem. Phys.* **2012**, *136*, 164302 (9 pp.).

24 Schnitzler, E. G.; Jäger, W. The benzoic acid-water complex: A potential atmospheric nucleation precursor studied using microwave spectroscopy and *ab initio* calculations. *Phys. Chem. Chem. Phys.* **2014**, *16*, 2305-2314.

25 Schnitzler, E. G.; Zenchyzen, B. L. M.; Jäger, W. Rotational spectroscopy of the atmospheric photo-oxidation product *o*-toluic acid and its monohydrate. *Phys. Chem. Chem. Phys.* **2016**, *18*, 448-457.

26 Ghosh, S.; Thomas, J.; Huang, W.; Xu, Y.; Jäger, W. Rotational spectra of two hydrogen-bonded methyl salicylate monohydrates: Relative stability and tunneling motions. *J. Phys. Chem. Lett.* **2015**, *6*, 3126-3131.

27 Balle, T. J.; Flygare, W. H. Fabry-Perot cavity Fourier transform microwave spectrometer with a pulsed nozzle particle source. *Rev. Sci. Instrum.* **1981**, *52*, 33-45.

28 Xu, Y.; Jäger, W. Evidence for heavy atom large amplitude motions in RG-cyclopropane van der Waals complexes (RG=Ne, Ar, Kr) from rotation-tunneling spectroscopy. *J. Chem. Phys.* **1997**, *106*, 7968-7980.

29 Xu, Y.; Van Wijngaarden, J.; Jäger, W. Microwave spectroscopy of ternary and quaternary van der Waals clusters. *Int. Rev. Phys. Chem.* **2005**, *24*, 301-338.

30 Schnitzler, E. G.; Poopari, M. R.; Xu, Y.; Jäger, W. Rotational spectroscopy of methyl benzoylformate and methyl mandelate: Structure and internal dynamics of a model reactant and product of enantioselective reduction. *Phys. Chem. Chem. Phys.* **2015**, *17*, 21942-21949.

31 Schnitzler, E. G.; Zenchyzen, B. L. M.; Jäger, W. High-resolution Fourier-transform microwave spectroscopy of methyl- and dimethylnapthalenes. *Astrophys. J.* **2015**, *805*, 141 (7 pp.).

32 Møller, C.; Plesset, M. S. Note on an approximation treatment for many-electron systems. *Phys. Rev.* **1934**, *46*, 618-622.

33 Krishnan, R.; Binkley, J. S.; Seeger, R; Pople, J. A. Self-consistent molecular orbital methods. XX. A basis set for correlated wave functions. *J. Chem. Phys.* **1980**, *72*, 650-654.

34 Frisch, M. J.; et al. *Gaussian 09*, Rev. D.01; Gaussian, Inc.: Wallingford, CT, **2013**. See bibliography for complete list of authors.

35 Fukui, K. The path of chemical reactions – the IRC approach. *Acc. Chem. Res.* **1981**, *14*, 363-368.

36 Boys, S. F.; Bernardi, F. The calculation of small molecular interactions by the difference of separate total energies. Some procedures with reduced errors. *Mol. Phys.* **1970**, *19*, 553-566.

37 Koch, U.; Popelier, P. L. A. Characterization of C-H-O hydrogen bonds on the basis of the charge density. *J. Phys. Chem.* **1995**, *99*, 9747-9754.

38 Bader, R. F. W. A bond path: A universal indicator of bonded interactions. *J. Phys. Chem. A* **1998**, *102*, 7314-7323.

39 Lu, T.; Chen, F. Multiwfn: A multifunctional wavefunction analyzer. *J. Comput. Chem.* **2012**, *33*, 580-592.

40 Western, C. M. *PGOPHER, A Program for Simulating Rotational Structure*, University of Bristol: Bristol, UK. http://pgopher.chm.bris.ac.uk.

41 Watson, J. K. G. Determination of centrifugal distortion coefficients of asymmetric-top molecules. *J. Chem. Phys.* **1967**, *46*, 1935-1949.

42 Back, R. A. The ultraviolet absorption spectrum of oxalic acid vapor. *Can. J. Chem.* **1984**, *62*, 1414-1428.

43 Godfrey, P. D.; Mirabella, M. J.; Brown, R. D. Structural studies of higher energy conformers by millimeter-wave spectroscopy: Oxalic acid. *J. Phys. Chem. A* **2000**, *104*, 258-264.

44 Maçôas, E. M. S.; Fausto, R.; Pettersson, M.; Khriachtchev, L.; Räsänen, M. Infrared-induced rotamerization of oxalic acid monomer in argon matrix. *J. Phys. Chem. A* **2000**, *104*, 6956-6961.

45 Evangelisti, L.; Caminati, W. Internal dynamics in complexes of water with organic molecules. Details of the internal motions in *tert*-butylalcohol-water. *Phys. Chem. Chem. Phys.* **2010**, *12*, 14433-14441.

46 Seifert, N. A; Finneran, I. A.; Perez, C.; Zaleski, D. P.; Neill, J. L.; Steber, A. L.; Suenram, R. D.; Lesarri, A.; Shipman, S. T.; Pate, B. H. AUTOFIT, an automated fitting tool for broadband rotational spectra, and applications to 1-hexanal. *J. Mol. Spectrosc.* **2015**, *312*, 13-21.

47 Schreiner, P. R.; Reisenauer, H. P. Spectroscopic identification of dihydroxycarbene. *Angew. Chem. Int. Ed.* **2008**, *47*, 7071-7074.

48 Nguyen, T. H.; Hibbs, D. E.; Howard, S. T. Conformations, energies, and intramolecular hydrogen bonds in dicarboxylic acids: Implications for the design of synthetic dicarboxylic acid receptors. *J. Comput. Chem.* **2005**, *26*, 1233-1241.

6 Rotational spectroscopy of secondary organic aerosol precursors: Methyl- and dimethylnaphthalenes

6.1. Introduction

Polycyclic aromatic hydrocarbons (PAHs) are abundant in Earth's atmosphere.[1] They are products of combustion, so they are emitted by both anthropogenic and biogenic sources (i.e. coal burning and forest fires, respectively).[2] PAHs are the principal component of soot; small PAHs, like naphthalene, contribute to the volatile mass fraction of soot,[3] and larger PAHs arranged in graphite-like layers constitute the non-volatile fraction of soot.[4] Small PAHs are representative intermediate volatility organic compounds,[5] so they are also present in the gas phase,[1] where they can be oxidized by OH radical to form secondary organic aerosol (SOA). SOA formation from PAHs has been investigated in smog chamber studies; for example, naphthalene,[5-7] 1- and 2-methylnaphthalene,[5,7] and 1,2-dimethylnaphthalene[5] have been used as SOA precursors. SOA formation from PAHs in the atmosphere has been modelled, as well.[8,9]

PAHs are also abundant in regions of our solar system, such as the atmosphere of Titan,[10] and they may be ubiquitous throughout the interstellar medium (ISM).[11] PAHs are likely carriers of several spectral features of the ISM,[12,12] including the unidentified infrared emission (UIE) bands between 3 and 20 μm, the range of stretching and bending vibrations of aromatic hydrocarbons.[14] Although the presence of PAHs can explain the UIE bands, no specific PAHs have been identified since vibrational bands are broad and not unique to individual molecules; in contrast, pure rotational transitions are unambiguous, making high-resolution microwave spectroscopy a candidate method for the identification of specific PAHs in the ISM.

The rotational spectra of several small PAHs, including azulene, acenaphthene, acenaphthylene, and fluorene,[15] have previously been measured. The rotational spectrum of corannulene, a symmetrical PAH with a large dipole moment, due to its bowl-shaped structure,

has also been observed.[16] However, many symmetrical, planar PAHs are nonpolar. Substitution in PAHs often results in non-zero dipole moments; for example, polycyclic aromatic nitrogen hetero-cycles (PANHs) have higher dipole moments than their parent PAHs, and the rotational spectra of several PANHs have been measured.[17] Alkyl substitution for hydrogen can also lead to non-zero dipole moments. Furthermore, laboratory-generated carbon nanoparticles containing alkyl-substituted naphthalenes have been shown to have infrared emission features consistent with dust in the ISM,[18] so alkylnaphthalenes are candidate species for identification in the ISM. Although rotationally resolved electronic spectra for 1-methylnapthalene, 2-methylnaphthalene,[19] and 2,3-dimethylnaphthalene[20] have been reported in the past, no pure rotational spectra have previously been measured for alkylnaphthalenes.

In an effort to aid in the rotational spectroscopic detection of PAHs in Earth's atmosphere and in the ISM, I measured the rotational spectra of 1-methylnaphthalene (1-MN), 2-methylnaphthalene (2-MN), 1,2-dimethylnaphthalene (1,2-DMN), and 1,3-dimethylnaphthalene (1,3-DMN) in the range of 6-15 GHz using a Fourier-transform microwave (FTMW) spectrometer. Assignments and structural characterizations were aided by density functional theory calculations. Barriers to internal rotation were derived and compared to results of relaxed and rigid scans of the potential energy surface using density functional theory.

6.2. Methods

6.2.1. Experimental

Reagent grade 1-MN (Aldrich, 95%), 2-MN (General Intermediates), 1,2-DMN (Aldrich, 95%), and 1,3-DMN (Aldrich, 96%) were used without purification. The alkylnaphthalenes have very low vapour pressures at room temperature, so it was necessary to heat each sample to approximately 473 K in a stainless steel container. The nozzle and the tubing connecting it to the sample container were also heated to prevent condensation of the alkylnaphthalenes. Ne (Praxair) was used as backing gas at 1-2 atm.

Rotational spectra of each sample were measured in the range of 6-15 GHz using a cavity-based FTMW spectrometer, which has been described in detail previously.[21,22] In short, the gaseous sample is first injected into an evacuated resonator, through a pulsed nozzle. As the molecules enter the resonator, they undergo supersonic expansion and are rapidly cooled

(rotationally) to 1-2 K by collisions with the backing gas. The resonator consists of two aluminum mirrors, whose separation is adjusted to match the frequency of a given rotational transition. A pulse of near-resonant microwave radiation is then used to excite the molecules, which in turn emit radiation at the transition frequency that is detected in the time domain, analog-to-digital converted, and then Fourier transformed to yield the frequency spectrum. Time domain signals from successive experiments are averaged until a reasonable signal to noise ratio is achieved. Because of the relatively small molecular dipole moments, a 0.5 W solid-state amplifier was used to increase the power of the excitation pulses.

6.2.2. Computational

Geometry optimization and vibrational analysis calculations were carried out using the Gaussian09 *ab initio* package[23] at the B3LYP/6-311++G(d,p) level of theory. B3LYP calculations have been shown to accurately predict rotational constants for other species.[17,24] Initial structures were generated and optimized using molecular mechanics in Avogadro[25] before being input into Gaussian; output structures and vibrational normal modes were visualized in Avogadro, as well. No imaginary frequencies were calculated for the stationary points, so the optimized structures are indeed minima on the potential energy surface. Rotational constants and centrifugal distortion constants were predicted (using keywords "Freq=VibRot" and "Output=Pickett"), and transition frequencies were calculated in PGOPHER,[26] using the *ab initio* rotational constants. The barriers to methyl internal rotation were determined by varying the dihedral angle between the aromatic plane and a certain hydrogen atom of the methyl substituent, calculating the energy at each point – with or without optimization of all the other internal coordinates (using keywords "Opt=ModRedundant" and "Scan", respectively).

The experimental transition frequencies were assigned and fitted using PGOPHER, which employs a semi-rigid rotor model, and XIAM,[27] which employs the combined axis method (CAM) to treat the methyl group internal rotation. In both programs, Watson's *A* reduction Hamiltonian in its I^r representation was employed.[28] The experimental rotational constants obtained from the final fits in either PGOPHER or XIAM were compared to the calculated rotational constants, to evaluate the quality of the *ab initio* calculations.

6.3. Results and discussion

6.3.1. Spectra

In general, my searches for rotational transitions were guided by theoretical rotational constants and dipole moments (see Table 6.1), calculated at the B3LYP/6-311++G(d,p) level of theory. The calculations gave one minimum energy structure for each alkylnaphthalene (see Figure 6.1). For 1-MN and 2-MN, transitions were easily located using previously-reported rotational constants, which were determined from the rotationally-resolved electronic spectra of the species.[19] For 1,2- and 1,3-DMN, automated frequency scans (consisting of 0.2 MHz frequency steps) were used to search for targeted *a*- and *b*-type transitions within 100 MHz intervals, centred at the predicted frequencies. For both species, the first three transition frequencies observed were assigned and used in preliminary fits to locate additional transitions whose frequencies were subsequently used in the final fits.

Representative transitions illustrate the features of the spectra. Each observed transition is split into a Doppler doublet as a result of the supersonic expansion being parallel to the

Table 6.1. Spectroscopic constants and dipole moments of the methyl and dimethylnaphthalenes, calculated using density functional theory at the B3LYP/6-311++G(d,p) level.

	1-MN	2-MN	1,2-DMN	1,3-DMN
A / MHz	1895.95	2810.86	1872.13	1572.52
B / MHz	1125.13	821.83	778.24	815.88
C / MHz	709.20	638.42	553.49	540.77
Δ_J / kHz	0.0175	0.00805	0.00683	0.00734
Δ_{JK} / kHz	0.0449	0.187	0.0507	0.0404
Δ_K / kHz	0.0127	0.0143	0.0124	0.0192
δ_J / kHz	0.00638	0.00203	0.00204	0.00238
δ_K / kHz	0.0324	0.0226	0.0176	0.0192
$\Delta A/A^a$ / %	0.07	0.23	0.07	-0.05
$\Delta B/B$ / %	-0.10	-0.12	-0.11	-0.10
$\Delta C/C$ / %	-0.07	-0.07	-0.10	-0.11
Ave[b] / %	0.08	0.14	0.09	0.09
κ[c]	-0.30	-0.83	-0.66	-0.47
$\lvert\mu_a\rvert$ / D	0.15	0.51	0.64	0.49
$\lvert\mu_b\rvert$ / D	0.34	0.03	0.36	0.30
$\lvert\mu_c\rvert$ / D	0.00	0.00	0.00	0.00

[a] Relative difference between calculated and experimental values; for example, $((A_{exp}-A_{calc})/A_{exp})100\%$. [b] Average magnitude of relative differences. [c] Asymmetry parameter.

microwave propagation direction. For 1-MN (see Figure 6.2), no splittings attributable to methyl internal rotation were observed, and its spectrum was fitted using the PGOPHER program.[26] When all distortion constants are optimized in the fit, the uncertainties are very large; with a

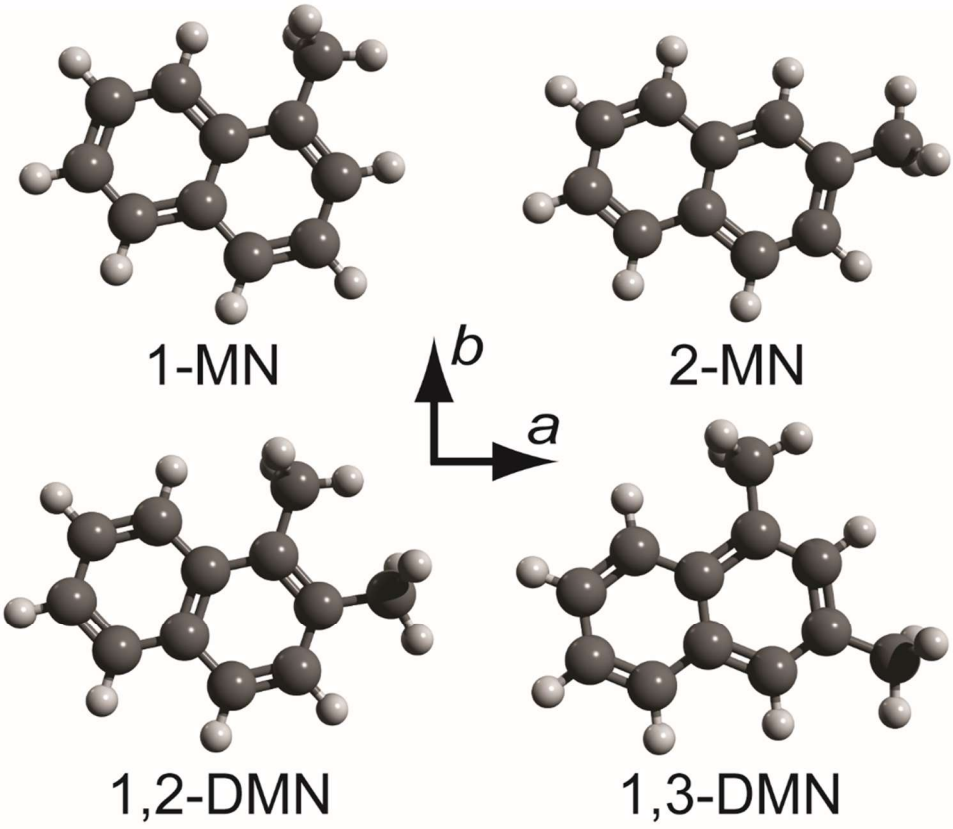

Figure 6.1. Minimum energy structures of (I) 1-MN, (II) 2-MN, (III) 1,2-DMN, and (IV) 1,3-DMN calculated at the B3LYP/6-311++G(d,p) level of theory and oriented with respect to their *a* and *b* principal inertial axes.

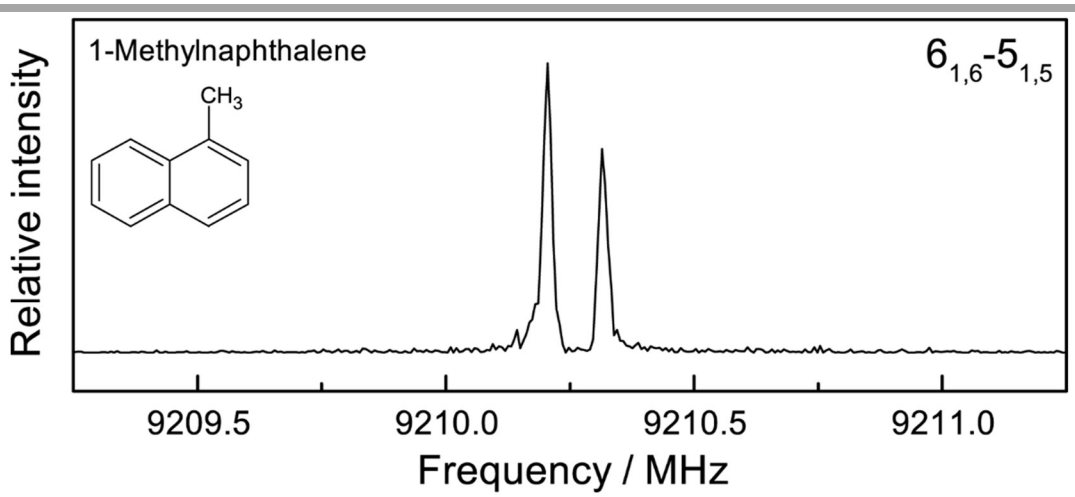

Figure 6.2. Representative *a*-type transition ($6_{1,6}$-$5_{1,5}$) of 1-MN, measured using an excitation pulse length of 1 μs and 250 averaging cycles.

value of 0.03 ± 0.03 kHz, Δ_K is the most problematic. Rather than fixing Δ_K at zero, I fixed it at the value predicted from harmonic vibrational frequency calculations, 0.0449 kHz, at the B3LYP/6-311++G(d,p) level of theory; in the fits for the other alkylnaphthalenes, as well, Δ_K was fixed at the respective calculated values (see Table 6.1).

For 2-MN (see Figure 6.3) and 1,3-DMN (see Figure 6.4), methyl internal rotation splittings were observed, so two pairs of Doppler components, corresponding to the A and E symmetry components, were detected for each transition. The XIAM program[27] was used to fit all the spectra that exhibit splitting of rotational lines due to methyl internal rotation. For 1,2-DMN (see Figure 6.5), additional splittings due to internal rotation of both methyl

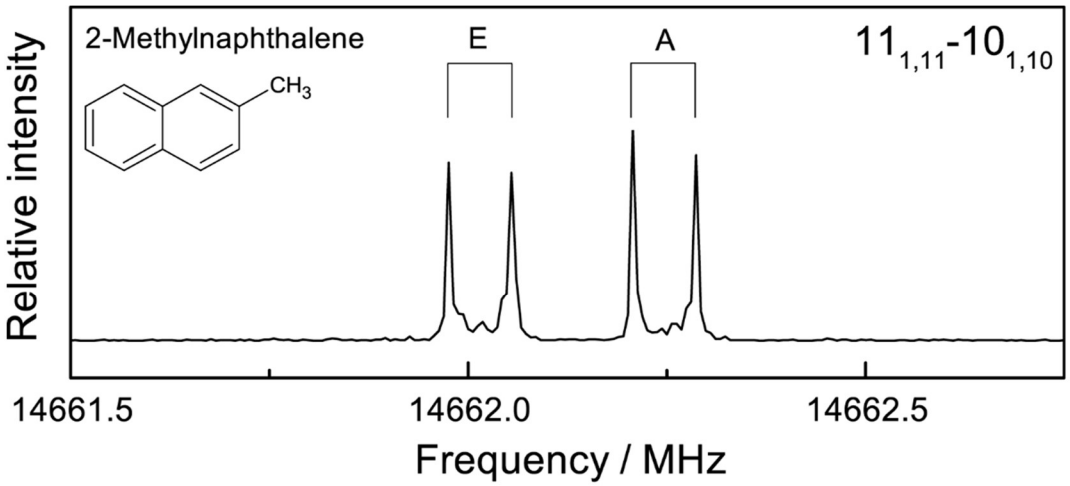

Figure 6.3. Representative *a*-type transition ($11_{1,11}$-$10_{1,10}$) of 2-MN, measured using an excitation pulse length of 0.15 μs and 1000 averaging cycles.

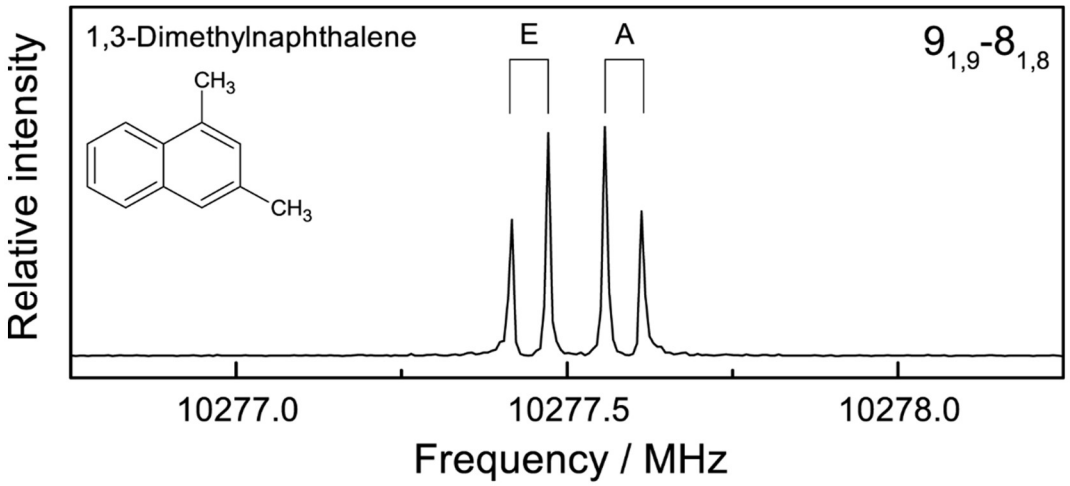

Figure 6.4. Representative *a*-type transition ($9_{1,9}$-$8_{1,8}$) of 1,3-DMN, measured using an excitation pulse length of 0.15 μs and 300 averaging cycles.

substituents occurred, resulting in five fine structure components with symmetry labels AA, AE, EA, EE, and EE'. For most transitions, the EE and EE' components overlapped, so only four lines were observed. For some transitions, only two lines were observed, because of additional overlapping components. For example, the EA, EE, and EE' components of the $7_{2,6}$-$6_{2,5}$ transition are so close in frequency that they appear as one Doppler pair; however, in the fit, the

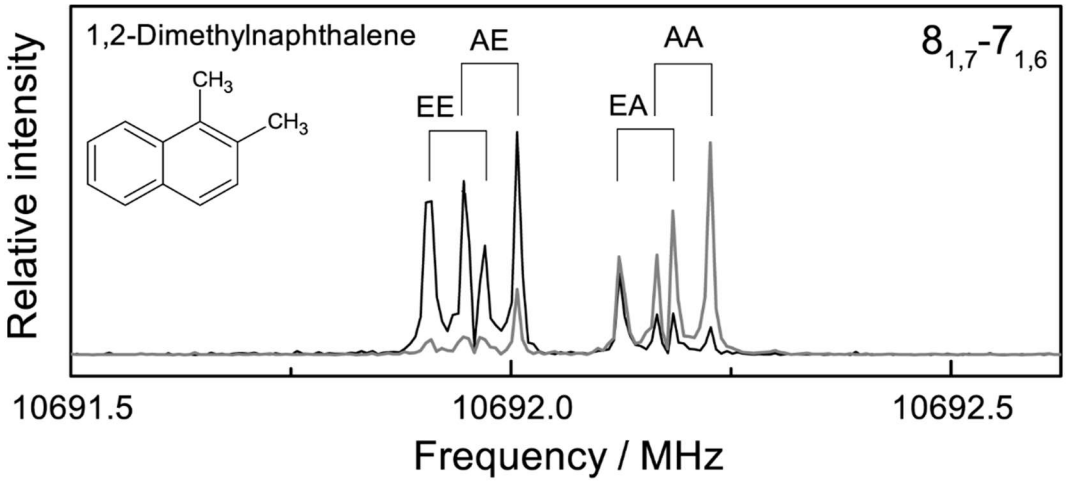

Figure 6.5. Representative *a*-type transition ($8_{1,7}$-$7_{1,6}$) of 1,2-DMN, collected at two different excitation frequencies using an excitation pulse length of 1 μs and number 500 averaging cycles.

Table 6.2. Experimental spectroscopic constants of the methyl and dimethylnaphthalenes.

	1-MN	2-MN[a]	1,2-DMN[a]	1,3-DMN[a]
A / MHz	1894.6564(1)[b]	2804.519(4)	1870.779(1)	1573.2606(4)
B / MHz	1126.2936(2)	822.8100(2)	779.1260(4)	816.7064(1)
C / MHz	709.68277(7)	638.8528(1)	554.0210(2)	541.37179(4)
Δ_J / kHz	0.016(2)	0.0084(7)	0.008(1)	0.0066(8)
Δ_{JK} / kHz	0.018(7)	0.016(5)	0.0124[c]	0.021(6)
Δ_K / kHz	0.0449[c]	0.187[c]	0.0507[c]	0.0404[c]
δ_J / kHz	0.0055(8)	0.0022(4)	0.003(1)	0.0021(4)
δ_K / kHz	0.034(7)	0.02(3)	0.0176[c]	0.012(5)
κ[d]	-0.30	-0.83	-0.66	-0.47
N[e]	48	39	35	37
N_T[f]	48	78	147	70
σ[g] / kHz	1.1	1.8	8.0	0.7

[a] Internal rotation constants, also determined from fit, are shown in Table 6.3. [b] Standard deviation in the last decimal place before the parentheses. [c] Constant fixed at *ab initio* value, because it could not be well-determined. [d] Asymmetry parameter. [e] Number of rotational transitions included in fit. [f] Total number of transitions, including methyl internal rotation symmetry components. [g] Root-mean-square deviation of residuals.

experimental frequency is 13 kHz too low and 10 kHz too high for the outer components, EE and EE', respectively. As a result, the standard deviation of the 1,2-DMN fit is higher than those of the other alkylnaphthalenes. In this fit, the distortion constants Δ_{JK} and δ_K, in addition to Δ_K, were fixed at their calculated values.

The final fits gave rotational, centrifugal distortion (see Table 6.2), and internal rotation constants (see Table 6.3). In all, I observed 48 transitions for 1-MN (see Table A.10), 39 transitions (including 78 methyl internal rotation components) for 2-MN (see Table A.11), 37 transitions (including 70 components) for 1,3-DMN (see Table A.12), and 35 transitions (including 147 components) for 1,2-DMN (see Table A.13). Both *a*- and *b*-type transitions were observed for 1-MN, 1,2-DMN, and 1,3-DMN; however, only *a*-type transitions were observed for 2-MN. The rotational transition line strength, *S*, was calculated using the experimental rotational and centrifugal distortion constants.

6.3.2. Structures

Optimized geometries of the alkylnaphthalenes are illustrated in Figure 6.1. The point group of each molecule is C_s, and one hydrogen atom from each methyl substituent in a given molecule is eclipsed by the plane of symmetry. In 1,2- and 1,3-DMN, the two in-plane hydrogen atoms of the methyl groups were found to be oriented in the same clockwise direction with respect to the *c* principal inertial axis, even when calculations were repeated with the hydrogen atoms initially oriented in opposite directions. As shown in Table 6.2, all the alkylnaphthalenes have

Table 6.3. Experimental internal rotation parameters of 2-MN, 1,2-DMN, and 1,3-DMN.

	2-MN	1,2-DMN		1,3-DMN
Position	2	1	2	3
V_3[a] (kJ mol^{-1})	2.717(5)	3.672(3)	5.239(9)	2.896(2)
δ[b] (°)	19.9	80.0	6.6	22.4
F_0[c] (GHz)	159.70	161.23	160.31	160.51
F_{12}[d] (MHz)	…	417	…	

[a] Height of the three-fold barrier to rotation of the methyl top. [b] Angle between the methyl top axis and the *a* principal inertial axis. Another parameter, ε, is the angle between the *b* principal axis and the projection of the methyl top axis onto the *bc* plane; ε was zero for all alkylnaphthalenes, since the axes of the methyl rotors are in the *ab* plane. [c] Internal rotation constant; analogous to the *A*, *B*, and *C* rotational constants, it is related to the inverse of the moment of inertia of the methyl top about its axis. [d] Methyl top-methyl top interaction constant.

negative values of the asymmetry parameter κ, calculated from their rotational constants, according to Equation (6.1).

$$\kappa = \frac{2B - A - C}{A - C} \tag{6.1}$$

As discussed in Section 2.2, these negative values indicate the alkylnaphthalenes have more prolate character than oblate.

Based on the calculated dipole moments (see Table 6.1), the molecules are moderately polar, so they are candidate species for detection in the ISM using radio-astronomy in the microwave region. For each molecule, the component of the dipole moment along the *c* principal axis is zero, because of the C_s symmetry. This is consistent with the absence of *c*-type transitions in the measured spectra. 1-MN is the only molecule in which the strongest component of the calculated dipole moment is along the *b* principal axis; the calculated value of 0.34 D is similar to that of acenaphthylene, 0.31 D.[15] In the other molecules, the strongest components of the dipole moments are along their *a* principal axes; 1,2-DMN is the most polar molecule, because the two methyl substituents occur at neighboring positions. In 2-MN, the dipole moment component along the *b* principal axis is so small that I was not able to detect *b*-type transitions in its experimental spectrum. Since the calculated dipole moments are consistent with the above observations, I conclude that they may be relied upon to identify intense candidate transitions for astronomical searches. Alternatively, dipole moments can in principle be measured using Stark spectroscopy.

The quality of the *ab initio* calculations was evaluated by comparing the experimental and predicted rotational constants. Agreement is very good for all the alkylnaphthalenes (see

Table 6.4. Low-lying out-of-plane vibrations of the methyl- and dimethylnaphthalenes, calculated using B3LYP/6-311++G(d,p).

	1-MN	2-MN	1,2-DMN	1,3-DMN
υ_1 / cm^{-1}	132	96	99	94
υ_2 / cm^{-1}	166	124	122	118
υ_3 / cm^{-1}	183	180	145	152
υ_4 / cm^{-1}	247	280	222	172
υ_5 / cm^{-1}	…	…	300	217
υ_6 / cm^{-1}	…	…	…	295
Δ^a / amu Å^2	-3.329	-3.340	-6.590	-6.516
$\Delta_{corr}{}^b$ / amu Å^2	-0.200	-0.214	-0.336	-0.261

[a] Inertial defect. [b] 'Methyl top-corrected inertial defect.'

Table 6.1), leading to very good agreement between the predicted and experimental spectra. (For instance, the $6_{0,6}$–$5_{0,5}$ transition of 1-MN is predicted to occur 6 MHz lower than it is observed, a difference of only –0.06%.) Similarly, theoretical rotational constants of small PANHs, calculated at the same level of theory, were previously found to be within 0.25% of experimental values.[17] Based on these low average discrepancies, B3LYP is an excellent method for predicting the rotational constants of PAHs.

The differences between experimental and calculated rotational constants can be attributed to shortcomings in the *ab initio* calculations and effects of zero-point vibrational motions and centrifugal distortion. For planar molecules, it has been shown that zero-point out-of-plane vibrational motions can contribute significantly to negative values for the inertial defect, which is calculated from the principal moments of inertia, according to Equation (6.2).[29]

$$\Delta = I_c - I_b - I_a \tag{6.2}$$

The inertial defect is zero for a rigid planar molecule. Values for Δ of the alkylnaphthalenes studied in this work are given in Table 6.4 and reflect primarily the contributions of the out-of-plane hydrogen atoms of the methyl groups. I can approximate the contribution to the inertial defect from out-of-plane vibrational motions by subtracting the equilibrium contribution from the out-of-plane hydrogen atoms to yield a 'methyl top-corrected inertial defect' (see Table 6.4), calculated according to Equation (6.3), which is also used in Section 4.3.1.

$$\Delta_{\text{corr}} = \Delta + 2\sum m_{\text{H}} c_{\text{H}}^2 \tag{6.3}$$

Here, m_{H} is the hydrogen atom mass in amu, c_{H} is the *c*-coordinate of the hydrogen atom from the *ab initio* calculations, and the sum is over the out-of-plane hydrogen atoms. The doubly-substituted molecules have the most significant 'methyl top-corrected inertial defects', because they have more low-lying out-of-plane vibrational modes with frequencies below 400 cm^{-1} (see Table 6.4) than the singly-substituted molecules. Planar PANHs exhibit the same trend; their inertial defects (like the 'methyl top-corrected inertial defects' in my study) have been shown to increase with the number of low-lying out-of-plane modes.[30]

6.3.3. Barriers to internal rotation

The experimentally-derived internal rotation parameters are given in Table 6.3. The parameters of the lone methyl substituent of 1-MN could not be determined, because no splitting was observed in the spectrum. This observation is indicative of a high barrier to internal rotation,

consistent with an earlier experimental study; the barrier has been determined to be 9.7 kJ mol^{-1}, based on the rotationally-resolved electronic spectrum.[19] In contrast, the methyl substituent of 2-MN causes splitting in the rotational spectrum, and the barrier was determined to be much lower, 2.717 kJ mol^{-1}, in close agreement with the previously measured value (2.8 kJ mol^{-1}).[19]

1,2-DMN is an interesting prototype of molecules that have two methyl substituents at adjacent carbon atoms of an aromatic ring, analogous to 3,4-dimethylbenzaldehyde, which has previously been studied in detail.[31] The methyl substituents at both the 1 and 2 positions of 1,2-DMN cause splittings in the rotational spectrum, and the barriers were determined to be 3.670 and 5.238 kJ mol^{-1}, respectively. No previous measurements have been reported; however, I can compare to calculated values. In general, barriers to internal rotation can be determined using *ab initio* calculations by stepping a single internal coordinate (in this case, a dihedral angle) and either fixing all the others or allowing them to simultaneously relax. The barriers to rotation of the methyl substituents at the 1 and 2 positions were calculated to be 2.70

Table 6.5. Barriers to internal rotation for the methyl- and dimethylnaphthalenes, calculated using B3LYP/6-311++G(d,p).

Species	Position	$V_{3,\text{rigid}}$ (kJ mol^{-1})	$V_{3,\text{relaxed}}$ (kJ mol^{-1})
1-MN	1	10.53	8.03
2-MN	2	2.70	2.57
1,2-DMN	1	6.91	2.70
1,2-DMN	2	8.38	4.41
1,3-DMN	1	10.45	7.98
1,3-DMN	3	2.78	2.68

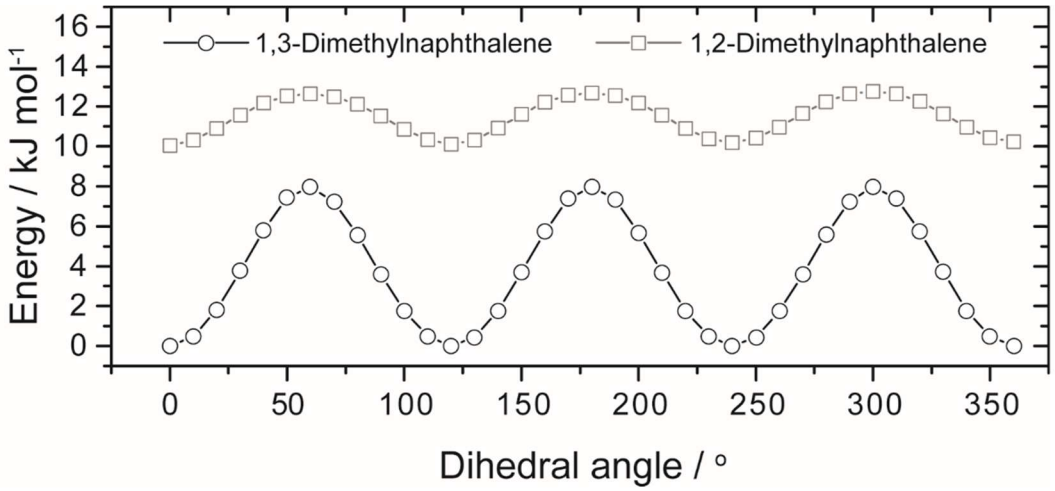

Figure 6.6. Potential energy of 1,3- and 1,2-DMN as a function of the dihedral angle between the aromatic plane and the initially in-plane hydrogen atom of the methyl substituent at position 1.

and 4.41 kJ mol^{-1} (see Table 6.5), respectively, when all the internal coordinates, besides the stepped dihedral angle, were allowed to relax at each value of the dihedral angle. Though these values are lower than those determined experimentally, their relative magnitude is similar. Interestingly, the barrier to rotation of the methyl substituent at position 1 is lower in 1,2-DMN than in 1-MN and 1,3-DMN, although the rotor is expected to experience much greater steric hindrance in 1,2-DMN. My calculations indicate that steric hindrance indeed increases the energy of the transition state of 1,2-DMN, compared to that of its isomer 1,3-DMN, but it increases the energy of the minimum to an even greater extent (see Figure 6.6); as a result, the energy difference between the minimum and the transition state is smaller. This observation is consistent with earlier calculations,[32] and it can be attributed to the environment around the methyl group becoming more isotropic. The barrier to internal rotation is greater for the methyl substituent at position 2 than 1, because in the equilibrium geometry the in-plane hydrogen atom of the methyl group at position 1 is oriented towards the methyl group at position 2. When all the internal coordinates, besides the stepped dihedral angle, were fixed, the barriers to rotation of both methyl substituents were calculated to be much higher; for example, the barrier height at position 1 is 6.91 kJ mol^{-1} (see Figure 6.7). Furthermore, using the rigid approach, I find that the three barrier heights calculated through a 360° rotation of the methyl substituent at position 1 differ slightly, because the group is not perfectly tetrahedral in the equilibrium geometry.

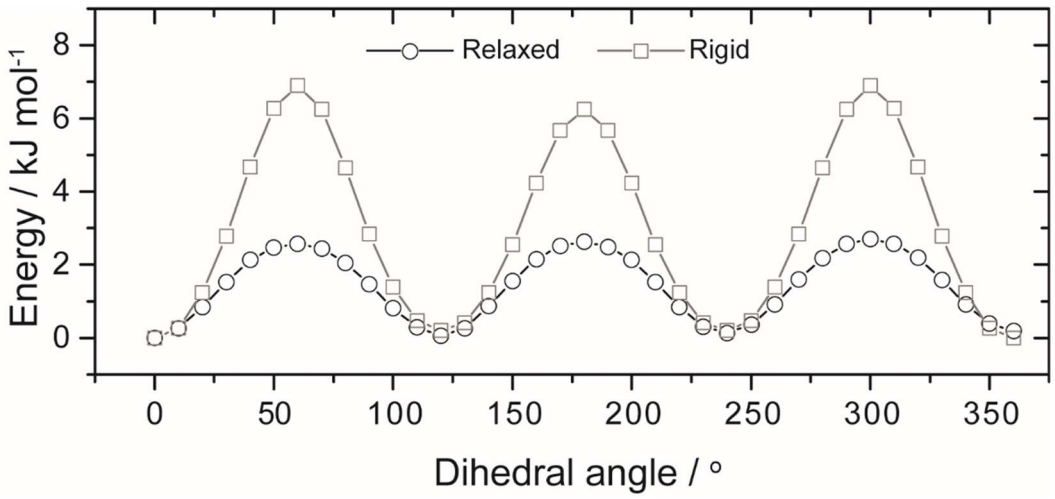

Figure 6.7. Potential energy of 1,2-DMN at fixed values of the dihedral angle between the aromatic plane and the initially in-plane hydrogen atom of the methyl substituent at position 1, with ("relaxed") and without ("rigid") optimization of all the other internal coordinates.

These features constitute a strong argument against using single point energy calculations to predict barriers to rotation – and tunneling motions, in general.[24]

Only one methyl substituent in 1,3-DMN causes splitting in the spectrum. Based on the angle, δ, between the methyl top axis and the *a* principal axis, 22.5°, the rotor at position 3 is responsible for the splitting. This assignment is consistent with theory, since the calculated barrier to rotation of the methyl substituent at position 1, 7.98 kJ mol^{-1}, is too high to expect this group to cause any splitting. The experimental height of the barrier to rotation of the methyl substituent at position 3 is 2.896 kJ mol^{-1}; since the methyl substituents are not as crowded as in 1,2-DMN, this value is in good agreement with the values predicted using both the relaxed and rigid approaches to barrier calculations, 2.68 of 2.78 kJ mol^{-1}, respectively.

6.4. Conclusions

The pure rotational spectra of four alkylnaphthalenes were measured in the range of 6-15 GHz. Density functional theory calculations gave accurately-predicted rotational constants, which aided in the assignments of the spectra. Methyl top-corrected inertial defects were found to be greater for 1,2- and 1,3-DMN than the singly methyl-substituted species, because the doubly methyl-substituted species have a greater number of low-lying out-of-plane vibrational modes. Barriers to internal rotation were derived, and they are consistent with relaxed barrier calculations. In particular, the spectroscopic fits confirm that the barrier for rotation of the methyl group at position 1 decreases with increased crowding, an unintuitive result of the environment becoming more isotropic. Finally, the four alkylnaphthalenes are moderately polar, so they are candidate species for rotational spectroscopic detection in Earth's atmosphere and in the ISM. Since the reported transitions are in the range of the Green Bank Telescope and the Arecibo Observatory, for example, they could facilitate further searches for specific PAHs in the ISM. Furthermore, extrapolation based on these low-*J* transitions could guide future laboratory measurements of transitions in the millimeter/sub-millimeter range of the Atacama Large Millimeter Array and other observatories.

References

1 Ravindra, K.; Bencs, L.; Wauters, E.; de Hoog, J.; Deutsch, F.; Roekens, E.; Bleux, N.; Berghmans, P.; Van Grieken, R. Seasonal and site-specific variation in vapour and aerosol

phase PAHs over Flanders (Belgium) and their relation with anthropogenic activities. *Atmos. Environ.* **2006**, *40*, 771-785.

2 Ravindra, K.; Sokhi, R.; Van Grieken, R. Atmospheric polycyclic aromatic hydrocarbons: Source attribution, emission factors and regulation. *Atmos. Environ.* **2008**, *42*, 2895-2921.

3 Slowik, J. G.; *et al.* An inter-comparison of instruments measuring black carbon content of soot particles. *Aerosol Sci. Technol.* **2007**, *41*, 295-314. See bibliography for complete list of authors.

4 Leyssale, J.-M.; Da Costa, J.-P.; Germain, C.; Weisbecker, P.; Vignoles, G. L. An image-guided atomistic reconstruction of pyrolytic carbons. *App. Phys. Lett.* **2009**, *95*, 231912 (3 pp.).

5 Chan, A. W. H.; Kautzman, K. E.; Chhabra, P. S.; Surratt, J. D.; Chan, M. N.; Crounse, J. D.; Kürten, A.; Wennberg, P. O.; Flagan, R. C.; Seinfeld, J. H. Secondary organic aerosol formation from photooxidation of naphthalene and alkylnaphthalenes: Implications for oxidation of intermediate volatility organic compounds (IVOCs). *Atmos. Phys. Chem.* **2009**, *9*, 3049-3060.

6 Riva, M.; Robinson, E. S.; Perraudin, E.; Donahue, N. M.; Villenave, E. Photochemical aging of secondary organic aerosols generated from the photooxidation of polycyclic aromatic hydrocarbons in the gas-phase. *Environ. Sci. Technol.* **2015**, *49*, 5407-5416.

7 Shakya, K. M.; Griffin, R. J. Secondary organic aerosol from photooxidation of polycyclic aromatic hydrocarbons. *Environ. Sci. Technol.* **2010**, *44*, 8134-8139.

8 Cohan, A.; Eiguren-Fernandez, A.; Miguel, A. H.; Dabdub, D. Secondary organic aerosol formation from naphthalene roadway emissions in the South Coast Air Basin of California. *Int. J. Environ. Pollut.* **2013**, *52*, 206-224.

9 Zhang, H.; Ying, Q. Secondary organic aerosol from polycyclic aromatic hydrocarbons in Southeast Texas. *Atmos. Environ.* **2012**, *55*, 279-287.

10 López-Puertas, M.; Dinelli, B. M.; Adriani, A.; Funke, B.; García-Comas, M.; Moriconi, M. L.; D'Aversa, E.; Boersma, C.; Allamandola, L. J. Large abundances of polycyclic aromatic hydrocarbons in Titan's upper atmosphere. *Astrophys. J.* **2013**, *770*, 132 (8 pp.).

11 Siebenmorgen, R.; Voshchinnikov, N. V.; Bagnulo, S. Dust in the diffuse interstellar medium. *Astron. Astrophys.* **2013**, *561*, A82 (18 pp.).

12 Van der Zwet, G. P.; Allamandola, L. J. Polycyclic aromatic hydrocarbons and the diffuse interstellar bands. *Astron. Astrophys.* **1985**, *146*, 76-70.

13 Vijh, U. P.; Witt, A. N.; Gordon, K. D. Discovery of blue luminescence in the red rectangle: Possible fluorescence from neutral polycyclic aromatic hydrocarbon molecules? *Astrophys. J.* **2004**, *606*, L65-L68.

14 Tielens, A. G. G. M. Interstellar polycyclic aromatic hydrocarbon molecules. *Annu. Rev. Astron. Astrophys.* **2008**, *46*, 289-337.

15 Thorwirth, S.; Theulé, P.; Gottlieb, C. A.; McCarthy, M. C.; Thaddeus, P. Rotational spectra of small PAHs: Acenaphthene, acenaphthylene, azulene, and fluorene. *Astrophys. J.* **2007**, *662*, 1309-1314.

16 Lovas, F. J.; McMahon, R. J.; Grabow, J.-U.; Schnell, M.; Mack, J.; Scott, L. T.; Kuczkowski, R. L. Interstellar chemistry: A strategy for detecting polycyclic aromatic hydrocarbons in space. *J. Am. Chem. Soc.* **2005**, *127*, 4345-4349.

17 McNaughton, D.; Godfrey, P. D.; Brown, R. D.; Thorwirth, S.; Grabow, J.-U. FT-MW and millimeter wave spectroscopy of PANHs: Phenanthridine, acridine, and 1,10-phenanthroline. *Astrophys. J.* **2008**, *678*, 309-315.

18 Duley, W. W.; Anming, H. The 217.5 nm band, infrared absorption, and infrared emission features in hydrogenated amorphous carbon nanoparticles. *Astrophys. J.* **2012**, *761*, 115 (16 pp.).

19 Tan, X.-Q.; Majewski, W. A.; Plusquellic, D. F.; Pratt, D. W. Methyl group torsional dynamics from rotationally resolved electronic spectra. 1- and 2-methynaphthalene. *J. Chem. Phys.* **1991**, *94*, 7721-7733.

20 Tan, X.-Q.; Clouthier, D. J.; Judge, R. H.; Plusquellic, D. F.; Tomer, J. L.; Pratt, D. W. Torsion-rotation interactions in a two-top molecule: High resolution $S_1 \leftarrow S_0$ electronic spectrum of 2,3-dimethylnaphthalene. *J. Chem. Phys.* **1991**, *95*, 7862-7871.

21 Xu, Y.; Van Wijngaarden, J.; Jäger, W. Microwave spectroscopy of ternary and quaternary van der Waals clusters. *Int. Rev. Phys. Chem.* **2005**, *24*, 301-338.

22 Xu, Y.; Jäger, W. Evidence for heavy atom large amplitude motions in RG-cyclopropane van der Waals complexes (RG=Ne, Ar, Kr) from rotation-tunneling spectroscopy. *J. Chem. Phys.* **1997**, *106*, 7968-7980.

23 Frisch, M. J.; *et al. Gaussian 09*, Rev. D.01; Gaussian, Inc.: Wallingford, CT, **2013**. See bibliography for complete list of authors.

24 Schnitzler, E. G.; Jäger, W. The benzoic acid-water complex: A potential atmospheric nucleation precursor studied using microwave spectroscopy and *ab initio* calculations. *Phys. Chem. Chem. Phys.* **2014**, *16*, 2305-2314.

25 Hanwell, M. D.; Curtis, D. E.; Lonie, D. C.; Vandermeersch, T.; Zurek, E.; Hutchison, G. R. Avogadro: An advanced semantic chemical editor, visualization, and analysis platform. *J. Cheminform.* **2012**, *4*, 17 (17 pp.).

26 Western, C. M. *PGOPHER, A Program for Simulating Rotational Structure*, University of Bristol: Bristol, UK. http://pgopher.chm.bris.ac.uk.

27 Hartwig, H.; Dreizler, H. The microwave spectrum of trans-2,3-dimethyloxirane in torsional excited states. *Z. Naturforsch.* **1996**, *51A*, 923-932.

28 Watson, J. K. G. Determination of centrifugal distortion coefficients of asymmetric-top molecules. *J. Chem. Phys.* **1967**, *46*, 1935-1949.

29 Oka, T. On negative inertial defect. *J. Mol. Struct.* **1995**, *352/353*, 225-233.

30 McNaughton, D.; Godfrey, P. D.; Brown, R. D.; Thorwirth, S. Millimetre wave spectroscopy of PANHs: Phenanthridine. *Phys. Chem. Chem. Phys.* **2007**, *9*, 591-595.

31 Tudorie, M.; Kleiner, I.; Jahn, M.; Grabow, J.-U.; Goubet, M.; Pirali, O. Coupled large amplitude motions: A case study of the dimethylbenzaldehyde isomers. *J. Phys. Chem. A* **2013**, *117*, 13636-13647.

32 Kassaee, M. H.; Keffer, D. J.; Steele, W. V. Theoretical calculation of thermodynamic properties of naphthalene, methylnaphthalenes, and dimethylnaphthalenes. *J. Chem. Eng. Data* **2007**, *52*, 1843-1850.

7 Aerosol instrumentation and smog chamber experiments for the investigation of secondary organic aerosol and soot aggregates

7.1. Introduction

In this chapter, I summarize how aerosol instrumentation can be used to study particle morphology and how photo-reaction ("smog") chambers can be used to study secondary organic aerosol (SOA) formation, resulting from condensation of photo-oxidation products, such as the carboxylic acids discussed in Chapters 3-5. In Section 7.2, I discuss the detection of particles, using a condensation particle counter, and the classification of particles by size, using a differential mobility analyzer, and mass, using a centrifugal particle mass analyzer – and how these instruments allow determination of particle morphology. In Section 7.3, I describe the smog chamber I used to investigate SOA, as well as the gas and particle losses that must be considered. In Section 7.4, I discuss the use of soot aggregates as seed particles in the smog chamber, in order to investigate internal mixtures of black carbon and SOA.

7.2. Aerosol instrumentation

The first step towards characterizing aerosol particles is counting them. Very small particles – for example, sub-10 nm particles resulting from homogeneous nucleation – have diameters much shorter than the wavelengths of visible light, and their size parameters, α, are much less than one, as calculated using Equation (7.1).[1]

$$\alpha = \frac{\pi d_p}{\lambda} \tag{7.1}$$

Here, d_p is the diameter of the particle, and λ is the wavelength of the incident light. Since $\alpha << 1$, the elastic light scattering of the particles is similar to that of gas molecules; specifically, Rayleigh scattering theory applies,[1,2] and the intensity of the scattered light is directly

proportional to d_p^6. Consequently, such small particles scatter very little light for optical detection.

In a condensation particle counter (CPC),[3,4] this problem is solved by passing particles through a heated region, saturated with water or *n*-butanol vapour, followed by a cooled region, leading to particle growth to about 10 μm by heterogeneous nucleation.[5] Downstream of the cooled region, the particles are passed through a nozzle and an optical detection region, consisting of a laser diode, focusing optics, a light stop, collecting optics, and a photo-detector. Since the laser diode is in the visible range, the size parameter of the 10 μm particles is much greater than one, so Mie scattering theory applies.[1,6] The 10 μm particles scatter significantly more light than sub-micrometre particles, facilitating measurements by the photo-detector. For carbonaceous particles, *n*-butanol is a better choice of condensing species than water, because the particles are hydrophobic.[5] The difference in temperatures of the saturator and condenser has to be chosen carefully to prevent homogenous nucleation of *n*-butanol, which would occur at very high saturation ratios. At a certain saturation ratio, S_r, the minimum size of particle, d_p^*, to nucleate the condensation of *n*-butanol and grow to larger sizes and be detected is calculated using the Kelvin equation – Equation (7.2).[7,8]

$$S = \frac{p}{p_s} = e^{\frac{4\gamma M}{\rho R T d_p^*}} \tag{7.2}$$

Here, p and p_s are the partial pressure and saturation vapour pressure, respectively, γ is the surface tension, M is the molar mass, and ρ is the liquid density. At the saturator and condenser temperatures of the Model 3771 CPC (TSI), the smallest particles to be detected with an efficiency of 50% are 10 nm in diameter. The maximum saturation ratio occurs at the centre of the condenser tubing. In the Model 3776 CPC (TSI), particles are confined to a narrow region about the centre of the condenser using sheath flow, so the smallest particles to be detected with an efficiency of 50% are 2.5 nm in diameter.

In Chapters 8 and 9, very low number concentrations were typically measured. At such low concentrations, counting a particle is a "rare event". Since each count is independent, a Poisson distribution dictates the particle counts, so the probability of obtaining a certain number of counts, x, in a certain sampling time can be calculated using Equation (7.3).[9]

$$f(x) = \frac{e^{-\bar{N}} \bar{N}^x}{x!} \tag{7.3}$$

Here, $\overline{N}$ is the mean number of counts measured. The standard error is the square root of $\overline{N}$. The relative error can be minimized by measuring more counts, simply because the denominator $\overline{N}$ increases more than the numerator $\overline{N}^{1/2}$. The particle concentration is the ratio of total number of counts to the total volume in the sampling period.

Particles can be classified by size using a differential mobility analyzer (DMA),[10,11] which consists of a vertical centre rod with a high applied negative voltage and an encompassing cylinder that is grounded. The electric field between the electrodes acts on positively-charged particles that enter at the top of the assembly, along the cylindrical electrode and separated from the inner electrode by clean, particle-free air, the sheath flow. At the bottom of the DMA, the majority of the flow is directed to the exhaust, but some (closest to the inner electrode) is sampled and directed to instrumentation downstream – a CPC, for example. In the radial direction, the electrostatic field is opposed by the drag force, which is often quantified in terms of electrical mobility, Z_p, calculated according to Equation (7.4).[12,13]

$$Z_p = neB_p \tag{7.4}$$

Here, n is the number of elementary charges, e, and B_p is the mechanical mobility, calculated according to Equation (7.5).[14,15]

$$B_p = \frac{V_{TS}}{F_D} = \frac{C_c(d_m)}{3\pi\mu d_m} \tag{7.5}$$

Here, V_{TS} is the terminal settling velocity, F_D is the drag force, C_c is the Cunningham slip correction factor at a particle mobility diameter, d_m, and μ is gas viscosity. The Cunningham slip correction factor accounts for the non-continuum experienced by particles with diameters approaching the mean free path of air. For example, at standard temperature and pressure (STP), 10 nm particles experience about 23 times less drag force than expected under the no-slip assumption, because they undergo short periods of "freefall", without collisions with the surrounding gas molecules.[14] Considering the geometry of the DMA, the electrical mobility classified can be calculated using Equation (7.6).[13]

$$Z_p = \frac{\left(Q_{in} - Q_{out}\right) \ln\left(\frac{r_2}{r_1}\right)}{2\pi VL} \tag{7.6}$$

Here, Q_{in} and Q_{out} are the flow rates defined by the initial and final radial positions (r_{in} and r_{out}, respectively) of the particles, r_1 and r_2 are the radii of the outer edge of the inner electron and the inner edge of the cylindrical electrode, V is the voltage, and L is the length of the DMA.

Particles within certain ranges of initial and final radial positions (and, most importantly, electrical mobilities) will be classified. The Model 3081 DMA (TSI) can classify particles with mobility diameters in the range of 10-1000 nm.

The charge of the particles dictates their electrical mobility,[12] as shown in Equation (7.4), so it is crucial to generate aerosol particles with a known and reproducible distribution of charges. Before the sample is injected to the DMA, then, it is passed through a small chamber with high concentrations of bipolar ions,[16,17] generated by X-ray bombardment (TSI, Model 3087). Once a particle collides with one positively charged ion, for instance, it is less likely to collide with another. The ions are in thermal equilibrium with the surrounding gas molecules, so their velocities are described by the Boltzmann distribution – Equation (2.13); consequently, ions with greater speeds may overcome the electrostatic repulsion and collide with the particle. On the other hand, collisions with negatively-charged ions will become more likely. Eventually, these collisions result in a near equilibrium Boltzmann charge distribution, and the fraction of particles at a certain size with a particular charge might be expected to be described by Equation (7.7).[12]

$$f(n) = \frac{e^{\frac{-k_E n^2 e^2}{d_p k_B T}}}{\sum_{n=-\infty}^{\infty} e^{\frac{-k_E n^2 e^2}{d_p k_B T}}} \tag{7.7}$$

Here, k_E is the Coulomb constant, k_B is the Boltzmann constant, and T is temperature. In fact, the charge distribution is not perfectly symmetrical about zero, because negative ions have slightly greater mobilities than positive ions. A thorough treatment of the ion-mobility-corrected charge distribution can be done only numerically;[18] an approximate parameterization is also available.[19] Larger particles can sustain higher charges than smaller particles; the fraction of their population with no charge is significantly lower. For example, 99% of 10 nm particles are neutral, but only 4% of 10 μm particles are neutral.

Equation (7.4) also shows that a particle with half the mechanical mobility of another may have the same electrical mobility if it has twice the charge. Removing particles larger than 1 μm before they enter the DMA is essential to measuring size distributions, because particles then measured just below 1 μm are sure to have a single charge and be of the correct mechanical mobility. The fraction of these particles that will appear at lower sizes, because they have two charges, is known. Consequently, the measured particle concentrations can be attributed to the

correct mechanical mobilities and, in turn, particle diameters. The large particles are removed using an impactor connected to the inlet of the DMA. An impactor consists of a nozzle and a downstream plate. A sample of gas molecules and aerosol particles are accelerated through the nozzle. Particles with significant inertia will not follow the streamlines of the gas molecules and instead collide with the plate. The aerodynamic diameter at which 50% of the particles collide with the plate, $d_a^{\perp}$, is given by Equation (7.8).[20]

$$d_a^{\perp} = \left(\frac{9\pi\mu D_j^3 Stk_{50}}{4\rho_p Q C_c(d_a^{\perp})} \right)^{1/2} \tag{7.8}$$

Here, D_j is the diameter of the nozzle, Stk_{50} is the Stokes number (also called the impaction parameter) for 50% impaction, ρ_p is particle density (assumed to be 1 g cm^{-3} for the definition of the aerodynamic diameter), and Q is flow rate through the nozzle. The Stokes number is the ratio of the particle stopping distance to the nozzle radius. Because the Cunningham slip correction factor depends on particle diameter, Equation (7.8) must be solved iteratively, until the particle diameter converges.[20] Following impaction, liquid particles are more prone to remain deposited on the plate than solid particles, so particle bounce can be used as a measure of particle phase.[21] (In passing, I mention a parallel between scattering and inertial impaction. As discussed above, in a CPC, condensation is used to grow particle to sizes at which they can be detected using elastic light scattering. Similarly, in a particle-into-liquid sampler, condensation is used to grow particles to masses at which they can be impacted and sampled in solution.[22])

In Chapter 8, particles are also classified by mass, using a centrifugal particle mass analyzer (CPMA),[23,24] which is similar in design to an aerosol particle mass (APM) analyzer.[25] Both the APM and CPMA operate analogously to the DMA, except that the electrical force is balanced by centrifugal force, instead of drag force. To produce the centrifugal force, the electrodes are rotated, and particles that enter the annulus between the electrodes experience an apparent force towards the outer electrode. Charged particles also experience an electrical force towards the inner electrode. In an APM analyzer, the electrodes are rotated with the same angular velocity, so the centrifugal force across the annulus changes with the square of the distance from the particle to the axis of rotation, r^2, while the electrical force changes with $1/r$. Consequently, even particles of the correct mass-to-charge ratio may not be transmitted by the APM analyzer, if they do not enter the annulus at the ideal radial position. If they enter too far

away from the centre electrode, the centrifugal force dominates, and they will deposit on the outer electrode. If they enter too close to the inner electrode, the electrical force dominates, and they will deposit on the inner electrode. In the CPMA, the mismatched scaling of centrifugal and electrical forces is solved by rotating the inner cylinder faster than the outer cylinder.[23] This results in much better particle transmission in the CPMA than the APM analyzer. Since the electrical force is involved, the above discussion of charging also applies to the CPMA. One difference between the two instruments with regards to charging is how uncharged particles behave. In the DMA, particle must change they radial position significantly, from along the outer electrode to along the inner electrode, to be classified. Uncharged particles are not acted upon by the electrical force, so they do not change they radial position and are not classified. In the CPMA, particles must *not* change their radial position significantly to be classified. As a result, uncharged particles may be transmitted if the centrifugal force is small – in particular, at low angular velocity and low particle mass. This is why, during the measurements discussed in Chapter 8, it was critical to avoid nucleation, which would produce many small particles that interfere with monitoring the growth of the pre-existing particles of interest.

The DMA and CPMA are particularly powerful when implemented together, because measurements of particle size and mass allow quantification of particle morphology. The measures of morphology used in Chapters 8 and 9 include the following: dynamic shape factor, χ, effective density, ρ_{eff}, and mass-mobility exponent, D_{m}. Dynamic shape factor is the ratio of the measured drag force on an actual particle to the calculated drag force on a hypothetical particle that is an equivalent volume sphere. Since both forces take the form of Equation (7.5), the terms not involving particle diameter cancel out, allowing the shape factor to be calculated from the mobility and volume-equivalent diameters (d_{m} and d_{ve}, respectively), according to Equation (7.9).[14]

$$\chi = \frac{d_{\text{m}} C_{\text{c}}(d_{\text{ve}})}{d_{\text{ve}} C_{\text{c}}(d_{\text{m}})} \tag{7.9}$$

Here, $C_{\text{c}}(d_{\text{m}})$ and $C_{\text{c}}(d_{\text{ve}})$ are the Cunningham slip corrections at d_{m} and d_{ve}, respectively. For a homogeneous particle, the volume-equivalent diameter can be calculated from the mass, m_{p}, measured directly using the CPMA, and material density, ρ_{p}, according to Equation (7.10).

$$d_{\text{ve}} = \left[\frac{6}{\pi}\left(\frac{m_{\text{p}}}{\rho_{\text{p}}}\right)\right]^{1/3} \tag{7.10}$$

For non-spherical particles, χ is greater than one. Even for spherical particles, χ may be greater than one if they are porous. Alternatively, an effective density, ρ_{eff}, can also be defined for a hypothetical spherical particle with mass m_{p} and mobility diameter d_{m}, according to Equation (7.11).

$$\rho_{\text{eff}} = \frac{6m_{\text{p}}}{\pi {d_{\text{m}}}^3} \tag{7.11}$$

For non-spherical particles, ρ_{eff} will always be lower than the density of the material. For example, the material density of soot is about 2 g cm^{-3}, but a typical effective density of a soot aggregate is about 0.7 g cm^{-3}. Finally, for a given morphology, particle mass scales with mobility diameter to a certain exponent, as shown in Equation (7.12).[26]

$$m_{\text{p}} = C_{\text{p}} {d_{\text{m}}}^{D_{\text{m}}} \tag{7.12}$$

Here, C_{p} is a pre-exponential factor, and D_{m} is the mass-mobility exponent. For spherical particles, porous or otherwise, D_{m} is three; the lower the value of D_{m}, the more fractal the particles. The morphology of soot aggregates, and its evolution due to coatings, is discussed further in Chapter 8.

7.3. Investigating secondary organic aerosol in smog chambers

Secondary organic aerosol (SOA) forms in the atmosphere in two steps. The first step, oxidation of volatile organic compounds (VOCs) by an oxidant, like hydroxyl radical or ozone, is discussed in Chapter 1. The resulting low vapour pressure products partition between the gas and particle phases. The theory of gas-to-particle partitioning was first derived in terms of a partitioning constant, K_{om}, which is inversely proportional to the saturation vapour pressure, based on Raoult's Law and the mole ratio of species i in the particle phase.[42] A revised treatment, based on the molality of species i in the particle phase, was later proposed in terms of an effective saturation concentration, C_i^*, according to Equation (7.13).[51]

$$C_i^* = \frac{10^6 M_i \varsigma_i p_{\text{s},i}}{760RT} \tag{7.13}$$

Here, M_i is the molecular mass, ς_i is the molality-based activity coefficient, $p_{\text{s},i}$ is the saturation vapour pressure at temperature, T. Since effective saturation concentration is directly proportional to saturation vapour pressure, low volatility oxidation products partition

significantly into the particle phase. The mass fraction of species *i* in the aerosol phase, F_i, can be determined using Equation (7.14).[51]

$$F_i = \left(1 + \frac{C_i^*}{C_{\mathrm{OA}}}\right)^{-1} \tag{7.14}$$

Here, C_{OA} is the organic aerosol mass concentration.

In the laboratory, the formation of SOA from the photo-oxidation of volatile organic compounds (VOCs) is often investigated using smog chamber experiments.[27,28] The smog chamber at the University of Alberta is a 1.8 m^3 cubic chamber constructed of 0.127 mm thick perfluoroalkoxy (PFA) film (Ingeniven Fluoropolymer Solutions) and supported in an aluminum enclosure.[29] Type T (copper-constantan) thermocouples, connected to an interface card (TCIC), measure temperatures of five faces of the chamber. Additionally, a probe (Omega, iSeries) measures the temperature and relative humidity inside the chamber. This probe is periodically baked to remove contaminants; otherwise, relative humidity measurements slowly drift up. An array of twenty-four 32 W fluorescent black lights, with peak emission at 350 nm, are arranged on three faces of the chamber. Fans are situated in the chamber and at the top and bottom of the enclosure to remove heat. PFA tubing is used at the chamber inlets; stainless steel tubing is used at the outlet. SOA precursors are introduced into the chamber from a bubbler, where filtered, dry air flows over the liquid hydrocarbons.

Hydrocarbon gas concentrations are measured using ultra-violet differential optical absorption spectroscopy (UV-DOAS).[30] Briefly, UV-DOAS involves fitting a polynomial to an absolute absorption spectrum, subtracting the fit from the spectrum, and scaling the resulting differential spectrum to a reference differential spectrum derived from the cross section of the species of interest. The light source is a broadband deuterium lamp with emission output from 215–400 nm (Ocean Optics, D-2000-S). An optical fiber and a collimating lens are used to direct UV light from the deuterium lamp through the chamber. Likewise, a collecting lens and an optical fiber are used to direct UV light to the spectrometer (Ocean Optics, HR-2000+). The deuterium lamp and the UV spectrometer are positioned outside the aluminum enclosure of the photo-reaction chamber and maintained at a temperature of about 294 K. Consequently, spectra are measured *in situ* over a path length of 1.2 m, a single pass through the chamber. Background spectra are collected for filtered, dry air at the start of each experiment and subsequently subtracted from the sample spectra. Absorption spectra are averages of 1500 samples, collected

over one minute; they are transformed to differential optical absorption spectra using a ninth order polynomial, as shown in Figure 7.1. The differential optical absorption spectra were scaled to high-resolution differential spectra, based on absorption cross sections from the literature, using an iterative least-squares fitting routine.

The SOA yield is the ratio of the mass concentration of SOA formed to the mass concentration of VOC reacted.[31] However, determining these concentrations is complicated by several loss processes. For example, not all of the change VOC concentration is due to reaction. If the chamber volume is to be maintained, clean, dry make-up air must be used, resulting in dilution of the VOC. The dilution rate constant, k_{dil}, is directly proportional to flow rate and indirectly proportional to chamber volume. (In passing, I mention that this volume dependence allows precise determination of the chamber volume by measuring the rates of exponential decay in gas concentrations due to dilution at two different flow rates.) Gases may also be lost to the walls. The wall loss rate constant, k_w, can be determined by simply measuring gas concentrations in the sealed chamber; for the aromatics used in Chapters 8 and 9, it is

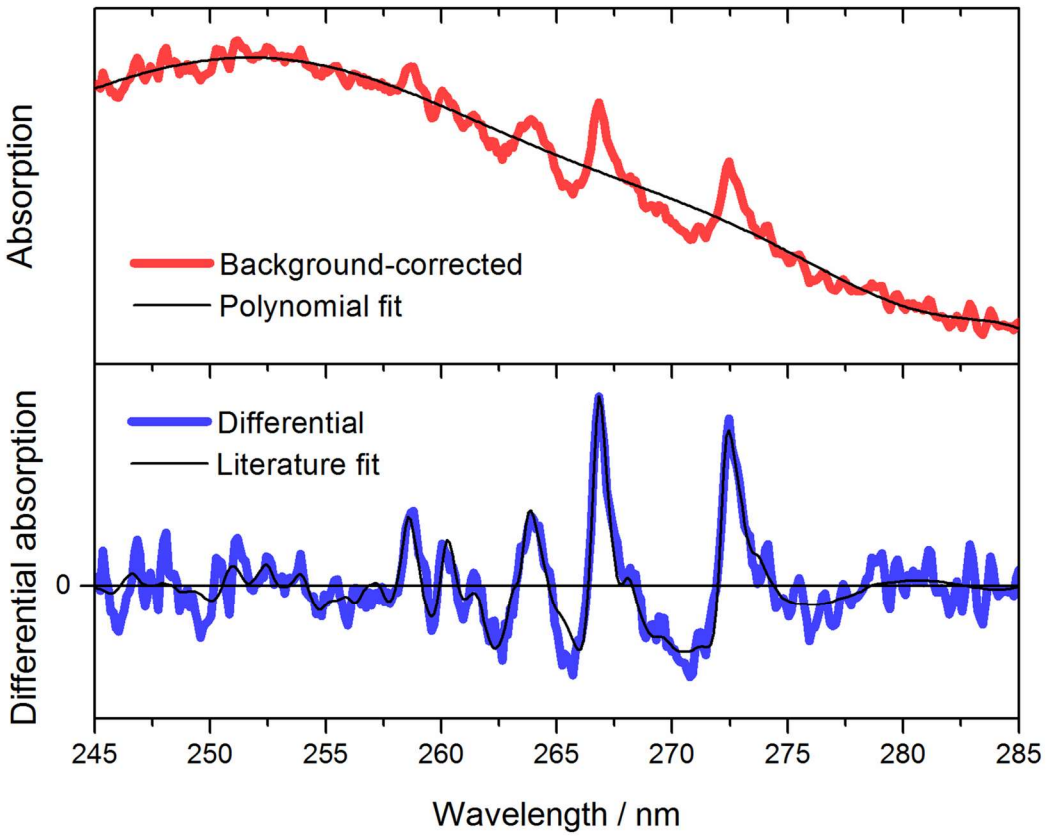

Figure 7.1. UV-DOAS measurement for a mixture of toluene and *p*-xylene.

insignificant. The reaction rate constant, k_{HC}, can be determined by subtracting k_{dil} and k_w from the total rate constant of the observed exponential decay in VOC concentration. Though the photo-oxidation of aromatics by hydroxyl radical is a second-order reaction, the concentration of hydroxyl radical in the chamber is constant, so it can be estimated from k_{HC}, a first-order rate constant, and the second-order rate constant from the literature.[32] Since three first-order processes occur in parallel, the amount of VOC reacted can be calculated using Equation (7.15).

$$\Delta HC = \frac{k_{HC}}{k_{dil} + k_w + k_{HC}} HC_0(1 - \exp[-(k_{dil} + k_w + k_{HC})t]) \quad (7.15)$$

Here, HC_0 is the initial hydrocarbon concentration, and t is reaction time. This correction is also discussed in Chapter 8 and illustrated in Figure 8.3.

Similarly, particles are lost due to dilution and deposition to the chamber walls. (Deposition to the stainless steel sampling tubing is negligible for large particles, which account for nearly all the particle mass.) The dilution rate constant for particles is the same as for gases; however, the wall loss rate constant is much greater. Particles are lost to the walls by both diffusion and settling. As shown in Equation (7.16), the diffusion coefficient is inversely proportional to mobility diameter, if the slip correction is neglected.

$$D = \frac{k_B T C_c(d_m)}{3\pi\mu d_m} \quad (7.16)$$

Thus, small particles diffuse to the walls faster than large particles. In contrast, the terminal settling velocity is directly proportional to the particle diameter squared, as shown in Equation (7.17).[14]

$$V_{TS} = \frac{g\rho_p {d_m}^2 C_c(d_m)}{18\mu} \quad (7.17)$$

Here, g is the gravitational constant. Thus, large particles settle faster than small particles. I have measured size dependent rate constants by injecting a broad distribution of ammonium sulfate particles and monitoring each size bin's exponential decay.[33] Unfortunately, if the chamber volume changes between experiments, the rate constants are no longer valid, so it is more common to determine a size-independent rate constant for each experiment by monitoring the exponential decay in particle mass (or volume) at the end of each photo-oxidation experiment when less than 10% of the precursor concentration remains, as shown in Figure 7.2.[34] With so little precursor still present, it is fair to assume no additional SOA forms, so the decay reflects only particle losses due to dilution and deposition. A linear regression of the natural logarithm

of particle mass verses time gives a slope equal to the sum of the rate constants. As long as the chamber volume is constant during the experiment, this rate constant can be applied to the entire duration, as shown in Equation (7.18).

$$\Delta SOA = M_{\mathrm{p}}(t) + (k_{\mathrm{dil}} + k_{\mathrm{dep}}) \int_0^t M_{\mathrm{p}}(t)\mathrm{d}t - M_{\mathrm{p,i}} \qquad (7.18)$$

Here, $M_{\mathrm{p,i}}$ is the initial aerosol mass, in the event that seed particles are used, as described below. An SOA yield can be calculated from the corrected precursor and particle concentrations.

Typically, in smog chamber experiments requiring dilution, either for injection of oxidant[35] or maintaining volume of the chamber,[36] only precursor hydrocarbon and SOA concentrations are corrected for dilution, as described above; however, the oxidation products in the gas phase are diluting simultaneously. If no dilution occurred, these products would go on to partition into the aerosol phase, so the above level of correction results in a lower limit of the SOA yield. (Condensable products are also lost due to deposition to the chamber walls.

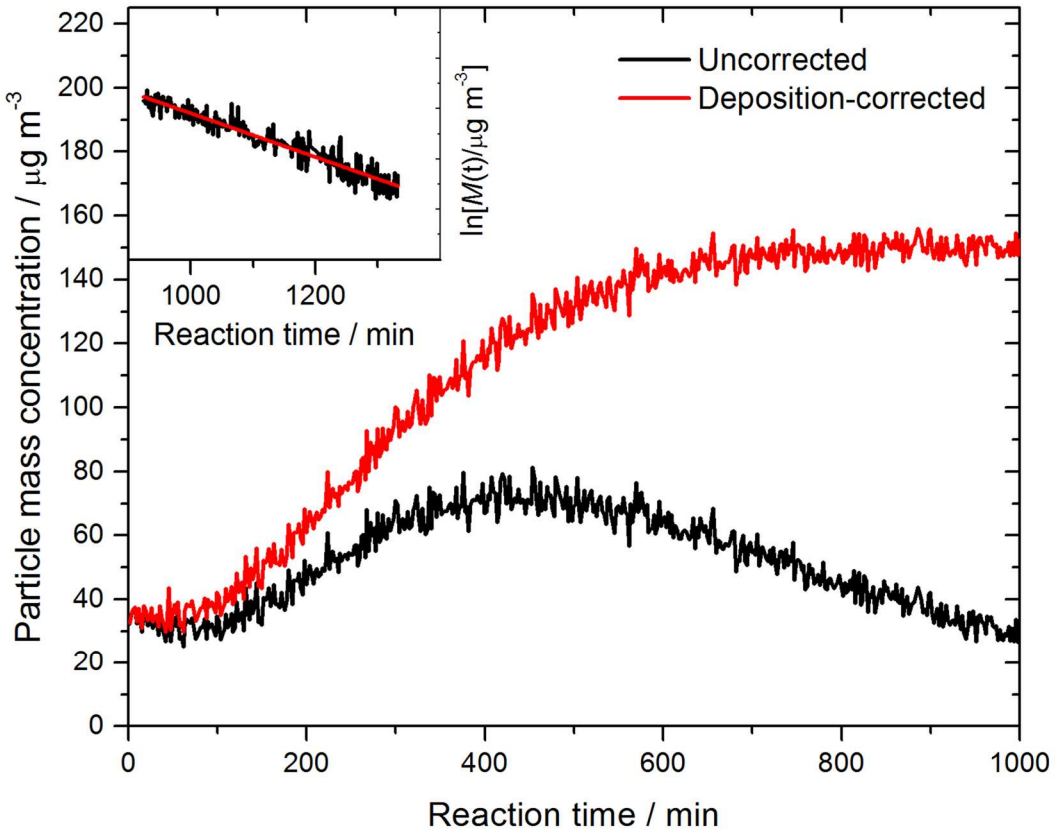

Figure 7.2. Determination of ($k_{\mathrm{dil}} + k_{\mathrm{dep}}$) from a linear fit to the natural logarithm of particle mass concentration following the reaction of 90% of the precursor (inset); particle mass concentration before and after correcting for aerosol dilution and deposition.

Correcting for this loss is the subject of entire studies,[37,38] and it will not be discussed here. Experimentally, wall losses of products can be minimized by introducing seed particles into the chamber – for example, using a home-built Laskin aerosol generator containing a dilute aqueous solution of ammonium sulfate.[39]) A simple conceptual mechanism, in place of an explicit chemical mechanism like that shown in Figure 1.1, can be fit to the raw measurements of hydrocarbon and aerosol concentrations to account for these additional losses. For example, the following mechanism describes SOA formation from photo-oxidation of *p*-xylene: the precursor reacts to form a volatile first-generation product, which reacts to form a condensable second-generation product that partitions reversibly into the organic aerosol phase, as shown in Figure 7.3.[40,41] All gas-phase species are lost to dilution; in addition to diluting and reacting, precursor hydrocarbon is allowed to deposit on the chamber walls, though k_w is negligible. The second-generation product in the particle phase, A_2^p, is lost to dilution and deposition on the chamber walls. Rate constants of all losses are constrained to experimental values, described above. The

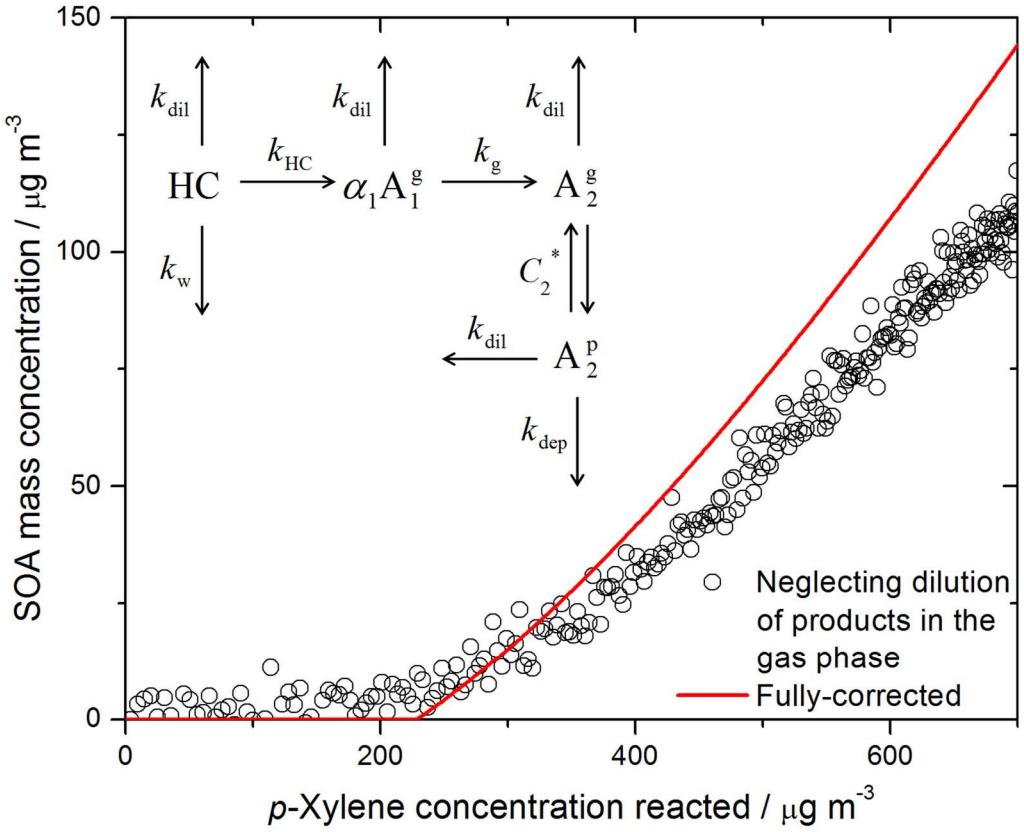

Figure 7.3. Conceptual kinetics and equilibrium model for SOA formation from *p*-xylene; SOA mass concentrations determined when correcting for losses of precursor and particles, but not losses of oxidation products in the gas phase due to dilution, and when correcting for all losses included in the mechanism.

equilibrium concentration of the second-generation product in the gas phase, $[A_2^g]_{eq}$, can be calculated from gas-to-particle partition theory, using Equation (7.19).[40]

$$[A_2^g]_{eq} = \frac{C_2^*[A_2^p]}{\Delta M_o} \tag{7.19}$$

Here, ΔM_o is the change in the organic aerosol mass concentration. Since the seed particles are inorganic, and product A_2 is the only source of organic aerosol, ΔM_o is technically equivalent to $[A_2^p]$; however, to avoid an undefined $[A_2^g]_{eq}$ at the beginning of the experiment, when $[A_2^p]$ is zero, an initial organic aerosol mass of 0.1 ng m^{-3} can be entered as input. This pretended mass is negligible compared to actual aerosol mass once it begins to form, so, for all practical purposes, $[A_2^g]_{eq} = C_2^*$. Thus, a constant value of $[A_2^g]$ occurs following the onset of SOA formation, as shown in Figure 7.4. Once the reaction and equilibrium parameters are fitted, the loss rate constants can be set to zero to determine the SOA mass concentration is the absence of

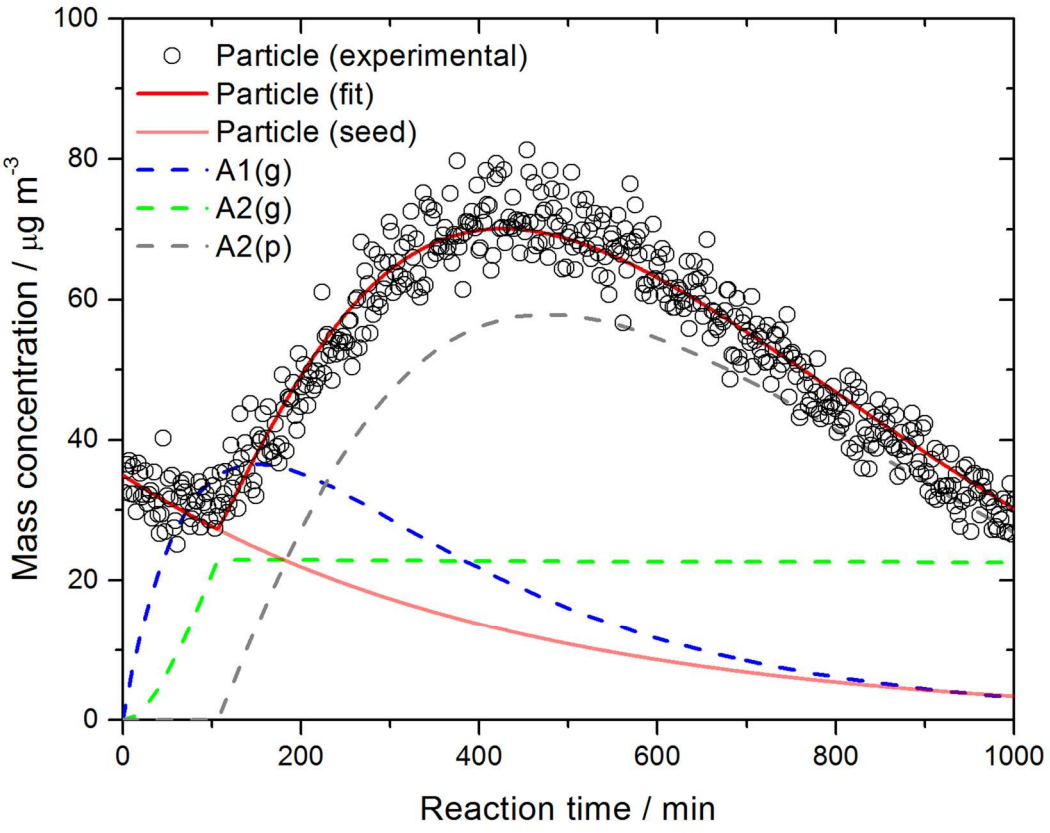

Figure 7.4. Reaction profiles for species in the conceptual kinetics and equilibrium model for SOA formation from *p*-xylene.

those losses. As shown in Figure 7.3, the result is higher than obtained by correcting for losses of only the precursor and SOA.

7.4. Investigating internal mixtures of soot and secondary organic aerosol

In some cases, seed particles may be introduced into the chamber not simply to provide suspended surface area, but to determine the effects of SOA on the seed particles themselves. For example, SOA affects the morphology and optical properties of soot particles.[43] In the experiments described in Chapters 8 and 9, soot aggregates were generated using a flat-flame McKenna burner (Holthuis),[44,45] in which pre-mixed ethylene and air are passed through a water-cooled plug of sintered bronze, and nitrogen as shroud gas is passed through an outer ring of sintered bronze. The morphology of the emitted soot aggregates depends on the combustion conditions of the burner,[46] in particular the equivalence ratio, ϕ, which is the ratio of the actual fuel-to-air mole (or mass) ratio to the stoichiometric fuel-to-air mole (or mass) ratio. For the combustion of ethylene, the stoichiometric fuel-to-oxygen mole ratio is 0.33, so the stoichiometric fuel-to-air mole ratio is 0.07. At a high equivalence ratio (3.75), about 80% of the mass of particles with diameters between 100 and 250 nm is volatile organic carbon.[46] At an equivalence ratio of two, this percentage decreases to about 20% over the same size range,[46] so this ratio was used in Chapters 8 and 9. To obtain an equivalence ratio of two, the actual fuel-to-air mole ratio must be 0.14, so the flow rate of air must be about seven times greater than that of ethylene.

To remove the small fraction of remaining volatile organic carbon, soot aggregates are passed through a thermo-denuder (TD),[47,48] which consists of a heating section and a cooling section. In the heating section, at a temperature of 473-573 K, even compounds with very low vapour pressures partition into the gas phase. With an adequate residence time, phase equilibrium at the elevated temperature is established.[48] If ingoing soot aggregates with a certain coating mass are transmitted by the TD with the same mobility diameter (or mass) at two flow rates, the residence time even at the higher flow rate is long enough to allow equilibration. In the cooling section, the equilibrium is shifted back towards the condensed phase. In principle, the vapours condense onto both the particles and the TD walls. However, the rate of diffusion to the walls is much greater than the rate of diffusion to the particles, particularly when the

number of particles is low, and their diameter is small.[47] As a result, the soot particles transmitted through the TD are effectively bare.

If an SOA coating forms on the soot aggregates in the smog chamber without the addition of a precursor, it is likely that volatile organic compounds emitted from the burner are being oxidized in the chamber. A counter-flow parallel-plate membrane denuder (CPMD) can be used to remove these trace gases.[49,50] A CPMD separates gases and particles based on their diffusion coefficients. It consists of three parallel rectangular chambers separated by a hydrophobic membrane. Just as water flows counter to heated vapour in a laboratory condenser during distillation, in order to maintain a steady temperature gradient, purge air in the top and bottom chambers flows counter to sample flow in the centre chamber in the CPMD, in order to maintain a steady concentration gradient. The ingoing and outgoing flow rates of each chamber are matched precisely to prevent convective flow between chambers. Both particles and gases diffuse from the sample chamber towards the sheath flow chambers, but the gases diffuse much more quickly, allowing them to pass through the membrane to enter the sheath chambers, given a certain residence time. The total outgoing gas concentration (exiting sample and sheath chambers) is the same as the ingoing concentration, so trace gases are indeed removed by diffusion, rather than adsorption to the chamber walls or membranes.

References

1 Hinds, W. C. Optical properties. *Aerosol Technology: Properties, Behavior, and Measurement of Airborne Particles*, 2nd ed.; Wiley: New York, 1999; pp. 349-378.

2 Seinfeld, J. H.; Pandis, S. N. Radiative effects of atmospheric aerosols: Visibility and climate. *Atmospheric Chemistry and Physics: From Air Pollution to Climate Change*; Wiley: New York, 1998; pp. 1113-1192.

3 Agarwal, J. K.; Sem, G. J. Continuous flow single-particle-counting condensation nuclei counter. *J. Aerosol Sci.* **1980**, *11*, 343-357.

4 Sinclair, D.; Hoopes, G. S. A continuous flow nucleus counter. *J. Aerosol Sci.* **1975**, *6*, 1-7.

5 Hinds, W. C. Condensation and evaporation. *Aerosol Technology: Properties, Behavior, and Measurement of Airborne Particles*, 2nd ed.; Wiley: New York, 1999; pp. 278-303.

6 Mie, G. Beiträge zur optik trüber medien, speziell kolloidaler metallösungen. *Ann. Phys.* **1908**, *330*, 377-445.

7 Thomson, W. On the equilibrium of vapour at a curved surface of liquid. *Proc. Roy. Soc. Edinb.* **1870**, *7*, 63-68.

8 Seinfeld, J. H.; Pandis, S. N. Thermodynamics of aerosols. *Atmospheric Chemistry and Physics: From Air Pollution to Climate Change*; Wiley: New York, 1998; pp. 491-544.

9 Fornasini, P. Distribution of Random Variable. *The Uncertainty in Physical Measurements: An Introduction to Data Analysis in the Physics Laboratory*; Springer: New York, 2008; pp. 94-133.

10 Knutson, E. O.; Whitby, K. T. Aerosol classification by electric mobility: Apparatus, theory, and applications. *J. Aerosol Sci.* **1975**, *6*, 443-451.

11 Fissan, H. J.; Helsper, C.; Thielen, H. J. Determination of particle size distribution by means of an electrostatic classifer. *J. Aerosol Sci.* **1983**, *14*, 354-357.

12 Hinds, W. C. Electrical properties. *Aerosol Technology: Properties, Behavior, and Measurement of Airborne Particles*, 2nd ed.; Wiley: New York, 1999; pp. 316-348.

13 Flagan, R. C. Electrical mobility methods for submicrometer particle characterization. In *Aerosol Measurement: Principles, Techniques, and Applications*; Kulkarni, P.; Baron, P. A.; Willeke, K., Eds.; Wiley: New York, 2011; pp. 339-364.

14 Hinds, W. C. Uniform particle motion. *Aerosol Technology: Properties, Behavior, and Measurement of Airborne Particles*, 2nd ed.; Wiley: New York, 1999; pp. 42-74.

15 Seinfeld, J. H.; Pandis, S. N. Dynamics of single aerosol particles. *Atmospheric Chemistry and Physics: From Air Pollution to Climate Change*; Wiley: New York, 1998; pp. 452-490.

16 Fuchs, N. A. On the stationary charge distribution on aerosol particles in a bipolar ionic atmosphere. *Geophys. Pura. Appl.* **1963**, *56*, 185-193.

17 Adachi, M.; Okuyama, K.; Kousaka, Y. Electrical neutralization of charged aerosol particles by bipolar ions. *J. Chem. Eng. Japan* **1983**, *16*, 229-235.

18 Fuchs, N. A. On the stationary charge distribution on aerosol particles in a bipolar ionic atmosphere. *Geofis. Pura Appl.* **1963**, *56*, 185-193.

19 Wiedensohler, A. An approximation of the bipolar charge distribution for particles in the submicron size range. *J. Aerosol Sci.* **1988**, *19*, 387-389.

20 Hinds, W. C. Straight-line acceleration and curvilinear particle motion. *Aerosol Technology: Properties, Behavior, and Measurement of Airborne Particles*, 2nd ed.; Wiley: New York, 1999; pp. 111-140.

21 Virtanen, A.; *et al.* An amorphous solid state of biogenic secondary organic aerosol particles. *Nature* **2010**, *467*, 824-827. See bibliography for complete list of authors.

22 Weber, R. J.; Orsini, D.; Daun, Y.; Lee, Y.-N.; Klotz, P.; Brechtel, F. A particle-into-liquid collector for rapid measurements of aerosol chemical composition. *Aerosol Sci. Technol.* **2001**, *35*, 718-727.

23 Olfert, J. S.; Collings, N. New method for particle mass classification – the Couette centrifugal particle mass analyzer. *J. Aerosol Sci.* **2005**, *36*, 1338-1352.

24 Olfert, J. S.; Reavell, K. St. J.; Rushton, M. G.; Collings, N. The experimental transfer function of the Couette centrifugal particle mass analyzer. *J. Aerosol Sci.* **2006**, *37*, 1840-1852.

25 Ehara, K.; Hagwood, C.; Coakley, K. J. Novel method to classify aerosol particles according to their mass-to-charge ratio – aerosol particle mass analyser. *J. Aerosol Sci.* **1996**, *27*, 217-234.

26 Park, K.; Cao, F.; Kittelson, D. B.; McMurry, P. H. Relationship between particle mass and mobility for diesel exhaust particles. *Environ. Sci. Technol.* **2003**, *37*, 577-583.

27 Borrás, E.; Torajada-Genaro, L. A. Secondary organic aerosol formation from the photo-oxidation of benzene *Atmos. Environ.* **2012**, *47*, 154-163.

28 Ng, N. L.; Kroll, J. H.; Chan, A. W. H.; Chhabra, P. S.; Flagan, R. C.; Seinfeld, J. H. Secondary organic aerosol formation from *m*-xylene, toluene, and benzene. *Atmos. Chem. Phys.* **2007**, *7*, 3909-3922.

29 Parsons, M. T.; Sydoryk, I.; Lim, A.; McIntyre, T. J.; Tulip, J.; Jäger, W.; McDonald, K. Real-time monitoring of benzene, toluene, and *p*-xylene in a photoreaction chamber with a tunable mid-infrared laser and ultraviolet differential optical absorption spectroscopy. *Appl. Opt.* **2011**, *50*, A90-A99.

30 Plane, J. M. C.; Saiz-Lopez, A. UV-Visible Differential Optical Absorption Spectroscopy. In *Analytical Techniques for Atmospheric Measurement*; Heard, D. E., Ed.; Blackwell: Cambridge, MA, 2006; pp. 147-188.

31 Odum, J. R.; Hoffmann, T.; Bowman, F.; Collins, D.; Flagan, R. C.; Seinfeld, J. H. Gas/particle partitioning and secondary organic aerosol yields. *Environ. Sci. Technol.* **1996,** *30*, 2580-2585.

32 Atkinson, R.; Arey, J. Atmospheric degradation of volatile organic compounds. *Chem. Rev.* **2003**, *103*, 4605-4638.

33 Takekawa, H.; Minoura, H.; Yamazaki, S. Temperature dependence of secondary organic aerosol formation by photo-oxidation of hydrocarbons. *Atmos. Environ.* **2003**, *37*, 3413-3424.

34 Pathak, R. K.; Stanier, C. O.; Donahue, N. M.; Pandis, S. N. Ozonolysis of *α*-pinene at atmospherically relevant concentrations: Temperature dependence of aerosol mass fractions (yield). *J. Geophys. Res.* **2007**, *112*, D03201 (8 pp.).

35 Hao, L. Q.; *et al.* Mass yields of secondary organic aerosols from the oxidation of alpha-pinene and real plant emissions. *Atmos. Chem. Phys.* **2011,** *11*, 1367-1378. See bibliography for complete list of authors.

36 Kelly, J. L.; Michelangeli, D. V.; Makar, P. A.; Hastie, D. R.; Mozurkewich, M.; Auld, J. Aerosol speciation and mass prediction from toluene oxidation under high NO_x conditions. *Atmos. Environ.* **2010,** *44*, 361-369.

37 Zhang, X.; Cappa, C. D.; Jathar, S. H.; McVay, R. C.; Ensberg, J. J.; Kleeman, M. J.; Seinfeld, J. H. Influence of vapor wall loss in laboratory chambers on yields of secondary organic aerosol. *Proc. Natl. Acad. Sci. U. S. A.* **2014**, *111*, 5802-5807.

38 Zhang, X.; Schwantes, R. H.; McVay, R. C.; Lignell, H.; Coggon, M. M.; Flagan, R. C.; Seinfeld, J. H. Vapor wall deposition in Teflon chambers. *Atmos. Chem. Phys.* **2015**, *15*, 4197-4214.

39 Drew, R. T.; Berstein, D. M.; Laskin, S. The Laskin aerosol generator. *J. Toxicol. Environ. Health* **1978**, *4*, 661-670.

40 Kroll, J. H.; Chan, A. W. H.; Ng, N. L.; Flagan, R. C.; Seinfeld, J. H. Reactions of semivolatile organics and their effects on secondary organics aerosol formation. *Environ. Sci. Technol.* **2007**, *41*, 3545-3550.

41 Chan, A. W. H.; Kroll, J. H.; Ng, N. L.; Seinfeld, J. H. Kinetic modeling of secondary organic aerosol formation: Effects of particle- and gas-phase reactions of semivolatile products. *Atmos. Chem. Phys.* **2007**, *7*, 4135-4147.

42 Pankow, J. F. An absorption model of gas-particle partitioning of organic compounds in the atmosphere. *Atmos Environ* **1994,** *28*, 185-188.

43 Peng, J.; *et al.* Markedly enhanced absorption and direct radiative forcing of black carbon under polluted urban environments. *Proc. Natl. Acad. U. S. A.* **2016**, doi: 10.1073/ pnas.1602310113. See bibliography for complete list of authors.

44 Olofsson, N.-E.; Bladh, H.; Bohlin, A.; Johnsson, J.; Bengtsson, P.-E. Are sooting premixed porous-plug burner flames one-dimensional? A laser-based experimental investigation. *Combust. Sci. Technol.* **2013**, *185*, 293-309.

45 Migliorini, F.; De Iuliis, S.; Cignoli, F.; Zizak, G. How "flat" is the rich pre-mixed flame produced by your McKenna burner? *Combust. Flame* **2008**, *153*, 384-393.

46 Ghazi, R.; Tjong, H.; Soewono, A.; Rogak, S. N.; Olfert, J. S. Mass, mobility, volatility, and morphology of soot particles generated by a McKenna and inverted burner *Aerosol Sci. Technol.* **2013**, *47*, 395-405.

47 Saleh, R.; Shihadeh, A. Hygroscopic growth and evaporation in an aerosol with boundary heat and mass transfer. *J. Aerosol Sci.* **2007**, *38*, 1-16.

48 Riipinen, I.; Pierce, J. R.; Donahue, N. M.; Pandis, S. N. Equilibration time scales of organic aerosol inside thermodenuders: Evaporation kinetics versus thermodynamics. *Atmos. Environ.* **2010**, *44*, 597-607.

49 Ruiz, P. A.; Lawrence, J. E.; Ferguson, S. T.; Wolfson, J. M.; Koutrakis, P. A counter-current parallel-plate membrane denuder for the non-specific removal of trace gases. *Environ. Sci. Technol.* **2006**, *40*, 5058-5063.

50 Bennett, J. F.; Collin, F.; Hastie, D. R. A laboratory flow reactor with gas particle separation and on-line MS/MS for product identification in atmospherically important reactions. *Atmos. Meas. Tech.* **2009**, *2*, 813-823.

51 Donahue, N. M.; Robinson, A. L.; Stanier, C. O.; Pandis, S. N. Coupled partitioning, dilution, and chemical aging of semivolatile organics. *Environ. Sci. Technol.* **2006**, *40*, 2635-2643.

8 Soot aggregate restructuring due to coatings of secondary organic aerosol derived from aromatic precursors

8.1. Introduction

Soot aggregates are composed of roughly spherical primary particles[1,2] that consist of many layers of graphitic carbon[3,4] bound by van der Waals forces.[5] The size of primary particles varies from roughly 5 to 60 nm,[6,7] depending on the source and conditions of combustion, such as fuel to air ratio. Soot aggregates are emitted by many sources, including diesel engines[8] and forest fires,[9] and they exert a large positive radiative forcing on Earth's climate by absorbing light at all visible wavelengths.[10] Non-absorbing species internally mixed with soot aggregates act as coatings and enhance absorption and scattering of light by the particles, by restructuring and/or lensing effects.[11,12] Aggregate restructuring has been observed to various degrees for many coatings, including water,[13-15] sulphuric acid,[12,13] oleic acid,[16,17] glutaric acid,[11] dioctyl sebacate,[16] ethanol,[18] and *n*-hexane.[19] Lensing has also been observed for aggregates coated, but not restructured, by succinic acid.[11]

Volatile organic compounds (VOCs) are emitted into the atmosphere by biogenic and anthropogenic sources, and they can react with oxidants, such as hydroxyl radical and ozone, to form semi-volatile products. In the absence of pre-existing particles, these oxidation products lead to nucleation by forming molecular clusters.[20,21] In the presence of pre-existing particles, the products establish equilibrium by partitioning from the gas phase to the particle phase, a process governed by their vapor pressures.[22,23] Both processes form secondary organic aerosol (SOA). If the pre-existing particles are soot aggregates, they will be coated and restructured by SOA. Since SOA is a complex mixture, it is more analogous to atmospheric coatings than neat species. In photo-reaction (smog) chamber experiments, restructuring of soot aggregates generated by different sources has been observed for SOA coatings derived from diesel

exhaust,[24] α-pinene,[25,26] isoprene,[27] and toluene.[28] Aromatic species, emitted by industry[29] and transportation,[30] are the most important anthropogenic SOA precursors, and they have been predicted to produce 12% of global SOA.[31] Consequently, it is important to investigate the restructuring of soot due to coatings of SOA from a variety of aromatic precursors, in addition to toluene. Furthermore, SOA-induced restructuring of soot aggregates from other sources, in addition to those generated by diesel engines,[24,26] Santoro burners,[27,28] and spark discharge[25] should be investigated, as well.

In the present study, monodisperse soot aggregates generated by a McKenna burner were exposed to products of hydroxyl radical-initiated oxidation of toluene, *p*-xylene, ethylbenzene, and benzene in a smog chamber. Using a differential mobility analyzer (DMA) and a centrifugal particle mass analyzer (CPMA), the formation of SOA coatings and the restructuring of soot aggregates were monitored. Mass-mobility relationships were determined for fresh and restructured soot aggregates. Trends in diameter growth factor, effective density, and dynamic shape factor with increasing coating mass were derived, and their atmospheric implications are discussed.

8.2. Methods

8.2.1. Soot preparation

The experimental setup during soot preparation and injection is illustrated in Figure 8.1.a. Soot aggregates were generated using a McKenna burner.[32,33] To achieve an equivalence ratio of two, ethylene and air were mixed at flow rates of 1.1 L min^{-1} and 8 L min^{-1}, respectively. Nitrogen was used as sheath gas at a flow rate of 30 L min^{-1}. Soot aggregates were sampled 27 cm above the flame from a chimney. Sampled aggregates were subsequently passed through a 25 cm diffusion dryer, consisting of tubular mesh surrounded by anhydrous calcium sulfate (Hammond Drierite Co.); an ejector dilutor (Air-Vac), supplied with dry nitrogen at 30 psi; a thermo-denuder (TD), heated to 473 K; a counter-flow parallel-plate membrane denuder (CPMD), similar in design to those described in the literature;[34,35] an X-ray aerosol neutralizer (TSI 3087); and a DMA (DMA1; TSI 3081), operated with a sheath air flow rate of 6.5 L min^{-1} and a sample flow rate of roughly 1.7 L min^{-1}. In every experiment, the DMA1 voltage was set to select 100, 150, 200, or 250 nm aggregates. Downstream of DMA1, size-selected aggregates were injected

into a smog chamber until the concentration measured by a condensation particle counter (CPC1; TSI 3771) reached about 1000 cm^{-3}.

The commercial scanning mobility particle sizer (SMPS) software (TSI) was not used to control the DMA, since the underlying data inversion process is inadequate when analyzing narrow size distributions,[36] like those investigated here. Instead, the DMA voltage was stepped. For every sample, number concentrations were measured at 11 DMA voltages, which were selected to give equally spaced points on a logarithmic mobility diameter scale. For each of the 11 points, DMA2 was set to a given voltage, and CPC2 was used to make 10 concentration measurements, which were subsequently averaged. For the first point, CPC2 was allowed to start measuring 20 s after the DMA2 voltage was set; for each of the following points, CPC2 was allowed to start measuring 10 s after the DMA2 voltage was set. At a particular voltage, no systematic changes in particle number concentration occurred during the 10 s measurement period. A lognormal function was fit to the 11 points to give the median mobility diameter of

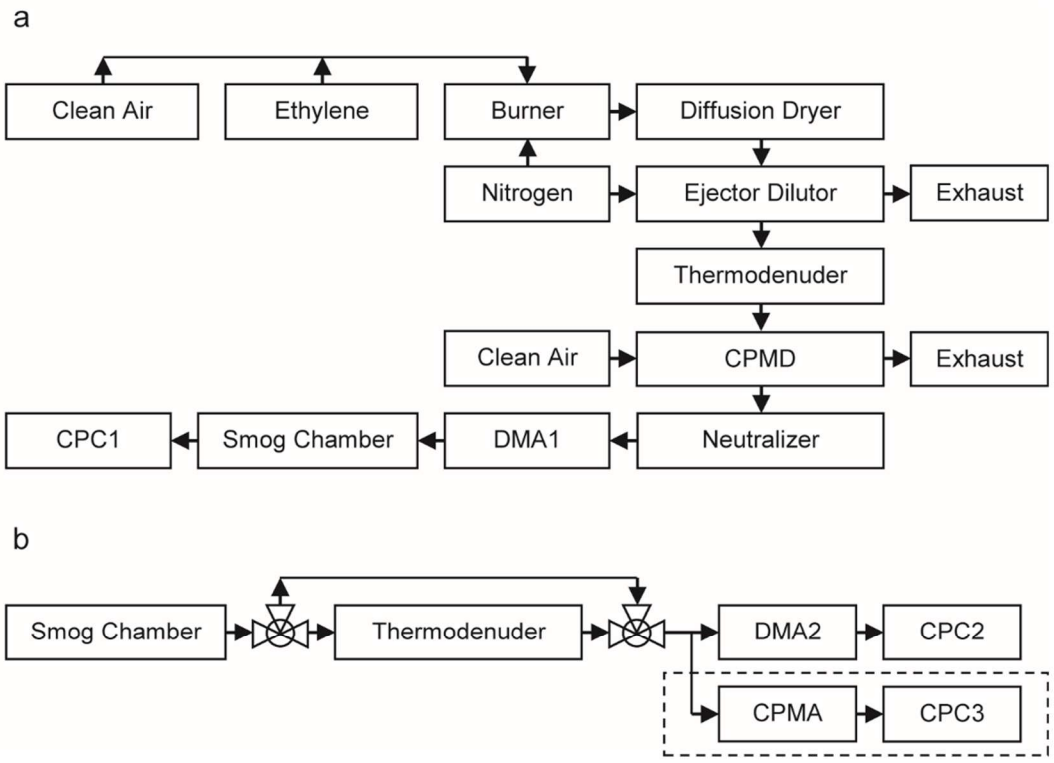

Figure 8.1. Experimental setup during (a) soot preparation/injection and (b) photo-oxidation/sampling. The dashed rectangle denotes the instruments not included in all experiments. Table 8.1 summarizes the instrumentation used in each experiment. CPMD: counter-flow parallel-plate membrane denuder; DMA: differential mobility analyzer; CPC: condensation particle counter; CPMA: centrifugal particle mass analyzer.

sampled particles, which should not be confused with the conventional count median mobility diameter of the actual particle distribution that can only be determined by data inversion. As photo-oxidation proceeded, the range of voltages was adjusted manually to be roughly centred at the mobility diameter with the highest number concentration.

I do not account for multiply-charged particles since the number of larger multiply-charged particles injected into the chamber compared to singly-charged particles of the desired diameter is insignificant; for example, the percentage of doubly-charged 410 nm aggregates to singly-charged 250 nm aggregates was calculated to be less than 6%.

Soot generated using McKenna burners is known to contain, in addition to black carbon (BC), semi-volatile organic species,[37,38] such as polycyclic aromatic hydrocarbons (PAHs) and aliphatic hydrocarbons.[39] In order to reduce the amount of semi-volatile material on the soot, I

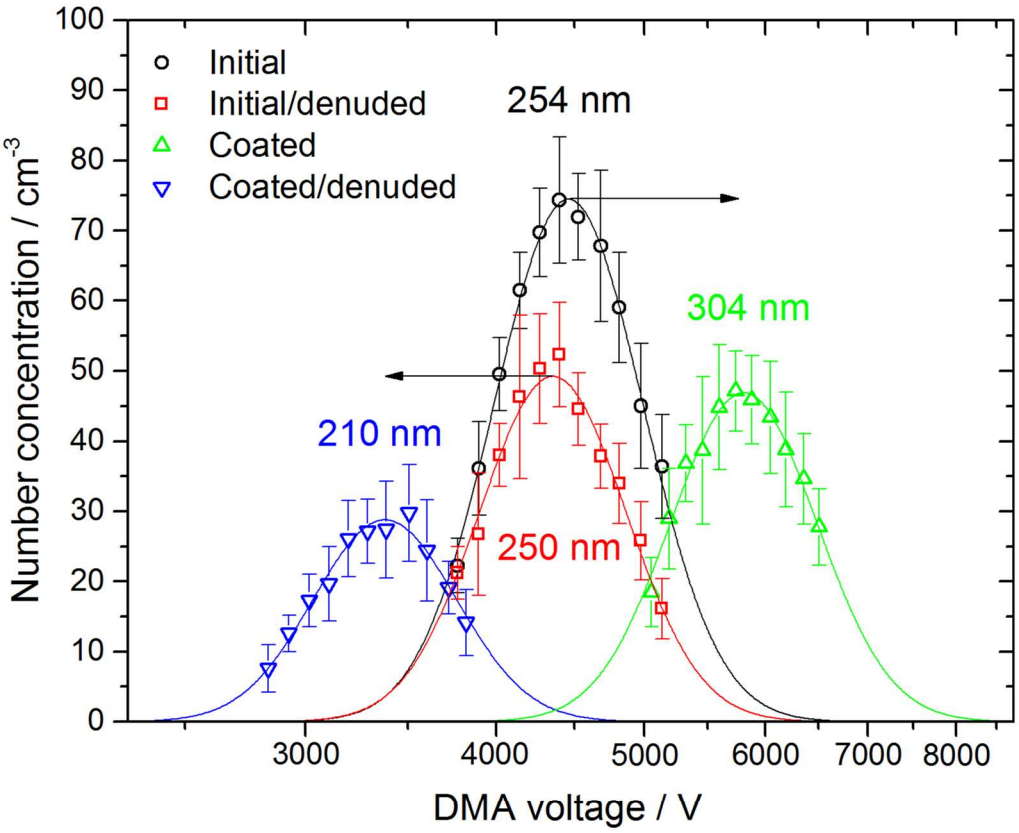

Figure 8.2. Particle concentrations, measured with and without thermo-denuding, at DMA voltage set-points at the beginning and end of a typical experiment, in which 250 nm soot aggregates were processed by SOA derived from *p*-xylene. Arrows indicate the direction of the change in mobility diameter for initial and initial/denuded particles during photo-oxidation, which leads to coated and coated/denuded particles. Error bars indicate one standard deviation of 10 consecutive number concentrations at each set-point.

treated particles with a TD and a CPMD. By measuring the mass of 250 nm particles with and without treatment, I found that semi-volatile material accounts for about 15% of the untreated soot aggregate mass, in excellent agreement with earlier measurements.[37] The mass fraction of semi-volatile material is known to increase as equivalence ratio increases or mobility diameter decreases.[37]

If all semi-volatile material was removed by denuding during soot preparation and injection, the aggregate number concentrations at certain mobility diameters should have been the same when first sampling from the chamber with or without the TD. However, as shown in Figure 8.2, there were differences in number concentration and median mobility diameter. The number concentration was lower when sampling through the TD due to thermophoretic losses. The thermophoretic losses should be independent of size, so they cannot explain the small differences in median mobility diameter (1.7 ± 0.2%) and mass (4 ± 2%). I observed this small but systematic difference even for particles treated with the TD set to a higher temperature (573 K) before being injected into the chamber. It is possible that some trace semi-volatile species condensed back onto the soot before the sample reached the trace gas denuder downstream of the TD. However, since the differences are so small, I use the terms soot and BC interchangeably for the treated aggregates.

Table 8.1. Instrumentation used to characterize particles in experiments with different SOA precursors and initial soot aggregate mobility diameters.

	Initial soot aggregate mobility diameter			
	100 nm	150 nm	200 nm	250 nm
Benzene	DMA2/CPC2[a]	DMA2/CPC2	DMA2/CPC2	DMA2/CPC2// CPMA/CPC3
Toluene	DMA2/CPC2	DMA2/CPC2	DMA2/CPC2	DMA2/CPC2// CPMA/CPC3
Ethylbenzene	DMA2/CPC2	DMA2/CPC2	DMA2/CPC2	DMA2/CPC2// CPMA/CPC3
p-Xylene	DMA2/CPC2// CPMA/CPC3	DMA2/CPC2// CPMA/CPC3	DMA2/CPC2// CPMA/CPC3	DMA2/CPC2// CPMA/CPC3

[a] See Figure 8.1 for further details regarding the experimental setup.

8.2.2. Hydrocarbon photo-oxidation

The experimental setup during photo-oxidation and sampling is illustrated in Figure 8.1.b. The smog chamber has been described previously.[40] Briefly, the cubic chamber is constructed of perfluoroalkoxy (PFA) film (Ingeniven), and it has a volume of 1.8 m^3. Three arrays of eight 32 W black lights with peak emission at a wavelength of 350 nm are arranged on the top and two opposite side faces of the chamber. Clean, dry air is supplied to the chamber from a pure air generator (Aadco, 737). A mixing fan and a temperature and relative humidity sensor are situated in the chamber. In order to facilitate spectroscopic measurements, the output from a broadband deuterium lamp (Ocean Optics, D-2000-S) is passed through the chamber, and the transmitted light is detected using a grating-based spectrometer (Ocean Optics, HR-2000+).

Following soot injection, the aggregate number concentrations at mobility diameter set-points were determined using DMA2 (TSI 3081) and CPC2 (TSI 3776). The DMA voltage was stepped, rather than scanned. A TD, again set to 473 K, was alternately sampled through or bypassed. In certain experiments (Table 8.1), a centrifugal particle mass analyzer (CPMA, Cambustion) was used to classify particles by mass.[41,42] Number concentrations at mass set-points were measured by CPC3 (TSI 3771).

A precursor hydrocarbon was then placed in a glass bubbler and injected into the chamber. The precursor hydrocarbon was either toluene (Fisher, 99.9%), *p*-xylene (Fisher, 99.9%), ethylbenzene (Sigma, 99.8%), or benzene (Caledon, 99.0%). Precursor hydrocarbon concentrations were measured using ultraviolet differential optical absorption spectroscopy (UV-DOAS).[40,43] About one hour after the injection of soot aggregates, during which no changes in the aggregate mobility diameter or mass were observed, hydrogen peroxide (Sigma, 30% w/w) was injected into the smog chamber. In spite of introducing water from the hydrogen peroxide solution into the chamber, the relative humidity was less than 15% in all experiments. The chamber was irradiated for the remainder of the experiment, causing photolysis of hydrogen peroxide to give hydroxyl radical.[44] Clean make-up air was continuously added to the chamber to maintain a constant volume, as well as a constant path-length for the *in situ* UV-DOAS measurements. Following each experiment, the chamber was flushed in two steps: for 12 hours, clean air was bubbled through a hydrogen peroxide solution at a flow rate of 10 L min^{-1} and directed into the chamber while the black lights were on; for an additional 12 hours, clean air was directed into the chamber at a flow rate of 10 L min^{-1} while the black lights were off.

I investigated the effects of UV irradiation and hydroxyl radical on soot aggregates, without generating SOA. I treated 250 nm soot particles with the TD and CPMD before injection, and subsequently exposed them to hydrogen peroxide and UV irradiation in the photo-oxidation chamber. A small increase (1.5%) from the initial particle diameter occurred over the course of four hours, but no change in the initial/denuded particle diameter occurred. It is possible that trace amounts of semi-volatile organic compounds were introduced during soot injection and oxidized in the gas phase to produce non-volatile organic compounds that condensed onto the soot. Nonetheless, exposure to hydroxyl radical did not change the morphology of the initial/denuded soot aggregates, so all aggregate restructuring was attributed to SOA coatings from oxidation of injected aromatic species by hydroxyl radical.

On the other hand, I cannot rule out that exposure to hydroxyl radical changed the soot surface properties, such as activation with respect to adsorption. However, such changes can be neglected since the coating process is due to the low vapour pressures of the oxidation products and not to activated adsorption by the soot surface. For instance, I exposed treated soot to toluene and UV irradiation, without hydrogen peroxide, and I observed no changes in mobility diameter of initial or initial/denuded particles over the course of four hours. I conclude that adsorption of hydrocarbons was insignificant. Furthermore, in the SOA coating experiments, as soon as oxidation products began to condense onto the soot, additional mass was *absorbed* by the pre-existing SOA.

8.2.3. Aggregate morphology

In the following discussion, restructuring is characterized in terms of morphology properties, including mass-mobility exponent, effective density, and dynamic shape factor, which are discussed in Chapter 7.[45] The mass-mobility exponent, D_m, which describes how particle mass scales with mobility diameter, is determined using Equation (7.12). For fractal, non-spherical aggregates, D_m is less than three. Effective density, ρ_{eff}, is calculated using Equation (7.11). The effective densities of coated and coated/denuded particles are denoted as ρ_{eff}^{0} and ρ_{eff}^{*}, respectively. Dynamic shape factor, χ, is calculated using Equation (7.9) and volume equivalent diameter, d_{ve}, which is calculating by adapting Equation (7.10) for internally-mixed particles of two components to give Equation (8.1).

$$d_{ve} = \left[\frac{6}{\pi}\left(\frac{m_{p,i}^{0}}{\rho_{soot}} + \frac{(m_{p}^{0} - m_{p,i}^{0})}{\rho_{SOA}}\right)\right]^{1/3} \quad (8.1)$$

Here, m_p^0 is the total mass of the soot aggregate and its SOA coating; $m_{p,i}^0$ is the mass of the initial soot, which has no SOA coating; and ρ_{soot} and ρ_{SOA} are the material densities of soot and the SOA coating, respectively. The density of soot is taken as 1.77 g cm^{-3}.[1] The densities of SOA from toluene and *p*-xylene are taken as 1.38 g cm^{-3} and 1.46 g cm^{-3}, respectively;[47] the densities of SOA from both ethylbenzene and benzene are taken as 1.30 g cm^{-3}.[47] For a truly spherical particle with no cavities, d_m and d_{ve} are equivalent, so χ is unity. The dynamic shape factors of coated and coated/denuded particles are denoted as χ^0 and χ^*, respectively.

8.3. Results and discussion

8.3.1. Hydrocarbon photo-oxidation leading to soot aggregate restructuring

Results from a typical experiment, in which 250 nm soot aggregates were coated by SOA from *p*-xylene, are summarized in Figure 8.3 and Figure 8.4. As shown in Figure 8.3, the concentration of *p*-xylene decreased exponentially, as a result of two parallel, first-order processes: dilution and reaction. (Hydrocarbon concentration did not decrease when the chamber was sealed and dark, so loss of precursor vapour to the walls of the chamber was negligible.) Oxidation of the aromatic hydrocarbon exhibited pseudo-first-order kinetics,[48,49] because the concentration of hydroxyl radical was constant. The change in hydrocarbon concentration due to reaction, ΔHC, is calculated according to Equation (8.2).

$$\Delta HC = \frac{k_{HC}}{k_{dil} + k_{HC}} HC_0(1 - \exp[-(k_{dil} + k_{HC})t]) \quad (8.2)$$

Here, k_{HC} is the pseudo-first-order reaction rate constant, k_{dil} is the dilution rate constant, HC_0 is initial hydrocarbon concentration, and t is reaction time. An exponential fit to the measured decay of hydrocarbon concentration gave the total first-order rate constant. The rate constant of dilution, k_{dil}, is equal to the make-up air flow rate divided by the chamber volume. By subtracting k_{dil} from the total rate constant, I obtained the reaction rate constant, k_{HC}. For the representative experiment shown in Figure 8.3, k_{HC} was about 6×10^{-4} min^{-1}, so, dividing k_{HC} by the second-order rate constant,[50] I calculate that the concentration of hydroxyl radical was about 7×10^5 molecule cm^{-3}. This concentration is lower than those typically reported (for example, 3×10^6 molecule cm^{-3}).[49]

In some experiments, I increased the estimated concentration of hydroxyl radical by increasing the intensity of irradiation in the chamber; in these experiments, nucleation (in addition to coating) occurred, and the many new particles quickly grew to completely envelope the coated soot particles on both the mobility diameter and mass scales. Nucleation does not occur in typical seed (for example, ammonium sulfate) particle experiments, because the concentration of seed particles is about 30 times greater than the initial concentration of soot particles in my experiments.[49] I cannot achieve such high concentrations using monodisperse soot particles, so I must use low hydroxyl radical concentrations. A further challenge is that I must produce a significant amount of SOA, if I am to assess the degree of restructuring at large coating masses before the concentration of soot particles decays too significantly due to dilution and rapid deposition to the chamber walls. Using low initial hydrocarbon concentrations at low hydroxyl radical concentrations produced very little SOA. Consequently, in order to form enough SOA, without suddenly incurring a super-saturation of semi-volatile oxidation products

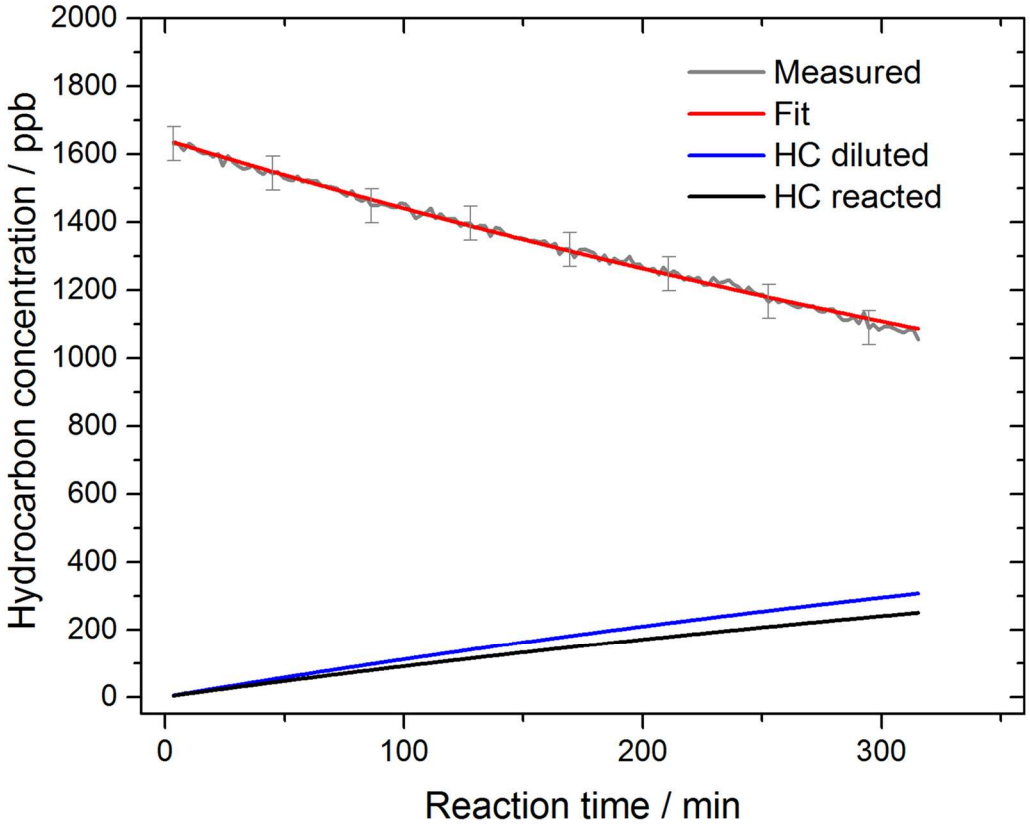

Figure 8.3. Measurements of aromatic hydrocarbon concentration during a typical experiment, in which 250 nm soot aggregates were coated by SOA derived from *p*-xylene. Error bars indicate three standard deviations of 40 consecutive measurements at a *p*-xylene concentration of zero.

in the gas-phase soon after the onset of photo-oxidation (which would lead to nucleation), I used high initial hydrocarbon concentrations at low hydroxyl radical concentrations. I note that, in the experiment shown, the initial concentration of *p*-xylene was greater than 1.6 ppm, but less than 300 ppb reacted with hydroxyl radical to form SOA. In general, the initial concentrations of hydrocarbons were too high to be strictly representative of atmospheric conditions; however, the purpose of these experiments was not to reproduce atmospheric oxidation kinetics but to generate atmospherically relevant SOA coatings. For instance, much higher hydrocarbon concentrations are commonly used to produce SOA in flow tube reactors.[51,52] Furthermore, it has been reported previously that at a given coating thickness (and, consequently, mass), the degree of soot aggregate restructuring due to SOA derived from toluene did not depend on initial hydrocarbon concentration.[28]

The changes in particle mobility diameter and mass during photo-oxidation are shown in Figure 8.4. Throughout this paper, the mobility diameters of coated and coated/denuded

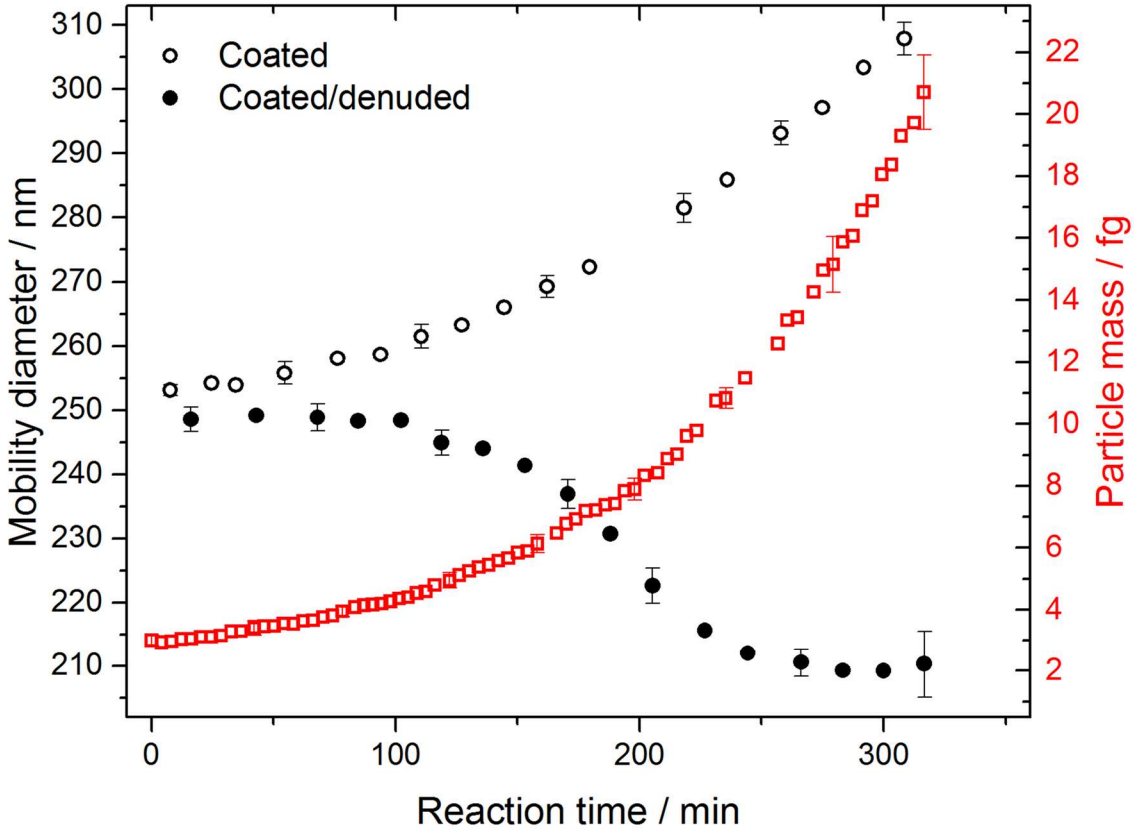

Figure 8.4. Measurements of particle mobility diameter and mass during a typical experiment, in which 250 nm soot aggregates were coated by SOA derived from *p*-xylene. Error bars indicate three standard deviations of log-normal fits to number concentrations at mobility diameter and mass set-points.

particles are denoted as d_m^0 and d_m^*, respectively; and the masses of coated and coated/denuded particles are denoted as m_p^0 – as in Equation (8.1) – and m_p^*, respectively. The semi-volatile oxidation products in the gas phase rapidly reach their saturation vapour pressures and partition into the aerosol phase by coating the soot aggregates. Since the oxidation of *p*-xylene was pseudo-first-order, the mass of oxidation products in the aerosol phase (and, consequently, m_p^0) increased exponentially. On the other hand, d_m^* decreased and eventually reached a steady value of about 210 nm, in spite of the continued increase in SOA coating mass; at this stage, I define the soot aggregates as being fully restructured. Furthermore, m_p^* was constant, since no primary particles of black carbon are gained or lost.

8.3.2. Size dependence of soot aggregate restructuring

I note that there is no current consensus on whether restructuring occurs during condensation or evaporation of coatings. For example, in a recent study, multi-angle light scattering was used to probe soot aggregates in bulk water, and their structure was found to be unchanged.[14] In contrast, soot aggregates thinly coated with oleic acid or dioctyl sebacate were shown to have a smaller mobility diameter than fresh aggregates, because the aggregates collapsed while the coating was present.[16] Since the highly oxygenated compounds that comprise my SOA coatings are more similar to these hydrocarbon coatings than to bulk water, I assume in the following discussion that restructuring occurs during condensation of SOA, rather than during evaporation in the TD. This assumption is addressed and resolved in Chapter 9.

Particle concentrations at mobility diameter set-points at the beginning and end of a typical experiment, in which *p*-xylene was used as the SOA precursor, are shown in Figure 8.2. Several samples of initial and initial/denuded particles were measured in every experiment and averaged to determine $d_{m,i}^0$ and $d_{m,i}^*$, respectively. During reaction, d_m^0 increased as SOA coating formed. The particle concentrations decreased with time due to deposition and dilution, loss processes that limited the duration of my experiments. Once d_m^* reached a steady value, several samples were measured and averaged to determine the final coated/denuded mobility diameter, $d_{m,f}^*$. For coated particles, the diameter growth factor, Gfd^0, and mass growth factor, Gfm^0, are calculated according to Equation (8.3) and Equation (8.4), respectively.

$$Gfd^0 = \frac{d_{\mathrm{m}}^0}{d_{\mathrm{m,i}}^0} \tag{8.3}$$

$$Gfm^0 = \frac{m_{\mathrm{p}}^0}{m_{\mathrm{p,i}}^0} \tag{8.4}$$

For coated/denuded particles, the diameter growth factor, Gfd^*, is calculated according to Equation (8.5).

$$Gfd^* = \frac{d_{\mathrm{m}}^*}{d_{\mathrm{m,i}}^*} \tag{8.5}$$

Absolute changes in mobility diameter, $\left|d_{\mathrm{m,f}}^* - d_{\mathrm{m,i}}^*\right|$, of soot aggregates of different initial sizes, coated with SOA from all four aromatic SOA precursors, are shown in Figure 8.5. As $d_{\mathrm{m,i}}^*$ increased, the magnitude of the final change in mobility diameter increased, as well. Similar

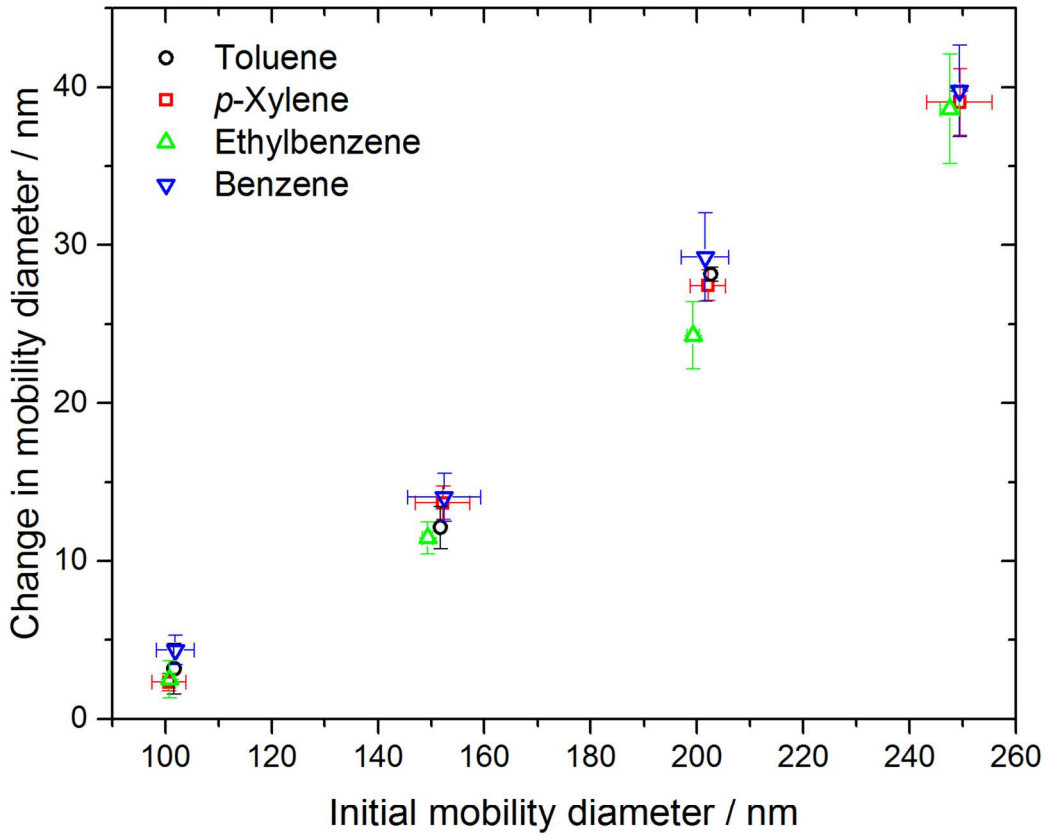

Figure 8.5. Change in soot aggregate mobility diameter after aggregates are fully restructured due to SOA from different precursors. Error bars in the *x*-axis indicate one standard deviation of several consecutive measurements of initial mobility diameter, before photo-oxidation begins; error bars in the *y*-axis indicate propagation of error of one standard deviation of several consecutive measurements of initial and final mobility diameters.

trends were previously observed for aggregates generated by a variety of sources (diesel exhaust, hydrocarbon combustion, and candle smoke) and coated with heptane[18] and for aggregates generated by an inverted burner and coated with dioctyl sebacate and oleic acid.[16] The size dependence occurs because larger aggregates have more branched and open structures than smaller aggregates.[8,37] For instance, as shown in Figure 8.6, the effective densities of initial/denuded soot aggregates decreased as mobility diameter increased. I note that the effective densities of spherical particles would not change with size, even if the particles had internal voids. The effective densities of initial/denuded aggregates are in good agreement with those previously reported for aggregates produced by a McKenna burner at an equivalence ratio

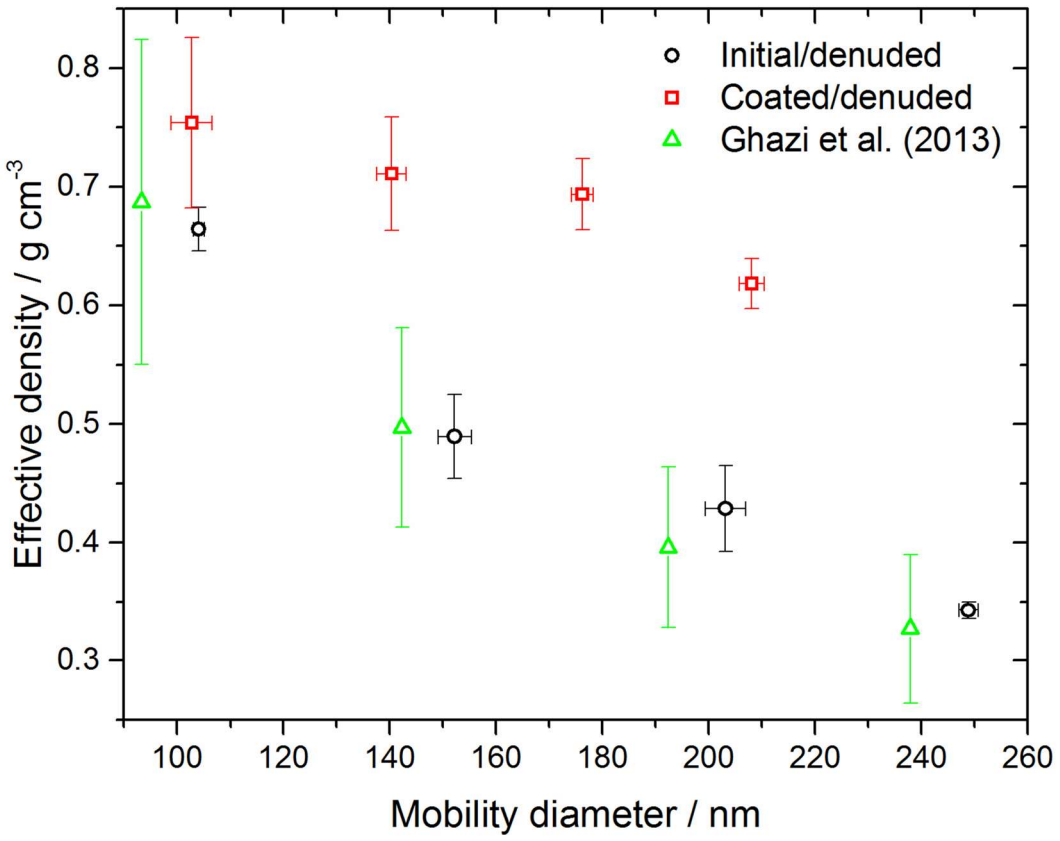

Figure 8.6. Effective densities of soot aggregates before (initial/denuded) and after (coated/denuded) restructuring due to SOA derived from *p*-xylene. Effective densities plotted as green triangles are taken from ref 37 and pertain to aggregates that were generated by a McKenna burner at an equivalence ratio of 2 and subsequently denuded. For my measurements, error bars in the *x*-axis indicate three standard deviations of several consecutive measurements of mobility diameter, either before photo-oxidation was initiated (initial/denuded) or after the mobility diameter had leveled off at large coating masses (coated/denuded); error bars in the *y*-axis indicate three standard deviations of effective densities calculated from several consecutive measurements of mobility diameter and particle mass.

of two.[37] Interestingly, the effective densities of coated/denuded aggregates (calculated at $d^*_{m,f}$) also decreased as mobility diameter increased, indicating that the fully-restructured aggregates, though significantly compacted, were not spherical.

The mass-mobility relationships of the soot aggregates before and after restructuring due to SOA derived from *p*-xylene are shown in Figure 8.7. The aggregates initially had a mass-mobility exponent of 2.24, which is typical of fresh soot, whether generated from burners[37] or diesel engines.[46] Following restructuring, the aggregates had a mass-mobility exponent of 2.78, which is greater than that observed for aggregates restructured due to coatings of oleic acid (2.44),[16] but still significantly less than three. As implied by the trend in effective densities discussed above, processing by SOA coatings alone does not make soot aggregates spherical. I note that the masses of initial/denuded and coated/denuded aggregates were the same, within

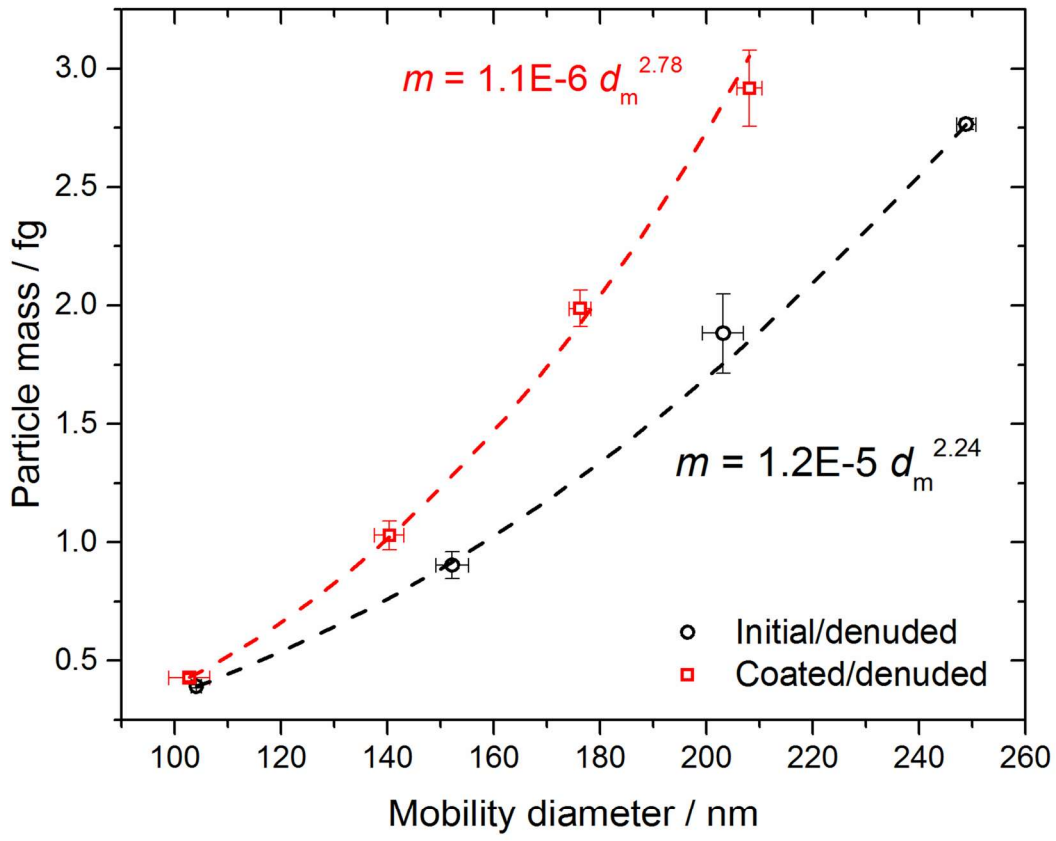

Figure 8.7. Particle mass-mobility relationships for soot aggregates before (initial/denuded) and after (coated/denuded) restructuring due to SOA derived from *p*-xylene. Dashed lines and the corresponding equations indicate the fits used to determine the mass-mobility exponents. Error bars in the *x*-axis indicate three standard deviations of several consecutive measurements at a given mobility diameter; error bars in the *y*-axis indicate three standard deviations of several consecutive measurements at a given particle mass.

their uncertainty, so the TD was operating efficiently, removing even very large coating masses. This is consistent with previous studies in which TDs were also set to 473 K to remove semi-volatile compounds.[16,37]

In contrast, the change in mobility diameter did not depend on the identity of the aromatic SOA precursor. Similarly, soot aggregates of the same initial mobility diameter bubbled through a variety of solvents were previously shown to collapse to the same final mobility diameter.[18]

8.3.3. Coating mass dependence of soot aggregate restructuring

Based on trends in ρ_{eff}^{0} and ρ_{eff}^{*} (Figure 8.8), as well as χ^{0} and χ^{*} (Figure 8.9), with increasing Gfm^{0}, three stages in the restructuring experiments were identified. Initially, at a Gfm^{0} of one, ρ_{eff}^{0} was about 0.35 g cm^{-3}, in good agreement with earlier measurements for aggregates generated by a McKenna burner operated at an equivalence ratio of two.[37] This value is much less than ρ_{soot} due to the fractal structure of the soot aggregates.[1,8] During the first stage of my

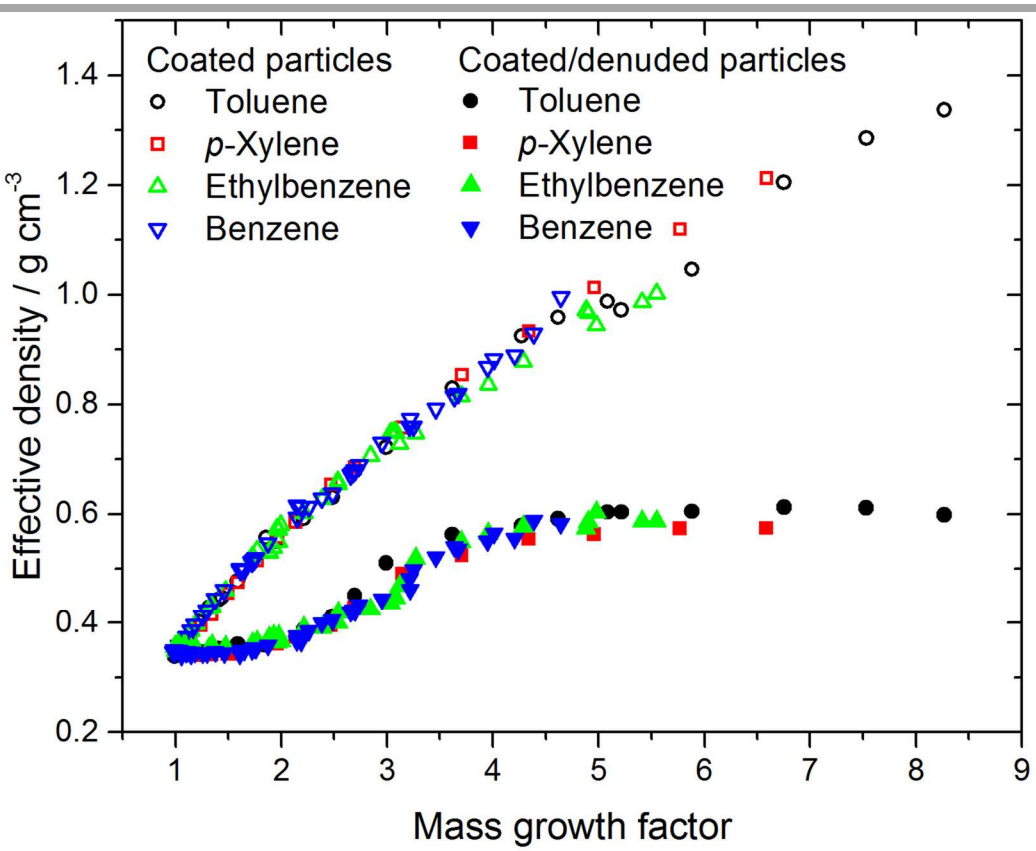

Figure 8.8. Mass coating dependence of effective density.

experiments, ρ_{eff}^{0} increased, and χ^{0} decreased, while ρ_{eff}^{*} and χ^{*} were constant, indicating that the coated particles were becoming denser and more spherical although the soot aggregates were unchanged. In other words, oxidation products began partitioning onto the soot, filling voids and/or forming a thin liquid layer, since Gfd^{0} was increasing before Gfd^{*} began to decrease (Figure 8.10).

During the second stage, beginning at a Gfd^{0} of about two, ρ_{eff}^{0} and ρ_{eff}^{*} both increased, while χ^{0} and χ^{*} both decreased, as coating mass was added. My observation that soot restructuring began only after a certain, threshold coating mass was reached is inconsistent with a recently proposed exponential model, based on soot restructuring due to coatings of oleic acid.[16] Instead, as shown in Figure 8.10, a sigmoidal model is in good agreement with my results. This inconsistency could be due to the low Gfm^{0}-scale resolution in the earlier study. For instance, no measurements were made at a Gfm^{0} of 1-2, the interval in which the threshold coating mass of oleic acid likely occurs. Alternatively, the inconsistency could be due to inherent differences in the soot generated by McKenna and inverted burners.

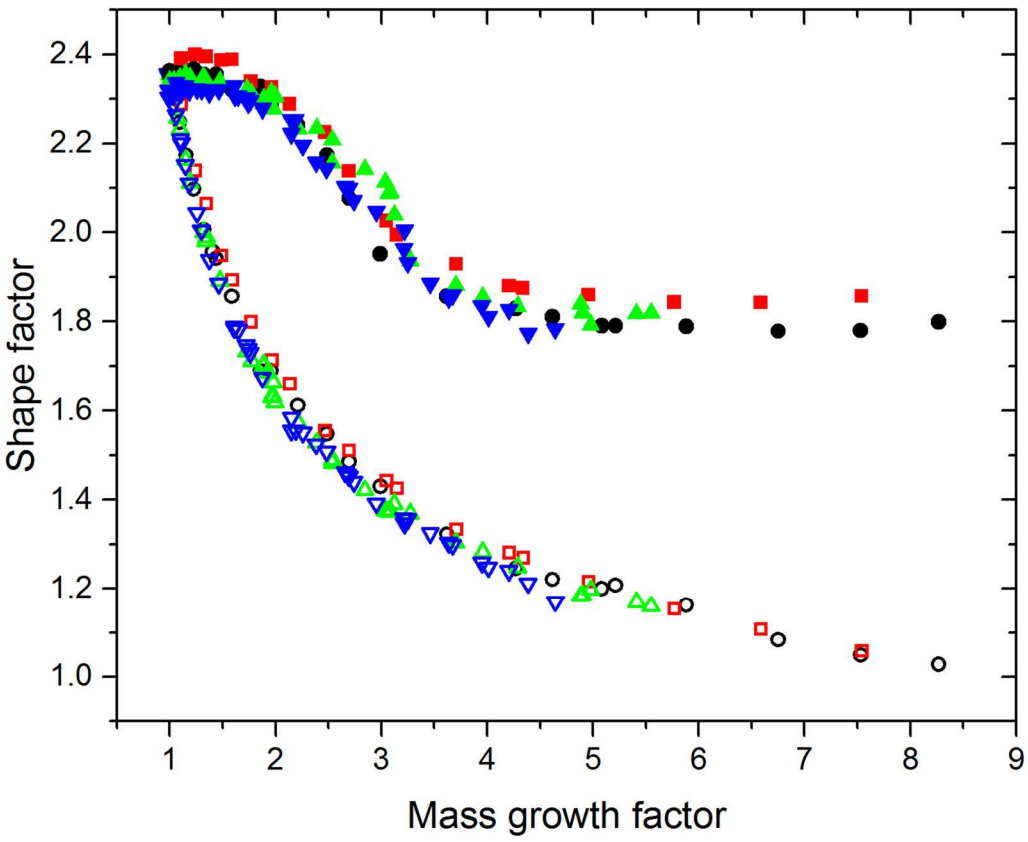

Figure 8.9. Mass coating dependence of dynamic shape factor. (See Figure 8.8 for legend.)

During the third stage of my experiments, beginning at a Gfm^0 of about four, ρ_{eff}^0 continued to increase, and χ^0 continued to decrease, while ρ_{eff}^* and χ^* were again constant, indicating that restructuring of the soot aggregates ceased. The final value of χ^* was about 1.8, which is consistent with my conclusion, based on their mass-mobility exponent (2.78), that the restructured aggregates are not spherical. (I note that shape factor alone is not adequate to determine the morphology of the aggregates; for instance, particles with a shape factor greater than unity could be spherical if they are porous.) Additional coating mass continued to fill indentations between compacted branches of the aggregate until, at a Gfm^0 of about eight, the coated particles were nearly spherical, as χ^0 approached unity. In contrast, earlier measurements of 250 nm soot aggregates coated with oleic acid showed that χ^0 and χ^* converged with their final values at approximately the same value of Gfm^0.[16] This discrepancy likely occurred because oleic acid has a much lower density (0.9 g cm^{-3}) than SOA, so less mass was required to completely fill indentations in the compacted soot aggregate. Furthermore, my observation is

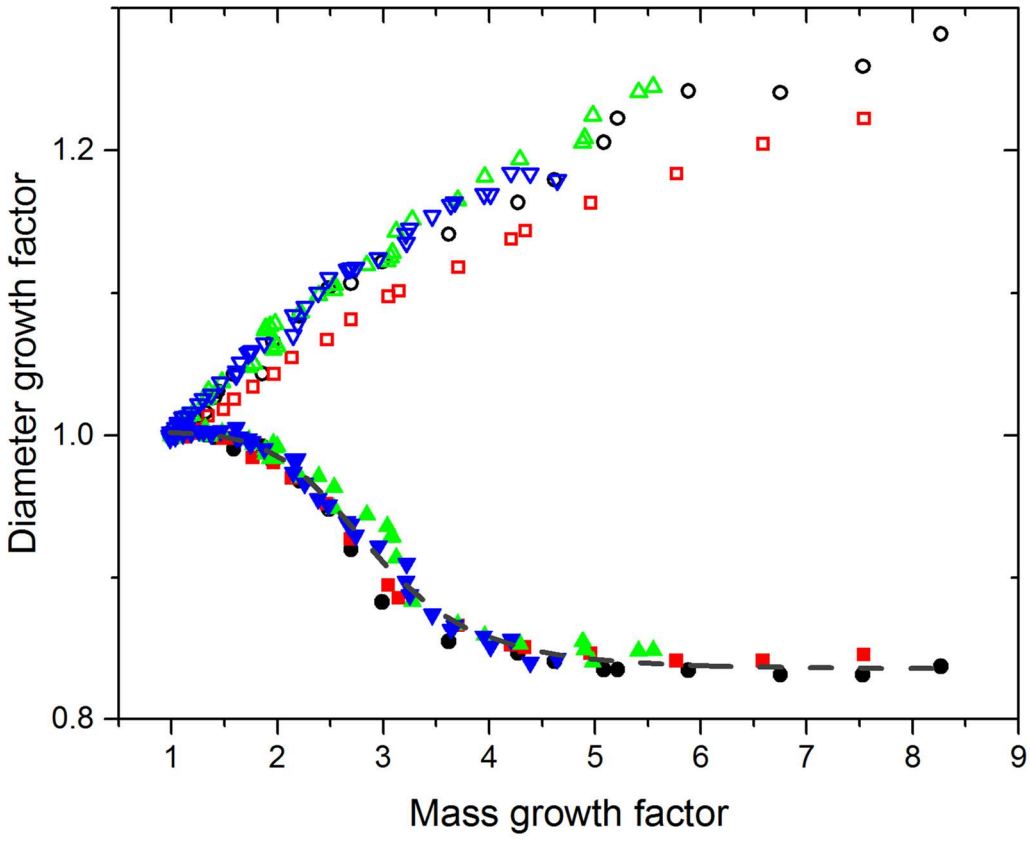

Figure 8.10. Mass coating dependence of diameter growth factor. The dashed gray line indicates the sigmoidal fit. (See Figure 8.8 for legend.)

consistent with recent experiments of soot aggregate restructuring due to SOA coatings derived from toluene, in which ρ_{eff}^{*} reached its final value before χ^{0} approached 1.[28] The high density of my coatings also explains why I did not observe a maximum in ρ_{eff}^{0}, followed by a slow decrease to the material density of the SOA coatings, as the contribution of the denser soot aggregate to the mass of the coated particles becomes less and less significant: the maximum in ρ_{eff}^{0} would occur at the same Gfm^{0} at which χ^{0} reaches unity, and this value is not yet reached by the end of my experiments. Also, since SOA derived from *p*-xylene has the highest density of the four SOA coatings, Gfd^{0} was lowest at a particular Gfm^{0} when *p*-xylene was the SOA precursor (Figure 8.10).

Finally, I note that trends in ρ_{eff}, χ, and *Gfd* during the above stages, like the final degree of restructuring, were the same regardless of SOA precursor. This consistency is strong evidence that these precursors result in SOA of roughly the same surface tension. My results do not allow us, then, to resolve whether or not the final degree and/or coating mass dependence of restructuring is influenced by surface tension, a question that is addressed in Chapter 9. Nonetheless, my results do provide unequivocal evidence that SOA derived from different aromatic species, representative of anthropogenic SOA precursors in general, processes BC similarly.

8.4. Conclusions

I have shown that the coating mass dependence and final degree of soot aggregate restructuring due to SOA coatings from aromatic precursors are the same for different precursors, due to the similar surface tensions of the coatings. Since aromatic hydrocarbons produce similar arrays of oxidation products, including many of the same species (for example, benzaldehyde forms from each of toluene,[53] *p*-xylene,[54] ethylbenzene,[55] and benzene[54]), the similarity in surface tensions is not altogether surprising. Consequently, these aromatic SOA precursors could be grouped in climate models of soot processing in the atmosphere. In general, the processing of BC in the atmosphere by anthropogenic SOA may depend only on the coating mass and not on the origin of the constituent oxidation products. The restructuring effects of SOA from a wider variety of precursors (alkanes[56,57] and PAHs,[58,59] for example) should be investigated in the future. Moreover, the changes I observed in morphological properties, such as effective density and

dynamic shape factor, are qualitatively consistent with those previously reported for soot aggregates generated from a different source (a Santoro burner) and coated with SOA derived from toluene,[28] suggesting that restructuring may depend more upon the properties of the coating than it depends upon those of the aggregates. However, the effects of similar SOA coatings on soot aggregates from different types of burners should be investigated systematically in the future.

I have shown that, for the SOA coatings in the present study, soot aggregate restructuring begins only once a threshold coating mass, at a mass growth factor of about two, is reached. Thus, a light coating of anthropogenic SOA in the atmosphere may not result in any structural change to nascent soot aggregates. Furthermore, soot aggregate restructuring ceases before the SOA coated particles reach a dynamic shape factor of one, inconsistent with observations for oleic acid,[16] a much less dense coating, suggesting that coating volume may dictate soot aggregate collapse.[13] The fully-restructured aggregates are not spherical; however, since SOA becomes more hygroscopic as it ages,[60] coated aggregates could uptake water in the atmosphere, resulting in a significantly higher coating surface tension.[61] Consequently, further collapse could occur. Only once a dynamic shape factor of one is reached, at a considerably larger mass growth factor than is required for the aggregate to become fully restructured, is a core-shell model of the aggregate and coating strictly accurate. This conclusion is qualitatively consistent with observations for soot aggregates coated with glutaric acid[11] and SOA from α-pinene ozonolysis.[26]

References

1 Park, K.; Kittelson, D. B.; Zachariah, M. R.; McMurry, P. H. Measurement of inherent material density of nanoparticle agglomerates. *J. Nanopart. Res.* **2004**, *6*, 267-272.

2 Akhter, M. S.; Chughtai, A. R.; Smith, D. M. The structure of hexane soot. I: Spectroscopic studies. *Appl. Spectrosc.* **1985**, *39*, 143-153.

3 Fernandez-Alos, V.; Watson, J. K.; vander Wal, R.; Mathews, J. P. Soot and char molecular representations generated directly from HRTEM lattice fringe images using Fringe3D. *Combust. Flame* **2011**, *158*, 1807-1813.

4 Leyssale, J.-M.; Da Costa, J.-P.; Germain, C.; Weisbecker, P.; Vignoles, G. L. An image-guided atomistic reconstruction of pyrolytic carbons. *Appl. Phys. Lett.* **2009**, *95*, 231912 (3 pp.).

5 Totten, T. S.; Chakrabarti, D.; Misquitta, A. J.; Sander, M.; Wales, D. J.; Kraft, M. Modelling the internal structure of nascent soot particles. *Combust. Flame* **2010**, *157*, 909-914.

6 Gysel, M.; Laborde, M.; Mensah, A. A.; Corbin, J. C.; Keller, A.; Kim, J.; Petzold, A.; Sierau, B. Technical note: The single particle soot photometer fails to reliably detect PALAS soot nanoparticles. *Atmos. Meas. Tech.* **2012**, *5*, 3099-3107.

7 Barone, T. L.; Storey, J. M. E.; Youngquist, A. D.; Szybist, J. P. An analysis of direct-injection spark-ignition (DISI) soot morphology. *Atmos. Environ.* **2012**, *49*, 268-274.

8 Olfert, J. S.; Symonds, J. P. R.; Collings, N. The effective density and fractal dimension of particles emitted from a light-duty diesel vehicle with a diesel oxidation catalyst. *J. Aerosol Sci.* **2007**, *38*, 69-82.

9 Keywood, M.; *et al.* Fire in the air: Biomass burning impacts in a changing climate. *Crit. Rev. Environ. Sci. Technol.* **2013**, *43*, 40-83. See bibliography for complete list of authors.

10 Ramanathan, V.; Carmichael, G. Global and regional climate changes due to black carbon. *Nature Geosci.* **2008**, *1*, 221-227.

11 Xue, H.; Khalizov, A. F.; Wang, L.; Zheng, J.; Zhang, R. Effects of dicarboxylic acid coating on the optical properties of soot. *Phys. Chem. Chem. Phys.* **2009**, *11*, 7869-7875.

12 Khalizov, A. F.; Xue, H.; Wang, L.; Zheng, J.; Zhang, R. Enhanced light absorption and scattering by carbon soot aerosol internally mixed with sulfuric acid. *J. Phys. Chem. A* **2009**, *113*, 1066-1074.

13 Pagels, J.; Khalizov, A. F.; McMurry, P. H.; Zhang, R. Y. Processing of soot by controlled sulphuric acid and water condensation – mass and mobility relationship *Aerosol Sci. Technol.* **2009**, *43*, 629-640.

14 Ma, X.; Zangmeister, C. D.; Gigault, J.; Mulholland, G. W.; Zachariah, M. R. Soot aggregate restructuring during water processing. *J. Aerosol Sci.* **2013**, *66*, 209-219.

15 Mikhailov, E. F.; Vlasenko, S. S. Structure and optical properties of soot aerosol in a moist atmosphere. 1. Structural changes of soot particles in the process of condensation *Izv. Atmos. Ocean. Phys.* **2007**, *43*, 181-194.

16 Ghazi, R.; Olfert, J. S. Coating mass dependence of soot aggregate restructuring due to coatings of oleic acid and dioctyl sebacate. *Aerosol Sci. Technol.* **2013**, *47*, 192-200.

17 Bambha, R. P.; Dansson, M. A.; Schrader, P. E.; Michelsen, H. A. Effects of volatile coatings and coating removal mechanisms on the morphology of graphitic soot. *Carbon* **2013**, *61*, 80-96.

18 Miljevic, B.; Surawski, N. C.; Bostrom, T.; Ristovski, Z. D. Restructuring of carbonaceous particles upon exposure to organic and water vapours *J. Aerosol Sci.* **2012**, *47*, 48-57.

19 Kütz, S.; Schmidt-Ott, A. Characterization of agglomerates by condensation-induced restructuring *J. Aerosol Sci.* **1992**, *23*, S357-S360.

20 Zhang, R.; Khalizov, A.; Wang, L.; Hu, M.; Xu, W. Nucleation and growth of nanoparticles in the atmosphere. *Chem. Rev.* **2012**, *112*, 1957-2011.

21 Schnitzler, E. G.; Jäger, W. The benzoic acid-water complex: A potential atmospheric nucleation precursor studied using microwave spectroscopy and *ab initio* calculations. *Phys. Chem. Chem. Phys.* **2014**, *16*, 2305-2314.

22 Donahue, N. M.; Robinson, A. L.; Stanier, C. O.; Pandis, S. N. Coupled partitioning, dilution, and chemical aging of semivolatile organics. *Environ. Sci. Technol.* **2006**, *40*, 2635-2643.

23 Schnitzler, E. G.; McDonald, K. M. Characterization of low temperature vapour pressure estimates for secondary organic aerosol applications. *Atmos. Environ.* **2012**, *56*, 9-15.

24 Tritscher, T.; *et al.* Changes of hygroscopicity and morphology during ageing of diesel soot. *Environ. Res. Lett.* **2011**, *6*, 034026 (10 pp.). See bibliography for complete list of authors.

25 Saathoff, H.; Naumann, K.-H.; Schnaiter, M.; Schöck, W.; Möhler, O.; Schurath, U.; Weingartner, E.; Gysel, M.; Baltensperger, U. Coating of soot and $(NH_4)_2SO_4$ particles by ozonolysis products of α-pinene *J. Aerosol Sci.* **2003**, *34*, 1297-1321.

26 Schnaiter, M.; Linke, C.; Möhler, O.; Naumann, K.-H.; Saathoff, H.; Wagner, R.; Schurath, U. Absorption amplification of black carbon internally mixed with secondary organic aerosol. *J. Geophys. Res.* **2005**, *110*, D19204 (11 pp.).

27 Khalizov, A. F.; Lin, Y.; Qiu, C.; Guo, S.; Collins, D.; Zhang, R. Role of OH-initiated oxidation of isoprene in aging of combustion soot. *Environ. Sci. Technol.* **2013**, *47*, 2254-2263.

28 Qui, C.; Khalizov, A. F.; Zhang, R. Soot aging from OH-initiated oxidation of toluene. *Environ. Sci. Technol.* **2012**, *46*, 9464-9472.

29 Simpson, I. J.; *et al.* Characterization of trace gases measured over Alberta oil sands mining operations: 76 speciated C_2-C_{10} volatile organic compounds (VOCs), CO_2, CH_4, CO, NO, NO_2, NO_y, O_3 and SO_2. *Atmos. Chem. Phys.* **2010**, *10*, 11931-11954. See bibliography for complete list of authors.

30 Buczynska, A. J.; Krata, A.; Stranger, M.; Locateli Godoi, A. F.; Kontozova-Deutsch, V.; Bencs, L. Naveau, I.; Roekens, E.; Van Grieken, R. Atmospheric BTEX-concentrations in an area with intensive street traffic. *Atmos. Environ.* **2009**, *43*, 311-318.

31 Henze, D. K.; Seinfeld, J. H.; Ng, N. L.; Kroll, J. H.; Fu, T.-M.; Jacob, D. J.; Heald, C. L. Global modeling of secondary organic aerosol formation from aromatic hydrocarbons: High- vs. low-yield pathways. *Atmos. Chem. Phys.* **2008**, *8*, 2405-2421.

32 Olofsson, N.-E.; Bladh, H.; Bohlin, A.; Johnsson, J.; Bengtsson, P.-E. Are sooting premixed porous-plug burner flames one-dimensional? A laser-based experimental investigation. *Combust. Sci. Technol.* **2013**, *185*, 293-309.

33 Migliorini, F.; De Iuliis, S.; Cignoli, F.; Zizak, G. How "flat" is the rich pre-mixed flame produced by your McKenna burner? *Combust. Flame* **2008**, *153*, 384-393.

34 Ruiz, P. A.; Lawrence, J. E.; Ferguson, S. T.; Wolfson, J. M.; Koutrakis, P. A counter-current parallel-plate membrane denuder for the non-specific removal of trace gases. *Environ. Sci. Technol.* **2006**, *40*, 5058-5063.

35 Bennett, J. F.; Collin, F.; Hastie, D. R. A laboratory flow reactor with gas particle separation and on-line MS/MS for product identification in atmospherically important reactions. *Atmos. Meas. Tech.* **2009**, *2*, 813-823.

36 Rader, D. J.; McMurry, P. H. Application of the tandem differential mobility analyzer to studies of droplet growth or evaporation. *J. Aerosol Sci.* **1986**, *7*, 771-787.

37 Ghazi, R.; Tjong, H.; Soewono, A.; Rogak, S. N.; Olfert, J. S. Mass, mobility, volatility, and morphology of soot particles generated by a McKenna and inverted burner *Aerosol Sci. Technol.* **2013**, *47*, 395-405.

38 Cross, E. S.; *et al.* Soot particle studies – instrument inter-comparison – project overview. *Aerosol Sci. Technol.* **2010**, *44*, 592-611. See bibliography for complete list of authors.

39 Slowik, J. G.; *et al.* An inter-comparison of instruments measuring black carbon content of soot particles. *Aerosol Sci. Technol.* **2007**, *41*, 295-314. See bibliography for complete list of authors.

40 Parsons, M. T.; Sydoryk, I.; Lim, A.; McIntyre, T. J.; Tulip, J.; Jäger, W.; McDonald, K. Real-time monitoring of benzene, toluene, and *p*-xylene in a photoreaction chamber with a tunable mid-infrared laser and ultraviolet differential optical absorption spectroscopy. *Appl. Opt.* **2011**, *50*, A90-A99.

41 Olfert, J. S.; Collings, N. New method for particle mass classification – the Couette centrifugal particle mass analyzer. *J. Aerosol Sci.* **2005**, *36*, 1338-1352.

42 Olfert, J. S.; Reavell, K. St. J.; Rushton, M. G.; Collings, N. The experimental transfer function of the Couette centrifugal particle mass analyzer. *J. Aerosol Sci.* **2006**, *37*, 1840-1852.

43 Plane, J. M. C.; Saiz-Lopez, A. UV-Visible Differential Optical Absorption Spectroscopy. In *Analytical Techniques for Atmospheric Measurement*; Heard, D. E., Ed.; Blackwell: Cambridge, MA, 2006; pp. 147-188.

44 Atkinson, R. Product studies of gas-phase reactions of organic compounds. *Pure Appl. Chem.* **1998**, *70*, 1335-1343.

45 Sorensen, C. M. The mobility of fractal aggregates: A review. *Aerosol Sci. Technol.* **2011**, *45*, 765-779.

46 Park, K.; Cao, F.; Kittelson, D. B.; McMurry, P. H. Relationship between particle mass and mobility for diesel exhaust particles. *Environ. Sci. Technol.* **2003**, *37*, 577-583.

47 Nakao, S.; Tang P.; Tang, X.; Clark, C. H.; Qi, L.; Seo, E.; Asa-Awuku, A.; Cocker, D., III. Density and elemental ratios of secondary organic aerosol: Application of a density prediction method *Atmos. Environ.* **2013**, *68*, 273-277.

48 Borrás, E.; Torajada-Genaro, L. A. Secondary organic aerosol formation from the photo-oxidation of benzene *Atmos. Environ.* **2012**, *47*, 154-163.

49 Ng, N. L.; Kroll, J. H.; Chan, A. W. H.; Chhabra, P. S.; Flagan, R. C.; Seinfeld, J. H. Secondary organic aerosol formation from *m*-xylene, toluene, and benzene. *Atmos. Chem. Phys.* **2007**, *7*, 3909-3922.

50 Atkinson, R.; Arey, J. Atmospheric degradation of volatile organic compounds. *Chem. Rev.* **2003**, *103*, 4605-4638.

51 Shrestha, M.; Zhang, Y.; Ebben, C. J.; Martin, S. T.; Geiger, F. M. Vibrational sum frequency generation spectroscopy of secondary organic material produced by condensational growth from α-pinene ozonolysis. *J. Phys. Chem. A* **2013**, *117*, 8427-8436.

52 Lui, P.; Zhang, Y.; Martin, S. T. Complex refractive indices of thin films of secondary organic materials by spectroscopic ellipsometry from 220 to 1200 nm. *Environ. Sci. Technol.* **2013**, *47*, 13594-13601.

53 White, S. J.; Jamie, I. M.; Angove, D. E. Chemical characterization of semi-volatile and aerosol compounds from the photooxidation of toluene and NO_x. *Atmos. Environ.* **2014**, *83*, 237-244.

54 Forstner, H. J. L.; Flagan, R. C.; Seinfeld, J. H. Secondary organic aerosol from the photooxidation of aromatic hydrocarbons: Molecular composition. *Environ. Sci. Technol.* **1997**, *31*, 1345-1358.

55 Huang, M.; Zhang, W.; Hao, L.; Wang, Z.; Fang, L.; Kong, R.; Shan, X.; Liu, F.; Sheng, L. Experimental study of photooxidation products of ethylbenzene. *J. Environ. Sci.* **2010**, *22*, 1570-1575.

56 Tkacik, D. S.; Presto, A. A.; Donahue, N. M.; Robinson, A. L. Secondary organic aerosol formation from intermediate-volatility organic compounds: Cyclic, linear, and branched alkanes. *Environ. Sci. Technol.* **2012**, *46*, 8773-8781.

57 Lambe, A. T.; *et al.* Transitions from functionalization to fragmentation reactions of laboratory secondary organic aerosol (SOA) generated from the OH oxidation of alkane precursors. *Environ. Sci. Technol.* **2012**, *46*, 5430-5437. See bibliography for complete list of authors.

58 Shakya, K. M.; Griffin, R. J. Secondary organic aerosol from photooxidation of polycyclic aromatic hydrocarbons. *Environ. Sci. Technol.* **2010**, *44*, 8134-8139.

59 Metcalf, A. R.; Loza, C. L.; Coggon, M. M.; Craven, J. S.; Jonsson, H. H.; Flagan, R. C.; Seinfeld, J. H. Secondary organic aerosol coating formation and evaporation: Chamber studies using black carbon seed aerosol and the singe-particle soot photometer *Aerosol Sci. Technol.* **2013**, *47*, 326-347.

60 Massoli, P.; *et al.* Relationship between aerosol oxidation level and hygroscopic properties of laboratory generated secondary organic aerosol (SOA) particles. *Geophys. Res. Lett.* **2010**, *37*, L24801 (5 pp.). See bibliography for complete list of authors.

61 Lee, J. Y.; Hildemann, L. M. Surface tensions of solutions containing dicarboxylic acid mixtures. *Atmos. Environ.* **2014**, *89*, 260-267.

9 Surface tension of secondary organic aerosol derived from *m*-xylene determined by soot aggregate aging

9.1. Introduction

Atmospheric aerosols impact climate both directly, by scattering and absorbing solar radiation, and indirectly, by altering cloud albedo and lifetime.[1] However, of all atmospheric constituents, aerosols have the greatest uncertainty in radiative forcing.[2] Secondary organic aerosol (SOA), generated from the photo-oxidation of volatile organic compounds (VOCs), exerts a negative radiative forcing on climate. Furthermore, in climate models, the concentration of cloud condensation nuclei (CCN) is influenced by SOA formation and growth,[3] processes that in turn depend on several physical properties of the particles, such as volatility, density, and surface tension. While many measurements of the volatility[4] and density[5] of SOA have been reported, no measurement of the surface tension of SOA has been reported, because prohibitively small samples are produced.[6]

In contrast to SOA, atmospheric black carbon (BC) exerts a positive radiative forcing on climate, lesser in magnitude to only that of carbon dioxide.[7] BC consists of soot aggregates that are emitted by biomass burning[8] or diesel combustion[9] and is composed of primary particles of graphitic carbon arranged in branched structures.[10] The optical properties of the aggregates can change during their lifetime, as a result of restructuring and/or lensing caused by coatings[11] (of SOA, for example[12]). Since the aggregates are fractal, a much more compact arrangement of the primary particles is possible. In laboratory experiments, restructuring of aggregates has been observed to occur due to a variety of atmospherically-relevant species, either by wetting (at saturation ratios of equal or less than one) or condensation (at saturation ratio greater than one). For example, soot aggregates decrease in mobility diameter when exposed to products of propene ozonolysis, although the products have such high saturation vapour pressures that they

never reach saturation to form SOA.[13] Soot aggregates also restructure due to persistent liquid coatings caused by condensation at (super-) saturation of less volatile oxidation products of α-pinene ozonolysis.[14] Restructuring, whether by wetting or condensation, is theoretically expected to depend on surface tension.[15] However, the most thorough studies to date have not demonstrated an unequivocal dependence. For example, soot aggregates exposed to saturated vapours of ethanol and dimethyl sulfoxide/water (1:1 mixture by volume) collapse to the same final mobility diameter, in spite of the large difference in surface tension.[16] Further complicating the issue is recent evidence that collapse of fractal aggregates across many orders of magnitude, from nano-particles to comets, is largely independent of aggregating forces.[17]

Here, using tandem differential mobility analysis, I provide key insights into two questions: (*i*) Does soot aggregate restructuring depend on coating surface tension? (*ii*) What is the surface tension of a representative anthropogenic SOA? I investigated the condensation-induced restructuring of mono-disperse soot aggregates generated by a pre-mixed ethylene flame. I demonstrate that soot aggregate restructuring due to different neat organic coatings increases with surface tension. In turn, I use soot aggregates as novel probes to make the first measurement of the surface tension of SOA produced from the photo-oxidation of *m*-xylene. I also discuss implications of the measured surface tension, particularly regarding nucleation, condensational growth, and volatility of SOA. My results may improve and constrain global climate models.

9.2. Methods

The experiments were carried out using a smog chamber, which has been described in detail previously.[12,22] The cubic chamber has an approximate volume of 1.8 m^3 and is constructed of 0.127 mm thick perfluoroalkoxy (PFA) film (Ingeniven). It can be irradiated by up to twenty-four 32 W black lights with peak emission at 350 nm. A mixing fan and a temperature and relative humidity probe are installed in the chamber. Emission from a broadband deuterium light source is directed through the chamber using fiber optics. The transmitted light is directed to a spectrometer to facilitate differential optical absorption spectroscopy at wavelengths of 240-286 nm.

A schematic of the experiment setup used during soot injection is shown in Figure 9.1.a. A pre-mixed flat-flame McKenna burner was used to generate the soot. The flow rates of

ethylene (Praxair, 99.5%) and air were 1.1 L min^{-1} and 8 L min^{-1}, respectively. Air was supplied by a pure air generator (Aadco, Model 737). Nitrogen was used as sheath gas, at a flow rate of 30 L min^{-1}. Soot aggregates were sampled from a height of 27 cm above the flame. The nascent aggregates were passed through a 30 cm diffusion dryer, composed of tubular mesh packed in anhydrous calcium sulfate (Hammond Drierite). The dried aggregates were then passed through an injector dilutor, supplied with 30 psi of nitrogen, and a thermo-denuder (TD), heated to 573 K. The denuded aggregates were passed through an X-ray neutralizer (TSI, Model 3087) to obtain an equilibrium charge distribution. The neutralized aggregates were passed through a differential mobility analyzer (DMA; TSI, Model 3081) set to a single voltage, with sample and sheath flow rates of 1.7 L min^{-1} and 6.5 L min^{-1}, respectively. The size-selected aggregates were then injected into the smog chamber, until the particle number concentration was at least 1000 cm^{-3}, as measured by a condensation particle counter (CPC; TSI, Model 3771). For example, in the experiment with aggregates initially 150 nm in mobility diameter, an initial number concentration of 3000 cm^{-3} was used; however, in the experiment with aggregates

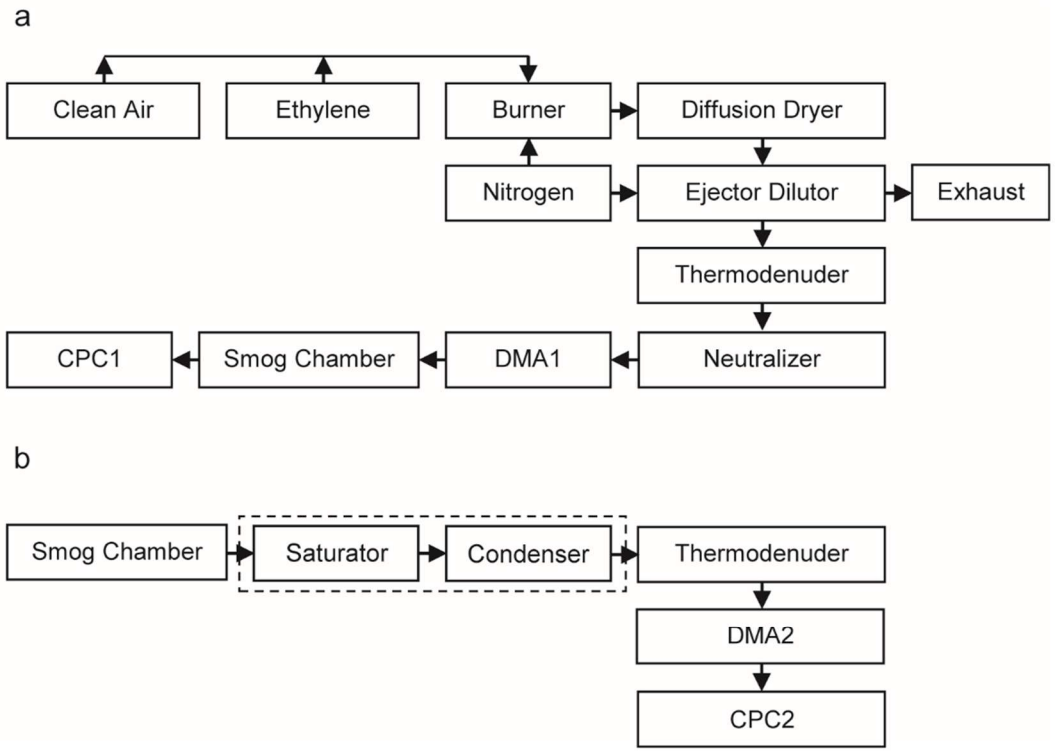

Figure 9.1. Schematic of experimental setup during (*a*) injection and (*b*) sampling. The rectangle with the dotted outline indicates the saturator-condenser apparatus that was used only when the smog chamber was used a residence chamber; during photo-oxidation, it was removed. DMA: differential mobility analyzer; CPC: condensation particle counter.

initially 300 nm in mobility diameter, an initial number concentration of about 1000 cm^{-3} was used, because very few of these larger particles are produced by the flame, as shown in Figure 9.2. The initial particle number concentration constrained the length of the experiments, as particles were continuously lost to the walls of the chamber. No make-up air was provided, so the volume of the chamber decreased, causing the rate of deposition to increase.

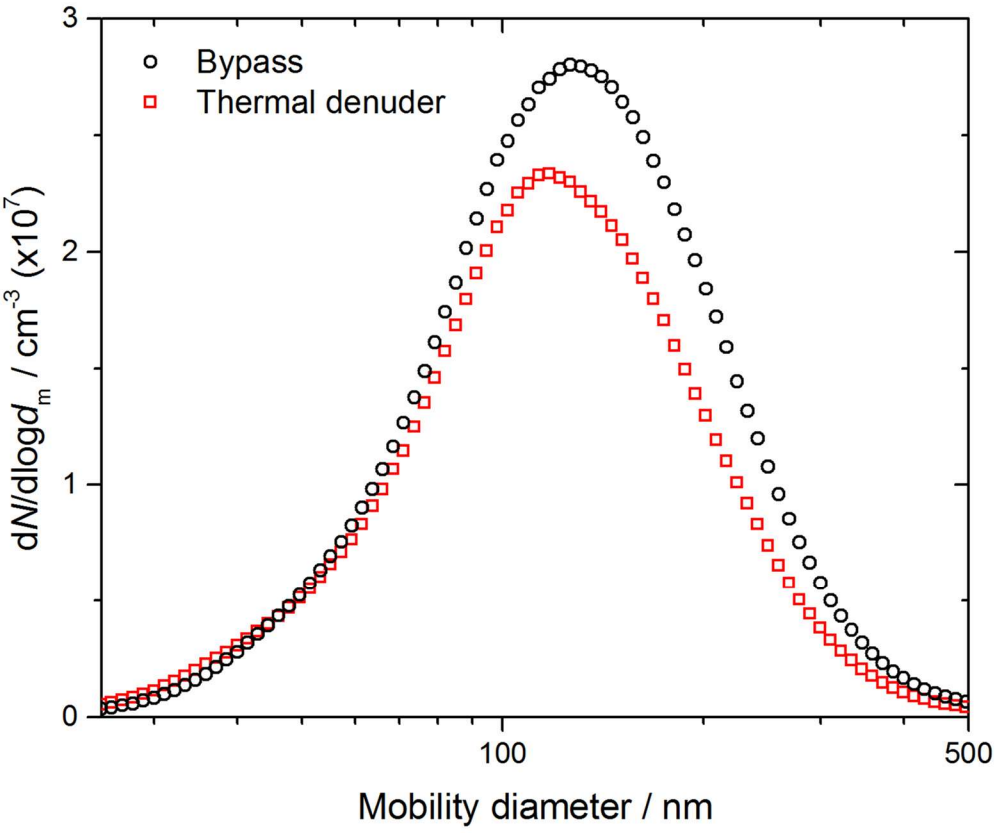

Figure 9.2. Size distributions of soot aggregates sampled from the McKenna burner with and without denuding.

Table 9.1. Liquid-air surface tensions of compounds in the basis set at 293 K.

	Surface tension / mN m^{-1}
Tridecane	26.1
Pentadecane	27.1
o-Xylene	30.1
Oleic acid	32.8
Furfural	41.9
Diethylene glycol	44.8
Ethylene glycol	47.7
Glycerol	64.0

Once a sufficient number concentration was obtained, aggregates were sampled from the chamber through a TD, as shown in Figure 9.1.b. The initial mobility diameter of the

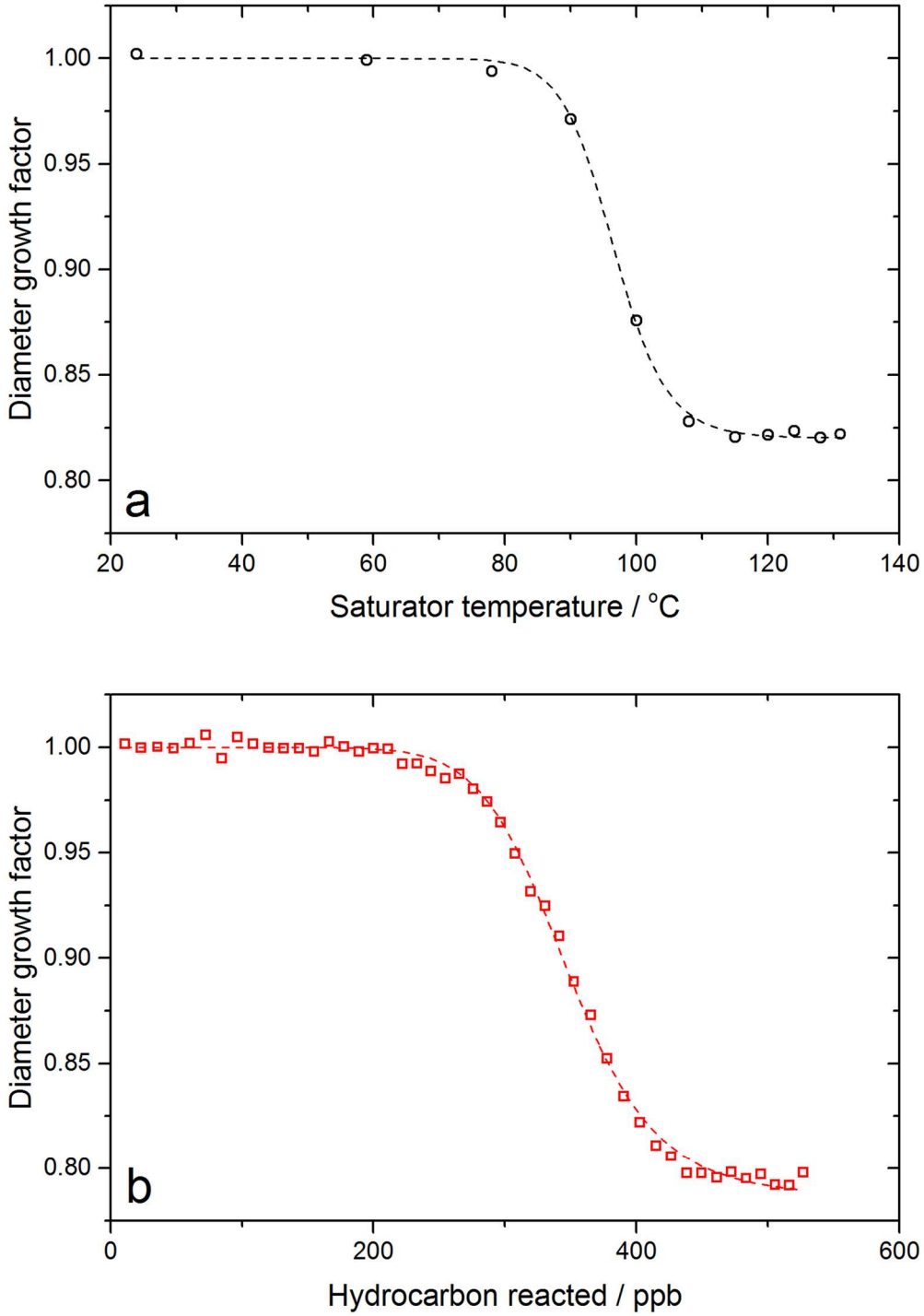

Figure 9.3. Decrease in diameter growth factor (ratio of final and initial mobility diameters) observed for initially 300 nm aggregates during (*a*) temperature ramp of saturator-condenser apparatus containing oleic acid and (*b*) photo-oxidation of *m*-xylene.

aggregates was measured using a DMA (TSI, Model 3081) and CPC (TSI, Model 3776), in the absence of the saturator-condenser apparatus. Since the aggregates were mono-disperse, the typical inversion used by commercial software was inadequate.[23] Consequently, the DMA voltage was stepped rather than scanned continuously – giving a response spectrum, rather than an inverted particle distribution. Each spectrum was measured in 11 voltage steps. At each voltage, the number concentration was taken as the average of 15 consecutive measurements. After setting the first voltage, there was a delay of 20 s before beginning to average with the CPC; after setting the remaining voltages, there was a delay of 10 s. Following these measurements, the saturator-condenser apparatus was placed between the chamber and the TD. The saturator consisted of a large test-tube containing 1-2 mL of a neat organic liquid, heated in an oil bath. The eight neat coatings and their liquid-air surface tensions at 293 K are listed in Table 9.1. At room temperature, no change in the mobility diameter of the aggregates was observed. As the temperature of the oil bath was increased, the vapour pressure of the organic species increased, so more coating formed as the sample suddenly cooled downstream of the saturator; as a result, the mobility diameter of the aggregates decreased until it converged at the final mobility diameter, as shown in Figure 9.3. A temperature ramp was done for each neat liquid coating. Following each, aggregates were again sampled directly from the chamber to verify that there was no change in the initial mobility diameter.

Once temperature ramps were done for all eight coatings, about 2 ppm of *m*-xylene (Fisher, 99.9%) was added to the chamber, followed by 1 mL of hydrogen peroxide (Sigma, 30% w/w in water). The black lights were then turned on to photolyze hydrogen peroxide, producing a steady concentration of hydroxyl radical, which initiated the pseudo-first-order photo-oxidation of *m*-xylene. The resulting oxidation products quickly reached their saturation concentrations and began to coat the soot aggregates. As the amount of *m*-xylene reacted increased, the mobility diameter of the aggregates decreased until it converged at the final mobility diameter.

Following each experiment, a flow rate of 10 L min^{-1} of clean dry air, supplied by the clean air generator, was passed through a bubbler of hydrogen peroxide into the irradiated chamber for at least 12 h. Afterwards, a flow rate of 10 L min^{-1} of clean dry air was passed into the dark chamber for at least 12 h.

9.3. Results and discussion

9.3.1. Surface tension dependence of soot aggregate restructuring

Aggregates were passed through a saturator-condenser apparatus, containing neat organic liquids with surface tensions between 25 and 65 mN m^{-1}. Groups of compounds known to be SOA precursors or constituents (alkane, aromatic, carboxylic acid, aldehyde, and alcohol representatives) are included in the experimental basis set. Soot aggregate restructuring is known to depend on coating mass (or volume).[12] Consequently, the mobility diameter of the soot aggregates decreased with the temperature of the saturator, an indirect measure of coating mass. Eventually, the mobility diameter reached a steady value, and I take this as the final mobility diameter.

The experimental results are summarized in Figure 9.4. All aggregates, except those with an initial mobility diameter of 100 nm (which have the highest initial effective density[12]), exhibit a range of values for the decrease in mobility diameter. In general, coatings with the lowest surface tensions (tridecane and pentadecane) induce less collapse than those with the highest

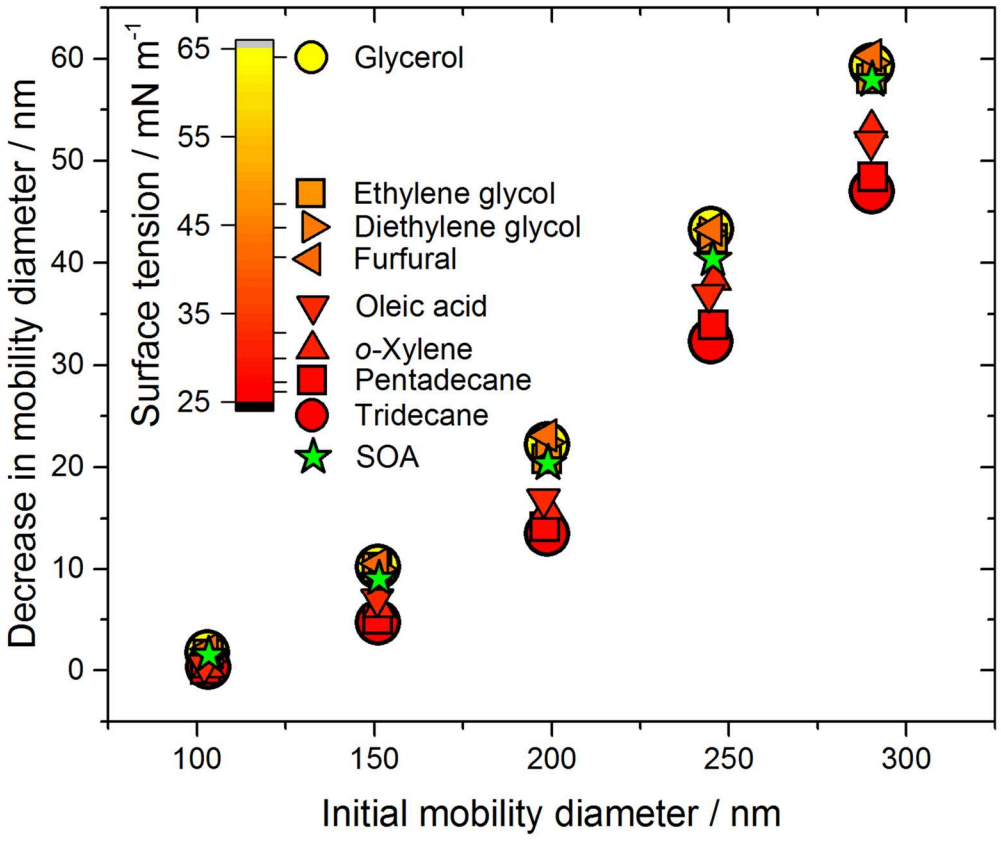

Figure 9.4. Extent of soot aggregate restructuring due to coatings of eight organic liquids and SOA.

surface tensions (diethylene glycol, ethylene glycol, and glycerol). The surface tension dependence is systematic, as shown in Figure 9.5, which gives the diameter growth factor, *Gfd* (the ratio of final and initial mobility diameters), as a function of coating surface tension for aggregates that are initially 150, 200, 250, and 300 nm in diameter. At these mobility diameters, there is an excellent correlation between *Gfd* and coating surface tension, and exponential fits result in R^2 values between 0.90 (for 300 nm aggregates) and 0.95 (for 150 nm aggregates). Consequently, my results provide unequivocal evidence that the extent of soot aggregate restructuring increases with the coating surface tension, answering the first question posed

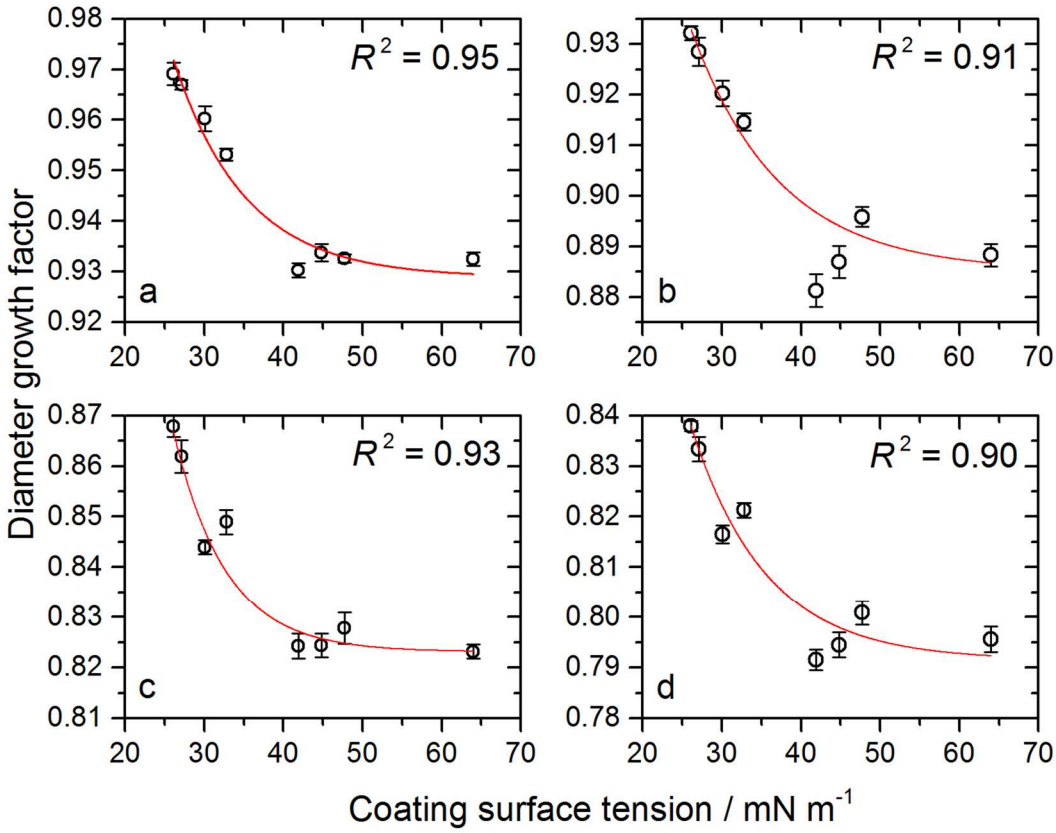

Figure 9.5. Coating surface tension dependence of soot aggregate restructuring. (*a*) Initial mobility diameter of 150 nm (exponential regression; $y = 0.9289 + 0.7613e^{-0.110x}$; R^2=0.95). (*b*) Initial mobility diameter of 200 nm (exponential regression; $y = 0.8851 + 0.5000e^{-0.090x}$; R^2=0.91). (*c*) Initial mobility diameter of 250 nm (exponential regression; $y = 0.8231 + 2.2656e^{-0.151x}$; R^2=0.93). (*d*) Initial mobility of 300 nm (exponential regression; $y = 0.7915+0.7326e^{-0.106x}$; R^2=0.90). Error bars indicate three standard deviations calculated from at least three consecutive measurements of initial and final mobility diameters. SOA-induced restructuring of soot aggregates of initial mobility diameters of 150, 200, 250, and 300 nm results in *Gfd* values of 0.940±0.002, 0.898±0.004, 0.835±0.004, and 0.801±0.006, respectively.

above. In other words, the collapse of soot – and likely fractal aggregates in general – is not as strictly independent of aggregating forces as recently proposed.[17]

The coating surface tension dependence of restructuring is well represented by the exponential fits (see Figure 9.5). Furthermore, this functional form is reproduced theoretically, based on a detailed dynamics model, in which soot restructuring was simulated numerically by solving the equations of motion of nine and 12 individual primary particles, taking into account van der Waals, capillary, and bridging forces.[24-27] Following restructuring, at a given coating surface tension, the larger aggregates have a lower value of *Gfd* than the smaller aggregates. For both sizes of aggregates, the *Gfd* is a strictly decreasing function of surface tension, and the dependence is well represented by an exponential fit, in agreement with my experiments. Furthermore, this agreement is evidence that restructuring occurs during condensation (because evaporation is not modelled) in contradiction of a recent proposal.[28]

In passing, I note that it is reasonable to adopt the mass-mobility relationship previously derived for the initial soot aggregates ($1.2\times10^{-5} d_m^{2.24}$), because the same combustion conditions

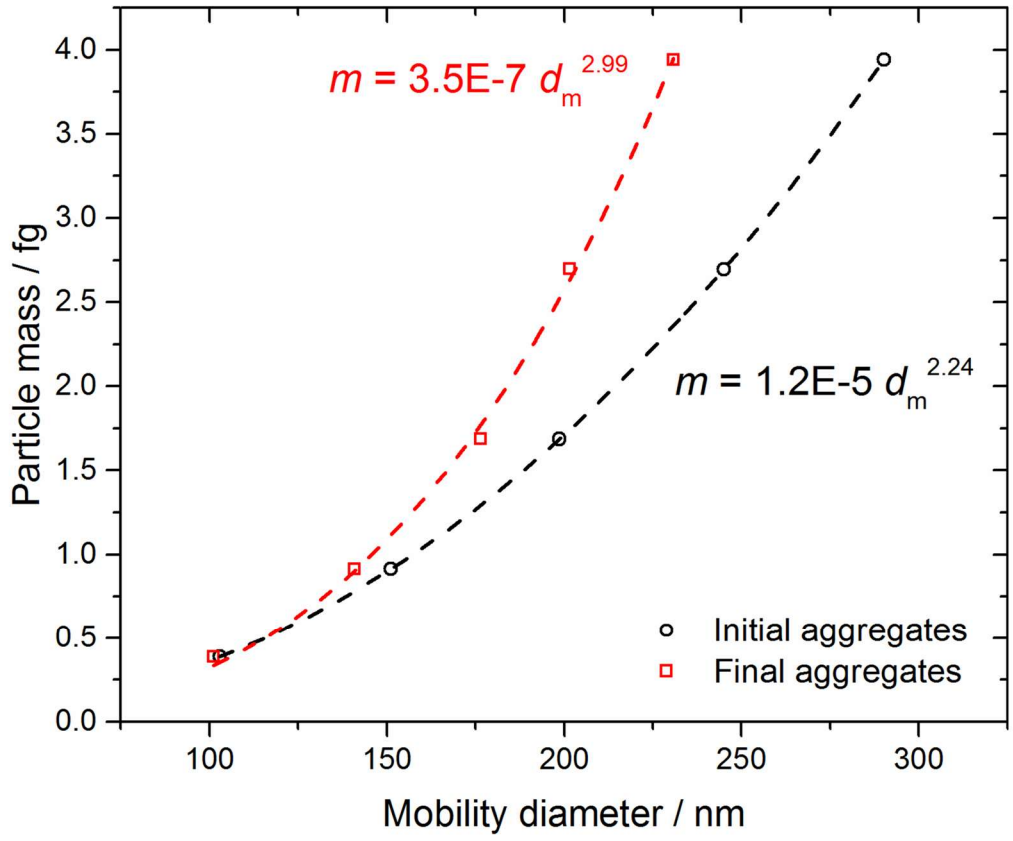

Figure 9.6. Mass-mobility relationship for aggregates restructured after coating with glycerol, when adopting the relationship for initial aggregates determined under the same combustion conditions in Reference 12.

were used.[12] Consequently, the masses of the aggregates can be estimated from their initial mobility diameters. Since the aggregates were denuded, the masses did not change – only the mobility diameters. Fitting to the final mobility diameters due to coatings of glycerol, the neat liquid coating with the highest surface tension, a mass-mobility relationship of $3.5\times10^{-7} d_m^{2.99}$ was determined, as shown in Figure 9.6. The exponent of about three indicates that the asymptotes in Figure 9.5 correspond to the greatest possible extent of restructuring, leading to spherical particles.[29] Of course, the effective density of the aggregate is still much less than the material density of soot, because the spherical aggregates are porous.

9.3.2. Surface tension of secondary organic aerosol

The basis set of liquids includes compounds with functional groups identified in precursors and constituents of SOA. Furthermore, SOA from *m*-xylene has previously been observed to be a liquid.[30] Consequently, my chamber-generated SOA lies within the domain of the exponential fits in Figure 9.5. For each initial size of aggregates, the aggregate population that was exposed to neat organic liquids was also exposed to photo-oxidation products of *m*-xylene in the smog chamber. Analogous to increasing saturator temperature, increasing reaction time led to a decrease in the mobility diameter of the aggregates until a final value was reached. I used initial *m*-xylene concentrations of about 2 ppm, which are too high to be representative of atmospheric concentrations; however, these concentrations were required to coat the aggregates sufficiently to reach complete restructuring before the aggregate concentrations decayed too much by deposition to the chamber walls. I note that even higher concentrations have been used in other studies of the optical and physical properties of SOA (for example, the refractive index[31]). Using the values of *Gfd* determined for coatings of SOA derived from the photo-oxidation of *m*-xylene as input for the exponential fits, the mean surface tension of this representative anthropogenic SOA was determined to be 39 ± 3 mN m^{-1}; the uncertainty indicates one standard deviation about the mean. The relative humidity in the smog chamber was less than 10%, so water uptake by the SOA coating is negligible, and the measured surface tension is representative of the SOA constituents. At any given coating mass, even before the final mobility diameter is reached, a surface tension dependence should be present; thus, for aggregates lightly coated with SOA, which becomes more hygroscopic with photo-chemical aging,[32] water uptake will result in further collapse, not due to additional coating volume alone, but also to the increase in surface

tension of the coating mixture. Furthermore, since SOA coatings generated from other aromatic precursors have previously been shown to result in the same final extent of restructuring,[12] I conclude that they must have approximately the same surface tension.

Though other methods to measure the surface tension of atmospheric aerosols are emerging,[33,34] the surface tension of SOA has not been measured to date, so my value can be compared to only a few previously assumed or estimated values. The surface tension of SOA has been estimated from experimental data in only one study: a highly uncertain value of 110 ± 90 mN m^{-1} was given for SOA derived from monoterpenes in a smog chamber.[35] Other values – for example, 25 and 50 mN m^{-1} – have been assumed in modelling studies.[19,20] My value falls within this range, and it is reasonable considering the oxygenated nature of SOA. However, it is expected to be even greater for ambient SOA, which has been further photochemically aged.[18] For example, second and third generation products will be more oxygenated than first generation products,[36] and those functional groups increase hydrogen bonding in the condensed phase, which in turn increases the surface tension. My value, then, is likely a lower limit for ambient SOA; consequently, a surface tension of 25 mN m^{-1}, sometimes assumed in modelling studies, is unrealistic. Based on the modelling of Pierce et al., increasing the surface tension of ambient SOA from 25 to 39 mN m^{-1} implies that the condensing species involved in nucleation and growth have comparatively low saturation vapour pressures,[20] consistent with recent field measurements.[21] Since surface tension is a critical parameter in predictions of CCN, my results provide an essential constraint on global climate models.[3,20]

Finally, I note that SOA can also occur in an amorphous solid phase under certain conditions.[37] For SOA derived from toluene, viscosity increases with decreasing RH; specifically, at 16.5 % RH, large droplets ($d_p > 20$ μm) of SOA have been shown to shatter when poked by a sharp needle.[38] If the SOA coatings in the present study are similar – namely, if they do not flow – soot restructuring would not be expected in the chamber but in the TD, because the coatings will have significantly lower viscosity and surface tension at elevated temperatures. On the other hand, the temperature in the smog chamber during the present experiments approached 313 K, relatively high compared to the temperature of the poke-flow experiments (295 K),[38] so the SOA may indeed flow and induce soot restructuring *in situ*. Future studies of the effect of RH on SOA-induced soot restructuring could help in unambiguously determining the phase of the SOA coatings.

9.4. Conclusions

I have shown that the restructuring of soot aggregates in the atmosphere depends on the surface tension of the coating; specifically, the extent of restructuring increases exponentially with coating surface tension. This finding provides a constraint on the direct effect of BC in climate models. I have also shown that the surface tension of SOA derived from *m*-xylene is 39 ± 3 mN m^{-1}. This finding is an important constraint on the indirect effect of CCN in climate models.

References

1 Levy, H., II; Horowitz, L. W.; Schwarzkopf, M. D.; Ming, Y.; Golaz, J.-C.; Naik, V.; Ramaswarmy, V. The roles of aerosol direct and indirect effects in past and future climate change. *J. Geophys. Res. Atmos.* **2013**, *118*, 4521-4532.

2 Boucher, O.; *et al.* Clouds and aerosols. In *Climate Change 2013: The Physical Science Basis. Contribution of Working Group I to the Fifth Assessment Report of the Intergovernmental Panel on Climate Change*; Stocker, T. F., Qin, G.-K., Plattner, M., Tignor, M., Allen, S. K., Boschung, J., Nauels, A., Xia, Y., Bex, V., Midgley, P. M., Eds.; Cambridge University Press: Cambridge, 2013; pp. 571-657. See bibliography for complete list of authors.

3 Riipinen, I.; Yli-Juuti, T.; Pierce, J. R.; Petäjä, T.; Worsnop, D. R.; Kulmala, M.; Donahue, N. M. The contribution of organics to atmospheric nanoparticle growth. *Nature Geosci.* **2012**, *5*, 453-458.

4 Tritscher, T.; *et al.* Volatility and hygroscopicity of aging secondary organic aerosol in a smog chamber. *Atmos. Chem. Phys.* **2011**, *11*, 11477-11496. See bibliography for complete list of authors.

5 Nakao, S.; Tang, P.; Tang, X.; Clark, C. H.; Qi, L.; Seo, E.; Asa-Awuku, A.; Cocker, D., III. Density and elemental ratios of secondary organic aerosol: Application of a density prediction model. *Atmos. Environ.* **2013**, *68*, 273-277.

6 Engelhart, G. J.; Moore, R. H.; Nenes, A.; Pandis, S. N. Cloud condensation nuclei activity of isoprene secondary organic aerosol. *J. Geophys. Res.* **2011**, *116*, D02207 (11 pp.).

7 Ramanathan, V.; Carmichael, G. Global and regional climate changes due to black carbon. *Nature Geosci.* **2008**, *1*, 221-227.

8 Keywood, M.; *et al.* Fire in the air: Biomass burning impacts in a changing climate. *Crit. Rev. Environ. Sci. Technol.* **2013**, *43*, 40-83. See bibliography for complete list of authors.

9 Olfert, J. S.; Symonds, J. P. R.; Collings, N. The effective density and fractal dimension of particles emitted from a light-duty diesel vehicle with a diesel oxidation catalyst. *J. Aerosol Sci.* **2007**, *38*, 69-82.

10 Akhter, M. S.; Chughtai, A. R.; Smith, D. M. The structure of hexane soot. I: Spectroscopic studies. *Appl. Spectrosc.* **1985**, *39*, 143-153.

11 Cappa, C. D.; *et al.* Radiative absorption enhancements due to the mixing state of atmospheric black carbon. *Science* **2012**, *337*, 1078-1081. See bibliography for complete list of authors.

12 Schnitzler, E. G.; Dutt, A.; Charbonneau, A. M.; Olfert, J. S.; Jäger, W. Soot aggregate restructuring due to coatings of secondary organic aerosol derived from aromatic precursors. *Environ. Sci. Technol.* **2014**, *48*, 14309-14316.

13 Lu, Z.; Hao, J.; Hu, L.; Takekawa, H. The compaction of soot particles generated by spark discharge in the propene ozonolysis system. *J. Aerosol Sci.* **2008**, *39*, 897-903.

14 Schnaiter, M.; Linke, C.; Möhler, O.; Naumann, K.-H.; Saathoff, H.; Wagner, R.; Schurath, U.; Wehner, B. Absorption amplification of black carbon internally mixed with secondary organic aerosol. *J. Geophys. Res.* **2005**, *110*, D19204 (11 pp.).

15 Kütz, S.; Schmidt-Ott, A. Characterization of agglomerates by condensation-induced restructuring. *J. Aerosol Sci.* **1992**, *23*, S357-S360.

16 Miljevic, B.; Surawski, N. C.; Bostrom, T.; Ristovski, Z. D. Restructuring of carbonaceous particles upon exposure to organic and water vapours *J. Aerosol Sci.* **2012**, *47*, 48-57.

17 Zangmeister, C. D.; Radney, J. G.; Dockery, L. T.; Young, J. T.; Ma, X.; You, R.; Zachariah, M. R. Packing density of rigid aggregates is independent of scale. *Proc. Natl. Acad. Sci. U. S. A.* **2014**, *111*, 9037-9041.

18 Jimenez, J. L.; *et al.* Evolution of organic aerosols in the atmosphere. *Science* **2009**, *326*, 1525-1529. See bibliography for complete list of authors.

19 Bowman, F. M.; Odum, J. R.; Seinfeld, J. H.; Pandis, S. N. Mathematical model for gas-particle partitioning of secondary organic aerosol. *Atmos. Environ.* **1997**, *31*, 3921-3931.

20 Pierce, J. R.; Riiponen, I.; Kulmala, M.; Ehn, M.; Petäjä, T.; Junninen, H.; Worsnop, D. R.; Donahue, N. M. Quantification of the volatility of secondary organic compounds in ultrafine particles during nucleation events. *Atmos. Chem. Phys.* **2011**, *11*, 9019-9036.

21 Ehn, M.; *et al.* A large source of low-volatility secondary organic aerosol. *Nature*, 2014, **506**, 476-479. See bibliography for complete list of authors.

22 Parsons, M. T.; Sydoryk, I.; Lim, A.; McIntyre, T. J.; Tulip, J.; Jäger, W.; McDonald, K. Real-time monitoring of benzene, toluene, and *p*-xylene in a photoreaction chamber with a tunable mid-infrared laser and ultraviolet differential optical absorption spectroscopy. *Appl. Opt.* **2011**, *50*, A90-A99.

23 Rader, D. J. & McMurry, P. H. Application of the tandem differential mobility analyzer to studies of droplet growth or evaporation. *J. Aerosol Sci.* **7**, 771-787 (1986).

24 Gac, J. M.; Sosnowski T.; Gradoń L. Turbulent flow energy for aerosolization of powder particles. *J. Aerosol Sci.* **2008**, *39*, 113-126.

25 Li, S.; Marshall, J. S.; Liu, G.; Yao, Q. Adhesive particulate flow: The discrete-element method and its application in energy and environmental engineering. *Prog. Energ. Combust.* **2011**, *37*, 633-668.

26 Dörmann, M.; Schmid, H.-J. Simulation of capillary bridges between nanoscale particles. *Langmuir* **2014**, *30*, 1055-1062.

27 Kralchevsky, P. A.; Nagayama, K. Capillary forces between colloidal particles. *Langmuir* **1994**, *10*, 23-36.

28 Ma, X.; Zangmeister, C. D.; Gigault, J.; Mulholland, G. W.; Zachariah, M. R. Soot aggregate restructuring during water processing. *J. Aerosol Sci.* **2013**, *66*, 209-219.

29 Park, K.; Cao, F.; Kittelson, D. B.; McMurry, P. H. Relationship between particle mass and mobility for diesel exhaust particles. *Environ. Sci. Technol.* **2003**, *37*, 577-583.

30 Li, K.; Wang, W.; Ge, M.; Li, J.; Wang, D. Optical properties of secondary organic aerosols generated by photooxidation of aromatic hydrocarbons. *Sci. Rep.* **2014**, *4*, 4922 (9 pp.).

31 Liu, P.; Zhang, Y.; Martin, S. T. Complex refractive indices of thin films of secondary organic materials by spectroscopic ellipsometry from 220 to 1200 nm. *Environ. Sci. Technol.* **2013**, *47*, 13594-13601.

32 Massoli, P.; *et al.* Relationship between aerosol oxidation level and hygroscopic properties of laboratory generated secondary organic aerosol (SOA) particles. *Geophys. Res. Lett.* **2010**, *37*, L24801 (5 pp.). See bibliography for complete list of authors.

33 Noziére, B.; Baduel, C.; Jaffrezo, J.-L. The dynamic surface tension of atmospheric aerosol surfactants reveals new aspects of cloud activation. *Nature Comm.* **2014**, *5*, 3335 (7 pp.).

34 Morris, H. S.; Grassian, V. H.; Tivanski, A. V. Humidity-dependent surface tension measurements of individual inorganic and organic submicrometre liquid particles. *Chem. Sci.* **2015**, *6*, 3242-3247.

35 Koch, S.; Winterhalter, R.; Urerek, E.; Kollof, A.; Neeb, P.; Moortgat, G. Formation of new particles in the gas-phase ozonolysis of monoterpenes. *Atmos. Environ.* **2000**, *34*, 4031-4042.

36 Donahue, N. M.; *et al.* Aging of biogenic secondary organic aerosol via gas-phase OH radical reaction. *Proc. Natl. Acad. Sci. U. S. A.* **2012**, *109*, 13503-13508. See bibliography for complete list of authors.

37 Virtanen, A.; *et al.* An amorphous solid state of biogenic secondary organic aerosol particles. *Nature* **2010**, *467*, 824-827. See bibliography for complete list of authors.

38 Song, M.; Liu, P. F.; Hanna, S. J.; Zaveri, R. A.; Potter, K.; You, Y.; Martin, S. T.; Bertram, A. K. Relative humidity-dependent viscosity of secondary organic material from toluene photo-oxidation and possible implications for organics particulate matter over megacities. *Atmos. Chem. Phys. Discuss.* **2016**, doi:10.5194/acp-2016-14.

10 Conclusions

In this thesis, I described my studies of intermolecular interactions in atmospheric aggregates ranging in size from molecular-scale complexes to nano-scale aerosols and involving photo-oxidation products of aromatic volatile organic compounds (VOCs), using two distinctive experimental techniques in an interdisciplinary approach. Using quantum chemistry calculations and rotational spectroscopy, I investigated intermolecular interactions in complexes of water and carboxylic acids, determining their structures and internal dynamics. Using smog chamber experiments, I investigated intermolecular interactions in internally-mixed particles of secondary organic aerosol (SOA) and black carbon (BC), determining their morphological evolution.

In Chapters 3 and 4, I described my investigations of the monohydrates of two aromatic carboxylic acids: benzoic acid (BA) and *o*-toluic acid (OTA). I determined the lowest-energy isomer of each species in the gas phase. I examined the internal dynamics of each species, as well. For example, splitting of rotational lines was observed for BA monohydrate, due to internal rotation of water; however, no splitting was observed for OTA monohydrate, because the same motion does not connect equivalent minima, due to a rocking motion of the carboxylic acid group and the presence of the methyl substituent. Though the percentage of each acid hydrated in the gas phase under atmospheric conditions is predicted to be low, the interactions investigated are important in aerosol chemistry. Water and carboxylic acids are both known to participate, along with sulfuric acid and ammonia, in the formation of critical nuclei leading to new particle formation.[1,2] Furthermore, since the aromatic rings of the carboxylic acids are hydrophobic, in contrast with the hydrophilic acid groups to which I showed water hydrogen-

bonds, BA and OTA are surface active at the air-water interface of aqueous aerosols,[3,4] where they may decrease surface tension[5] and gas uptake.[6,7]

In Chapter 5, I described my investigation of the monohydrate of oxalic acid (OA), the smallest and most atmospherically-abundant dicarboxylic acid. I determined the two most stable isomers in the gas phase. In the lowest-energy isomer, water bridges the two carboxylic acid groups, lowering the barrier to decarboxylation and possibly catalysing overtone-induced decarboxylation in the atmosphere. In the other isomer, water hydrogen-bonds to only one acid group, as in the monohydrates of the aromatic carboxylic acids above, increasing the barrier to decarboxylation. Using *ab initio* calculations, I also showed that OA is unique among the C_2-C_6 α-ω dicarboxylic acids; for each of the higher homologues, the terminal isomer is much more stable and abundant in the atmosphere. Consequently, single-water catalysed enhancement of overtone-induced decarboxylation is likely a plausible sink for only OA. The interactions between OA and water are also of interest to aerosol chemistry. For example, OA monohydrate could be a nucleation precursor, since sites are available for hydrogen bonding to sulfuric acid or ammonia.[8,9] Furthermore, owing to the strength of interactions between OA and water, OA particles are very hygroscopic, leading to water uptake at low relative humidity (RH).[10]

In Chapter 6, I described my investigation of four methyl- and dimethylnapthalenes, small polycyclic aromatic hydrocarbons (PAHs) present in the atmosphere.[11] I determined the lowest-energy structures, in particular the orientations of the methyl groups. I also used the rotational spectra to examine methyl internal rotation in these species; counter-intuitively, the barrier to rotation is lower for 1,2-dimethylnaphthalene than 1,3-dimethylnaphthalene, because the crowding of the methyl substituents increases the energy of the minimum more than that of the transition state. Other investigators could use the reported rotational spectra for atmospheric (or astronomical) detection of these species. These PAH monomers are the only species in this thesis that are not aggregates, but they are involved in aerosol chemistry as precursors to SOA[12] and constituents of nascent soot aggregates,[13] so this chapter bridges the preceding chapters regarding rotational spectroscopy of complexes and the following chapters regarding smog chamber studies of SOA and BC.

In Chapters 8 and 9, I described my investigations of the morphological evolution of BC particles due to liquid coatings in smog chamber experiments. I determined the mass-dependence of BC restructuring due to coatings of SOA from a homologous series of four

aromatic precursors: benzene, toluene, ethylbenzene, and *p*-xylene. Below a certain threshold coating mass, corresponding to a mass growth factor of about two, no restructuring occurs. Once this threshold is reached, restructuring increases with coating mass until the particles reach a final, much more compact morphology. The restructured particles have a mass-mobility exponent less than three, so they are not spherical. The mass-dependence and final extent of restructuring are the same for SOA coatings from all four precursors. I also demonstrated the surface tension-dependence of BC restructuring, using a test set of organic liquid coatings. After being coated with the highest-surface-tension liquid, glycerol, the restructured particles have a mass-mobility exponent of three, so they are spherical, but porous. Subsequently using BC particles as novel probes, I estimated the surface tension of SOA derived from the photo-oxidation of *m*-xylene at low RH to be 39 ± 3 mN m^{-1}, much higher than a value of 25 mN m^{-1} that has been sometimes assumed in the past.[14,15] Since different aromatic precursors lead to SOA coatings that restructure BC similarly, the SOA coatings from different precursors must have similar surface tensions. If a surface tension of 39 mN m^{-1}, instead of 25 mN m^{-1}, were assumed in a model of nucleation and condensational growth fitted to ambient observations, the SOA constituents would be required to have comparatively low vapour pressures.[15] This implication is consistent with the recent observation of low-volatility compounds in SOA.[16] These findings constrain both the direct and indirect aerosol effects on climate: the morphological (and optical) aging of BC was shown to depend on coating surface tension; the growth of new particles into cloud condensation nuclei is known to depend on surface tension,[15,17] which was determined for SOA.

The questions currently faced by atmospheric chemists are complex, and an inter-disciplinary approach is being increasingly adopted, as in the collaborative "Center for Aerosol Impacts on Climate and the Environment," to benefit from a wide variety of theoretical and experimental techniques.[18] In the preceding chapters, I showed how the distinctive techniques of computational chemistry, rotational spectroscopy, and photo-oxidation in a smog chamber can provide answers to fundamental and applied questions regarding atmospheric aggregates, including molecular complexes and internally-mixed aerosols. Cumulatively, the findings outlined above further our understanding of the fate and impact of atmospheric oxidation products of aromatic VOCs in the gas phase, at the air-water interface, and in the bulk aerosol phase.

References

1 Zhang, R.; Suh, I.; Zhao, J.; Zhang, D.; Fortner, E. C.; Tie, X.; Molina, L. T.; Molina, M. J. Atmospheric new particle formation enhanced by organic acids. *Science* **2004**, *304*, 1487-1490.

2 Zhao, J.; Khalizov, A.; Zhang, R.; McGraw, R. Hydrogen-bonding interaction in molecular complexes and clusters of aerosol nucleation precursors. *J. Phys. Chem. A* **2009**, *113*, 680-689.

3 Ottosson, N.; Romanova, A. O.; Söderström, J.; Björneholm, O.; Öhrwall, G.; Fedorov, M. V. Molecular sinkers: X-ray photoemission and atomistic simulations of benzoic acid and benzoate at the aqueous solution/vapor interface. *J. Phys. Chem. B* **2012**, *116*, 13017-13023.

4 McNeill, V. F.; Sareen, N.; Schwier, A. N. Surface-active organics in atmospheric aerosols. *Top. Curr. Chem.* **2014**, *339*, 201-260.

5 Facchini, M. C.; Mircea, M.; Fuzzi, S.; Charlson, R. J. Cloud albedo enhancement by surface-active organic solutes in growing droplets. *Nature* **1999**, *401*, 257-259.

6 McNeill, V. F.; Patterson, J.; Wolfe, G. M.; Thornton, J. A. The effect of varying levels of surfactant on the reactive uptake of N_2O_5 to aqueous aerosol. *Atmos. Chem. Phys.* **2006**, *6*, 1635-1644.

7 Shaloski, M. A.; Sobyra, T. B.; Nathanson, G. M. DCI transport through dodecyl sulfate films on salty glycerol: Effects of seawater ions on gas entry. *J. Phys. Chem. A* **2015**, *119*, 12357-12366.

8 Xu, Y.; Nadykto, A. B.; Yu, F.; Jiang, L.; Wang, W. Formation and properties of hydrogen-bonded complexes of common organic oxalic acid with atmospheric nucleation precursors. *THEOCHEM* **2010**, *951*, 28-33.

9 Xu, W.; Zhang, R. Theoretical investigation of interaction of dicarboxylic acids with common aerosol nucleation precursors. *J. Phys. Chem. A* **2012**, *116*, 4539-4550.

10 Ma, Q.; He, H.; Liu, C. Hygroscopic properties of oxalic acid and atmospherically relevant oxalates. *Atmos. Environ.* **2013**, *69*, 281-288.

11 Ravindra, K.; Bencs, L.; Wauters, E.; de Hoog, J.; Deutsch, F.; Roekens, E.; Bleux, N.; Berghmans, P.; Van Grieken, R. Seasonal and site-specific variation in vapour and aerosol phase PAHs over Flanders (Belgium) and their relation with anthropogenic activities. *Atmos. Environ.* **2006**, *40*, 771-785.

12 Chan, A. W. H.; Kautzman, K. E.; Chhabra, P. S.; Surratt, J. D.; Chan, M. N.; Crounse, J. D.; Kürten, A.; Wennberg, P. O.; Flagan, R. C.; Seinfeld, J. H. Secondary organic aerosol formation from photooxidation of naphthalene and alkylnaphthalenes: Implications for oxidation of intermediate volatility organic compounds (IVOCs). *Atmos. Phys. Chem.* **2009**, *9*, 3049-3060.

13 Slowik, J. G.; *et al.* An inter-comparison of instruments measuring black carbon content of soot particles. *Aerosol Sci. Technol.* **2007**, *41*, 295-314. See bibliography for complete list of authors.

14 Bowman, F. M.; Odum, J. R.; Seinfeld, J. H.; Pandis, S. N. Mathematical model for gas-particle partitioning of secondary organic aerosol. *Atmos. Environ.* **1997**, *31*, 3921-3931.

15 Pierce, J. R.; Riiponen, I.; Kulmala, M.; Ehn, M.; Petäjä, T.; Junninen, H.; Worsnop, D. R.; Donahue, N. M. Quantification of the volatility of secondary organic compounds in ultrafine particles during nucleation events. *Atmos. Chem. Phys.* **2011**, *11*, 9019-9036.

16 Ehn, M.; *et al.* A large source of low-volatility secondary organic aerosol. *Nature*, 2014, **506**, 476. See bibliography for complete list of authors.

17 Riipinen, I.; Yli-Juuti, T.; Pierce, J. R.; Petäjä, T.; Worsnop, D. R.; Kulmala, M.; Donahue, N. M. The contribution of organics to atmospheric nanoparticle growth. *Nature Geosci.* **2012**, *5*, 453-458.

18 Prather, K. A.; *et al.* Bringing the ocean into the laboratory to probe the chemical complexity of sea spray aerosol. *Proc. Natl. Acad. Sci. U. S. A.* **2013**, *110*, 7550-7555. See bibliography for complete list of authors.

Bibliography

Aarset, K.; Page, E. M.; Rice, D. A. Molecular structures of benzoic acid and 2-hydroxybenzoic acid, obtained by gas-phase electron diffraction and theoretical calculations. *J. Phys. Chem. A* **2006**, *110*, 9014-9019.

Adachi, M.; Okuyama, K.; Kousaka, Y. Electrical neutralization of charged aerosol particles by bipolar ions. *J. Chem. Eng. Japan* **1983**, *16*, 229-235.

Agarwal, J. K.; Sem, G. J. Continuous flow single-particle-counting condensation nuclei counter. *J. Aerosol Sci.* **1980**, *11*, 343-357.

Akhter, M. S.; Chughtai, A. R.; Smith, D. M. The structure of hexane soot. I: Spectroscopic studies. *Appl. Spectrosc.* **1985**, *39*, 143-153.

Albert, S.; Lerch, P.; Prentner, R.; Quack, M. Tunneling and tunneling switching dynamics in phenol and its isotopomers from high-resolution FTIR spectroscopy with synchrotron radiation. *Angew. Chem. Int. Ed.* **2013**, *52*, 346-367.

Allen, L.; Eberly, J. H. Two-level atoms in steady fields. *Optical Resonance and Two-Level Atoms*; Dover: New York, 1987; pp. 52-77.

Anson, C. W.; Thamattoor, D. M. Influence of substituents on the through-space shielding of aromatic rings. *J. Org. Chem.* **2012**, *77*, 1693-1700.

Atkins, P. Statistical thermodynamics: The machinery. *Physical Chemistry*, 6th ed.; Freeman: New York, 1998; pp. 593-617.

Atkinson, R. Product studies of gas-phase reactions of organic compounds. *Pure Appl. Chem.* **1998**, *70*, 1335-1343.

Atkinson, R.; Arey, J. Atmospheric degradation of volatile organic compounds. *Chem. Rev.* **2003**, *103*, 4605-4638.

Aviles-Moreno, J.-R.; Demaison, J.; Huet, T. R. Conformational flexibility in hydrated sugars: The glycolaldehyde-water complex. *J. Am. Chem. Soc.* **2006**, *128*, 10467-10473.

Azofra, L. M.; Quesada-Moreno, M. M.; Alkorta, I.; Avilés-Moreno, J. R.; López-González, J. J.; Elguero, J. Carbohydrates in the gas phase: Conformational preference of D-ribose and 2-deoxy-D-ribose. *New J. Chem.* **2014**, *38*, 529-538.

Babu, P. D. S.; Periandy, S.; Ramalingam, S. Vibrational spectroscopic (FTIR and FTRaman) investigation using ab initio (HF) and DFT (LSDA and B3LYP) analysis on the structure on toluic acid. *Spectrochim. Acta, Part A* **2011**, *78*, 1321-1328.

Back, R. A. The ultraviolet absorption spectrum of oxalic acid vapor. *Can. J. Chem.* **1984**, *62*, 1414-1428.

Bader, R. F. W. A bond path: A universal indicator of bonded interactions. *J. Phys. Chem. A* **1998**, *102*, 7314-7323.

Bader, R. F. W. A quantum theory of molecular structure and its applications. *Chem. Rev.* **1991**, *91*, 893-928.

Balle, T. J.; Flygare, W. H. Fabry-Perot cavity Fourier transform microwave spectrometer with a pulsed nozzle particle source. *Rev. Sci. Instrum.* **1981**, *52*, 33-45.

Bambha, R. P.; Dansson, M. A.; Schrader, P. E.; Michelsen, H. A. Effects of volatile coatings and coating removal mechanisms on the morphology of graphitic soot. *Carbon* **2013**, *61*, 80-96.

Barone, T. L.; Storey, J. M. E.; Youngquist, A. D.; Szybist, J. P. An analysis of direct-injection spark-ignition (DISI) soot morphology. *Atmos. Environ.* **2012**, *49*, 268-274.

Becke, A. D. Density-functional thermochemistry. III. The role of exact exchange. *J. Chem. Phys.* **1993**, *98*, 5648-5652.

Bell, R. J.; Davey, N. G.; Martinsen, M.; Collin-Hansen, C.; Krogh, E. T.; Gill, C. G. A field-portable membrane introduction mass spectrometer for real-time quantification and spatial mapping of atmospheric and aqueous contaminants. *J. Am. Soc. Mass. Spectrom.* **2015**, *26*, 212-223.

Bennett, J. F.; Collin, F.; Hastie, D. R. A laboratory flow reactor with gas particle separation and on-line MS/MS for product identification in atmospherically important reactions. *Atmos. Meas. Tech.* **2009**, *2*, 813-823.

Bock, C. W.; Redington, R. L. Isomerization and unimolecular dissociation channels of the oxalic acid monomer. *J. Chem. Phys.* **1986**, *85*, 5391-5400.

Borrás, E.; Torajada-Genaro, L. A. Secondary organic aerosol formation from the photo-oxidation of benzene *Atmos. Environ.* **2012**, *47*, 154-163.

Boucher, O.; Randall, D.; Artaxo, P.; Bretherton, C.; Feingold, G.; Forster, P.; Kerminen, V.-M.; Kondo, Y.; Liao, H.; Lohmann, U.; Rasch, P.; Satheesh, S. K.; Sherwood, S.; Stevens,

B.; Zhang, X. Y. Clouds and aerosols. In *Climate Change 2013: The Physical Science Basis. Contribution of Working Group I to the Fifth Assessment Report of the Intergovernmental Panel on Climate Change*; Stocker, T. F., Qin, G.-K., Plattner, M., Tignor, M., Allen, S. K., Boschung, J., Nauels, A., Xia, Y., Bex, V., Midgley, P. M., Eds.; Cambridge University Press: Cambridge, 2013; pp. 571-657.

Bowman, F. M.; Odum, J. R.; Seinfeld, J. H.; Pandis, S. N. Mathematical model for gas-particle partitioning of secondary organic aerosol. *Atmos. Environ.* **1997**, *31*, 3921-3931.

Boys, S. F.; Bernardi, F. The calculation of small molecular interactions by the difference of separate total energies. Some procedures with reduced errors. *Mol. Phys.* **1970**, *19*, 553-566.

Brauer, C.; Sedo, G.; Leopold, K. R. Dipole moment of the H_2SO_4-H_2O complex. *Geophys. Res. Lett.* **2006**, *33*, L23805 (5 pp.).

Brendel, K.; Mäder, H.; Xu, Y.; Jäger, W. The rotational spectra of the fluorobenzene···water and *p*-difluorobenzene···water dimers: Structure and internal dynamics. *J. Mol. Spectrosc.* **2011**, *268*, 47-52.

Brook, R. D.; Kousha, T. Air pollution and emergency department visits for hypertension in Edmonton and Calgary, Canada: A case-crossover study. *Am. J. Hypertens.* **2015**, *28*, 1121-1126.

Brovarets, O. O.; Zhurakivsky, R. O.; Hovorun, D. M. Is the DPT tautomerization of the long A·G Watson-Crick DNA base mispair a source of the adenine and guanine mutagenic tautomers? A QM and QTAIM response to the biologically important question. *J. Comput. Chem.* **2014**, *35*, 451-466.

Buczynska, A. J.; Krata, A.; Stranger, M.; Locateli Godoi, A. F.; Kontozova-Deutsch, V.; Bencs, L. Naveau, I.; Roekens, E.; Van Grieken, R. Atmospheric BTEX-concentrations in an area with intensive street traffic. *Atmos. Environ.* **2009**, *43*, 311-318.

Bunker, P. R.; Jensen, P. Nonrigid molecules. *Molecular Symmetry and Spectroscopy*, 2nd ed.; NRC Research Press: Ottawa, 2006; pp 476-549.

Bunker, P. R.; Jensen, P. The Born-Oppenheimer approximation and the electronic wavefunction. *Molecular Symmetry and Spectroscopy*, 2nd ed.; NRC Research Press: Ottawa, 2006; pp 173-201.

Bunker, P. R.; Jensen, P. The rotation and vibration wavefunctions. *Molecular Symmetry and Spectroscopy*, 2nd ed.; NRC Research Press: Ottawa, 2006; pp 238-264.

Canagaratna, M.; Phillips, J. A.; Ott, M. E.; Leopold, K. R. The nitric acid-water complex: Microwave spectrum, structure, and tunneling. *J. Phys. Chem. A* **1998**, *102*, 1489-1497.

Cappa, C. D.; Onasch, T. B.; Massoli, P.; Worsnop, D. R.; Bates, T. S.; Cross, E. S.; Davidovits, P.; Hakala, J.; Hayden, K. L.; Jobson, T.; Kolestar, K. R.; Lack, D. A.; Lerner, B. M.; Li, S.-M.; Mellon, D.; Nuaaman, I.; Olfert, J. S.; Petäjä, T.; Quinn, P. K.; Song, C.; Subramanian, R.; Williams, E. J.; Zaveri, R. A. Radiative absorption enhancements due to the mixing state of atmospheric black carbon. *Science* **2012**, *337*, 1078-1081.

Chan, A. W. H.; Kautzman, K. E.; Chhabra, P. S.; Surratt, J. D.; Chan, M. N.; Crounse, J. D.; Kürten, A.; Wennberg, P. O.; Flagan, R. C.; Seinfeld, J. H. Secondary organic aerosol formation from photooxidation of naphthalene and alkylnaphthalenes: Implications for oxidation of intermediate volatility organic compounds (IVOCs). *Atmos. Phys. Chem.* **2009**, *9*, 3049-3060.

Chan, A. W. H.; Kroll, J. H.; Ng, N. L.; Seinfeld, J. H. Kinetic modeling of secondary organic aerosol formation: Effects of particle- and gas-phase reactions of semivolatile products. *Atmos. Chem. Phys.* **2007**, *7*, 4135-4147.

Chuang, W.-T.; Sheu, H.-S.; Jeng, U.-S.; Wu, H. H.; Hong, P. D.; Lee, J.-J. Tetragonally perforated layer structure via columnar ordering of 4'-(3,4,5-trioctyloxybenzoyloxy)-benzoic acid in a supramolecular complex with polystyrene-*block*-poly(4-vinylpyridine). *Chem. Mater.* **2009**, *21*, 975-978.

Clean Air Strategic Alliance Data Warehouse. http://www.casadata.org (accessed April 2013).

Clifford, G. M.; Hadj-Aïssa, A.; Healy, R. M.; Mellouki, A.; Muñoz, A.; Wirtz, K.; Martín-Reviejo, M.; Borrás, E.; Wenger, J. C. The atmospheric photolysis of *o*-tolualdehyde. *Environ. Sci. Technol.* **2011**, *45*, 9649-9657.

Cohan, A.; Eiguren-Fernandez, A.; Miguel, A. H.; Dabdub, D. Secondary organic aerosol formation from naphthalene roadway emissions in the South Coast Air Basin of California. *Int. J. Environ. Pollut.* **2013**, *52*, 206-224.

Coudert, L. H.; Lovas, F. J.; Suenram, R. D.; Hougen, J. T. New measurements of microwave transitions in the water dimer. *J. Chem. Phys.* **1987**, *87*, 6290-6299.

Cross, E. S.; Onasch, T. B.; Ahern, A.; Wrobel, W.; Slowik, J. G.; Olfert, J.; Lack, D. A.; Massoli, P.; Cappa, C. D.; Schwarz, J. P.; Spackman, J. R.; Fahey, D. W.; Sedlacek, A.; Trimborn, A.; Jayne, J. T.; Freedman, A.; Williams, L. R.; Ng, N. L.; Mazzoleni, C.; Dubey, M.; Brem, B.; Kok, G.; Subramanian, R.; Freitag, S.; Clarke, A.; Thornhill, D.; Marr, L. C.; Kolb, C. E.; Worsnop, D. R.; Davidovits, P. Soot particle studies—instrument inter-comparison—project overview. *Aerosol Sci. Technol.* **2010**, *44*, 592-611.

Darvas, M.; Picaud, S.; Jedlovszky, P. Water adsorption around oxalic acid aggregates: A molecular dynamics simulation of water nucleation on organic aerosols. *Phys. Chem. Chem. Phys.* **2011**, *13*, 19830-19839.

De Kruif, C. G.; Blok, J. G. The vapour pressure of benzoic acid. *J. Chem. Thermodynamics* **1982**, *14*, 201-206.

Ditchfield, R.; Hehrf, W. J.; Pople, J. A. Self-consistent molecular-orbital methods. IX. An extended Gaussian-type basis for molecular-orbital studies of organic molecules. *J. Chem. Phys.* **1971**, *54*, 724-728.

Donahue, N. M.; Henry, K. M.; Mentel, T. F.; Kiendler-Scharr, A.; Spindler, C.; Bohn, B.; Brauers, T.; Dorn, H. P.; Fuchs, H.; Tillmann, R.; Wahner, A.; Saathoff, H.; Naumann, K.-H.; Möhler, O.; Leisner, T.; Müller, L.; Reinnig, M.-C.; Hoffmann, T.; Salo, K.; Hallquist, M.; Frosch, M.; Bilde, M.; Tritscher, T.; Barmet, P.; Praplan, A. P.; DeCarlo, P. F. Dommen, J.; Prévôt, A. S. H.; Baltensperger, U. Aging of biogenic secondary organic aerosol via gas-phase OH radical reaction. *Proc. Natl. Acad. Sci. U. S. A.* **2012**, *109*, 13503-13508.

Donahue, N. M.; Robinson, A. L.; Stanier, C. O.; Pandis, S. N. Coupled partitioning, dilution, and chemical aging of semivolatile organics. *Environ. Sci. Technol.* **2006**, *40*, 2635-2643.

Dörmann, M.; Schmid, H.-J. Simulation of capillary bridges between nanoscale particles. *Langmuir* **2014**, *30*, 1055-1062.

Drew, R. T.; Berstein, D. M.; Laskin, S. The Laskin aerosol generator. *J. Toxicol. Environ. Health* **1978**, *4*, 661-670.

Duley, W. W.; Anming, H. The 217.5 nm band, infrared absorption, and infrared emission features in hydrogenated amorphous carbon nanoparticles. *Astrophys. J.* **2012**, *761*, 115 (16 pp.).

Écija, P.; Basterretxea, F. J.; Lesarri, A.; Millán, J.; Castano, F.; Cocinero, E. J. Single hydration of the peptide bond: The case of the Vince lactam. *J. Phys. Chem. A* **2012**, *116*, 10099-10106.

Ehara, K.; Hagwood, C.; Coakley, K. J. Novel method to classify aerosol particles according to their mass-to-charge ratio – aerosol particle mass analyser. *J. Aerosol Sci.* **1996**, *27*, 217-234.

Ehn, M.; Thornton, J. A.; Kleist, E.; Sipilä, M.; Junninen, H.; Pullinen, I.; Springer, M.; Rubach, F.; Tillman, R.; Lee, B.; Lopez-Hilfiker, F.; Andres, S.; Acir, I.-H.; Rissanen, M.; Jokinen, T.; Schobesberger, S.; Kangasluoma, J.; Kontkanen, J.; Nieminen, T.; Kurtén, T.; Nielsen, L. B.; Jørgensen, S.; Kjaergaard, H. G.; Canagaratna, M.; Dal Maso, M.; Berndt, T.; Petäjä, T.; Wahner, A.; Kerminen, V.-M.; Kulmala, M.; Worsnop, D. R.; Wildt, J.; Mentel, T. F. A large source of low-volatility secondary organic aerosol. *Nature*, 2014, **506**, 476.

Ellingson, R. G.; Ellis, J.; Fels, S. The intercomparison of radiation codes used in climate models: Long wave results. *J. Geophys. Res.* **1991**, *96*, 8929-8953.

Elm, J.; Bilde, M.; Mikkelsen, K. V. Assessment of density functional theory in predicting structures and free energies of reaction of atmospheric prenucleation clusters. *J. Chem. Theory Comput.* **2012**, *8*, 2071-2077.

Enami, S.; Hoffmann, M. R.; Colussi, A. J. Stepwise oxidation of aqueous dicarboxylic acids by gas-phase OH radicals. *J. Phys. Chem. Lett.* **2015**, *6*, 527-534.

Engelhart, G. J.; Moore, R. H.; Nenes, A.; Pandis, S. N. Cloud condensation nuclei activity of isoprene secondary organic aerosol. *J. Geophys. Res.* **2011**, *116*, D02207 (11 pp.).

Ercolani, G. Numerical evaluation of energy levels and wave functions for hindered internal rotation. *J. Chem. Ed.* **2000**, *77*, 1495.

Espinosa, E.; Molins, E.; Lecomte, C. Hydrogen bond strengths revealed by topological analyses of experimentally observed electron densities. *Chem. Phys. Lett.* **1998**, *285*, 170-173.

Evangelisti, L.; Caminati, W. Internal dynamics in complexes of water with organic molecules. Details of the internal motions in *tert*-butylalcohol-water. *Phys. Chem. Chem. Phys.* **2010**, *12*, 14433-14441.

Evangelisti, L.; Écija, P.; Cocinero, E. J.; Castano, F.; Lesarri, A.; Caminati, W.; Meyer, R. Proton tunneling in heterodimers of carboxylic acids: A rotational study of the benzoic acid-formic acid bimolecule. *J. Phys. Chem. Lett.* **2012**, *3*, 3770-3775.

Facchini, M. C.; Mircea, M.; Fuzzi, S.; Charlson, R. J. Cloud albedo enhancement by surface-active organic solutes in growing droplets. *Nature* **1999**, *401*, 257-259.

Feng, G.; Gou, Q.; Evangelisti, L.; Xia, Z.; Caminati, W. Conformational equilibria in carboxylic acid bimolecules: A rotational study of acrylic acid-formic acid. *Phys. Chem. Chem. Phys.* **2013**, *15*, 2917-2922.

Fernandez-Alos, V.; Watson, J. K.; vander Wal, R.; Mathews, J. P. Soot and char molecular representations generated directly from HRTEM lattice fringe images using Fringe3D. *Combust. Flame* **2011**, *158*, 1807-1813.

Fernández-Ramos, A.; Ellingson, B. A.; Meana-Pañeda, R.; Marques, J. M. C.; Truhlar, D. G. Symmetry numbers and chemical reaction rates. *Theor. Chem. Acc.* **2007**, *118*, 813-826.

Fissan, H. J.; Helsper, C.; Thielen, H. J. Determination of particle size distribution by means of an electrostatic classifer. *J. Aerosol Sci.* **1983**, *14*, 354-357.

Flagan, R. C. Electrical mobility methods for submicrometer particle characterization. In *Aerosol Measurement: Principles, Techniques, and Applications*; Kulkarni, P.; Baron, P. A.; Willeke, K., Eds.; Wiley: New York, 2011; pp. 339-364.

Flores, N.; Jiménez, I. A.; Giménez, A.; Ruiz, G.; Gutiérrez, D.; Bourdy, G.; Bazzocchi, I. L. Antiparasitic activity of prenylated benzoic acid derivatives from Piper species. *Phytochemistry* **2009**, *70*, 621-627.

Fornasini, P. Distribution of Random Variable. *The Uncertainty in Physical Measurements: An Introduction to Data Analysis in the Physics Laboratory*; Springer: New York, 2008; pp. 94-133.

Forstner, H. J. L.; Flagan, R. C.; Seinfeld, J. H. Secondary organic aerosol from the photooxidation of aromatic hydrocarbons: Molecular composition. *Environ. Sci. Technol.* **1997**, *31*, 1345-1358.

Frisch, M. J.; Trucks, G. W.; Schlegel, H. B.; Scuseria, G. E.; Robb, M. A.; Cheeseman, J. R.; Scalmani, G.; Barone, V.; Mennucci, B.; Petersson, G. A.; Nakatsuji, H.; Caricato, M.; Li, X.; Hratchian, H. P.; Izmaylov, A. F.; Bloino, J.; Zheng, G.; Sonnenberg, J. L.; Hada, M.; Ehara, M.; Toyota, K.; Fukuda, R.; Hasegawa, J.; Ishida, M.; Nakajima, T.; Honda,

Y.; Kitao, O.; Nakai, H.; Vreven, T.; Montgomery, J. A., Jr.; Peralta, J. E.; Ogliaro, F.; Bearpark, M.; Heyd, J. J.; Brothers, E.; Kudin, K. N.; Staroverov, V. N.; Keith, T.; Kobayashi, R.; Normand, J.; Raghavachari, K.; Rendell, A.; Burant, J. C.; Iyengar, S. S.; Tomasi, J.; Cossi, M.; Rega, N.; Millam, J. M.; Klene, M.; Knox, J. E.; Cross, J. B.; Bakken, V.; Adamo, C.; Jaramillo, J.; Gomperts, R.; Stratmann, R. E.; Yazyev, O.; Austin, A. J.; Cammi, R.; Pomelli, C.; Ochterski, J. W.; Martin, R. L.; Morokuma, K.; Zakrzewski, V. G.; Voth, G. A.; Salvador, P.; Dannenberg, J. J.; Dapprich, S.; Daniels, A. D.; Farkas, O.; Foresman, J. B.; Ortiz, J. V.; Cioslowski, J.; Fox, D. J. *Gaussian 09*, Rev. D.01; Gaussian, Inc.: Wallingford, CT, **2013**.

Fu, P. P.; Herreno-Saenz, D.; Von Tungeln, L. S.; Lay, J. O.; Wu, Y.-S.; Lai, J.-S.; Evans, F. E. DNA adducts and carcinogenicity of nitro-polycyclic aromatic hydrocarbons. *Environ. Health Perspect.* **1994**, *102*, 177-184.

Fu, P. Q.; Kawamura, K.; Chen, J.; Li, J.; Sun, Y. L.; Liu, Y.; Tachibana, E.; Aggarwal, S. G.; Okuzawa, K.; Tanimoto, H.; Kanaya, Y.; Wang, Z. F. Diurnal variations of organic molecular tracers and stable carbon isotopic composition in atmospheric aerosols over Mt. Tai in the North China Plain: An influence of biomass burning. *Atmos. Chem. Phys.* **2012**, *12*, 8359-8375.

Fuchs, N. A. On the stationary charge distribution on aerosol particles in a bipolar ionic atmosphere. *Geophys. Pura. Appl.* **1963**, *56*, 185-193.

Fukui, K. The path of chemical reactions – the IRC approach. *Acc. Chem. Res.* **1981**, *14*, 363-368.

Gac, J. M.; Sosnowski T.; Gradoń L. Turbulent flow energy for aerosolization of powder particles. *J. Aerosol Sci.* **2008**, *39*, 113-126.

Gaie-Levrel, F.; Gutlé, C.; Jochims, H.-W.; Rühl, E.; Schwell, M. Photoionization of atmospheric aerosol constituents and precursors in the 7-15 eV energy region: Experimental and theoretical study. *J. Phys. Chem. A* **2008**, *112*, 5138-5151.

Gerhard, D.; Hellweg, A.; Merke, I.; Stahl, W.; Baudelet, M.; Petitprez, D.; Wlodarczak, G. Internal rotation and chlorine nuclear quadrupole coupling of *o*-chlorotoluene studied by microwave spectroscopy and ab initio calculations. *J. Mol. Spectrosc.* **2003**, *220*, 234-241.

Ghazi, R.; Olfert, J. S. Coating mass dependence of soot aggregate restructuring due to coatings of oleic acid and dioctyl sebacate. *Aerosol Sci. Technol.* **2013**, *47*, 192-200.

Ghazi, R.; Tjong, H.; Soewono, A.; Rogak, S. N.; Olfert, J. S. Mass, mobility, volatility, and morphology of soot particles generated by a McKenna and inverted burner *Aerosol Sci. Technol.* **2013**, *47*, 395-405.

Ghosh, S.; Thomas, J.; Huang, W.; Xu, Y.; Jäger, W. Rotational spectra of two hydrogen-bonded methyl salicylate monohydrates: Relative stability and tunneling motions. *J. Phys. Chem. Lett.* **2015**, *6*, 3126-3131.

Godfrey, P. D.; McNaughton, D. Structural studies of aromatic carboxylic acids via computational chemistry and microwave spectroscopy. *J. Chem. Phys.* **2013**, *138*, 024303 (8 pp.).

Godfrey, P. D.; Mirabella, M. J.; Brown, R. D. Structural studies of higher energy conformers by millimeter-wave spectroscopy: Oxalic acid. *J. Phys. Chem. A* **2000**, *104*, 258-264.

Gordy, W.; Smith, W. V.; Trambarulo, R. F. Microwave spectroscopy of gases. *Microwave Spectroscopy*; Wiley: New York, 1953; pp 84-153.

Guo, Z.; Li, Z.; Farquhar, J.; Kaufman, A. J.; Wu, N.; Li, C.; Dickerson, R. R.; Wang, P. Identification of sources and formation processes of atmospheric sulfate by sulfur isotope and scanning electron microscope measurements. *J. Geophys. Res.* **2010**, *115*, D00K07.

Gysel, M.; Laborde, M.; Mensah, A. A.; Corbin, J. C.; Keller, A.; Kim, J.; Petzold, A.; Sierau, B. Technical note: The single particle soot photometer fails to reliably detect PALAS soot nanoparticles. *Atmos. Meas. Tech.* **2012**, *5*, 3099-3107.

Hale, B. N. Temperature dependence of homogeneous nucleation rates for water: Near equivalence of the empirical fit of Wölk and Strey, and the scaled nucleation model. *J. Chem. Phys.* **2005**, *122*, 204509 (3 pp.).

Hamilton, J. F.; Webb, P. J.; Lewis, A. C.; Reviejo, M. M. Quantifying small molecules in secondary organic aerosol formed during the photo-oxidation of toluene with hydroxyl radicals. *Atmos. Environ.* **2005**, *39*, 7263-7275.

Hammett, L. P. The effect of structure upon the reactions of organic compounds. Benzene derivatives. *J. Am. Chem. Soc.* **1937**, *59*, 96-103.

Hanwell, M. D.; Curtis, D. E.; Lonie, D. C.; Vandermeersch, T.; Zurek, E.; Hutchison, G. R. Avogadro: An advanced semantic chemical editor, visualization, and analysis platform. *J. Cheminform.* **2012**, *4*, 17 (17 pp.).

Hao, L. Q.; Romakkaniemi, S.; Yli-Pirila, P.; Joutsensaari, J.; Kortelainen, A.; Kroll, J. H.; Miettinen, P.; Vaattovaara, P.; Tiitta, P.; Jaatinen, A.; Kajos, M. K.; Holopainen, J. K.; Heijari, J.; Rinne, J.; Kulmala, M.; Worsnop, D. R.; Smith, J. N.; Laaksonen, A. Mass yields of secondary organic aerosols from the oxidation of alpha-pinene and real plant emissions. *Atmos. Chem. Phys.* **2011,** *11*, 1367-1378.

Hartwig, H.; Dreizler, H. The microwave spectrum of trans-2,3-dimethyloxirane in torsional excited states. *Z. Naturforsch.* **1996**, *51A*, 923-932.

Heidrich, D.; Quapp, W. Saddle points of index 2 on potential energy surfaces and their role in theoretical reactivity investigations. *Theor. Chim. Acta* **1986**, *70*, 89-98.

Henze, D. K.; Seinfeld, J. H.; Ng, N. L.; Fu, T.-M.; Jacob, D. J.; Heald, C. L. Global modelling of secondary organic aerosol formation from aromatic hydrocarbons: High- vs. low-yield pathways. *Atmos. Chem. Phys.* **2008**, *8*, 2405-2420.

Heyder, J.; Gebhart, J.; Rudolf, G.; Schiller, C. F.; Stahlhofen, W. Deposition of particles in the human respiratory tract in the size range 0.005-15 μm. *J. Aerosol Sci.* **1986**, *17*, 811-825.

Higgins, J.; Zhou, X.; Liu, R.; Huang, T. T.-S. Theoretical study of thermal decomposition mechanism of oxalic acid. *J. Phys. Chem. A* **1997**, *101*, 2702-2708.

Hinds, W. C. Condensation and evaporation. *Aerosol Technology: Properties, Behavior, and Measurement of Airborne Particles*, 2nd ed.; Wiley: New York, 1999; pp. 278-303.

Hinds, W. C. Electrical properties. *Aerosol Technology: Properties, Behavior, and Measurement of Airborne Particles*, 2nd ed.; Wiley: New York, 1999; pp. 316-348.

Hinds, W. C. Optical properties. *Aerosol Technology: Properties, Behavior, and Measurement of Airborne Particles*, 2nd ed.; Wiley: New York, 1999; pp. 349-378.

Hinds, W. C. Straight-line acceleration and curvilinear particle motion. *Aerosol Technology: Properties, Behavior, and Measurement of Airborne Particles*, 2nd ed.; Wiley: New York, 1999; pp. 111-140.

Hinds, W. C. Uniform particle motion. *Aerosol Technology: Properties, Behavior, and Measurement of Airborne Particles*, 2nd ed.; Wiley: New York, 1999; pp. 42-74.

Ho, K. F.; Ho, S. S. H.; Lee, S. C.; Kawamura, K.; Zou, S. C.; Cao, J. J.; Xu, H. M. Summer and winter variations of dicarboxylic acids, fatty acids and benzoic acid in $PM_{2.5}$ in Pearl Delta River Region, China. *Atmos. Chem. Phys.* **2011**, *11*, 2197-2208.

Ho, K. F.; Huang, R.-J.; Kawamura, K.; Tachibana, E.; Lee, S. C.; Ho, S. S. H.; Zhu, T.; Tian, L. Dicarboxylic acids, ketocarboxylic acids, *α*-dicarbonyls, fatty acids and benzoic acid in $PM_{2.5}$ aerosol collected during CAREBeijing-2007: An effect of traffic restriction on air quality. *Atmos. Chem. Phys.* **2015**, *15*, 3111-3123.

Holloway, A. M.; Wayne, R. P. Sources and sinks of atmospheric species. *Atmospheric Chemistry*; RSC: Cambridge, 2010; pp 25-40.

Holt, B. D.; Kumar, R.; Cunningham, P. T. Primary sulfates in atmospheric sulfates: Estimation by oxygen isotope ratio measurements. *Science* **1982**, *217*, 51-53.

Huang, M.; Zhang, W.; Hao, L.; Wang, Z.; Fang, L.; Kong, R.; Shan, X.; Liu, F.; Sheng, L. Experimental study of photooxidation products of ethylbenzene. *J. Environ. Sci.* **2010**, *22*, 1570-1575.

Huang, M.; Zhang, W.; Wang, Z.; Hao, L.; Zhao, W.; Liu, X.; Long, B.; Fang, L. Theoretical investigation on the detailed mechanism of the OH-initiated atmospheric photooxidation of *o*-xylene. *Int. J. Quantum Chem.* **2008**, *108*, 954-966.

Hyland, R. W.; Wexler, A. Formulations for the thermodynamic properties of the saturated phases of H_2O from 173.15 K to 473.15 K. *ASHRAE Trans.* **1983**, *89*, 500-519.

Ito, M.; Tsukioka, H.; Imanishi, S. Effect of temperature on ultraviolet absorption spectra of benzoic acids and its relation to hydrogen bonding. *J. Am. Chem. Soc.* **1960**, *82*, 1559-1564.

Jacobsen, S.; Anderson, U.; Mäder, H. Microwave spectra of *o*-fluorotoluene and its ^{13}C isotopic species: Methyl internal rotation and molecular structure. *Struct. Chem.* **2003**, *14*, 217-225.

Jaenicke, R. Abundance of cellular material and proteins in the atmosphere. *Science* **2005**, *308*, 73.

Jang, M.; Kamens, R. M. Characterization of secondary organic aerosol from the photooxidation of toluene in the presence of NO_x and 1-propene. *Environ. Sci. Technol.* **2001**, *35*, 3626-3639.

Jeffrey, G. A. Nature and properties. *An Introduction to Hydrogen Bonding*; Oxford: New York, 1997; pp. 11-32.

Jensen, J. H. Calculating the energy. *Molecular Modeling Basics*; CRC Press: Boca Raton, 2010; pp. 25-76.

Jensen, J. H. The potential energy surface. *Molecular Modeling Basics*; CRC Press: Boca Raton, 2010; pp. 1-24.

Jeziorski, B.; Moszynski, R.; Szalewicz, K. Perturbation theory approach to intermolecular potential energy surfaces of van der Waals complexes. *Chem. Rev.* **1994**, *94*, 1887-1930.

Jimenez, J. L.; Caragaratna, M. R.; Donahue, N. M.; Prevot, A. S. H.; Zhang, Q.; Kroll, J. H.; DeCarlo, P. F.; Allan, J. D.; Coe, H.; Ng, N. L.; Aiken, A. C.; Docherty, K. S.; Ulbrich, I. M.; Grieshop, A. P.; Robinson, A. L.; Duplissy, J.; Smith, J. D.; Wilson, K. R.; Lanz,, V. A.; Hueglin, C.; Sun, Y. L.; Tian, J.; Laaksonen, A.; Raatikainen, T.; Rautiainen, J.; Vaattovaara P.; Ehn, M.; Kulmala, M.; Tomlinson, J. M.; Collins, D. R.; Cubison, M. J.; Dunlea, E. J.; Huffman, J. A.; Onasch, T. B.; Alfarra, M. R.; Williams, P. I.; Bower K.; Kondo, Y.; Schneider, J.; Drewnick, F.; Borrmann, S.; Weimer, S.; Demerjian, K.; Salcedo, D.; Cottrell, L.; Griffin, R.; Takami, A.; Miyoshi, T.; Hatakeyama, S.; Shimono, A.; Sun, J. Y.; Zhang, Y. M.; Dzepina, K.; Kimmel, J. R.; Sueper, D.; Jayne, J. T.; Herndon, S. C.; Trimborn, A. M.; Williams, L. R.; Wood, E. C.; Middlebrook, A. M.; Kolb, C. E.; Baltensperger, U.; Worsnop, D. R. Evolution of organic aerosols in the atmosphere. *Science* **2009**, *326*, 1525-1529.

Johnson, R. D., III. *FGH1D*, National Institute of Standards and Technology: Gaithersburg. http://nist.gov/mml/csd/informatics_research/fourier_grid_hamiltonian_interface.cfm#11.

Johnston, M. V. Supersonic jet expansions in analytical spectroscopy. *Trends Anal. Chem.* **1984**, *3*, 58-61.

Kassaee, M. H.; Keffer, D. J.; Steele, W. V. Theoretical calculation of thermodynamic properties of naphthalene, methylnaphthalenes, and dimethylnaphthalenes. *J. Chem. Eng. Data* **2007**, *52*, 1843-1850.

Kawamura, K.; Ng, L.-L.; Kaplan, I. R. Determination of organic acids (C_1-C_{10}) in the atmosphere, motor exhausts, and engine oils. *Environ. Sci. Technol*. **1985**, *19*, 1082-1086.

Kawamura, K.; Sakaguchi, F. Molecular distributions of water soluble dicarboxylic acids in marine aerosols over the Pacific Ocean including tropics. *J. Geophys. Res.* **1999**, *104*, 3501-3509.

Kelly, J. L.; Michelangeli, D. V.; Makar, P. A.; Hastie, D. R.; Mozurkewich, M.; Auld, J. Aerosol speciation and mass prediction from toluene oxidation under high NO_x conditions. *Atmos. Environ.* **2010,** *44*, 361-369.

Keywood, M.; Kanakidou, M.; Stohl, A.; Dentener, F.; Grassi, G.; Meyer, C. P.; Torseth, K.; Edwards, D.; Thompson, A. M.; Lohmann, U.; Burrows, J. Fire in the air: Biomass burning impacts in a changing climate. *Crit. Rev. Environ. Sci. Technol.* **2013**, *43*, 40-83.

Khalizov, A. F.; Lin, Y.; Qiu, C.; Guo, S.; Collins, D.; Zhang, R. Role of OH-initiated oxidation of isoprene in aging of combustion soot. *Environ. Sci. Technol.* **2013**, *47*, 2254-2263.

Khalizov, A. F.; Xue, H.; Wang, L.; Zheng, J.; Zhang, R. Enhanced light absorption and scattering by carbon soot aerosol internally mixed with sulfuric acid. *J. Phys. Chem. A* **2009**, *113*, 1066-1074.

Kim, Y. H.; Hwang, J.; Son, J. I.; Shim, Y. B. Synthesis, electrochemical, and spectroelectrochemical properties of conductive poly-[2,5-di-(2-thienyl)-1*H*-pyrrole-1-(*p*-benzoic acid)]. *Synthetic Met.* **2010**, *160*, 413-418.

Kisiel, Z. Assignment and Analysis of Complex Rotational Spectra. In *Spectroscopy from Space*; Demaison, J., Sarka, K., Cohen, E. A., Eds.; Kluwer: Dordrecht, 2001; pp. 91-106.

Klemperer, W.; Vaida, V. Molecular complexes in close and far away. *Proc. Natl. Acad. Sci. U. S. A.* **2006**, *103*, 10584-10588.

Knutson, E. O.; Whitby, K. T. Aerosol classification by electric mobility: Apparatus, theory, and applications. *J. Aerosol Sci.* **1975**, *6*, 443-451.

Koch, S.; Winterhalter, R.; Urerek, E.; Kollof, A.; Neeb, P.; Moortgat, G. Formation of new particles in the gas-phase ozonolysis of monoterpenes. *Atmos. Environ.* **2000**, *34*, 4031-4042.

Koch, U.; Popelier, P. L. A. Characterization of C-H-O hydrogen bonds on the basis of the charge density. *J. Phys. Chem.* **1995**, *99*, 9747-9754.

Kralchevsky, P. A.; Nagayama, K. Capillary forces between colloidal particles. *Langmuir* **1994**, *10*, 23-36.

Kramer, Z. C.; Takahashi, K.; Skodje, R. T. Water catalysis and anticatalysis in photochemical reactions: Observation of a delayed threshold effect in the reaction quantum yield. *J. Am. Chem. Soc.* **2010**, *132*, 15154-15157.

Kramer, Z. C.; Takahashi, K.; Vaida, V.; Skodje, R. T. Will water act as a photocatalyst for cluster phase chemical reactions? Vibrational overtone-induced dehydration reaction of methanediol. *J. Chem. Phys.* **2012**, *136*, 164302 (9 pp.).

Krishnan, R.; Binkley, J. S.; Seeger, R; Pople, J. A. Self-consistent molecular orbital methods. XX. A basis set for correlated wave functions. *J. Chem. Phys.* **1980**, *72*, 650-654.

Kroll, J. H.; Chan, A. W. H.; Ng, N. L.; Flagan, R. C.; Seinfeld, J. H. Reactions of semivolatile organics and their effects on secondary organics aerosol formation. *Environ. Sci. Technol.* **2007**, *41*, 3545-3550.

Kroto, H. W. Angular momentum and the energy levels of a rigid rotor. *Molecular Rotation Spectra*; Dover: New York, 1992; pp. 22-60.

Kroto, H. W. Flexible molecules. *Molecular Rotation Spectra*; Dover: New York, 1992; pp. 196-223.

Kroto, H. W. Interaction of radiation with a rotating molecule. *Molecular Rotation Spectra*; Dover: New York, 1992; pp. 61-94.

Kütz, S.; Schmidt-Ott, A. Characterization of agglomerates by condensation-induced restructuring *J. Aerosol Sci.* **1992**, *23*, S357-S360.

Lambe, A. T.; Onasch, T. B.; Croasdale, D. R.; Wright, J. P.; Martin, A. T.; Franklin, J. P.; Massoli, P.; Kroll, J. H.; Canagaratna, M. R.; Brune, W. H.; Worsnop, D. R.; Davidovits, P. Transitions from functionalization to fragmentation reactions of laboratory secondary organic aerosol (SOA) generated from the OH oxidation of alkane precursors. *Environ. Sci. Technol.* **2012**, *46*, 5430-5437.

Langmann, B.; Folch, A.; Hensch, M.; Matthias, V. Volcanic ash over Europe during the eruption of Eyjafjallajökull on Iceland, April-May 2010. *Atmos. Environ.* **2012**, *48*, 1-8.

Lee, A. K. Y.; Zhao, R.; Gao, S. S.; Abbatt, J. P. D. Aqueous-phase OH oxidation of glyoxal: Application of a novel analytical approach employing aerosol mass spectrometry and complementary off-line techniques. *J. Phys. Chem. A* **2011**, *115*, 10517-10526.

Lee, J. Y.; Hildemann, L. M. Surface tensions of solutions containing dicarboxylic acid mixtures. *Atmos. Environ.* **2014**, *89*, 260-267.

Leopold, K. R. Hydrated acid clusters. *Annu. Rev. Phys. Chem.* **2011**, *62*, 327-349.

Levine, I. N. Rotation of polyatomic molecules. *Molecular Spectroscopy*; Wiley: New York, 1975; pp 195-234.

Levine, I. N. Time-dependent states and spectroscopy. *Molecular Spectroscopy*; Wiley: New York, 1975; pp 110-141.

Levy, H., II; Horowitz, L. W.; Schwarzkopf, M. D.; Ming, Y.; Golaz, J.-C.; Naik, V.; Ramaswamy, V. The roles of aerosol direct and indirect effects in past and future climate change. *J. Geophys. Res. Atmos.* **2013**, *118*, 4521-4532.

Leyssale, J.-M.; Da Costa, J.-P.; Germain, C.; Weisbecker, P.; Vignoles, G. L. An image-guided atomistic reconstruction of pyrolytic carbons. *Appl. Phys. Lett.* **2009**, *95*, 231912 (3 pp.).

Li, K.; Wang, W.; Ge, M.; Li, J.; Wang, D. Optical properties of secondary organic aerosols generated by photooxidation of aromatic hydrocarbons. *Sci. Rep.* **2014**, *4*, 4922 (9 pp.).

Li, S.; Marshall, J. S.; Liu, G.; Yao, Q. Adhesive particulate flow: The discrete-element method and its application in energy and environmental engineering. *Prog. Energ. Combust.* **2011**, *37*, 633-668.

Lippmann, M.; Yeates, D. B.; Albert, R. E. Deposition, retention, and clearance of inhaled particles. *Brit. J. Ind. Med.* **1980**, *37*, 337-362.

Liu, P.; Zhang, Y.; Martin, S. T. Complex refractive indices of thin films of secondary organic materials by spectroscopic ellipsometry from 220 to 1200 nm. *Environ. Sci. Technol.* **2013**, *47*, 13594-13601.

Liu, S.; Day, D. A.; Shields, J. E.; Russell, L. M. Ozone-driven daytime formation of secondary organic aerosol containing carboxylic acid groups and alkane groups. *Atmos. Chem. Phys.* **2011**, *11*, 8321-8341.

López-Puertas, M.; Dinelli, B. M.; Adriani, A.; Funke, B.; García-Comas, M.; Moriconi, M. L.; D'Aversa, E.; Boersma, C.; Allamandola, L. J. Large abundances of polycyclic aromatic hydrocarbons in Titan's upper atmosphere. *Astrophys. J.* **2013**, *770*, 132 (8 pp.).

Lovas, F. J.; McMahon, R. J.; Grabow, J.-U.; Schnell, M.; Mack, J.; Scott, L. T.; Kuczkowski, R. L. Interstellar chemistry: A strategy for detecting polycyclic aromatic hydrocarbons in space. *J. Am. Chem. Soc.* **2005**, *127*, 4345-4349.

Lu, K.-T.; Weinhold, F.; Weisshaar, J. C. Understanding barriers to internal rotation in substituted toluenes and their cations. *J. Chem. Phys.* **1995**, *102*, 6787-6805.

Lu, T.; Chen, F. Multiwfn: A multifunctional wavefunction analyzer. *J. Comput. Chem.* **2012**, *33*, 580-592.

Lu, Z.; Hao, J.; Hu, L.; Takekawa, H. The compaction of soot particles generated by spark discharge in the propene ozonolysis system. *J. Aerosol Sci.* **2008**, *39*, 897-903.

Lui, P.; Zhang, Y.; Martin, S. T. Complex refractive indices of thin films of secondary organic materials by spectroscopic ellipsometry from 220 to 1200 nm. *Environ. Sci. Technol.* **2013**, *47*, 13594-13601.

Ma, Q.; He, H.; Liu, C. Hygroscopic properties of oxalic acid and atmospherically relevant oxalates. *Atmos. Environ.* **2013**, *69*, 281-288.

Ma, X.; Zangmeister, C. D.; Gigault, J.; Mulholland, G. W.; Zachariah, M. R. Soot aggregate restructuring during water processing. *J. Aerosol Sci.* **2013**, *66*, 209-219.

Maçôas, E. M. S.; Fausto, R.; Pettersson, M.; Khriachtchev, L.; Räsänen, M. Infrared-induced rotamerization of oxalic acid monomer in argon matrix. *J. Phys. Chem. A* **2000**, *104*, 6956-6961.

Mani, D.; Arunan, E. The X-C···Y (X=O/F, Y=O/S/F/Cl/Br/N/P) 'carbon bond' and hydrophobic interactions. *Phys. Chem. Chem. Phys.* **2013**, *15*, 14377-14383.

Massoli, P.; Lambe, A. T.; Ahern, A. T.; Williams, L. R.; Ehn, M.; Mikkilä, J.; Canagaratna, M. R.; Brune, W. H.; Onasch, T. B.; Jayne, J. T.; Petäjä, T.; Kulmala, M.; Laaksonen, A.; Kolb, C. E.; Davidovits, P.; Worsnop, D. R. Relationship between aerosol oxidation level and hygroscopic properties of laboratory generated secondary organic aerosol (SOA) particles. *Geophys. Res. Lett.* **2010**, *37*, L24801 (5 pp.).

Matta, C. F.; Boyd, R. J. An Introduction to the Quantum Theory of Atoms in Molecules. In *The Quantum Theory of Atoms in Molecules: From Solid State to DNA and Drug Design*; Matta, C. F., Boyd, R. J., Eds.; Wiley: New York, 2007; pp. 1-34.

McCarthy, S. P.; Thakkar, A. J. When does the non-variational nature of second-order Møller-Plesset energies manifest itself? All-electron correlation energies for open-shell atoms from K to Br. *J. Chem. Phys.* **2012**, *136*, 054107 (8 pp.).

McClelland, B. J. Equilibrium constants. *Statistical Thermodynamics*; Studies in Chemical Physics Series; Chapman and Hall: London, 1973; pp. 168-182.

McClelland, B. J. Maxwell-Boltzmann statistics. *Statistical Thermodynamics*; Studies in Chemical Physics Series; Chapman and Hall: London, 1973; pp. 13-28.

McGraw, R.; Zhang, R. Multivariate analysis of homogeneous nucleation rate measurements. Nucleation in the *p*-toluic acid/sulfuric acid/water system. *J. Chem. Phys.* **2008**, *128*, 064508 (9 pp.).

McNaughton, D.; Godfrey, P. D.; Brown, R. D.; Thorwirth, S. Millimetre wave spectroscopy of PANHs: Phenanthridine. *Phys. Chem. Chem. Phys.* **2007**, *9*, 591-595.

McNaughton, D.; Godfrey, P. D.; Brown, R. D.; Thorwirth, S.; Grabow, J.-U. FT-MW and millimeter wave spectroscopy of PANHs: Phenanthridine, acridine, and 1,10-phenanthroline. *Astrophys. J.* **2008**, *678*, 309-315.

McNeill, V. F.; Patterson, J.; Wolfe, G. M.; Thornton, J. A. The effect of varying levels of surfactant on the reactive uptake of N_2O_5 to aqueous aerosol. *Atmos. Chem. Phys.* **2006**, *6*, 1635-1644.

McNeill, V. F.; Sareen, N.; Schwier, A. N. Surface-active organics in atmospheric aerosols. *Top. Curr. Chem.* **2014**, *339*, 201-260.

Meng, J.; Wang, G.; Li, J.; Cheng, C.; Cao, J. Atmospheric oxalic acid and related secondary organic aerosols in Qinghai Lake, a continental background site in Tibet Plateau. *Atmos. Environ.* **2013**, *79*, 582-589.

Messer, J. K.; De Lucia, F. C.; Helminger, P. The pure rotational spectrum of water vapor – a millimeter, submillimeter, and far infrared analysis. *Int. J. Infrared Milli.* **1983**, *4*, 505-539.

Metcalf, A. R.; Loza, C. L.; Coggon, M. M.; Craven, J. S.; Jonsson, H. H.; Flagan, R. C.; Seinfeld, J. H. Secondary organic aerosol coating formation and evaporation: Chamber studies using black carbon seed aerosol and the singe-particle soot photometer *Aerosol Sci. Technol.* **2013**, *47*, 326-347.

Mie, G. Beiträge zur optik trüber medien, speziell kolloidaler metallösungen. *Ann. Phys.* **1908**, *330*, 377-445.

Migliorini, F.; De Iuliis, S.; Cignoli, F.; Zizak, G. How “flat” is the rich pre-mixed flame produced by your McKenna burner? *Combust. Flame* **2008**, *153*, 384-393.

Mikhailov, E. F.; Vlasenko, S. S. Structure and optical properties of soot aerosol in a moist atmosphere. 1. Structural changes of soot particles in the process of condensation *Izv. Atmos. Ocean. Phys.* **2007**, *43*, 181-194.

Miljevic, B.; Surawski, N. C.; Bostrom, T.; Ristovski, Z. D. Restructuring of carbonaceous particles upon exposure to organic and water vapours *J. Aerosol Sci.* **2012**, *47*, 48-57.

Millen, D. J. Determination of stretching force constants of weakly bound dimers from centrifugal distortion constants. *Can. J. Chem.* **1985**, *63*, 1477-1479.

Møller, C.; Plesset, M. S. Note on an approximation treatment for many-electron systems. *Phys. Rev.* **1934**, *46*, 618-622.

Morris, H. S.; Grassian, V. H.; Tivanski, A. V. Humidity-dependent surface tension measurements of individual inorganic and organic submicrometre liquid particles. *Chem. Sci.* **2015**, *6*, 3242-3247.

Morse, M. D. Supersonic beam sources. In *Atomic, Molecular, and Optical Physics: Atoms and Molecules*; Dunning, F. B., Hulet, R. G., Eds.; Experimental Methods in the Physical Sciences; Academic Press: San Diego, 1996; Vol. 29B, pp. 21-47.

Müller, J.; Limban, C.; Stadelmann, B.; Missir, A. V.; Chirita, I. C.; Chifiriuc, M. C.; Nitulescu, G. M.; Hemphill, A. Thioureides of 2-(phenoxymethyl)-benzoic acid 4-R substituted: A novel class of anti-parasitic compounds. *Parasitol. Int.* **2009**, *58*, 128-135.

Murphy, D. M.; Koop, T. Review of the vapour pressures of ice and supercooled water for atmospheric applications. *Q. J. R. Meteorol. Soc.* **2005**, *131*, 1539-1565.

Nagy, P. I.; Smith, D. A.; Alagona, G.; Ghio, C. Ab initio studies of free and monohydrated carboxylic acids in the gas phase. *J. Phys. Chem.* **1994**, *98*, 486-493.

Nakao, S.; Tang P.; Tang, X.; Clark, C. H.; Qi, L.; Seo, E.; Asa-Awuku, A.; Cocker, D., III. Density and elemental ratios of secondary organic aerosol: Application of a density prediction method *Atmos. Environ.* **2013**, *68*, 273-277.

Narukawa, M.; Kawamura, K.; Li, S.-M.; Bottenheim, J. W. Dicarboxylic acids in the Arctic aerosols and snowpacks collected during ALERT 2000. *Atmos. Environ.* **2002**, *36*, 2491-2499.

Ng, N. L.; Kroll, J. H.; Chan, A. W. H.; Chhabra, P. S.; Flagan, R. C.; Seinfeld, J. H. Secondary organic aerosol formation from *m*-xylene, toluene, and benzene. *Atmos. Chem. Phys.* **2007**, *7*, 3909-3922.

Nguyen, T. H.; Hibbs, D. E.; Howard, S. T. Conformations, energies, and intramolecular hydrogen bonds in dicarboxylic acids: Implications for the design of synthetic dicarboxylic acid receptors. *J. Comput. Chem.* **2005**, *26*, 1233-1241.

Nikolaienko, T. Y.; Bulavin, L. A.; Hovorun, D. M. Bridging QTAIM with vibrational spectroscopy: The energy of intramolecular hydrogen bonds in DNA-related biomolecules. *Phys. Chem. Chem. Phys.* **2012**, *14*, 7441-7447.

Novick, S. E.; Harris, S. J.; Janda, K. C.; Klemperer, W. Structure and bonding of KrClF: Intermolecular force fields in van der Waals molecules. *Can. J. Phys.* **1975**, *53*, 2007-2015.

Noziére, B.; Baduel, C.; Jaffrezo, J.-L. The dynamic surface tension of atmospheric aerosol surfactants reveals new aspects of cloud activation. *Nature Comm.* **2014**, *5*, 3335 (7 pp.).

Odum, J. R.; Hoffmann, T.; Bowman, F.; Collins, D.; Flagan, R. C.; Seinfeld, J. H. Gas/particle partitioning and secondary organic aerosol yields. *Environ. Sci. Technol.* **1996,** *30*, 2580-2585.

Oka, T. On negative inertial defect. *J. Mol. Struct.* **1995**, *352/353*, 225-233.

Okuyama, K.; Kousaka, Y.; Motouchi, T. Condensational growth of ultrafine aerosol particles in a new particle size magnifier. *Aerosol Sci. Technol.* **1984**, *3*, 353-366.

Olbert-Majkut, A.; Ahokas, J.; Pettersson, M.; Lundell, J. Visible light-driven chemistry of oxalic acid in solid argon, probed by Raman spectroscopy. *J. Phys. Chem. A* **2013**, *117*, 1492-1502.

Olfert, J. S.; Collings, N. New method for particle mass classification – the Couette centrifugal particle mass analyzer. *J. Aerosol Sci.* **2005**, *36*, 1338-1352.

Olfert, J. S.; Reavell, K. St. J.; Rushton, M. G.; Collings, N. The experimental transfer function of the Couette centrifugal particle mass analyzer. *J. Aerosol Sci.* **2006**, *37*, 1840-1852.

Olfert, J. S.; Symonds, J. P. R.; Collings, N. The effective density and fractal dimension of particles emitted from a light-duty diesel vehicle with a diesel oxidation catalyst. *J. Aerosol Sci.* **2007**, *38*, 69-82.

Olofsson, N.-E.; Bladh, H.; Bohlin, A.; Johnsson, J.; Bengtsson, P.-E. Are sooting premixed porous-plug burner flames one-dimensional? A laser-based experimental investigation. *Combust. Sci. Technol.* **2013**, *185*, 293-309.

Onda, M.; Asai, M.; Takise, K.; Kuwae, K.; Hayami, K.; Kuroe, A.; Mori, M.; Miyazaki, H.; Suzuki, N.; Yamaguchi, I. Microwave spectrum of benzoic acid. *J. Mol. Struct.* **1999**, *482-483*, 301-303.

Ottosson, N.; Romanova, A. O.; Söderström, J.; Björneholm, O.; Öhrwall, G.; Fedorov, M. V. Molecular sinkers: X-ray photoemission and atomistic simulations of benzoic acid and benzoate at the aqueous solution/vapor interface. *J. Phys. Chem. B* **2012**, *116*, 13017-13023.

Ouyang, B.; Howard, B. J. High-resolution microwave spectroscopic and ab initio studies of propanoic acid and its hydrates. *J. Phys. Chem. A* **2008**, *112*, 8208-8214.

Ouyang, B.; Howard, B. J. The monohydrate and dihydrate of acetic acid: A high-resolution microwave spectroscopic study. *Phys. Chem. Chem. Phys.* **2009**, *11*, 366-373.

Ouyang, B.; Starkey, T. G.; Howard, B. J. High-resolution microwave studies of ring-structured complexes between trifluoroacetic acid and water. *J. Phys. Chem. A* **2007**, *111*, 6165-6175.

Ouyang, B.; Starkey, T. G.; Howard, B. J. High-resolution microwave studies of ring-structured complexes between trifluoroacetic acid and water. *J. Phys. Chem. A* **2007**, *111*, 6165-6175.

Pagels, J.; Khalizov, A. F.; McMurry, P. H.; Zhang, R. Y. Processing of soot by controlled sulphuric acid and water condensation – mass and mobility relationship *Aerosol Sci. Technol.* **2009**, *43*, 629-640.

Paluch, M.; Dynarowicz, P. Electrical properties of adsorbed films of some aromatic compounds at the water/air interface. *J. Colloid Interface Sci.* **1987**, *115*, 307-311.

Pankow, J. F. An absorption model of gas-particle partitioning of organic compounds in the atmosphere. *Atmos Environ* **1994,** *28*, 185-188.

Park, K.; Cao, F.; Kittelson, D. B.; McMurry, P. H. Relationship between particle mass and mobility for diesel exhaust particles. *Environ. Sci. Technol.* **2003**, *37*, 577-583.

Park, K.; Kittelson, D. B.; Zachariah, M. R.; McMurry, P. H. Measurement of inherent material density of nanoparticle agglomerates. *J. Nanopart. Res.* **2004**, *6*, 267-272.

Parker, T. M.; Burns, L. A.; Parrish, R. M.; Ryno, A. G.; Sherill, C. D. Levels of symmetry adapted perturbation theory (SAPT). I. Efficiency and performance for interaction energies. *J. Chem. Phys.* **2014**, *140*, 094106 (16 pp.).

Parsons, M. T.; Sydoryk, I.; Lim, A.; McIntyre, T. J.; Tulip, J.; Jäger, W.; McDonald, K. Real-time monitoring of benzene, toluene, and *p*-xylene in a photoreaction chamber with a

tunable mid-infrared laser and ultraviolet differential optical absorption spectroscopy. *Appl. Opt.* **2011**, *50*, A90-A99.

Pathak, R. K.; Stanier, C. O.; Donahue, N. M.; Pandis, S. N. Ozonolysis of *α*-pinene at atmospherically relevant concentrations: Temperature dependence of aerosol mass fractions (yield). *J. Geophys. Res.* **2007**, *112*, D03201 (8 pp.).

Pauling, L.; Wilson, E. B., Jr. Many-electron atoms. *Introduction to Quantum Mechanics with Applications to Chemistry*; Dover: New York, 1985; pp 230-258.

Pauling, L.; Wilson, E. B., Jr. The rotation and vibration of molecules. *Introduction to Quantum Mechanics with Applications to Chemistry*; Dover: New York, 1985; pp 259-293.

Pauling, L.; Wilson, E. B., Jr. The variation method and other approximate methods. *Introduction to Quantum Mechanics with Applications to Chemistry*; Dover: New York, 1985; pp 180-206.

Peng, C.; Ayala, P. Y.; Schlegel, H. B.; Frisch, M. J. Using redundant internal coordinates to optimize equilibrium geometries and transition states. *J. Comp. Chem.* **1996**, *17*, 49-56.

Peng, J.; Hu, M.; Guo, S.; Du, Z.; Zheng, J.; Shang, D.; Zamora, M. L.; Zeng, L.; Shao, M.; Wu, Y.-S.; Zheng, J.; Wang, Y.; Glen, C. R.; Collins, D. R.; Molina, M. J.; Zhang, R. Markedly enhanced absorption and direct radiative forcing of black carbon under polluted urban environments. *Proc. Natl. Acad. Sci. U. S. A.* **2016**, doi: 10.1073/pnas.1602310113.

Perri, M. J.; Seitzinger, S.; Turpin, B. J. Secondary organic aerosol production from aqueous photooxidation of glycolaldehyde: Laboratory experiments. *Atmos. Environ.* **2009**, *43*, 1487-1497.

Petković, M.; Etinski, M. Intramolecular OHO bonding in dibenzoylmethane: Symmetry and spectral manifestations. *RSC Adv.* **2014**, *4*, 38517-38526.

Pierce, J. R.; Riiponen, I.; Kulmala, M.; Ehn, M.; Petäjä, T.; Junninen, H.; Worsnop, D. R.; Donahue, N. M. Quantification of the volatility of secondary organic compounds in ultrafine particles during nucleation events. *Atmos. Chem. Phys.* **2011**, *11*, 9019-9036.

Plane, J. M. C.; Saiz-Lopez, A. UV-Visible Differential Optical Absorption Spectroscopy. In *Analytical Techniques for Atmospheric Measurement*; Heard, D. E., Ed.; Blackwell: Cambridge, MA, 2006; pp. 147-188.

Polito, M.; D'Oria, E.; Maina, L.; Karamertzanis, P. G.; Grepioni, F.; Braga, D.; Price, S. L. The crystal structures of chloro and methyl *ortho*-benzoic acids and their co-crystal: Rationalizing similarities and differences. *Cryst. Eng. Comm.* **2008**, *10*, 1848-1854.

Pope, C. A., III; Dockery, D. W. Health effects of fine particulate air pollution: Lines that connect. *J. Air Waste Manage. Assoc.* **2006**, *56*, 709-742.

Prather, K. A.; Bertram, T. H.; Grassian, V. H.; Deane, G. B.; Stokes, M. D.; DeMott, P. J.; Aluwihare, L. I.; Palenik, B. P.; Azam, F.; Seinfeld, J. H.; Moffet, R. C.; Molina, M. J.; Cappa, C. D.; Geiger, F. M.; Roberts, G. C.; Russell, L. M.; Ault, A. P.; Baltrusaitis, J.; Collins, D. B.; Corrigan, C. E.; Cuadra-Rodriguez, L. A.; Ebben, C. J.; Forestieri, S.; Guasco, T. L.; Hersey, S. P.; Kim, M. J.; Lambert, W.; Modini, R. L.; Mui, W.; Pedler, B. L.; Ruppel, M. J.; Ryder, O. S.; Schoepp, N.; Sullivan, R. C.; Zhao, D. Bringing the ocean into the laboratory to probe the chemical complexity of sea spray aerosol. *Proc. Natl. Acad. Sci. U. S. A.* **2013**, *110*, 7550-7555.

Priem, D.; Ha, T.-K.; Bauder, A. Rotational spectra and structures of three hydrogen-bonded complexes between formic acid and water. *J. Chem. Phys.* **2000**, *113*, 169-175.

Qui, C.; Khalizov, A. F.; Zhang, R. Soot aging from OH-initiated oxidation of toluene. *Environ. Sci. Technol.* **2012**, *46*, 9464-9472.

Rader, D. J. & McMurry, P. H. Application of the tandem differential mobility analyzer to studies of droplet growth or evaporation. *J. Aerosol Sci.* **7**, 771-787 (1986).

Ramanathan, V.; Carmichael, G. Global and regional climate changes due to black carbon. *Nature Geosci.* **2008**, *1*, 221-227.

Ravindra, K.; Bencs, L.; Wauters, E.; de Hoog, J.; Deutsch, F.; Roekens, E.; Bleux, N.; Berghmans, P.; Van Grieken, R. Seasonal and site-specific variation in vapour and aerosol phase PAHs over Flanders (Belgium) and their relation with anthropogenic activities. *Atmos. Environ.* **2006**, *40*, 771-785.

Ravindra, K.; Sokhi, R.; Van Grieken, R. Atmospheric polycyclic aromatic hydrocarbons: Source attribution, emission factors and regulation. *Atmos. Environ.* **2008**, *42*, 2895-2921.

Ray, B. S. Über die Eigenwerte des asymmetrischen Kreisels. *Z. Phys.* **1932**, *78*, 74-91.

Riccobono, F.; Schobesberger, S.; Scott, C. E.; Dommen, J.; Ortega, I. K.; Rondo, L.; Almeida, J.; Amorim, A.; Bianchi, F.; Breitenlechner, M.; David, A.; Downard, A.; Dunne, E. M.; Duplissy, J.; Ehrhart, S.; Flagan, R. C.; Franchin, A.; Hansel, A.; Junninen, H.; Kajos, M.;

Keskinen, H.; Kupc, A.; Kürten, A.; Kvashin, A. N.; Laaksonen, A.; Lehtipalo, K.; Makhmutov, V.; Mathot, S.; Nieminen, T.; Onnela, A.; Petäjä, T.; Praplan, A. P.; Santos, F. D.; Schallhart, S.; Seinfeld, J. H.; Sipilä, M.; Spracklen, D. V.; Stozhkov, Y.; Stratmann, F.; Tomé, A.; Tsagkogeorgas, G.; Vaattovaara, P.; Viisanen, Y.; Vrtala, A.; Wagner, P. E.; Weingartner, E.; Wex, H.; Wimmer, D.; Carslaw, K. S.; Curtius, J.; Donahue, N. M.; Kirkby, J.; Kulmala, M.; Worsnop, D. R.; Baltensperger, U. Oxidation products of biogenic emissions contribute to nucleation of atmospheric particles. *Science*, 2014, **344**, 717-721.

Riipinen, I.; Pierce, J. R.; Donahue, N. M.; Pandis, S. N. Equilibration time scales of organic aerosol inside thermodenuders: Evaporation kinetics versus thermodynamics. *Atmos. Environ.* **2010**, *44*, 597-607.

Riipinen, I.; Yli-Juuti, T.; Pierce, J. R.; Petäjä, T.; Worsnop, D. R.; Kulmala, M.; Donahue, N. M. The contribution of organics to atmospheric nanoparticle growth. *Nature Geosci.* **2012**, *5*, 453-458.

Riva, M.; Robinson, E. S.; Perraudin, E.; Donahue, N. M.; Villenave, E. Photochemical aging of secondary organic aerosols generated from the photooxidation of polycyclic aromatic hydrocarbons in the gas-phase. *Environ. Sci. Technol.* **2015**, *49*, 5407-5416.

Ruiz, P. A.; Lawrence, J. E.; Ferguson, S. T.; Wolfson, J. M.; Koutrakis, P. A counter-current parallel-plate membrane denuder for the non-specific removal of trace gases. *Environ. Sci. Technol.* **2006**, *40*, 5058-5063.

Saathoff, H.; Naumann, K.-H.; Schnaiter, M.; Schöck, W.; Möhler, O.; Schurath, U.; Weingartner, E.; Gysel, M.; Baltensperger, U. Coating of soot and $(NH_4)_2SO_4$ particles by ozonolysis products of α-pinene *J. Aerosol Sci.* **2003**, *34*, 1297-1321.

Saleh, R.; Shihadeh, A. Hygroscopic growth and evaporation in an aerosol with boundary heat and mass transfer. *J. Aerosol Sci.* **2007**, *38*, 1-16.

Salvador, P.; Szczęśniak, M. M. Counterpoise-corrected geometries and harmonic frequencies of *N*-body clusters: Application to $(HF)_n$ (n=3,4). *J. Chem. Phys.* **2003**, *118*, 537-549.

Sareen, N.; Schwier, A. N.; Lathem, T. L.; Nenes, A.; McNeill, V. F. Surfactants from the gas phase may promote cloud droplet formation. *Proc. Natl. Acad. U. S. A.* **2012**, *110*, 2723-2728.

Schnaiter, M.; Linke, C.; Möhler, O.; Naumann, K.-H.; Saathoff, H.; Wagner, R.; Schurath, U. Absorption amplification of black carbon internally mixed with secondary organic aerosol. *J. Geophys. Res.* **2005**, *110*, D19204 (11 pp.).

Schnitzler, E. G.; Dutt, A.; Charbonneau, A. M.; Olfert, J. S.; Jäger, W. Soot aggregate restructuring due to coatings of secondary organic aerosol derived from aromatic precursors. *Environ. Sci. Technol.* **2014**, *48*, 14309-14316.

Schnitzler, E. G.; Jäger, W. The benzoic acid-water complex: A potential atmospheric nucleation precursor studied using microwave spectroscopy and *ab initio* calculations. *Phys. Chem. Chem. Phys.* **2014**, *16*, 2305-2314.

Schnitzler, E. G.; McDonald, K. M. Characterization of low temperature vapour pressure estimates for secondary organic aerosol applications. *Atmos. Environ.* **2012**, *56*, 9-15.

Schnitzler, E. G.; Poopari, M. R.; Xu, Y.; Jäger, W. Rotational spectroscopy of methyl benzoylformate and methyl mandelate: Structure and internal dynamics of a model reactant and product of enantioselective reduction. *Phys. Chem. Chem. Phys.* **2015**, *17*, 21942-21949.

Schnitzler, E. G.; Zenchyzen, B. L. M.; Jäger, W. High-resolution Fourier-transform microwave spectroscopy of methyl- and dimethylnapthalenes. *Astrophys. J.* **2015**, *805*, 141 (7 pp.).

Schnitzler, E. G.; Zenchyzen, B. L. M.; Jäger, W. Rotational spectroscopy of the atmospheric photo-oxidation product *o*-toluic acid and its monohydrate. *Phys. Chem. Chem. Phys.* **2016**, *18*, 448-457.

Schrader, W. Atmosphere, a chemical reactor – formation pathways of secondary organic aerosols. *Angew. Chem. Int. Ed.* **2005**, *44*, 1444-1446.

Schreiner, P. R.; Reisenauer, H. P. Spectroscopic identification of dihydroxycarbene. *Angew. Chem. Int. Ed.* **2008**, *47*, 7071-7074.

Scott, C. E.; Rap, A.; Spracklen, D. V.; Forster, P. M.; Carslaw, K. S.; Mann, G. W.; Pringle, K. J.; Kivekäs, N.; Kulmala, M.; Lihavainen, H.; Tunved, P. The direct and indirect radiative effects of biogenic secondary organic aerosol. *Atmos. Chem. Phys.* **2014**, *14*, 447-470.

Seifert, N. A; Finneran, I. A.; Perez, C.; Zaleski, D. P.; Neill, J. L.; Steber, A. L.; Suenram, R. D.; Lesarri, A.; Shipman, S. T.; Pate, B. H. AUTOFIT, an automated fitting tool for

broadband rotational spectra, and applications to 1-hexanal. *J. Mol. Spectrosc.* **2015**, *312*, 13-21.

Seinfeld, J. H.; Pandis, S. N. Atmospheric composition, global cycles, and lifetimes. *Atmospheric Chemistry and Physics: From Air Pollution to Climate Change*; Wiley: New York, 1998; pp. 49-124.

Seinfeld, J. H.; Pandis, S. N. Dynamics of single aerosol particles. *Atmospheric Chemistry and Physics: From Air Pollution to Climate Change*; Wiley: New York, 1998; pp. 452-490.

Seinfeld, J. H.; Pandis, S. N. Radiative effects of atmospheric aerosols: Visibility and climate. *Atmospheric Chemistry and Physics: From Air Pollution to Climate Change*; Wiley: New York, 1998; pp. 1113-1192.

Seinfeld, J. H.; Pandis, S. N. Thermodynamics of aerosols. *Atmospheric Chemistry and Physics: From Air Pollution to Climate Change*; Wiley: New York, 1998; pp. 491-544.

Sennikov, P. G.; Ignatov, S. K.; Schrems, O. Complexes and clusters of water relevant to atmospheric chemistry: H_2O complexes with oxidants. *ChemPhysChem* **2005**, *6*, 392-412.

Shakya, K. M.; Griffin, R. J. Secondary organic aerosol from photooxidation of polycyclic aromatic hydrocarbons. *Environ. Sci. Technol.* **2010**, *44*, 8134-8139.

Shaloski, M. A.; Sobyra, T. B.; Nathanson, G. M. DCI transport through dodecyl sulfate films on salty glycerol: Effects of seawater ions on gas entry. *J. Phys. Chem. A* **2015**, *119*, 12357-12366.

Shrestha, M.; Zhang, Y.; Ebben, C. J.; Martin, S. T.; Geiger, F. M. Vibrational sum frequency generation spectroscopy of secondary organic material produced by condensational growth from α-pinene ozonolysis. *J. Phys. Chem. A* **2013**, *117*, 8427-8436.

Siebenmorgen, R.; Voshchinnikov, N. V.; Bagnulo, S. Dust in the diffuse interstellar medium. *Astron. Astrophys.* **2013**, *561*, A82 (18 pp.).

Simpson, I. J.; Blake, N. J.; Barletta, B.; Diskin, G. S.; Fuelberg, H. E.; Gorham, K.; Huey, L. G.; Meinardi, S.; Rowland, F. S.; Vay, S. A.; Weinheimer, A. J.; Yang, M.; Blake, D. R. Characterization of trace gases measured over Alberta oil sands mining operations: 76 speciated C_2-C_{10} volatile organic compounds (VOCs), CO_2, CH_4, CO, NO, NO_2, NO_y, O_3 and SO_2. *Atmos. Chem. Phys.* **2010**, *10*, 11931-11954.

Sinclair, D.; Hoopes, G. S. A continuous flow nucleus counter. *J. Aerosol Sci.* **1975**, *6*, 1-7.

Slowik, J. G.; Cross, E. S.; Han, J.-H.; Davidovits, P.; Onasch, T. B.; Jayne, J. T.; Williams, L. R.; Canagaratna, M. R.; Worsnop, D. R.; Chakrabarty, R. K.; Moosmüller, H.; Arnott, W. P.; Schwarz, J. P.; Gao, R.-S., Fahey, D. W.; Kok, G. L.; Petzold, A. An inter-comparison of instruments measuring black carbon content of soot particles. *Aerosol Sci. Technol.* **2007**, *41*, 295-314.

Song, C.; Na, K.; Warren, B.; Malloy, Q.; Cocker, D. R, III. Secondary organic aerosol formation from the photooxidation of *p*- and *o*-xylene. *Environ. Sci. Technol.* **2007**, *41*, 7403-7408.

Song, M.; Liu, P. F.; Hanna, S. J.; Zaveri, R. A.; Potter, K.; You, Y.; Martin, S. T.; Bertram, A. K. Relative humidity-dependent viscosity of secondary organic material from toluene photo-oxidation and possible implications for organics particulate matter over megacities. *Atmos. Chem. Phys. Discuss.* **2016**, doi:10.5194/acp-2016-14.

Sorensen, C. M. The mobility of fractal aggregates: A review. *Aerosol Sci. Technol.* **2011**, *45*, 765-779.

Staikova, M.; Oh, M.; Donaldson, D. J. Overtone-induced decarboxylation: A potential sink for atmospheric diacids. *J. Phys. Chem. A* **2005**, *109*, 597-602.

Steinfeld, J. I. From molecular beams to masers to lasers. *Molecules and Radiation: An Introduction to Modern Molecular Spectroscopy*; Dover: New York, 2005; pp. 293-326.

Steinfeld, J. I. Optical resonance spectroscopy. *Molecules and Radiation: An Introduction to Modern Molecular Spectroscopy*; Dover: New York, 2005; pp. 327-355.

Szabo, A.; Ostlund, N. S. Many electron wave functions and operators. *Modern Quantum Chemistry: Introduction to Advanced Electronic Structure Theory*; Dover: New York, 1996; pp. 39-107.

Szabo, A.; Ostlund, N. S. The Hartree-Fock approximation. *Modern Quantum Chemistry: Introduction to Advanced Electronic Structure Theory*; Dover: New York, 1996; pp. 108-230.

Takahashi, K.; Plath, K. L.; Axson, J. L.; Nelson, G. C.; Skodje, R. T.; Vaida, V. Dynamics and spectroscopy of vibrational overtone excited glyoxylic acid and 2,2-dihydroxyacetic acid in the gas-phase. *J. Chem. Phys.* **2010**, *132*, 094305 (10 pp.).

Takahashi, K.; Plath, K. L.; Skodje, R. T.; Vaida, V. Dynamics of vibrational overtone excited pyruvic acid in the gas phase: Line broadening through hydrogen-atom chattering. *J. Phys. Chem. A* **2008**, *112*, 7321-7331.

Takekawa, H.; Minoura, H.; Yamazaki, S. Temperature dependence of secondary organic aerosol formation by photo-oxidation of hydrocarbons. *Atmos. Environ.* **2003**, *37*, 3413-3424.

Tan, X.-Q.; Clouthier, D. J.; Judge, R. H.; Plusquellic, D. F.; Tomer, J. L.; Pratt, D. W. Torsion-rotation interactions in a two-top molecule: High resolution $S_1 \leftarrow S_0$ electronic spectrum of 2,3-dimethylnaphthalene. *J. Chem. Phys.* **1991**, *95*, 7862-7871.

Tan, X.-Q.; Majewski, W. A.; Plusquellic, D. F.; Pratt, D. W. Methyl group torsional dynamics from rotationally resolved electronic spectra. 1- and 2-methynaphthalene. *J. Chem. Phys.* **1991**, *94*, 7721-7733.

Tanjaroon, C.; Jäger, W. High-resolution microwave spectrum of the weakly bound helium-pyridine complex. *J. Chem. Phys.* **2007**, *127*, 034302 (6 pp.).

Telloli, C.; Malaguti, A.; Mircea, M.; Tassinari, R.; Vaccaro, C.; Berico, M. Properties of agricultural aerosol released during wheat harvest threshing, plowing and sowing. *J. Environ. Sci. (China)* **2014**, *26*, 1903-1912.

Textor, C.; Schulz, M.; Guibert, S.; Kinne, S.; Balkanski, Y.; Bauer, S.; Bernsten, T.; Berglen, T.; Boucher, O.; Chin, M.; Dentener, F.; Diehl, T.; Easter, R.; Feichter, H.; Fillmore, D.; Ghan, S.; Ginoux, P.; Gong, S.; Grini, A.; Hendricks, J.; Horowitz, L.; Huang, P.; Isaksen, I.; Iverson, T.; Kloster, S.; Koch, D.; Kirkevåg, A.; Kristjansson, J. E.; Krol, M.; Lauer, A.; Lamarque, J. F.; Liu, X.; Montanaro, V.; Myhre, G.; Penner, J.; Pitari, G.; Reddy, S.; Seland, Ø.; Stier, P.; Takemura, T.; Tie, X. Analysis and quantification of the diversities of aerosol life cycles with AeroCom. *Atmos. Chem. Phys.* **2006**, *6*, 1777-1813.

Thomas, J.; Serrato, A., III; Lin, W.; Jäger, W.; Xu, Y. Perfluorobutyric acid and its monohydrate: A chirped pulse and cavity based Fourier transform microwave spectroscopic study. *Chem. Eur. J.* **2014**, *20*, 6148-6153.

Thomson, W. On the equilibrium of vapour at a curved surface of liquid. *Proc. Roy. Soc. Edinb.* **1870**, *7*, 63-68.

Thorwirth, S.; Theulé, P.; Gottlieb, C. A.; McCarthy, M. C.; Thaddeus, P. Rotational spectra of small PAHs: Acenaphthene, acenaphthylene, azulene, and fluorene. *Astrophys. J.* **2007**, *662*, 1309-1314.

Tie, X.; Wu, D.; Brasseur, G. Lung cancer mortality and exposure to atmospheric aerosol particles in Guangzhou, China. *Atmos. Environ.* **2009**, *43*, 2375-2377.

Tielens, A. G. G. M. Interstellar polycyclic aromatic hydrocarbon molecules. *Annu. Rev. Astron. Astrophys.* **2008**, *46*, 289-337.

Tkacik, D. S.; Presto, A. A.; Donahue, N. M.; Robinson, A. L. Secondary organic aerosol formation from intermediate-volatility organic compounds: Cyclic, linear, and branched alkanes. *Environ. Sci. Technol.* **2012**, *46*, 8773-8781.

Totten, T. S.; Chakrabarti, D.; Misquitta, A. J.; Sander, M.; Wales, D. J.; Kraft, M. Modelling the internal structure of nascent soot particles. *Combust. Flame* **2010**, *157*, 909-914.

Townes, C. H.; Schawlow, A. L. Asymmetric-top molecules. *Microwave Spectroscopy*; Dover: New York, 1975; pp 83-114.

Townes, C. H.; Schawlow, A. L. The ammonia spectrum and hindered motions. *Microwave Spectroscopy*; Dover: New York, 1975; pp 300-335.

Tritscher, T.; Dommen, J.; DeCarlo, P. F.; Gysel, M.; Barmet, P. B.; Praplan, A. P.; Weingartner, E.; Prévôt, A. S. H.; Riipinen, I.; Donahue, N. M.; Baltensperger, U. Volatility and hygroscopicity of aging secondary organic aerosol in a smog chamber. *Atmos. Chem. Phys.* **2011**, *11*, 11477-11496.

Tritscher, T.; Jurányi, Z.; Martin, M.; Chirico, R.; Gysel, M.; Heringa, M. F.; DeCarlo, P. F.; Sierau, B.; Prévôt, A. S. H.; Weingartner, E.; Baltensperger, U. Changes of hygroscopicity and morphology during ageing of diesel soot. *Environ. Res. Lett.* **2011**, *6*, 034026 (10 pp.).

Tudorie, M.; Kleiner, I.; Jahn, M.; Grabow, J.-U.; Goubet, M.; Pirali, O. Coupled large amplitude motions: A case study of the dimethylbenzaldehyde isomers. *J. Phys. Chem. A* **2013**, *117*, 13636-13647.

Turney, J. M.; Simmonett, A. C.; Parrish, R. M.; Hohenstein, E. G.; Evangelista, F. A.; Fermann, J. T.; Mintz, B. J.; Burns, L. A.; Wilke, J. J.; Abrams, M. L.; Russ, N. J.; Leininger, M. L.; Janssen, C. L.; Seidl, E. T.; Allen, W. D.; Schaefer, H. F.; King, R. A.; Valeev, E. F.; Sherrill, C. D.; Crawford, T. D. PSI4: An open-source *ab initio* electronic structure program. *WIREs Comput. Mol. Sci.*, 2012, **2**, 556-565.

Vaida, V.; Donaldson, D. J. Red-light initiated atmospheric reactions of vibrationally excited molecules. *Phys. Chem. Chem. Phys.* **2014**, *16*, 827-836.

Vaida, V.; Headrick, J. E. Physicochemical properties of hydrated complexes in the Earth's atmosphere. *J. Phys. Chem. A* **2000**, *104*, 5401-5412.

Valavanidis, A.; Fiotakis, K.; Vlachogianni, T. Airborne particulate matter and human health: Toxicological assessment and importance of size and composition of particles for oxidative damage and carcinogenic mechanisms. *J. Environ. Sci. Health C* **2008**, *26*, 339-362.

Van de Meerakker, S. Y. T.; Bethlem, H. L.; Meijer, G. Taming molecular beams. *Nature Phys.* **2008**, *4*, 595-602.

Van der Zwet, G. P.; Allamandola, L. J. Polycyclic aromatic hydrocarbons and the diffuse interstellar bands. *Astron. Astrophys.* **1985**, *146*, 76-70.

Van Duijneveldt, F. B.; van Duijneveldt-van de Rijdt, J. G. C. M.; van Lenthe, J. H. State of the art in counterpoise theory. *Chem. Rev.* **1994**, *94*, 1873-1885.

Varadwaj, P. R.; Varadwaj, A.; Jin, B.-Y. Significant evidence of C···O and C···C long-range contacts in several heterodimeric complexes of CO with CH_3-X, should one refer to them as carbon and dicarbon bonds! *Phys. Chem. Chem. Phys.* **2014**, *16*, 17238-17252.

Vijh, U. P.; Witt, A. N.; Gordon, K. D. Discovery of blue luminescence in the red rectangle: Possible fluorescence from neutral polycyclic aromatic hydrocarbon molecules? *Astrophys. J.* **2004**, *606*, L65-L68.

Virtanen, A.; Joutsensaari, J.; Koop, T.; Kannosto, J.; Yli-Pirilä, P.; Leskinen, J. Mäkelä, J. M.; Holopainen, J. K.; Pöschl, U.; Kulmala, M.; Worsnop, D. R.; Laaksonen, A. An amorphous solid state of biogenic secondary organic aerosol particles. *Nature* **2010**, *467*, 824-827.

Vivanco, M. G.; Santiago, M.; Martínez-Tarifa, A.; Borrás, E.; Ródenas, M.; Garciá-Diego, C.; Sánchez, M. SOA formation in a photoreactor from a mixture of organic gases and HONO for different experimental conditions. *Atmos. Environ.* **2011**, *45*, 708-715.

Watson, J. K. G. Determination of centrifugal distortion coefficients of asymmetric-top molecules. *J. Chem. Phys.* **1967**, *46*, 1935-1949.

Weber, K. H.; Liu, Q.; Tao, F.-M. Theoretical study on stable small clusters of oxalic acid with ammonia and water. *J. Phys. Chem. A* **2014**, *118*, 1451-1468.

Weber, K. H.; Morales, F. J.; Tao, F.-M. Theoretical study on the structure and stabilities of molecular clusters of oxalic acid with water. *J. Phys. Chem. A* **2012**, *116*, 11601-11617.

Weber, R. J.; Orsini, D.; Daun, Y.; Lee, Y.-N.; Klotz, P.; Brechtel, F. A particle-into-liquid collector for rapid measurements of aerosol chemical composition. *Aerosol Sci. Technol.* **2001**, *35*, 718-727.

Western, C. M. *PGOPHER, A Program for Simulating Rotational Structure*, University of Bristol: Bristol, UK. http://pgopher.chm.bris.ac.uk.

White, S. J.; Jamie, I. M.; Angove, D. E. Chemical characterization of semi-volatile and aerosol compounds from the photooxidation of toluene and NO_x. *Atmos. Environ.* **2014**, *83*, 237-244.

Wiedensohler, A. An approximation of the bipolar charge distribution for particles in the submicron size range. *J. Aerosol Sci.* **1988**, *19*, 387-389.

Wilson, E. B., Jr.; Decius, J. C.; Cross, P. C. The separation of rotation and vibration. *Molecular Vibrations: The Theory of Infrared and Raman Vibrational Spectra*; Dover: New York, 1980; pp 273-284.

Wilson, E. B., Jr.; Decius, J. C.; Cross, P. C. The vibration of molecules. *Molecular Vibrations: The Theory of Infrared and Raman Vibrational Spectra*; Dover: New York, 1980; pp 11-33.

Wollrab, J. E. Internal rotation. *Rotational spectra and molecular structure*; Physical Chemistry Series; Academic Press: New York, 1967; pp. 145-202.

Woodbury, G. Three exactly solvable models. *Physical Chemistry*; Brooks/Cole: Pacific Grove, 1997; pp. 413-454.

Xu, W.; Zhang, R. Theoretical investigation of interaction of dicarboxylic acids with common aerosol nucleation precursors. *J. Phys. Chem. A* **2012**, *116*, 4539-4550.

Xu, Y.; Jäger, W. Evidence for heavy atom large amplitude motions in RG-cyclopropane van der Waals complexes (RG=Ne, Ar, Kr) from rotation-tunneling spectroscopy. *J. Chem. Phys.* **1997**, *106*, 7968-7980.

Xu, Y.; Nadykto, A. B.; Yu, F.; Jiang, L.; Wang, W. Formation and properties of hydrogen-bonded complexes of common organic oxalic acid with atmospheric nucleation precursors. *THEOCHEM* **2010**, *951*, 28-33.

Xu, Y.; Van Wijngaarden, J.; Jäger, W. Microwave spectroscopy of ternary and quaternary van der Waals clusters. *Int. Rev. Phys. Chem.* **2005**, *24*, 301-338.

Xue, H.; Khalizov, A. F.; Wang, L.; Zheng, J.; Zhang, R. Effects of dicarboxylic acid coating on the optical properties of soot. *Phys. Chem. Chem. Phys.* **2009**, *11*, 7869-7875.

Yamamoto, S.; Back, R. The gas-phase photochemistry of oxalic acid. *J. Phys. Chem.* **1985**, *89*, 622-625.

Yu, J.; Jeffries, H. E.; Sexton, K. G. Atmospheric photooxidation of alkylbenzenes – I. Carbonyl product analyses. *Atmos. Environ.* **1997**, *31*, 2261-2280.

Zangmeister, C. D.; Radney, J. G.; Dockery, L. T.; Young, J. T.; Ma, X.; You, R.; Zachariah, M. R. Packing density of rigid aggregates is independent of scale. *Proc. Natl. Acad. Sci. U. S. A.* **2014**, *111*, 9037-9041.

Zhang, H.; Ying, Q. Secondary organic aerosol from polycyclic aromatic hydrocarbons in Southeast Texas. *Atmos. Environ.* **2012**, *55*, 279-287.

Zhang, Q.; Jimenez, J. L.; Canagaratna, M. R.; Allan, J. D.; Coe, H.; Ulbrich, I.; Alfarra, M. R.; Takemi, A.; Middlebrook, A. M.; Sun, Y. L.; Dzepina, K.; Dunlea, E.; Docherty, K.; DeCarlo, P. F.; Salcedo, D.; Onasch, T.; Jayne, J. T.; Miyoshi, T.; Shimono, A.; Hatakeyama, S.; Takegawa, N.; Kondo, Y.; Schneider, J.; Drewnick, F.; Borrmann, S.; Weimer, S.; Demerjian, K.; Williams, P.; Bower, K.; Bahreini, R.; Cottrell, L.; Griffin, R. J.; Rautiainen, J.; Sun, J. Y.; Zhang, Y. M.; Worsnop, D. R. Ubiquity and dominance of oxygenated species in organic aerosols in anthropogenically-influenced Northern Hemisphere midlatitudes. *Geophys. Res. Lett.* **2007**, *34*, L13801 (6 pp.).

Zhang, R. Getting to the critical nucleus of aerosol formation. *Science* **2010**, *328*, 1366-1367.

Zhang, R.; Khalizov, A.; Wang, L.; Hu, M.; Xu, W. Nucleation and growth of nanoparticles in the atmosphere. *Chem. Rev.* **2012**, *112*, 1957-2011.

Zhang, R.; Suh, I.; Zhao, J.; Zhang, D.; Fortner, E. C.; Tie, X.; Molina, L. T.; Molina, M. J. Atmospheric new particle formation enhanced by organic acids. *Science* **2004**, *304*, 1487-1490.

Zhang, X.; Cappa, C. D.; Jathar, S. H.; McVay, R. C.; Ensberg, J. J.; Kleeman, M. J.; Seinfeld, J. H. Influence of vapor wall loss in laboratory chambers on yields of secondary organic aerosol. *Proc. Natl. Acad. Sci. U. S. A.* **2014**, *111*, 5802-5807.

Zhang, X.; Schwantes, R. H.; McVay, R. C.; Lignell, H.; Coggon, M. M.; Flagan, R. C.; Seinfeld, J. H. Vapor wall deposition in Teflon chambers. *Atmos. Chem. Phys.* **2015**, *15*, 4197-4214.

Zhao, J.; Khalizov, A.; Zhang, R.; McGraw, R. Hydrogen-bonding interaction in molecular complexes and clusters of aerosol nucleation precursors. *J. Phys. Chem. A* **2009**, *113*, 680-689.

Zhao, Y.; Truhlar, D. G. The M06 suite of density functionals for main group thermochemistry, thermochemical kinetics, noncovalent interactions, excited states, and transition elements: Two new functionals and systematic testing of four M06-class functionals and 12 other functionals. *Theor. Chem. Acc.* **2008**, *120*, 215-241.

Zhou, Y.; Zhang, H.; Parikh, H. M.; Chen, E. H.; Rattanavaraha, W.; Rosen, E. P.; Wang, W.; Kamens, R. M. Secondary organic aerosol formation from xylenes and mixtures of toluene and xylenes in an atmospheric urban hydrocarbon mixture: Water and particle seed effects (II). *Atmos. Environ.* **2011**, *45*, 3882-3890.

Appendix

Table A.1. Rotational transition frequencies and quantum number assignments of benzoic acid.

J'	K_a'	K_c'	J	K_a	K_c	Frequency / MHz	Residual / MHz
2	1	1	1	1	0	4614.5070	-0.0017
5	1	4	5	0	5	5590.6400	-0.0005
3	1	3	2	1	2	6023.4968	-0.0002
3	0	3	2	0	2	6387.4470	0.0000
4	0	4	3	1	3	6405.3717	0.0007
3	2	2	2	2	1	6479.6393	0.0005
2	1	2	1	0	1	6669.9763	0.0011
3	1	2	2	1	1	6906.5863	0.0000
6	1	5	6	0	6	6947.3359	0.0004
6	2	4	6	1	5	6964.3665	-0.0001
5	2	3	5	1	4	7043.4289	0.0006
7	2	5	7	1	6	7122.8844	-0.0006
4	2	2	4	1	3	7290.5265	0.0008
6	1	5	5	2	4	7347.7732	-0.0004
8	2	6	8	1	7	7573.4758	-0.0009
3	2	1	3	1	2	7623.4145	0.0005
2	2	0	2	1	1	7958.1695	-0.0002
4	1	4	3	1	3	8006.7165	-0.0004
7	1	6	7	1	7	8020.5498	0.0008
9	2	7	9	1	8	8357.4062	0.0012
3	1	3	2	0	2	8396.9981	0.0006
4	0	4	3	0	3	8414.9210	-0.0004
7	1	6	7	0	7	8597.1333	-0.0004
4	3	2	3	3	1	8682.8182	0.0006
4	3	1	3	3	0	8689.7133	-0.0006
5	0	5	4	1	4	8770.6082	0.0000
2	2	1	2	1	2	8819.1273	-0.0013
4	1	3	3	1	2	9178.8098	-0.0001
10	2	8	10	1	9	9499.8732	-0.0005
4	2	3	4	1	4	9889.9290	-0.0003
5	1	5	4	1	4	9972.0190	0.0000
4	1	4	3	0	3	10016.2667	-0.0007
5	0	5	4	0	4	10371.9550	0.0007
5	2	4	4	2	3	10747.6694	-0.0008
5	3	3	4	3	2	10867.9973	-0.0012
5	2	3	4	2	2	11174.7247	0.0009
5	1	4	4	1	3	11421.8220	0.0005

Table A.1 continued. Rotational transition frequencies and quantum number assignments of benzoic acid.

J'	K_a'	K_c'	J	K_a	K_c	Frequency / MHz	Residual / MHz
6	1	6	5	1	5	11918.4576	0.0000
6	0	6	5	0	5	12267.4293	0.0007
2	2	1	1	1	0	12549.3924	-0.0003
6	2	5	5	2	4	12854.9309	0.0000
2	2	0	1	1	1	12867.4268	0.0001
6	3	4	5	3	3	13057.4422	0.0002
6	3	3	5	3	2	13120.2329	-0.0001
7	0	7	6	1	6	13270.1318	0.0005
6	2	4	5	2	3	13545.0629	0.0004
6	1	5	5	1	4	13624.1238	-0.0004
7	1	7	6	1	6	13846.7162	0.0003
7	0	7	6	0	6	14122.5701	-0.0004
3	2	2	2	1	1	14414.5225	-0.0002
7	1	7	6	0	6	14699.1551	0.0000
7	2	6	6	2	5	14939.9433	0.0003
7	3	5	6	3	4	15247.5478	-0.0004
7	3	4	6	3	3	15385.0137	-0.0001
3	2	1	2	1	2	15414.2455	0.0007
8	1	8	7	1	7	15758.7571	0.0000
7	1	6	6	1	5	15772.3680	-0.0006
7	2	5	6	2	4	15930.8871	0.0001
8	0	8	7	0	7	15960.1065	0.0002
4	2	3	3	1	2	16129.3123	0.0000
8	2	7	7	2	6	17000.1038	-0.0009
9	1	9	8	1	8	17657.3054	0.0003
8	3	5	7	3	4	17696.6274	0.0003
5	2	4	4	1	3	17698.1728	0.0001
9	0	9	8	0	8	17795.5940	-0.0002
8	1	7	7	1	6	17853.1554	0.0002

Table A.2. Rotational transition frequencies and quantum number assignments of benzoic acid-H_2O.

J'	K_a'	K_c'	J	K_a	K_c	Frequency / MHz	Residual / MHz
4	1	4	3	1	3	4651.5951	0.0013
4	0	4	3	0	3	4823.2474	-0.0007
4	1	3	3	1	2	5027.6071	-0.0010
5	1	5	4	1	4	5810.8267	-0.0013
5	0	5	4	0	4	6013.8889	0.0007
5	1	4	4	1	3	6280.4666	-0.0007
6	1	6	5	1	5	6967.7672	-0.0011
6	0	6	5	0	5	7194.7980	0.0007
6	2	5	5	2	4	7256.3164	-0.0001
6	2	4	5	2	3	7327.0540	-0.0009
6	1	5	5	1	4	7530.4747	0.0003
4	1	4	3	0	3	7611.1471	-0.0008
7	1	7	6	1	6	8122.1002	0.0000
7	0	7	6	0	6	8364.6482	-0.0003
7	2	6	6	2	5	8460.5179	-0.0003
7	3	5	6	3	4	8491.7904	0.0012
7	3	4	6	3	3	8495.3000	-0.0003
7	2	5	6	2	4	8572.2956	0.0009
7	1	6	6	1	5	8776.9013	0.0005
8	1	8	7	1	7	9273.5807	-0.0001
8	0	8	7	0	7	9522.6825	-0.0004
8	2	7	7	2	6	9662.3389	-0.0002
8	3	6	7	3	5	9708.5702	-0.0007
8	3	5	7	3	4	9715.5724	0.0001
8	2	6	7	2	5	9826.9275	0.0006
8	1	7	7	1	6	10018.9317	0.0000
9	1	9	8	1	8	10422.0446	0.0001
7	1	7	6	0	6	10479.9117	0.0009
9	0	9	8	0	8	10668.8746	0.0002
9	2	8	8	2	7	10861.4534	-0.0001
9	2	7	8	2	6	11090.6124	0.0009
9	1	8	8	1	7	11255.6561	0.0013
10	1	10	9	1	9	11567.4056	0.0009
10	0	10	9	0	9	11803.9992	0.0000
10	2	9	9	2	8	12057.5450	-0.0012
10	2	8	9	2	7	12362.1918	0.0005
10	1	9	9	1	8	12486.0540	-0.0009
11	1	11	10	1	10	12709.6535	0.0006
11	0	11	10	0	10	12929.5543	-0.0013
11	2	10	10	2	9	13250.3179	0.0004
11	2	9	10	2	8	13639.7632	-0.0018
11	1	10	10	1	9	13709.0189	0.0014

Table A.3. Rotational transition frequencies and quantum number assignments of benzoic acid-D_2O.

J'	K_a'	K_c'	J	K_a	K_c	Frequency / MHz	Residual / MHz
6	1	6	5	1	5	6689.4949	0.0092
6	0	6	5	0	5	6902.2381	0.0131
6	1	5	5	1	4	7207.1625	0.0104
7	1	7	6	1	6	7798.4638	0.0024
7	0	7	6	0	6	8027.6124	0.0101
7	2	6	6	2	5	8109.0922	0.0000
7	1	6	6	1	5	8401.0980	0.0069
8	0	8	7	0	7	9142.6926	0.0053
8	1	7	7	1	6	9591.3666	-0.0029
9	1	9	8	1	8	10008.8668	-0.0155
9	0	9	8	0	8	10247.2503	-0.0062
9	1	8	8	1	7	10777.2247	-0.0172

Table A.4. Rotational transition frequencies and quantum number assignments of *o*-toluic acid.

J'	K_a'	K_c'	J	K_a	K_c	Frequency / MHz	Residual / MHz
3	1	2	2	1	1	6551.3821	-0.0003
4	1	4	3	1	3	6976.9249	-0.0002
4	0	4	3	0	3	7180.5499	-0.0005
4	2	3	3	2	2	7909.3256	-0.0003
4	3	2	3	3	1	8166.7224	0.0007
4	3	1	3	3	0	8268.7504	-0.0025
8	2	6	8	1	7	8321.3193	-0.0004
6	2	5	6	1	6	8370.8383	-0.0010
5	4	2	5	3	3	8386.4772	-0.0006
6	4	3	6	3	4	8494.9656	-0.0001
7	3	5	7	2	6	8499.7610	0.0017
5	0	5	4	1	4	8531.6256	-0.0002
4	1	3	3	1	2	8565.3368	0.0006
5	1	5	4	1	4	8609.7272	-0.0003
5	0	5	4	0	4	8715.8030	0.0002
4	2	2	3	2	1	8720.7769	0.0011
5	1	5	4	0	4	8793.9037	-0.0009
8	4	5	8	3	6	9244.3895	0.0003
8	3	6	8	2	7	9653.9507	-0.0004
5	2	4	4	2	3	9755.1041	0.0002
6	1	6	5	1	5	10214.0190	0.0004
5	3	3	4	3	2	10215.9616	0.0007
6	0	6	5	0	5	10261.3046	0.0001
5	1	4	4	1	3	10401.2061	0.0010
5	3	2	4	3	1	10537.2328	0.0003
5	2	3	4	2	2	11013.4340	0.0009
6	2	5	5	2	4	11527.6311	0.0007
7	0	7	6	1	6	11790.9173	-0.0005
7	1	7	6	1	6	11802.5072	-0.0002
7	0	7	6	0	6	11821.7334	-0.0004
7	1	7	6	0	6	11833.3232	-0.0002
6	1	5	5	1	4	12041.7618	0.0001
6	3	4	5	3	3	12225.1508	0.0010
6	4	3	5	4	2	12333.6379	0.0002
6	4	2	5	4	1	12414.0476	-0.0015
6	3	3	5	3	2	12930.1272	-0.0006
8	0	8	7	1	7	13379.2282	0.0000
8	1	8	7	1	7	13383.4407	-0.0004
8	0	8	7	0	7	13390.8185	0.0007
8	1	8	7	0	7	13395.0308	0.0001

Table A.5. Rotational transition frequencies and quantum number assignments of *o*-toluic acid monohydrate.

J'	K_a'	K_c'	J	K_a	K_c	Frequency / MHz	Residual / MHz
5	1	5	4	1	4	5308.6728	0.0003
5	0	5	4	0	4	5525.8203	-0.0007
5	2	4	4	2	3	5682.3695	-0.0006
5	2	3	4	2	2	5859.7853	-0.0004
5	1	4	4	1	3	6015.0663	-0.0006
5	1	5	4	0	4	6329.6376	0.0005
6	1	6	5	1	5	6349.9946	-0.0009
6	0	6	5	0	5	6551.0898	-0.0007
6	2	5	5	2	4	6801.6520	-0.0001
6	2	4	5	2	3	7094.0887	0.0006
6	1	5	5	1	4	7185.9722	0.0014
7	1	7	6	1	6	7383.0492	-0.0003
7	0	7	6	0	6	7553.2356	0.0020
7	2	6	6	2	5	7911.7895	0.0009
7	3	5	6	3	4	8040.5871	0.0000
7	3	4	6	3	3	8087.9626	0.0000
7	1	6	6	1	5	8335.9875	0.0009
7	2	5	6	2	4	8341.6283	-0.0009
8	1	8	7	1	7	8408.3638	-0.0006
8	0	8	7	0	7	8541.8123	0.0006
8	1	8	7	0	7	8840.9011	-0.0004
4	2	3	3	1	2	8992.7770	0.0000
8	2	7	7	2	6	9011.5757	-0.0014
8	3	6	7	3	5	9194.9882	0.0007
8	3	5	7	3	4	9286.9634	0.0002
9	1	9	8	1	8	9426.8718	0.0005
8	1	7	7	1	6	9459.5335	-0.0003
9	0	9	8	0	8	9525.2848	-0.0001
8	2	6	7	2	5	9590.7447	-0.0004
9	1	9	8	0	8	9725.9603	-0.0009
9	2	8	8	2	7	10100.0821	0.0004
10	1	10	9	1	9	10439.7173	0.0000
10	0	10	9	0	9	10508.9374	0.0009
9	1	8	8	1	7	10551.4965	-0.0007
9	2	7	8	2	6	10830.4742	0.0001
11	1	11	10	1	10	11448.0896	-0.0004

Table A.6. Rotational transition frequencies and quantum number assignments of the lowest-energy isomer of oxalic acid monohydrate (0^- state).

J'	K_a'	K_c'	J	K_a	K_c	Frequency / MHz	Residual / MHz
3	1	3	2	1	2	8413.7174	0.0000
3	0	3	2	0	2	8930.8369	-0.0004
3	2	2	2	2	1	9442.1557	-0.0013
4	3	1	4	2	2	9583.5619	0.0000
3	1	3	2	0	2	9758.8613	-0.0015
3	2	1	2	2	0	9953.4680	-0.0008
3	1	2	2	1	1	10295.0558	0.0009
4	0	4	3	1	3	10657.9880	0.0003
4	1	4	3	1	3	11095.9375	0.0001
4	3	2	4	2	3	11203.2875	-0.0003
4	0	4	3	0	3	11486.0135	0.0003
4	1	4	3	0	3	11923.9612	-0.0017
2	2	1	1	1	0	12452.3456	0.0007
4	2	3	3	2	2	12481.4708	-0.0008
4	3	2	3	3	1	12816.0809	0.0010
4	3	1	3	3	0	12927.0844	0.0009
2	2	0	1	1	1	13223.1275	-0.0016
5	0	5	4	1	4	13507.4483	0.0011
4	1	3	3	1	2	13518.8489	0.0016
4	2	2	3	2	1	13582.7332	0.0008
5	1	5	4	1	4	13714.7686	0.0002
5	0	5	4	0	4	13945.3970	0.0002
5	1	5	4	0	4	14152.7179	-0.0002
3	2	2	2	1	1	14966.2190	0.0009
5	2	4	4	2	3	15432.9736	-0.0010
5	4	2	4	4	1	16040.5891	0.0007
5	3	3	4	3	2	16043.7399	-0.0013
5	4	1	4	4	0	16057.8242	-0.0006
6	0	6	5	1	5	16195.5661	0.0000
6	1	6	5	1	5	16286.7517	-0.0010
6	0	6	5	0	5	16402.8870	-0.0004
5	3	2	4	3	1	16404.5763	-0.0001
6	1	6	5	0	5	16494.0750	0.0012
5	1	4	4	1	3	16521.0327	0.0002
4	2	3	3	1	2	17152.6365	0.0016
5	2	3	4	2	2	17207.0899	-0.0005
3	2	1	2	1	2	17515.3050	-0.0003

Table A.7. Rotational transition frequencies and quantum number assignments of the lowest-energy isomer of oxalic acid monohydrate (0^+ state).

J'	K_a'	K_c'	J	K_a	K_c	Frequency / MHz	Residual / MHz
3	1	3	2	1	2	8413.7174	0.0016
3	0	3	2	0	2	8930.8369	-0.0025
3	2	2	2	2	1	9442.1747	0.0138
4	3	1	4	2	2	9583.6184	0.0001
3	1	3	2	0	2	9758.8613	-0.0087
3	2	1	2	2	0	9953.4919	0.0137
3	1	2	2	1	1	10295.0558	-0.0106
4	0	4	3	1	3	10657.9880	0.0055
4	1	4	3	1	3	11095.9375	0.0024
4	3	2	4	2	3	11203.3569	-0.0024
4	0	4	3	0	3	11486.0135	0.0003
4	1	4	3	0	3	11923.9612	-0.0046
2	2	1	1	1	0	12452.3914	0.0005
4	2	3	3	2	2	12481.4708	-0.0029
4	3	2	3	3	1	12816.0809	-0.0023
4	3	1	3	3	0	12927.0844	-0.0045
2	2	0	1	1	1	13223.1821	0.0000
5	0	5	4	1	4	13507.4483	0.0048
4	1	3	3	1	2	13518.8489	-0.0091
4	2	2	3	2	1	13582.7332	-0.0118
5	1	5	4	1	4	13714.7686	0.0022
5	0	5	4	0	4	13945.3970	0.0009
5	1	5	4	0	4	14152.7179	-0.0011
3	2	2	2	1	1	14966.2612	0.0024
5	2	4	4	2	3	15432.9736	0.0005
5	4	2	4	4	1	16040.5891	0.0027
5	3	3	4	3	2	16043.7399	-0.0019
5	4	1	4	4	0	16057.8242	0.0008
6	0	6	5	1	5	16195.5661	0.0008
6	1	6	5	1	5	16286.7517	-0.0012
6	0	6	5	0	5	16402.8870	-0.0013
5	3	2	4	3	1	16404.5763	-0.0066
6	1	6	5	0	5	16494.0750	-0.0008
5	1	4	4	1	3	16521.0327	-0.0060
4	2	3	3	1	2	17152.6728	0.0066
5	2	3	4	2	2	17207.1190	0.0160
3	2	1	2	1	2	17515.3700	0.0016

Table A.8. Rotational transition frequencies and quantum number assignments of the second lowest-energy isomer of oxalic acid monohydrate (0^- state).

J'	K_a'	K_c'	J	K_a	K_c	Frequency / MHz	Residual / MHz
3	0	3	2	0	2	7438.4068	-0.0018
3	2	2	2	2	1	7481.9865	-0.0034
3	2	1	2	2	0	7525.5899	-0.0008
3	1	2	2	1	1	7864.9217	0.0020
5	0	5	4	1	4	8789.2820	-0.0005
2	1	2	1	0	1	9230.4129	-0.0005
4	1	4	3	1	3	9435.0948	0.0016
4	0	4	3	0	3	9867.8048	-0.0010
4	2	3	3	2	2	9967.4500	0.0007
4	2	2	3	2	1	10075.6165	0.0004
4	1	3	3	1	2	10473.0819	0.0014
3	1	3	2	0	2	11338.7411	-0.0006
5	1	5	4	1	4	11775.2092	-0.0002
5	0	5	4	0	4	12256.9037	0.0007
5	2	4	4	2	3	12445.6059	0.0000
5	2	3	4	2	2	12658.5731	0.0007
5	1	4	4	1	3	13068.8098	0.0015
3	2	1	3	1	2	13178.5891	0.0000
4	1	4	3	0	3	13335.4276	0.0012
2	2	0	2	1	1	13517.9178	-0.0002
6	1	6	5	1	5	14104.3593	-0.0005
6	0	6	5	0	5	14600.8902	0.0004
6	2	5	5	2	4	14914.6701	-0.0008
6	1	5	5	1	4	15647.8880	-0.0020
7	1	7	6	1	6	16421.7108	-0.0008
7	0	7	6	0	6	16900.2087	0.0005
7	2	6	6	2	5	17372.9088	0.0009

Table A.9. Rotational transition frequencies and quantum number assignments of the second lowest-energy isomer of oxalic acid monohydrate (0^+ state).

J'	K_a'	K_c'	J	K_a	K_c	Frequency / MHz	Residual / MHz
3	0	3	2	0	2	7438.4068	-0.0003
3	2	2	2	2	1	7481.9865	-0.0035
3	2	1	2	2	0	7525.5899	-0.0011
3	1	2	2	1	1	7864.9217	0.0010
5	0	5	4	1	4	8789.2290	-0.0038
2	1	2	1	0	1	9230.4670	0.0007
4	1	4	3	1	3	9435.0948	0.0069
4	0	4	3	0	3	9867.8048	0.0011
4	2	3	3	2	2	9967.4500	0.0008
4	2	2	3	2	1	10075.6165	0.0002
4	1	3	3	1	2	10473.0819	-0.0011
3	1	3	2	0	2	11338.7895	-0.0012
5	1	5	4	1	4	11775.2092	0.0044
5	0	5	4	0	4	12256.9037	0.0030
5	2	4	4	2	3	12445.6059	0.0002
5	2	3	4	2	2	12658.5731	0.0014
5	1	4	4	1	3	13068.8098	0.0005
3	2	1	3	1	2	13178.7574	0.0008
4	1	4	3	0	3	13335.4628	-0.0087
2	2	0	2	1	1	13518.0893	0.0011
6	1	6	5	1	5	14104.3593	0.0021
6	0	6	5	0	5	14600.8902	0.0016
6	2	5	5	2	4	14914.6701	-0.0006
6	1	5	5	1	4	15647.8880	-0.0006
7	1	7	6	1	6	16421.7108	-0.0021
7	0	7	6	0	6	16900.2087	-0.0015
7	2	6	6	2	5	17372.9088	0.0006

Table A.10. Rotational transition frequencies and quantum number assignments of 1-methylnaphthalene.

J'	K_a'	K_c'	J	K_a	K_c	Frequency / MHz	Residual / MHz
5	1	5	4	0	4	7869.7251	0.0010
4	2	2	3	2	1	8128.0811	-0.0012
5	1	4	4	2	3	8230.1119	0.0008
5	2	4	4	2	3	8895.5740	0.0015
4	2	3	3	1	2	9019.0185	-0.0007
6	0	6	5	1	5	9198.3039	0.0020
6	1	6	5	1	5	9210.2517	-0.0027
6	0	6	5	0	5	9233.4406	-0.0025
6	1	6	5	0	5	9245.3947	-0.0009
5	1	4	4	1	3	9417.1262	-0.0016
5	3	3	4	3	2	9418.6988	-0.0015
5	4	2	4	4	1	9464.1728	0.0019
5	4	1	4	4	0	9498.2649	0.0000
3	2	1	2	1	2	9643.0810	-0.0005
5	3	2	4	3	1	9857.3241	-0.0010
5	2	4	4	1	3	10082.5899	0.0007
6	1	5	5	2	4	10155.0704	0.0016
5	2	3	4	2	2	10206.7686	-0.0004
3	3	1	2	2	0	10333.4961	0.0002
6	2	5	5	2	4	10470.4073	0.0008
3	3	0	2	2	1	10488.9723	-0.0010
7	0	7	6	1	6	10632.2402	-0.0004
7	1	7	6	1	6	10636.1208	-0.0001
7	0	7	6	0	6	10644.1931	0.0001
7	1	7	6	0	6	10648.0736	0.0002
6	1	5	5	1	4	10820.5321	0.0019
6	2	5	5	1	4	11135.8687	0.0008
6	3	4	5	3	3	11236.8870	0.0013
6	4	3	5	4	2	11412.9603	-0.0012
7	1	6	6	2	5	11847.2809	0.0003
4	3	2	3	2	1	11915.9202	0.0014
8	0	8	7	1	7	12056.3641	0.0006
8	1	8	7	1	7	12057.5815	-0.0005
8	0	8	7	0	7	12060.2444	0.0005
8	1	8	7	0	7	12061.4625	0.0001
6	2	4	5	2	3	12112.4120	0.0004
6	3	3	5	3	2	12119.7117	0.0003
7	1	6	6	1	5	12162.6179	-0.0004
4	3	1	3	2	2	12670.0656	0.0009
7	3	5	6	3	4	12972.5942	-0.0006
5	3	3	4	2	2	13206.5358	-0.0010
8	1	7	7	2	6	13391.6737	-0.0010
8	2	7	7	2	6	13442.0630	-0.0008

Table A.10 continued. Rotational transition frequencies and quantum number assignments of 1-methylnaphthalene.

J'	K_a'	K_c'	J	K_a	K_c	Frequency / MHz	Residual / MHz
9	0	9	8	1	8	13477.1133	0.0009
9	1	9	8	1	8	13477.4852	-0.0004
9	0	9	8	0	8	13478.3319	0.0010
9	1	9	8	0	8	13478.7034	-0.0007
8	2	7	7	1	6	13573.6553	-0.0004

Table A.11. Rotational transition frequencies and quantum number assignments of 2-methylnaphthalene.

J'	K_a'	K_c'	J	K_a	K_c	State	Frequency / MHz	Residual / MHz
5	1	5	4	1	4	A	6800.1010	0.0011
5	1	5	4	1	4	E	6800.8682	0.0008
5	0	5	4	0	4	E	7078.5153	0.0016
5	0	5	4	0	4	A	7078.8459	0.0005
5	2	4	4	2	3	A	7281.2551	0.0003
5	2	4	4	2	3	E	7314.9415	-0.0022
5	3	3	4	3	2	A	7345.2851	0.0008
5	3	2	4	3	1	E	7350.1874	-0.0014
5	3	3	4	3	2	E	7350.8029	-0.0012
5	3	2	4	3	1	A	7355.8616	0.0003
5	2	3	4	2	2	E	7476.9202	-0.0018
5	2	3	4	2	2	A	7510.6579	0.0007
5	1	4	4	1	3	E	7708.2229	0.0028
5	1	4	4	1	3	A	7709.3546	-0.0005
6	1	6	5	1	5	A	8133.7481	0.0003
6	1	6	5	1	5	E	8134.1001	0.0010
6	0	6	5	0	5	E	8391.0712	-0.0009
6	0	6	5	0	5	A	8391.4946	-0.0005
6	2	5	5	2	4	A	8715.2683	-0.0002
6	2	5	5	2	4	E	8734.4484	-0.0015
6	3	4	5	3	3	A	8823.8814	0.0000
6	3	4	5	3	3	E	8837.5479	-0.0009
6	3	3	5	3	2	E	8837.9543	-0.0003
6	3	3	5	3	2	A	8851.7725	0.0003
6	2	4	5	2	3	E	9073.9783	-0.0016
6	2	4	5	2	3	A	9093.2093	0.0005
6	1	5	5	1	4	E	9208.7829	0.0026
6	1	5	5	1	4	A	9209.6489	-0.0007
7	1	7	6	1	6	A	9456.7313	0.0010
7	1	7	6	1	6	E	9456.8546	0.0003
7	0	7	6	0	6	E	9673.9816	-0.0013
7	0	7	6	0	6	A	9674.4719	-0.0004
7	2	6	6	2	5	A	10137.4561	0.0003
7	2	6	6	2	5	E	10146.9015	-0.0070
7	4	4	6	4	3	A	10291.7463	0.0015
7	4	4	6	4	3	E	10292.2396	0.0010
7	4	3	6	4	2	E	10293.1103	-0.0013
7	4	3	6	4	2	A	10293.8260	-0.0003
7	3	5	6	3	4	A	10303.9625	0.0001
7	3	5	6	3	4	E	10330.5609	0.0023
7	3	4	6	3	3	E	10338.8190	0.0018
7	3	4	6	3	3	A	10365.5422	0.0015
7	1	6	6	1	5	E	10682.0775	0.0040

Table A.11 continued. Rotational transition frequencies and quantum number assignments of 2-methylnaphthalene.

J'	K_a'	K_c'	J	K_a	K_c	State	Frequency / MHz	Residual / MHz
7	1	6	6	1	5	A	10682.8840	-0.0008
7	2	5	6	2	4	E	10683.0753	-0.0023
7	2	5	6	2	4	A	10692.6397	0.0005
8	1	8	7	1	7	E	10769.7263	0.0000
8	1	8	7	1	7	A	10769.7452	0.0018
8	0	8	7	0	7	E	10939.6389	-0.0024
8	0	8	7	0	7	A	10940.1582	-0.0002
8	2	7	7	2	6	A	11546.2656	-0.0002
8	2	7	7	2	6	E	11550.9677	0.0009
8	3	6	7	3	5	A	11783.3061	0.0002
8	3	6	7	3	5	E	11822.8733	0.0004
8	3	5	7	3	4	E	11863.1659	-0.0030
8	3	5	7	3	4	A	11902.8186	0.0014
9	1	9	8	1	8	E	12073.8869	0.0000
9	1	9	8	1	8	A	12074.0016	0.0021
8	1	7	7	1	6	E	12120.9851	0.0034
8	1	7	7	1	6	A	12121.8378	-0.0016
9	0	9	8	0	8	E	12198.9236	-0.0014
9	0	9	8	0	8	A	12199.4364	0.0008
8	2	6	7	2	5	E	12288.8828	-0.0032
8	2	6	7	2	5	A	12293.8422	0.0014
9	2	8	8	2	7	A	12940.4957	0.0006
9	2	8	8	2	7	E	12942.8715	0.0004
10	1	10	9	1	9	E	13370.8053	-0.0007
10	1	10	9	1	9	A	13370.9879	0.0017
10	0	10	9	0	9	E	13458.5598	-0.0030
10	0	10	9	0	9	A	13459.0474	0.0002
9	1	8	8	1	7	E	13518.9583	0.0015
9	1	8	8	1	7	A	13519.9228	-0.0025
9	2	7	8	2	6	E	13879.8295	0.0004
9	2	7	8	2	6	A	13882.6844	-0.0002
11	1	11	10	1	10	E	14662.0096	-0.0013
11	1	11	10	1	10	A	14662.2412	0.0017
11	0	11	10	0	10	E	14721.4316	-0.0017
11	0	11	10	0	10	A	14721.8876	0.0021

Table A.12. Rotational transition frequencies and quantum number assignments of 1,3-dimethylnaphthalene.

J'	K_a'	K_c'	J	K_a	K_c	State	Frequency / MHz	Residual / MHz
6	1	6	5	1	5	E	7011.2402	0.0011
6	1	6	5	1	5	A	7011.3265	-0.0001
6	0	6	5	0	5	E	7055.3151	-0.0004
6	0	6	5	0	5	A	7055.5187	0.0001
5	1	4	4	1	3	E	7110.9647	0.0009
5	1	4	4	1	3	A	7111.4950	0.0013
5	2	3	4	2	2	A	7438.0024	-0.0006
6	2	5	5	2	4	A	7877.0219	0.0003
6	2	5	5	2	4	E	7877.5876	0.0003
7	0	7	6	1	6	E	8091.8122	0.0006
7	0	7	6	1	6	A	8091.8855	-0.0007
7	1	7	6	1	6	E	8105.155	0.0001
7	1	7	6	1	6	A	8105.2742	-0.0006
5	2	4	4	1	3	E	8106.2559	-0.0004
5	2	4	4	1	3	A	8109.6405	-0.0003
7	0	7	6	0	6	E	8124.6373	-0.0001
7	0	7	6	0	6	A	8124.8147	0.0005
7	1	7	6	0	6	E	8137.9804	-0.0003
7	1	7	6	0	6	A	8138.2028	0.0000
6	1	5	5	1	4	E	8271.9451	-0.0015
6	1	5	5	1	4	A	8272.5636	0.0005
6	3	4	5	3	3	A	8300.2489	-0.0002
7	1	6	6	2	5	A	8735.2467	0.0002
7	1	6	6	2	5	E	8736.2445	-0.0003
6	2	4	5	2	3	A	8932.8800	-0.0002
7	2	6	6	2	5	A	9058.4357	-0.0004
7	2	6	6	2	5	E	9058.4733	-0.0018
8	0	8	7	1	7	E	9187.5324	0.0003
8	0	8	7	1	7	A	9187.6482	-0.0002
8	1	8	7	1	7	E	9192.7723	0.0007
8	1	8	7	1	7	A	9192.9065	-0.0007
8	0	8	7	0	7	E	9200.8758	0.0005
8	0	8	7	0	7	A	9201.0370	0.0000
8	1	8	7	0	7	E	9206.1154	0.0006
8	1	8	7	0	7	A	9206.2947	-0.0011
7	1	6	6	1	5	E	9337.1780	-0.0001
7	1	6	6	1	5	A	9337.8529	0.0008
7	3	5	6	3	4	A	9638.5724	-0.0002
8	2	7	7	2	6	E	10202.7937	0.0001
8	2	7	7	2	6	A	10202.9958	0.0009
9	0	9	8	1	8	E	10275.4329	0.0007
9	0	9	8	1	8	A	10275.5662	-0.0009
9	1	9	8	1	8	E	10277.4372	0.0001

Table A.12 continued. Rotational transition frequencies and quantum number assignments of 1,3-dimethylnaphthalene.

J'	K_a'	K_c'	J	K_a	K_c	State	Frequency / MHz	Residual / MHz
9	1	9	8	1	8	A	10277.5800	0.0000
9	0	9	8	0	8	E	10280.6716	0.0000
9	0	9	8	0	8	A	10280.8258	-0.0001
9	1	9	8	0	8	E	10282.6772	0.0006
9	1	9	8	0	8	A	10282.8380	-0.0008
7	2	5	6	2	4	E	10324.4486	0.0001
7	2	5	6	2	4	A	10325.3605	0.0006
8	1	7	7	1	6	E	10367.6309	0.0000
8	1	7	7	1	6	A	10368.2791	0.0001
9	1	8	8	2	7	E	11248.2323	-0.0015
9	1	8	8	2	7	A	11248.3029	-0.0001
9	2	8	8	2	7	E	11320.1238	0.0008
9	2	8	8	2	7	A	11320.4475	0.0001
10	0	10	9	1	9	E	11360.0914	0.0019
10	0	10	9	1	9	A	11360.2317	-0.0006
10	1	10	9	1	9	E	11360.8418	0.0003
10	1	10	9	1	9	A	11360.9871	-0.0004
10	0	10	9	0	9	E	11362.0945	0.0001
10	0	10	9	0	9	A	11362.2442	-0.0010
9	1	8	8	1	7	E	11405.6269	0.0001
9	1	8	8	1	7	A	11406.2090	0.0005
8	2	6	7	2	5	E	11587.4995	0.0002
8	2	6	7	2	5	A	11588.4597	-0.0002
11	1	11	10	1	10	E	12443.7508	0.0005
11	1	11	10	1	10	A	12443.8964	-0.0012
11	0	11	10	0	10	E	12444.2258	0.0010
11	0	11	10	0	10	A	12444.3735	-0.0004

Table A.13. Rotational transition frequencies and quantum number assignments of 1,2-dimethylnaphthalene.

J'	K_a'	K_c'	J	K_a	K_c	State	Frequency / MHz	Residual / MHz
5	2	4	4	2	3	AA	6596.3305	-0.0009
5	1	4	4	1	3	EA	7061.0702	-0.0130
5	1	4	4	1	3	EE	7061.0702	0.0040
5	1	4	4	1	3	EE'	7061.0702	-0.0063
5	1	4	4	1	3	AE	7061.4561	-0.0027
5	1	4	4	1	3	AA	7061.4746	0.0039
5	2	3	4	2	2	AE	7095.0884	-0.0008
5	2	3	4	2	2	AA	7095.1114	-0.0065
6	1	6	5	1	5	EA	7138.0834	0.0036
6	1	6	5	1	5	EE	7138.0834	0.0090
6	1	6	5	1	5	EE'	7138.0834	0.0106
6	1	6	5	1	5	AE	7138.1579	-0.0049
6	1	6	5	1	5	AA	7138.1579	-0.0110
6	0	6	5	0	5	EE	7254.6472	0.0028
6	0	6	5	0	5	EE'	7254.6472	0.0026
6	0	6	5	0	5	EA	7254.6676	0.0050
6	0	6	5	0	5	AE	7254.6840	-0.0061
6	0	6	5	0	5	AA	7254.7057	-0.0024
6	2	5	5	2	4	EA	7859.5879	0.0018
6	2	5	5	2	4	EE'	7859.5879	0.0213
6	2	5	5	2	4	EE	7859.6322	0.0111
6	2	5	5	2	4	AA	7859.8376	-0.0054
6	2	5	5	2	4	AE	7859.8494	-0.0014
6	3	3	5	3	2	AE	8245.5720	-0.0045
6	3	3	5	3	2	AA	8246.1954	-0.0044
7	1	7	6	1	6	EE	8270.7574	0.0049
7	1	7	6	1	6	EE'	8270.7574	0.0058
7	1	7	6	1	6	EA	8270.7691	0.0086
7	1	7	6	1	6	AE	8270.8293	-0.0060
7	1	7	6	1	6	AA	8270.8412	-0.0025
7	0	7	6	0	6	EE	8340.6600	-0.0012
7	0	7	6	0	6	EE'	8340.6600	-0.0014
7	0	7	6	0	6	EA	8340.6837	0.0050
7	0	7	6	0	6	AE	8340.6999	-0.0075
7	0	7	6	0	6	AA	8340.7251	0.0003
6	1	5	5	1	4	EE	8347.7945	-0.0094
6	1	5	5	1	4	EA	8347.8168	-0.0118
6	1	5	5	1	4	EE'	8347.8168	0.0053
6	1	5	5	1	4	AE	8348.1782	0.0021
6	1	5	5	1	4	AA	8348.1994	0.0024
6	2	4	5	2	3	EE	8596.5889	0.0090
6	2	4	5	2	3	EE'	8596.6390	0.0049
6	2	4	5	2	3	EA	8596.6390	0.0258

Table A.13 continued. Rotational transition frequencies and quantum number assignments of 1,2-dimethylnaphthalene.

J'	K_a'	K_c'	J	K_a	K_c	State	Frequency / MHz	Residual / MHz
6	2	4	5	2	3	AA	8597.1358	-0.0046
6	2	4	5	2	3	AE	8597.1358	0.0016
7	2	6	6	2	5	EE'	9095.8276	0.0104
7	2	6	6	2	5	EA	9095.8276	-0.0062
7	2	6	6	2	5	EE	9095.8276	-0.0129
7	2	6	6	2	5	AA	9096.1037	-0.0044
7	2	6	6	2	5	AE	9096.1037	0.0006
8	0	8	7	1	7	EE'	9352.2002	0.0104
8	0	8	7	1	7	EE	9352.2002	0.0100
8	0	8	7	1	7	EA	9352.2002	0.0086
8	0	8	7	1	7	AE	9352.3010	-0.0065
8	0	8	7	1	7	AA	9352.3010	-0.0081
8	1	8	7	1	7	EE	9393.4324	0.0017
8	1	8	7	1	7	EE'	9393.4324	0.0023
8	1	8	7	1	7	EA	9393.4463	0.0059
8	1	8	7	1	7	AE	9393.4980	-0.0098
8	1	8	7	1	7	AA	9393.5151	-0.0026
8	0	8	7	0	7	EE	9432.3482	-0.0007
8	0	8	7	0	7	EE'	9432.3482	-0.0010
8	0	8	7	0	7	EA	9432.3718	0.0067
8	0	8	7	0	7	AE	9432.3937	-0.0071
8	0	8	7	0	7	AA	9432.4178	0.0009
7	3	5	6	3	4	EA	9453.3823	0.0091
7	3	5	6	3	4	AA	9453.6210	-0.0031
7	3	5	6	3	4	AE	9453.8169	-0.0022
7	3	5	6	3	4	EE	9453.9251	0.0034
7	4	3	6	4	2	AA	9502.8430	-0.0037
7	1	6	6	1	5	EE	9557.3358	0.0010
7	1	6	6	1	5	EE'	9557.3358	-0.0034
7	1	6	6	1	5	EA	9557.3608	-0.0095
7	1	6	6	1	5	AE	9557.6363	0.0051
7	1	6	6	1	5	AA	9557.6664	0.0019
12	4	9	12	3	10	AE	9739.9239	0.0063
7	3	4	6	3	3	EE	9740.8093	0.0137
7	3	4	6	3	3	AE	9741.8668	-0.0047
7	3	4	6	3	3	AA	9742.0407	-0.0028
7	2	5	6	2	4	EE	10063.9899	0.0066
7	2	5	6	2	4	EA	10063.9899	-0.0126
7	2	5	6	2	4	EE'	10063.9899	-0.0214
7	2	5	6	2	4	AE	10064.6194	-0.0002
7	2	5	6	2	4	AA	10064.6194	-0.0054
8	2	7	7	2	6	EE'	10304.1734	0.0078

Table A.13 continued. Rotational transition frequencies and quantum number assignments of 1,2-dimethylnaphthalene.

J'	K_a'	K_c'	J	K_a	K_c	State	Frequency / MHz	Residual / MHz
8	2	7	7	2	6	EE	10304.1734	-0.0032
8	2	7	7	2	6	EA	10304.1952	0.0108
8	2	7	7	2	6	AE	10304.4427	-0.0033
8	2	7	7	2	6	AA	10304.4594	0.0001
9	1	9	8	1	8	EE	10509.6326	0.0035
9	1	9	8	1	8	EE'	10509.6326	0.0042
9	1	9	8	1	8	EA	10509.6472	0.0074
9	1	9	8	1	8	AE	10509.6922	-0.0089
9	1	9	8	1	8	AA	10509.7073	-0.0049
9	0	9	8	0	8	EE	10530.2258	-0.0034
9	0	9	8	0	8	EE'	10530.2258	-0.0038
9	0	9	8	0	8	EA	10530.2455	0.0013
9	0	9	8	0	8	AE	10530.2863	-0.0010
9	0	9	8	0	8	AA	10530.3053	0.0032
8	1	7	7	1	6	EE	10691.9330	-0.0002
8	1	7	7	1	6	EE'	10691.9330	-0.0020
8	1	7	7	1	6	EA	10691.9718	-0.0075
8	1	7	7	1	6	AE	10692.1496	0.0068
8	1	7	7	1	6	AA	10692.1900	0.0019
8	3	6	7	3	5	EA	10784.0555	0.0072
8	3	6	7	3	5	EE	10784.2598	0.0132
8	3	6	7	3	5	AA	10784.4414	-0.0030
8	3	6	7	3	5	AE	10784.5129	0.0007
8	3	5	7	3	4	EE	11283.1303	0.0118
8	3	5	7	3	4	AE	11283.9950	-0.0033
8	3	5	7	3	4	AA	11284.0348	-0.0053
8	2	6	7	2	5	EE	11475.9488	-0.0221
8	2	6	7	2	5	EA	11475.9787	-0.0156
8	2	6	7	2	5	EE'	11475.9787	-0.0120
8	2	6	7	2	5	AE	11476.6606	0.0018
8	2	6	7	2	5	AA	11476.6777	0.0054
9	2	8	8	2	7	EA	11486.2194	0.0080
9	2	8	8	2	7	AE	11486.4555	-0.0011
9	2	8	8	2	7	AA	11486.4742	-0.0024
10	1	10	9	1	9	EE	11621.9514	-0.0025
10	1	10	9	1	9	EE'	11621.9514	-0.0011
10	1	10	9	1	9	EA	11621.9664	0.0015
10	1	10	9	1	9	AE	11622.0176	-0.0032
10	1	10	9	1	9	AA	11622.0313	-0.0013
10	0	10	9	0	9	EE	11632.4733	0.0000
10	0	10	9	0	9	EE'	11632.4733	-0.0013
10	0	10	9	0	9	EA	11632.4908	0.0029

Table A.13 continued. Rotational transition frequencies and quantum number assignments of 1,2-dimethylnaphthalene.

J'	K_a'	K_c'	J	K_a	K_c	State	Frequency / MHz	Residual / MHz
10	0	10	9	0	9	AE	11632.5354	-0.0021
10	0	10	9	0	9	AA	11632.5546	0.0031
9	1	8	8	1	7	EE	11775.2235	-0.0015
9	1	8	8	1	7	EE'	11775.2235	-0.0021
9	1	8	8	1	7	EA	11775.2706	-0.0069
9	1	8	8	1	7	AE	11775.3848	0.0061
9	1	8	8	1	7	AA	11775.4342	0.0033
9	3	7	8	3	6	EA	12090.8789	0.0026
9	3	7	8	3	6	EE	12090.9708	0.0191
9	3	7	8	3	6	AA	12091.3339	0.0008
9	3	7	8	3	6	AE	12091.3523	-0.0019
9	2	7	8	2	6	EE	12816.9827	-0.0220
9	2	7	8	2	6	EA	12817.0226	-0.0179
9	2	7	8	2	6	EE'	12817.0226	0.0027
9	2	7	8	2	6	AE	12817.6766	0.0069
9	2	7	8	2	6	AA	12817.7020	0.0041
9	3	6	8	3	5	EE	12841.9827	0.0096
9	3	6	8	3	5	EE'	12842.0957	0.0165
9	3	6	8	3	5	AA	12842.8667	-0.0032
9	3	6	8	3	5	AE	12842.8667	-0.0022